UNIVERSITÀ DELLA CALABRIA

UNIVERSITA' DELLA CALABRIA

Dipartimento di Fisica

Dottorato di Ricerca in

Scienze e Tecnologie Fisiche, Chimiche e dei Materiali

CICLO XXXVI

TITOLO TESI

Non-destructive material investigation: advanced techniques across disciplines.

Settore Scientifico Disciplinare FIS/01, FIS/07

Coordinatore: Ch.ma Prof.ssa Gabriella Cipparrone

Firma ______________________

Gabriella Cipparrone
10.01.2025 12:31:55
GMT+02:00

Supervisore/Tutor: Ch.mo Prof. Raffaele Giuseppe Agostino

Firma____________________

RAFFAELE
GIUSEPPE
AGOSTINO
09.01.2025
12:26:56
UTC

Supervisore/Tutor: Ch.ma Prof.ssa Rita Guzzi

Firma____________________

RITA
GUZZI

Dottorando: Dott.ssa Maria Caterina Crocco

Firma ____________________

Maria
Caterina
Crocco
09.01.2025
13:53:42
GMT+02:00

Abstract

The advancement of experimental physical techniques has significantly improved the study of materials across a range of scales, from micro to macro, and has allowed for probing various material characteristics with remarkable precision. Among these techniques, X-ray microtomography and Fourier transform infrared (FTIR) spectroscopy stand out as powerful tools that provide critical insights into the structural and molecular properties of materials. This thesis investigates the complementary applications of these techniques across multiple scientific disciplines, including biology, engineering, and photonics.

X-ray microtomography offers high-resolution, non-destructive imaging capabilities, enabling the detailed visualization of internal structures of materials. In contrast, FTIR spectroscopy provides molecular-level information through the identification of vibrational modes, offering a deeper understanding of chemical composition and bonding environments. By combining these techniques, it is possible to bridge the gap between structural and chemical analysis, thus achieving a more holistic characterization of complex systems.

This thesis presents a detailed exploration of how the integration of X-ray microtomography, FTIR spectroscopy, and other experimental methods can lead to a more comprehensive understanding of diverse classes of materials. Through case studies in biological sample analysis, defect analysis in engineering materials, and the characterization of optical fibers, this work demonstrates the synergistic potential of these techniques. The overall findings underscore that a multidisciplinary and integrated approach, utilizing advanced physical techniques, not only enriches scientific understanding but also fosters technological innovation across various fields.

Keywords: X-ray microtomography, Fourier transform infrared spectroscopy, biological systems, engineering, photonics research, multiple sclerosis, hearts, cells.

Riassunto

Il progresso delle tecniche fisiche sperimentali ha notevolmente migliorato lo studio dei materiali su diverse scale, dal micro al macro, e ha permesso di sondare con grande precisione varie caratteristiche dei materiali. Tra queste tecniche, la microtomografia a raggi X e la spettroscopia infrarossa in trasformata di Fourier (FTIR) si distinguono come strumenti potenti che forniscono informazioni fondamentali sulle proprietà strutturali e molecolari dei materiali. Questa tesi indaga le applicazioni complementari di queste tecniche in diversi ambiti scientifici, tra cui la biologia, l'ingegneria e la fotonica. La microtomografia a raggi X offre capacità di imaging ad alta risoluzione e non distruttive, permettendo la visualizzazione dettagliata delle strutture interne dei materiali. Al contrario, la spettroscopia FTIR fornisce informazioni a livello molecolare attraverso l'identificazione delle modalità vibrazionali, offrendo una comprensione più profonda della composizione chimica e degli ambienti di legame. Combinando queste tecniche, è possibile colmare il divario tra l'analisi strutturale e chimica, ottenendo così una caratterizzazione più completa dei sistemi complessi.

Questa tesi presenta un'esplorazione dettagliata di come l'integrazione della microtomografia a raggi X, della spettroscopia FTIR e di altri metodi sperimentali possa portare a una comprensione più esaustiva di diverse classi di materiali. Attraverso studi di caso sull'analisi di campioni biologici, sull'analisi dei difetti nei materiali ingegneristici e sulla caratterizzazione delle fibre ottiche, questo lavoro dimostra il potenziale sinergico di queste tecniche. I risultati complessivi sottolineano che un approccio multidisciplinare e integrato, che utilizza tecniche fisiche avanzate, non solo arricchisce la comprensione scientifica, ma favorisce anche l'innovazione tecnologica in diversi campi.

Parole chiave: microtomografia a raggi X, spettroscopia infrarossa in trasformata di Fourier, sistemi biologici, ingegneria, ricerca fotonica, sclerosi multipla, cuore, cellule.

Contents

Acronyms **v**

List of publications **viii**

Introduction **1**

1 Experimental methods **3**
1.1 X-ray microtomography . . . 3
1.1.1 Principle of computed tomography . . . 6
1.1.2 Data acquisition and tomographic reconstruction . . . 11
1.1.3 Data analysis: Image visualization and post-processing . . . 16
1.1.4 Experimental setup: μTomo1 station - STAR IR . . . 18
1.1.5 μ-CT in biological and solid-state materials . . . 23
1.2 Attenuated total reflection Fourier transformed infrared spectroscopy . . 25
1.2.1 Physical principle of ATR-FTIR spectroscopy and data acquisition 26
1.2.2 Pre-processing and data analysis . . . 34
1.2.3 Experimental setup . . . 35
1.2.4 ATR-FTIR in biological materials . . . 36

2 Advanced Spectroscopic and Imaging Techniques for Diagnosing Neurodegenerative and Cardiovascular Diseases **38**
2.1 Case study 1: Protective effects of PSELT peptide in cardiovascular disease 39
2.1.1 Introduction . . . 40
2.1.2 Scientific rational . . . 40
2.1.3 Materials and methods . . . 41
2.1.4 Results and discussion . . . 45
2.1.5 Conclusions . . . 63
2.2 Case study 2: Discrimination of Multiple Sclerosis Patients Using ATR-FTIR . . . 64
2.2.1 Introduction . . . 64
2.2.2 Scientific rational . . . 66
2.2.3 Materials and methods . . . 67
2.2.4 Results and discussion . . . 70
2.2.5 Conclusions . . . 86
2.3 Case study 3: Characterization of 3D-heart shape in a model of cardiac plasticity . . . 88
2.3.1 Introduction . . . 88
2.3.2 Scientific rational . . . 89

2.3.3 Materials and methods 90
2.3.4 Results and discussion 91
2.3.5 Conclusions 100

3 Characterization of Manufacturing Defects in 3D-Printed Materials Using X-ray Micro-Computed Tomography (μ-CT) 101
3.1 Case study 4: Effects of porosity on specimens printed by selective laser sintering 102
3.1.1 Introduction 103
3.1.2 Scientific rational 104
3.1.3 Materials and methods 104
3.1.4 Results and discussion 108
3.1.5 Conclusions 120
3.2 Case study 5: Evaluation of crack growth in additive manufactured Ti-6Al-4V alloy samples under stress condition 121
3.2.1 Introduction 121
3.2.2 Scientific rational 122
3.2.3 Materials and methods 122
3.2.4 Results and discussion 124
3.2.5 Conclusions 130

4 Application of X-ray μ-CT for Advanced Characterization of Photonics-Related Optical Fibers 131
4.1 Case study 6: Characterization of the index profile of optical fibers . . . 131
4.1.1 Introduction 132
4.1.2 Scientific rational 133
4.1.3 Materials and methods 133
4.1.4 Results and discussion 135
4.1.5 Conclusions 146

Conclusions 147

Bibliography 150

A Appendix 177
A.1 Architectural Terracruda Sculptures of the Silk Roads: New Conservation Insights Through a Diagnostic Approach Based on Non-Destructive X-ray μ-CT 177
A.2 Influence of Chemical Composition and Microvesiculation on the Chromatic Features of the Obsidian of Sierra de las Navajas (Hidalgo, Mexico) 179
A.3 Multiphoton ionization of standard optical fibers 181
A.4 A Non-destructive Archaeometric Study of a Hellenistic Gold Jewel . . . 183
A.5 Experimental Study on the Mechanical Properties of Basalt FRCM Made of Various Matrices: Validation by X-Ray Microtomography 185
A.6 Nonlinear optical effects in natural topaz 187
A.7 A non-destructive archaeometric study of Roman coins 189

Acronyms

μ-CT X-ray microtomography

2D two-dimensional

3D three-dimensional

A atrium

AM additive manufacturing

Aor aorta

ATR attenuated total reflection

ATR-FTIR attenuated total reflection Fourier transformed infrared

AUC area under this curve

AV atrium-ventricular

BA bulbus arteriosus

BBB blood-brain barrier

CA conus arteriosus

CIS clinical isolated syndrome

CNS central nervous system

CSF cerebrospinal fluid

CT computed tomography

DiBEST Department of Biology, Ecology and Earth Sciences

DPBS Dulbecco Phosphate Buffer Saline

EDSS Expanded Disability Status Scale

EPR Electron paramagnetic resonance

FP fingerprint

FTIR Fourier transformed infrared

GIF graded-index fiber

H9C2 rat heart cells

HC healthy control

HR high region

HSA human serum albumin

I/R global ischemia

IgG immunoglobulin

IR infrared

IVS interventricular septum

LA left atrium

LOF lack of fusion

LV left ventricle

LVW left ventricular wall

MIRI myocardial ischemia/reperfusion injury

MMF multimode optical fiber

MRI magnetic resonance imaging

MS multiple sclerosis

PA palmitic acid

PCA-LDA principal component linear discriminant analysis

PCF photonic crystal fiber

PLS-DA partial least-squares discriminant analysis

PM papillary muscle

PP primary progressive

PSELT peptide fragment (43-52) of Selenoprotein T

RA right atrium

RF random forest

ROC Receiver Operating Characteristic

RR relapsing-remitting

RV right ventricle

RVW right ventricular wall

SDD source-detector distance

SELENOT selenoprotein T

SIF step-index fiber

SLM selective laser melting

SLS selective laser sintering

SOD source-object distance

SP secondary progressive

SV sinus venosus

V ventricle

WHO World Health Organization

List of publications

Papers published in scientific journals

This thesis work is based on the following papers published in scientific journals:

1. Carmine Rocca, Anna De Bartolo, Rita Guzzi, **Maria Caterina Crocco**, Vittoria Rago, Naomi Romeo, Ida Perrotta, Ernestina Marianna De Francesco, Maria Grazia Muoio, Maria Concetta Granieri, et al. Palmitate-induced cardiac lipotoxicity is relieved by the redox-active motif of selenot through improving mitochondrial function and regulating metabolic state. *Cells*, 12 (7):1042, 2023. `https://doi.org/10.3390/cells12071042`

2. **Maria Caterina Crocco**, María Fernanda Heredia Moyano, Ferdinanda Annesi, Rosalinda Bruno, Domenico Pirritano, Francesco Del Giudice, Alfredo Petrone, Francesca Condino, and Rita Guzzi. ATR-FTIR spectroscopy of plasma supported by multivariate analysis discriminates multiple sclerosis disease. *Scientific Reports*, 13(1):2565, 2023. `https://doi.org/10.1038/s41598-023-29617-6`

3. Francesca Condino, **Maria Caterina Crocco**, Domenico Pirritano, Alfredo Petrone, Francesco Del Giudice, and Rita Guzzi. A linear predictor based on FTIR spectral biomarkers improves disease diagnosis classification: An application to multiple sclerosis. *Journal of Personalized Medicine*, 13(11):1596, 2023. `https://doi.org/10.3390/jpm13111596`

4. Mariacristina Filice, **Maria Caterina Crocco**, Raffaele G Agostino, Riccardo C Barberi, Daniela Amelio, Sandra Imbrogno, Vincenzo Formoso, Maria Carmela Cerra (2024). "An X-ray computed μ-tomography analysis for the characterization of 3D-heart shape in a model of cardiac plasticity". In **Vascular pharmacology**, 155 (2024) 107310, **Co-first author**. `https://doi.org/10.1016/j.vph.2024.107310`

5. Chiara Morano, **Maria Caterina Crocco**, Vincenzo Formoso, Leonardo Pagnotta. Effect of induced plastic strain on the porosity of PA12 printed through selective laser sintering studied by X-ray computed micro-tomography. *The International Journal of Advanced Manufacturing Technology*, 125(7-8), 3229-3240, 2023. **Co-first author** `https://doi.org/10.1007/s00170-022-10791-2`

6. Danilo A Renzo, **Maria Caterina Crocco**, Carmine Maletta, Leonardo Pagnotta, Emanuele Sgambitterra, Filippo Berto, Franco Furgiuele, Raffaele Filosa, Joseph J Beltrano, Riccardo C Barberi, Raffaele G Agostino, Vincenzo Formoso. X-ray computed μ-tomography analysis to evaluate the crack growth

in an additive manufactured Ti-6Al-4V alloy sample stressed with in-phase axial and torsional loading. *International Journal of Fatigue*, 175, 107727, 2023. `https://doi.org/10.1016/j.ijfatigue.2023.107727`

7. Mario Ferraro, **Maria Caterina Crocco**, Fabio Mangini, Maxime Jonard, Francesco Sangiovanni, Mario Zitelli, Raffaele Filosa, Joseph J Beltrano, Antonio De Luca, Riccardo C Barberi, et al. "X-ray computed μ-tomography for the characterization of optical fibers". In: *Optical Materials Express* 12.11 (2022), 4210–4222- **Co-first and corresponding author** `https://doi.org/10.1364/OME.458951`
8. **Maria Caterina Crocco**, Fabio Mangini, Raffaele Filosa, Andrea solano, Raffaele Agostino, Riccardo Barberi, Vincent Couderc, Mariusz Klimczak, Adam Filipkowski, Ryszard Buczynski, Stefan Wabnitz, Vincenzo Formoso, Mario Ferraro. "Soft glass optical fiber characterization with X-ray computed microtomography". *Optical Materials Express* - (2023) - 14.1: 70-81. `https://doi.org/10.1364/OME.504422`
9. Kevin Kiedrowski, Mario Ferraro, Raphaël Jauberteau, Stefan Wabnitz, **Maria Caterina Crocco**, Vincenzo Formoso, Marco Jupé, Detlev Ristau. “Comparing the Laser-Induced Damage Distribution in POFs with Raytracing Simulations”. *Optical Materials Express.* (2024) - vol. 14, no. 5, 1430–1445. `https://doi.org/10.1364/OME.520782`

Other published papers:

10. Mònica López-Prat, Raffaele Giuseppe Agostino, Sudipa Ray Bandyopadhyay, Begoña Carrascosa, **Maria Caterina Crocco**, Raffaella De Luca, Raffaele Filosa, Vincenzo Formoso, Carla Lancelotti, Noor Agha Noori, et al. “Architectural terracruda sculptures of the silk roads: new conservation insights through a diagnostic approach based on non-destructive X-ray micro-computed tomography ”. *Studies in Conservation* 67.4 (2022), pp. 209–221. `https://doi.org/10.1080/00393630.2020.1862605`
11. Paola Donato, Sandro Donato, Luis Barba, Gino Mirocle Crisci, **Maria Caterina Crocco**, Mariano Davoli, Raffaele Filosa, Vincenzo Formoso, Giancarlo Niceforo, Alejandro Pastrana, et al. “Influence of Chemical Composition and Microvesiculation on the Chromatic Features of the Obsidian of Sierra de las Navajas (Hidalgo, Mexico)”. *Minerals* 12.2 (2022), p. 177. `https://doi.org/10.3390/min12020177`
12. Mario Ferraro, Fabio Mangini, Yifan Sun, Mario Zitelli, Alioune Niang, **Maria Caterina Crocco**, Vincenzo Formoso, RG Agostino, Riccardo Barberi, Antonio De Luca, et al. "Multiphoton ionization of standard optical fibers”. *Photonics Research* 10.6 (2022), pp. 1394–1400. `https://doi.org/10.1364/PRJ.451417`
13. Andrea Smeriglio, Giuseppe Elettivo, Simone Caputo, **Maria Caterina Crocco**, Joseph John Beltrano, Antonello Nucera, Marco Castriota, Vincenzo Formoso, Riccardo Cristoforo Barberi, Armando Taliano Grasso, et al. “A Non-destructive Archaeometric Study of a Hellenistic Gold Jewel”. In: *International Conference Florence HeriTech: the Future of Heritage Science and Technologies. Springer.* 2022, pp. 61–74. `https://doi.org/10.1007/978-3-031-15676-2_5`

14. **Maria Caterina Crocco**, Carmelo Scuro, Raffaele Filosa, Rosamaria Codispoti, Mario Ferraro, Andrea Solano, Raffaele G. Agostino, Riccardo C. Barberi, Renato S. Olivito, and Vincenzo Formoso. "Experimental study on the mechanical properties of Basalt FRCM made of various matrices: validation by X-ray microtomography". *Journal of Materials in Civil Engineering* - (2023). `https://doi.org/10.1061/JMCEE7.MTENG-15116.`

15. Raffaele Filosa, Giuseppe S. Elettivo, Mario Ferraro, Salvatore Procopio, Antonella Nicolino, **Maria Caterina Crocco**, Joseph J. Beltrano, Riccardo C. Barberi, Vincenzo Formoso, Rita Guzzi, Antonio De Luca, Giovanna Agrosì, Gioacchino Tempesta, Raffaele G. Agostino. "Nonlinear optical effects in natural topaz". *Journal of Luminescence* - (2023) - 263, 120076. `https://doi.org/10.1016/j.jlumin.2023.120076`

16. Andrea Smeriglio, Raffaele Filosa, **Maria Caterina Crocco**, Vincenzo Formoso, Riccardo Cristoforo Barberi, Andrea Solano, Maria Cerzoso, Annalisa Polosa, Valerio Cerrone, Raffaele Giuseppe Agostino. "A numismatic study of Roman coins through X-ray fluorescence and X-ray computed μ-tomography analysis". *Acta Imeko* - (2023) - vol. 12, no. 4, article 13, December 2023, identifier: IMEKO-ACTA-12 (2023)-04-13. `https://doi.org/10.21014/actaimeko.v12i4.1504`

17. **Maria Caterina Crocco**, Andrea Smeriglio, Raffaele Filosa, Vincenzo Formoso, Riccardo Cristoforo Barberi, Andrea Solano, Maria Cerzoso, Annalisa Polosa, Valerio Cerrone, Raffaele Giuseppe Agostino. "A non-destructive numismatic and archaeometric study of Roman coins". *Journal of Instrumentation* - (2024) - vol. 10, no. 05, C05025. **Corresponding author**. `https://doi.org/10.1088/1748-0221/19/05/C05025`

Contributions in conference proceedings:

1. P Donato, L Barba, **M.C. Crocco**, M Davoli, R De Rosa, S Donato, R Filosa, G Lanzafame, G Niceforo, A Pastrana, et al. "Study of the micro-vesiculation of the obsidian source of Sierra de Las Navajas (State of Hidalgo, Mexico)". In: *2019 International Obsidian Conference. Prime Rate Kft.* 2021, pp. 9–18.

2. Mario Ferraro, Fabio Mangini, Yifan Sun, Mario Zitelli, Rocco Crescenzi, Alioune Niang, **Maria Caterina Crocco**, Vincenzo Formoso, Raffaele G Agostino, Riccardo Barberi, et al. "Laser-induced damages in silica multimode optical fibers". In: *Fiber Lasers and Glass Photonics: Materials through Applications III.* Vol. 12142. SPIE. 2022, pp. 166–172. `https://doi.org/10.1117/12.2623746`

3. **Maria Caterina Crocco**, Mario Ferraro, Fabio Mangini, Maxime Jonard, Francesco Sangiovanni, Mario Zitelli, Raffaele Filosa, Joseph J Beltrano, Antonio De Luca, Riccardo C Barberi, et al. "X-ray tomography for the refractive index profiling of standard glass optical fibers". In: *Specialty Optical Fibers. Optica Publishing Group. 2022*, SoTh3G–2. `https://doi.org/10.1364/SOF.2022.SoTh3G.2`

4. Ferraro Mario, Mangini Fabio, Sun Yifan, Zitelli Mario, **Crocco Maria Caterina**, Formoso Vincenzo, Agostino Raffaele Giuseppe, Barberi Riccardo Cristoforo, De Luca Antonio, Tonello Alessandro, Couderc Vincent, Wabnitz Stefan.

"Fiber Optics in the Multiphoton Ionization Regime". In *2022 Italian Conference on Optics and Photonics (ICOP)*, pp. 1-4. 2022. IEEE. `https://doi.org/10.1109/ICOP56156.2022.10044375`

5. Smeriglio Andrea, **Crocco Maria Caterina**, Filosa Raffaele, Formoso Vincenzo, Solano Andrea, Barberi Riccardo Cristoforo, Cerzoso Maria, Agostino Raffaele Giuseppe. "Roman coins from the “Brettii and Enotri” museum: a non-destructive archaeometric study by X-ray fluorescence spectroscopy and X-ray microtomography". In: *IMEKO TC-4 International Conference on Metrology for Archaeology and Cultural Heritage.* 2022, pp. 7–11. `https://doi.org/10.21014/tc4-ARC-2022.002`

6. Mario Ferraro, **Maria Caterina Crocco**, Raffaele Filosa, Andrea Solano, Raffaele G. Agostino, Riccardo C. Barberi, Fabio Mangini, Mario Zitelli, Vincent Couderc, Mariusz Klimczak, Adam Filipkowski, Ryszard Buczynski, Stefan Wabnitz, Vincenzo Formoso. “Soft Glass Optical Fiber Characterization with X-Ray Computed Microtomography (STh3G.6) ”. In: *CLEO, Conference on Lasers and Electro-Optics.* 2023. `https://doi.org/10.1364/CLEO-SI.2023.STh3G.6`

7. Kevin Kiedrowski, Mario Ferraro, Raphaël Jauberteau, Stefan Wabnitz, **Maria Caterina Crocco**, Vincenzo Formoso, Marco Jupé, Detlev Ristau. “Laser-Induced Damage Analysis of PMMA Optical Fibers Using Raytracing Simulations and X-Ray Tomography”. In: *Conference: Laser-Induced Damage in Optical Materials 2023.* 2023. `https://doi.org/10.1117/12.2685164`

8. Mario Ferraro, **Maria Caterina Crocco**, Fabio Mangini, Raffaele Filosa, Andrea Solano, Raffaele G. Agostino, Riccardo C. Barberi, Vincent Couderc, Mariusz Klimczak, Adam Filipkowski, Ryszard Buczynski, Stefan Wabnitz, Vincenzo Formoso. "Refractive index profiling of multimode specialty optical fibers by absorption contrast X-ray computed microtomography". In: *EPJ Web Conf.* Volume 287, 2023 EOS Annual Meeting (EOSAM 2023). Article Number 10004, Section Focused Sessions (FS) 1- Special Optical Fibers. `https://doi.org/10.1051/epjconf/202328710004`

9. **M.C. Crocco**, M.F. Heredia Moyano, F. Annesi, R. Bruno, D. Pirritano, F. Del Giudice, A. Petrone, F. Condino, R. Guzzi (2023). "Blood based infrared spectroscopy supported by chemometric methods discriminates Multiple Sclerosis disease". In *Physica Medica: European Journal of Medical Physics*, 115S1 (2023) 102956. `https://doi.org/10.1016/j.ejmp.2023.102956`

10. F. Condino, **M.C. Crocco**, R Guzzi (2024). "PAM clustering algorithm for ATR-FTIR spectral data selection: an application to multiple sclerosis". In **Proceedings of the Statistics and Data Science 2024 Conference. New perspectives on Statistics and Data Science**, (2024), *ISBN Ebook 978-88-5509-645-4.*

Introduction

The study of materials has greatly benefited from advancements in experimental physical techniques. Across various scales, from cells to organs and from powders to engineering components, advanced physical technologies provide valuable insights into the fundamental properties of materials.

Techniques such as X-ray microtomography and Fourier transform infrared spectroscopy enhance our understanding of complex biological systems and material science. The combined use of these techniques offers a comprehensive approach to analyzing diverse samples.

In this thesis, X-ray microtomography and Fourier transform infrared spectroscopy are applied across different scientific fields, including research in biology, engineering, and photonics. Their versatility and applicability make these techniques powerful tools for advancing scientific knowledge and technological innovation, particularly in the biological domain. The synergy between different disciplines in utilizing these techniques fosters interdisciplinary collaboration and drives innovation.

In this context, these techniques have been used for various purposes:

- Analysis of biological samples, including:
- Rat heart (cells and organ) to study the effects of drugs;
- Blood samples for the identification of spectral biomarkers to support the diagnosis of multiple sclerosis;
- Studies on the cardiac plasticity of goldfish hearts under normoxic and hypoxic conditions.
- Development of innovative methods to study defects and fracture propagation in materials for advanced engineering systems.

- Exploration of new methods for investigating optical fibers and characterizing the refractive index profile in the hard X-ray region.

The thesis is structured as follows:

- Chapter 1: the basic concept of the employed techniques is presented; in particular, attention is focused on the physical principles underlying X-ray microtomography (Section 1.1) and Fourier transform infrared spectroscopy (Section 1.2).
- Chapter 2: in Section 2.1 are analyzed the protective effects of a peptide in cardiovascular disease on different scales (cellular size and whole rat heart). In Section 2.2, Fourier transform infrared spectroscopy will be used to analyze plasma samples to discriminate patients with multiple sclerosis from healthy control individuals. Section 2.3 is devoted to the morphological study of goldfish hearts to investigate cardiac plasticity.
- Chapter 3: in Section 3.1 are reported the effects of porosity in samples 3D printed by selective laser sintering. Section 3.2 is devoted to the study of the crack evolution in titanium samples, produced by additive manufacturing, and subjected to mechanical stress.
- Chapter 4: X-ray microtomography will be proposed for the first time as a new method to characterize the refractive index profile of different optical fibers (from glass fibers to soft glass and to plastic fibers). In addition, will be discussed the ability of the technique to detect laser-induced defects on optical fibers.

Chapter 1

Experimental methods

This chapter explains the physical principles underlying the main experimental methods used in this thesis. For other experimental techniques, refer to textbooks. Specifically, in the first paragraph, we will discuss X-ray microtomography (μ-CT), and in the second paragraph, the attenuated total reflection Fourier transformed infrared (ATR-FTIR) spectroscopy.

1.1 X-ray microtomography

Computed tomography (CT) is the cross-sectional representation of an object obtained from transmission or reflection data collected by irradiating the sample with different angles [1]. Tomographic imaging allows the reconstruction of an object from its projections.

The discovery of this technique led to a revolution in medical diagnostics as it allows the investigation of a patient's internal organs in a non-invasively manner. Medical diagnostic imaging uses X-rays to reconstruct images of tissues based on the attenuation coefficient. The finding of the CT scanner is due to Godfrey Hounsfield and Allan Cormack, who in 1979 were awarded the Nobel Prize in medicine [2].

Among the various imaging methodologies, X-ray microtomography (μ-CT) is a non-destructive technique capable of generating three-dimensional (3D) images with micrometer resolution, which is the highest quality and resolution than can be currently obtained in the diagnostic investigation in the clinical setting. The application of this technique embraces different areas of science: innovative materials, engineering, geology, bio-materials, cultural heritage, medicine, etc.

Particular attention deserves the study of samples for biomedical applications. Through the X-ray imaging technique, it is possible to derive the 3D conformation of tissues to identify any changes associated with pathological states [3]. In fact, through μ-CT it is possible to obtain consistent and reproducible images, allowing a quantitative assessment of the 3D microstructures of a tissue.

In the field of biology, X-ray μ-CT is used to study small-size organisms (insects, fish, mice) and/or their organs [4–6]. The reconstructed images can have micrometer resolution and clearly show the density variations within the material being examined. 3D imaging of tissue structures by μ-CT provides information on the spatial heterogeneity and connectivity of the tissue, which is not accessible by two-dimensional (2D) studies. The non-destructive and high resolution of 3D X-ray histology also allows visualization of the entire specimen *ex-vivo* down to the microscopic level, minimizing the risk of inadequate tissue sampling.

In the field of engineering and innovative materials, μ-CT has been used for non-destructive evaluations of correct fabrication and/or for the study of materials under physical stress and/or the identification of internal defects in samples [7, 8].

In recent years, μ-CT has also been greatly interested in various geological-environmental applications, including mineral and oil deposits, hydrogeology, structural geology, environmental geology, etc. An aspect of interest in the geological sciences is the knowledge of the three-dimensional morphology and texture of the rock components. This information may be achieved by μ-CT, which makes it possible through the investigation of the internal features of rocks in a non-destructive way and high resolution. In particular, it is possible to obtain, for example, information on the orientation and distribution of fractures, pores, grains, minerals, sedimentary structures, fossils, and fluid inclusions. This can help to understand how different components interact and influence the overall properties of geological samples [9–11].

In cultural heritage, X-ray μ-CT enables the study of ancient artifacts without damaging them. The analysis can give helpful information, for example, to understand the fabrication techniques of the artifacts and/or the identification of internal fractures that are not accessible from a view of the surface area (for example, SEM measurement) [12–14].

The realization of the CT virtual reconstruction consists of three major steps:

1. Data acquisition (Paragraph 1.1.2);
2. Image reconstruction: processes the acquired data and forms a digital image (Paragraph 1.1.2);
3. Image visualization and post-processing (Paragraph 1.1.3).

Figure 1.1 shows the schematic workflow to obtain a microtomographic image. In particular, a sketch of a μ-CT setup (Figure 1.1a) and an example of projection images obtained for different rotation angles (Figure 1.1b) is shown. Then, the object is reconstructed by numerical routines using the Feldkamp-Davis-Kress back-projection algorithm (Figure 1.1c). Finally, from the obtained data, 3D visualization (Figure 1.1d) and data analysis (Figure 1.1e) are performed.

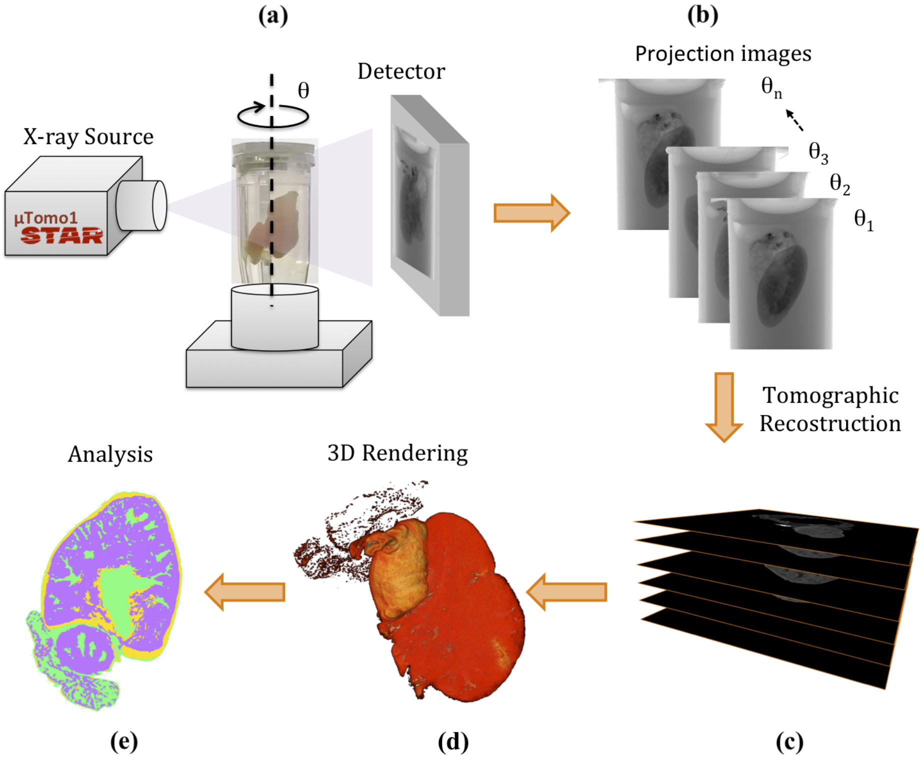

Figure 1.1: Schematic representation of a cone beam microtomography apparatus and processes.

In this thesis work, will be applied μ-CT to different topics in different scientific fields: biology, engineering, and telecommunications.

1.1.1 Principle of computed tomography

X-ray interaction with matter: attenuation and refraction

When a sample is crossed by a monochromatic X-ray beam of intensity I_0, the intensity of the transmitted radiation will decrease, according to Lambert Beer's exponential law for homogeneous objects (eq. 1.1, Figure 1.2):

$$I(x) = I_0 \; e^{\mu_l x} \tag{1.1}$$

where x (cm) is the thickness of the object and μ_l (cm^{-1}) is the linear absorption coefficient. μ_l is related to the mass attenuation coefficient μ ($\frac{cm^2}{g}$) and the density ρ ($\frac{g}{cm^3}$) of the sample from $\mu_l = \mu\rho$ [15, 16]. Therefore, the X-ray beam passing through an object will be attenuated more if it passes through materials with high atomic numbers.

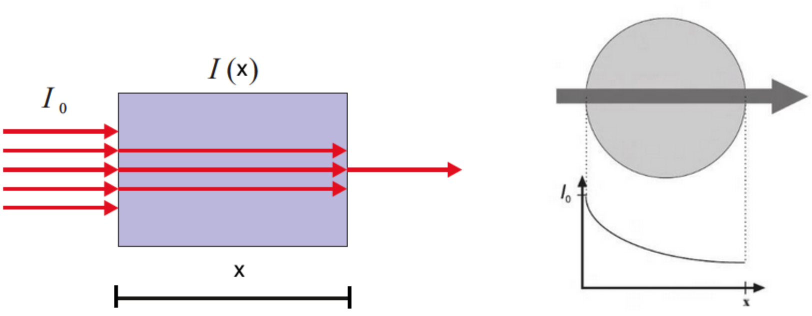

(a) (b)

Figure 1.2: (a) Schematization incident radiation - sample - outgoing radiation [17]. (b) Lambert-Beer law for homogeneous object and monochromatic radiation [18].

For a homogeneous sample, the mass attenuation coefficient is related to the total atomic absorption cross-section σ_a by:

$$\mu = \frac{N_A}{A}\sigma_a \tag{1.2}$$

where A is the atomic weight of the material and N_A is the Avogadro.

For inhomogeneous samples, the mass coefficient will be given by the sum of the absorption cross-sections of the different materials (i) that constitute it:

$$\mu = \frac{N_A}{\sum_i x_i A_i} \sum_i x_i \sigma_{a_i} \tag{1.3}$$

where x atoms of type i are considered.

Then the attenuation of X-ray beam will be high if it interacts with high density and high atomic number samples. Whereas, the attenuation will be minimal for small thickness and low atomic number samples.

Figure 1.3 shows the mass absorption coefficient, on a logarithmic scale, for samples having different Z, such as hydrogen, H, and carbon, C, as a function of photon energy. In particular, it can be seen that the plot related to carbon shows discontinuities (Figure 1.3b), whereas for the hydrogen, the spectrum is continuous (Figure 1.3a). The discontinuity occurs when the energy of the incident photon coincides with the binding energy of the electron of an atomic shell of the examined sample.

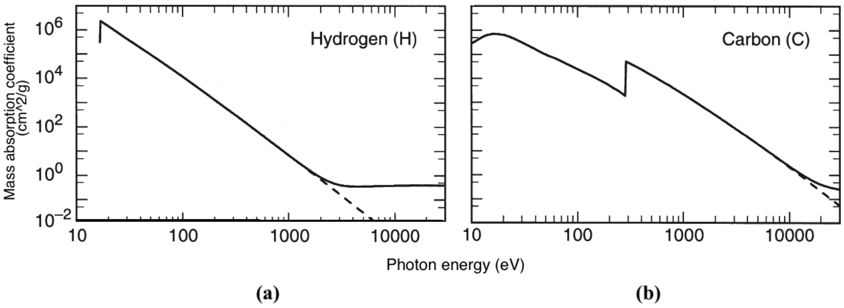

Figure 1.3: Mass absorption coefficient for (a) hydrogen and (b) carbon [16].

It is possible to introduce an important relationship concerning the optical properties of X-rays in interaction with matter by means of the *complex refractive index*:

$$\tilde{n} = 1 - \delta + i\beta \tag{1.4}$$

where the real part δ, which for a long time has been neglected, corresponds to the phase shift due to the scattering of X-rays passing through the sample and the imaginary part β corresponds to the absorption of the wave [19–21].

The two parameters, δ and β, are defined as [22, 23]:

$$\delta = \frac{\lambda}{2\pi}\rho_{\mathrm{A}}\sigma_{\mathrm{p}} \tag{1.5}$$

$$\beta = \frac{\lambda}{4\pi}\rho_{\mathrm{A}}\sigma_{\mathrm{a}} \tag{1.6}$$

where λ is the wavelength, ρ_{A} is the atomic number density, and σ_{p} and σ_{a} represent the phase shift and absorption cross sections, respectively.
The linear absorption coefficient can also be defined in terms of β and λ [20]:

$$\mu_l = \beta \frac{4\pi}{\lambda} \tag{1.7}$$

Figure 1.4 shows plots of δ (red line) and β (blue line) for H and C as a function of photon energy.

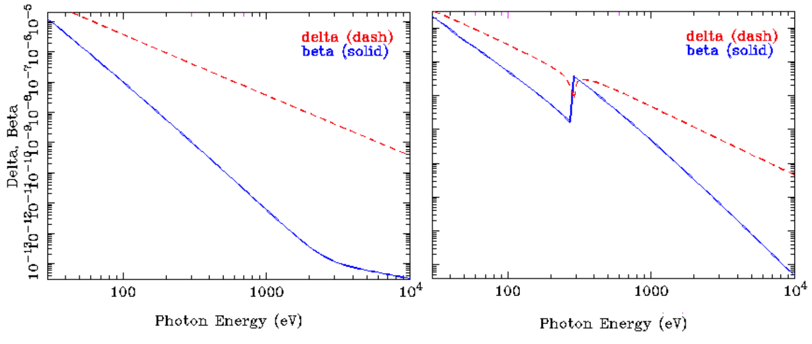

(a) **(b)**

Figure 1.4: δ and β for (a) hydrogen and (b) carbon [24].

Again, discontinuities are observed in C (Figure 1.4b), while the spectrum of H is continuous (Figure 1.4a).
The ratio of the phase shift and the absorption cross sections gives:

$$\frac{\sigma_p}{\sigma_a} = \frac{\delta}{2\beta} \tag{1.8}$$

δ and β have rather small values (Figure 1.5a); however, the phase shift δ is a few orders of magnitude greater than the absorption β (δ is approximately 3 orders of magnitude larger than β, their typical values being 10^{-6} - 10^{-7} and 10^{-9} - 10^{-10} respectively) (Figure 1.5b) [20, 25]. This difference allows the acquisition of phase-contrast images. In particular, the effects of phase perturbation can be detected with a source of adequate spatial coherence, which improves image contrast compared to the standard absorption images [22].

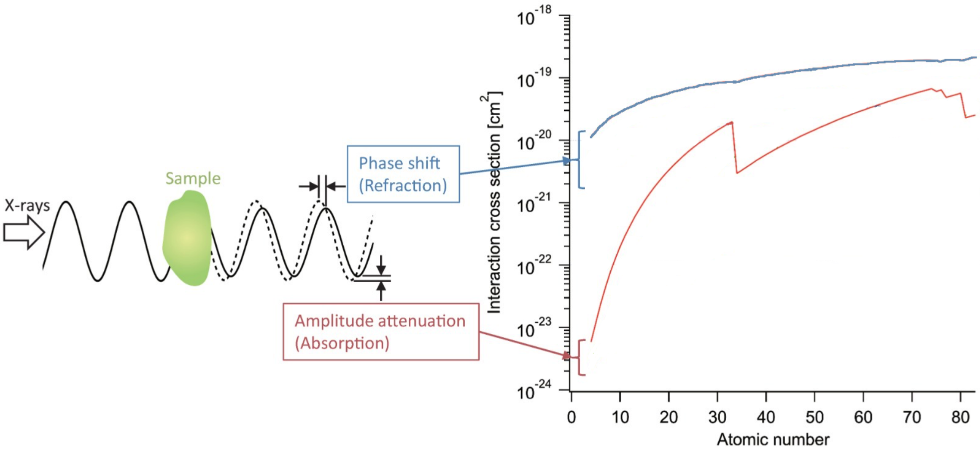

(a)

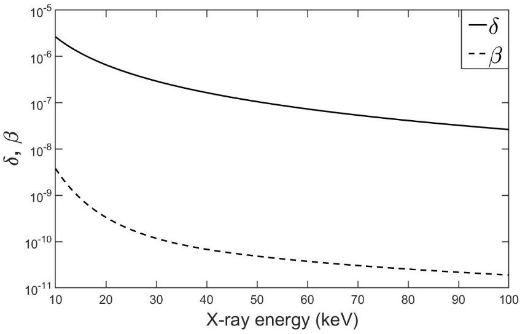

(b)

Figure 1.5: Trend of δ and β vs (a) atomic number and (b) X-ray energy for polymethyl methacrylate (PMMA), commonly utilized in phantoms [26, 27].

The absorption term β, away from the absorption edge, is inversely proportional to the fourth power of the energy of the radiation incident on the sample ($\beta \propto E^{-4}$), while δ is inversely proportional to the square of the energy ($\delta \propto E^{-2}$) [20]. Knowing δ and β dependence on energy and for different Z, let us use $\tilde{n}$ to describe the interaction of X-rays with matter. We can describe the electric field E of a wave passing through a material as follows:

$$E(r) = E_0 e^{ink\cdot r} = E_0 e^{i(1-\delta)k\cdot r} e^{-\beta k\cdot r} \tag{1.9}$$

where k is the wave vector, r is the position vector and E_0 is the amplitude of the electric field.

Figure 1.6 gives an example of how a plane wave changes as it interacts with a sample [28].

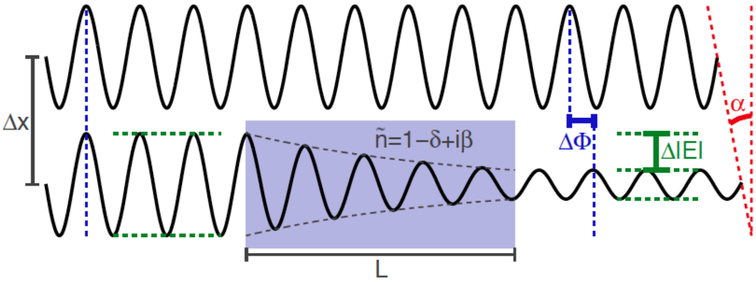

Figure 1.6: Schematic representation of a plane wave interacting with a sample with thickness L [28].

As the wave interacts with the sample with thickness L, this one absorbs part of the wave, resulting in a change in amplitude $\Delta|E|$ and in phase $\Delta\Phi$. The difference in the amplitude is given by:

$$\Delta|E| = E_0(1 - e^{-\beta k L}) \tag{1.10}$$

while the phase difference is given by:

$$\Delta\Phi = \delta k L \tag{1.11}$$

Lambert-Beer law for inhomogeneous samples

The Lambert-Beer law (eq. 1.1) applies to a homogeneous sample and monochromatic radiation (Figure 1.2b).
For a real system characterized by various thickness and composition (different Z, where the linear attenuation coefficient μ_l varies with x), the attenuation of the intensity of the incident monochromatic radiation is obtained from the integral along the beam direction (Figure 1.7a) [18]:

$$I(x) = I_0 e^{-\int_a^b \mu_l(x) dx} \tag{1.12}$$

this provides information on the composition of the object.

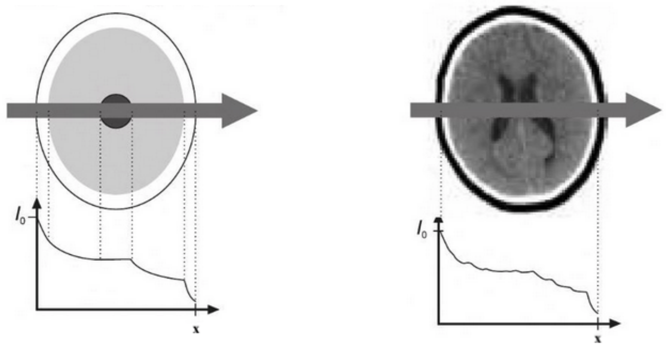

(a) (b)

Figure 1.7: Lambert-Beer law for inhomogeneous object and (a) monochromatic radiation and (b) polychromatic radiation [18].

Classical X-ray sources used for imaging are polychromatic, so energy dependence must also be considered (Figure 1.7b). In this case, eq. 1.12 must be replaced with the following expression [18]:

$$I(x) = \int_0^{E_{max}} I_0(E) e^{-\int_a^b \mu_l(x)dx} dE \tag{1.13}$$

where E_{max} is the maximum energy of the X-ray spectrum.

1.1.2 Data acquisition and tomographic reconstruction

Before tomographic image reconstruction, the acquired data must be preprocessed through numerous steps. These include, for example, the enhancement of geometries due to incorrect alignment between detector and sample. The attenuation profile, p, is calculated by:

$$p = ln(\frac{I_0}{I}) \tag{1.14}$$

The data used for reconstruction are linear with respect to the linear attenuation coefficient. The latter is determined by the sample's composition and density (voxel by voxel). μ_{l} (total) can be decomposed by considering the different linear coefficients $\mu_{\mathrm{l_i}}$ of each Δx_{i} along the attenuation path x as follows:

$$\mu_l x = \mu_{l_1}\Delta x + \mu_{l_2}\Delta x + ... + \mu_{l_N}\Delta x \tag{1.15}$$

The object to be reconstructed can be considered as a distribution in two dimensions of the object's linear attenuation coefficient. Suppose we have collected a series of measurements at different angles (angular increment constant throughout the scan). Each measurement represents the sum (or line integral) of the attenuation coefficients of the object along a particular X-ray path. These measurements form a projection, p. It becomes important to understand how to estimate the attenuation distribution of the scanned object based on these measurements [29].
Assume the case where the object consists of four small blocks in 2D (Fig 1.8). The attenuation coefficients are homogeneous within each block.

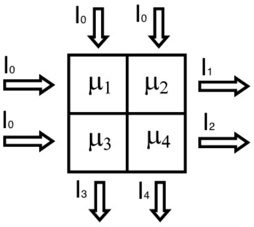

Figure 1.8: A simple case consisting of only four blocks in 2D [29].

Assuming we acquire the projections on two different orthogonal angles, we can write the Lambert-Beer equations as follows:

$$I_1(x) = I_0 e^{-(\mu_1+\mu_2)\mathrm{x}} \tag{1.16}$$

$$I_2(x) = I_0 e^{-(\mu_3+\mu_4)\mathrm{x}}$$

$$I_3(x) = I_0 e^{-(\mu_1+\mu_3)\mathrm{x}}$$

$$I_4(x) = I_0 e^{-(\mu_2+\mu_4)\mathrm{x}}$$

From elementary algebra, we know there is only one solution of the problem because the number of equations equals the number of unknowns. Therefore, we can uniquely solve the distribution of the object attenuation coefficient. The eqs. 1.16 are also valid for a more general case of a sample divided into N blocks with μ_N linear absorption coefficients. The number of projections (N_p) to be acquired is defined by the following equation:

$$N_p = \frac{\pi}{2} N_{pd} \tag{1.17}$$

where N_{pd} is the width of the object in pixels [30].

The projection (p(t,θ)) of the object that will be reconstructed (f(x, y)) in a given direction for a given angle will be provided by the attenuation profile (Figure 1.9)

$$p(t,\theta) = \int_{-\infty}^{+\infty} f'(t,s)ds \tag{1.18}$$

where

$$f'(t,s) = f(x,y) \tag{1.19}$$

f(x, y) can be represented by f'(t, s) in the rotated coordinate system (rotated by θ) [31, 32]:

$$\begin{cases} t = xcos\theta + ysin\theta \\ s = -xsin\theta + ycos\theta \end{cases} \tag{1.20}$$

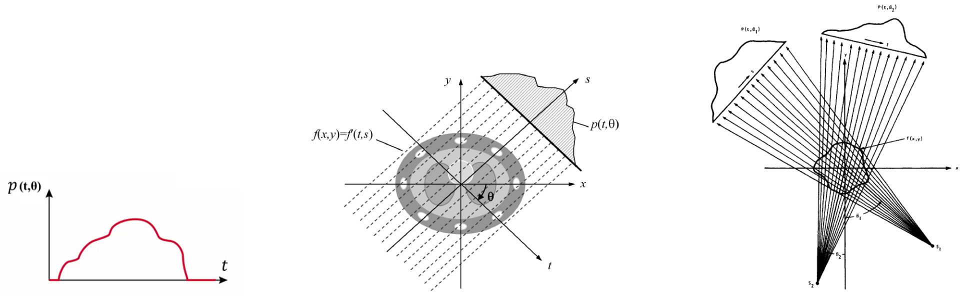

(a) **(b)** **(c)**

Figure 1.9: (a) Example of an attenuation profile [33]; example object to be reconstructed and its attenuation profile for (b) a parallel beam and (c) cone beam. f(x,y) represents the object to be reconstructed, while p(t,θ) denotes the attenuation profile of the object [1, 29].

The theorem at the basis of tomographic image reconstruction is the central slice theorem or Fourier Slice [1, 34]. This theorem relates the Fourier transform of a projection p(t,θ), denoted P(u,θ), to the Fourier transform of the object f(x, y) along a single (one-dimensional) line, denoted by F(u,ν) [33].

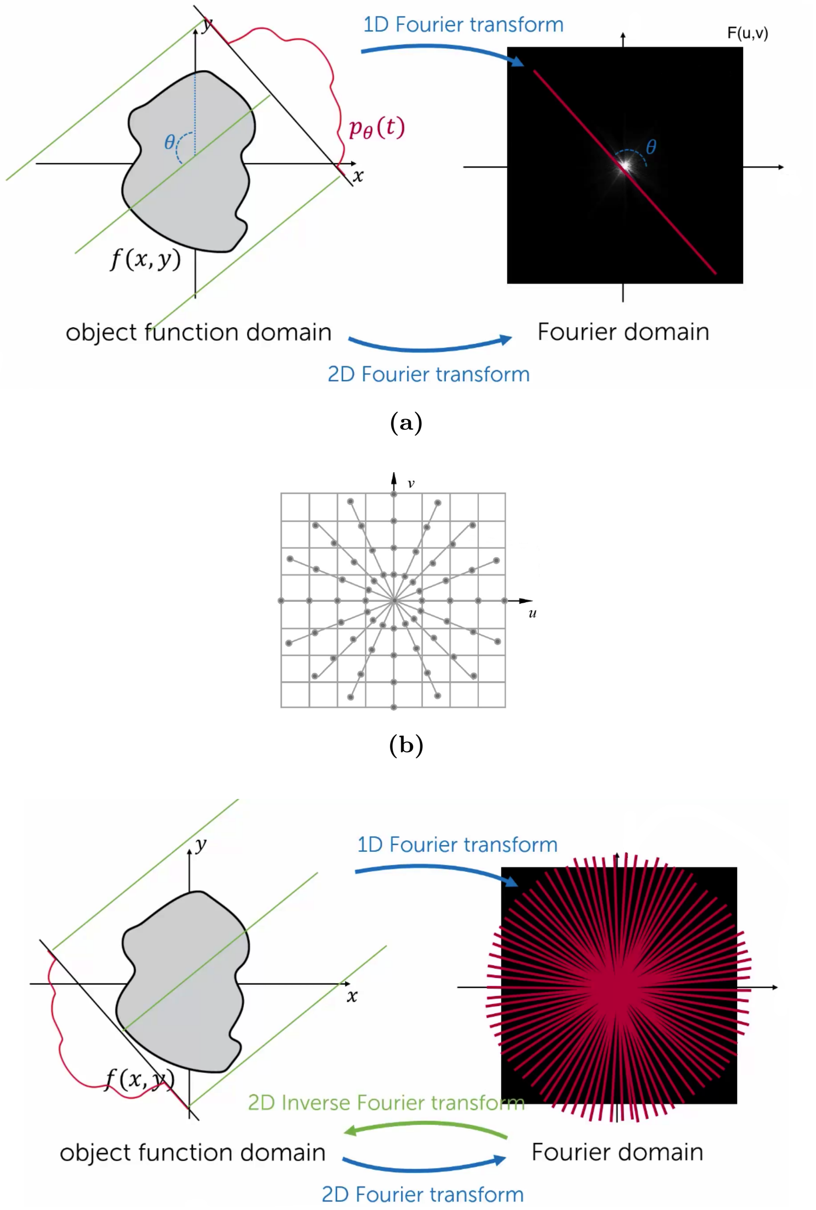

(a)

(b)

(c)

Figure 1.10: Diagram of the Fourier Slice theorem [33].

The collection of projections of the object for a given number of angles (from 0 to 2π) provides an estimate of the Fourier transform of the object along radial lines. The points represent the effective position of the objects of Fourier transform estimates (Figure 1.10a). From the origin of the frequency space, the "density" of points decreases; therefore, high-frequency components are more subject to error than the lower spatial frequencies (Figure 1.10b) [35]. At this point, doing the inverse Fourier transform in

2D on the point set obtained, an estimate of the object is derived (Figure 1.10c). Below are indicated the equations for the Fourier transform of the object and the projection:

$$P(u,\theta) = \int\int_{-\infty}^{+\infty} f'(t,s)e^{-i2\pi ut}dt \tag{1.21}$$

$$F(u,\nu) = \int\int_{-\infty}^{+\infty} f(x,y)e^{-i2\pi(xu+y\ni)}dxdy \tag{1.22}$$

The filtered back-projection algorithm is applied in almost all tomographic applications, which derives from using the Fourier Slice theorem. This filtered back-projection algorithm involves multiplying (filtering) $P(u,\theta)$ by a filter function:

$$H(u) = |u|q(u) \tag{1.23}$$

where:

$$q(u) = \begin{cases} 1, & |u| < \mathit{\Gamma} \\ 0, & else \end{cases} \tag{1.24}$$

and Γ is the Nyquist factor. Sampling must respect this criterion:

$$\Gamma = \frac{1}{2\tau} cycle/mm \tag{1.25}$$

where τ is the sampling interval of the projection in millimeters. The product of $P(u,\theta)$ by H(u) gives:

$$Q(u,\theta) = P(u,\theta)H(u) \tag{1.26}$$

Performing Fourier anti-transform of $Q(u,\theta)$, it is obtained $q(t,\theta)$ (Figure 1.11).

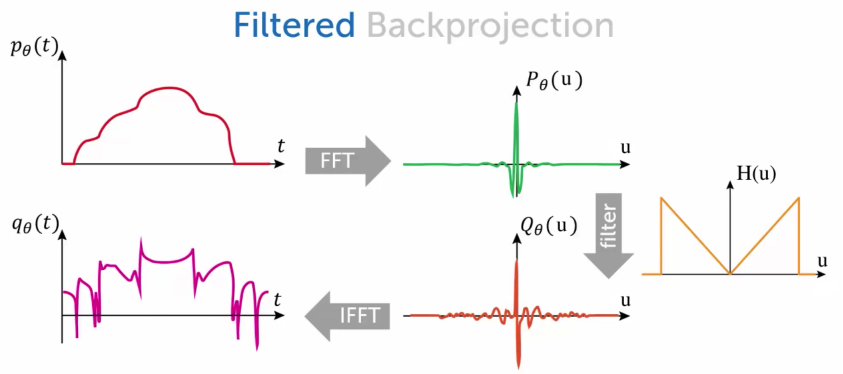

Figure 1.11: Filtered back-projection algorithm [33].

The various back-projections $q(t, \theta)$, for the different angles, are added to obtain the desired image (Figure 1.12).

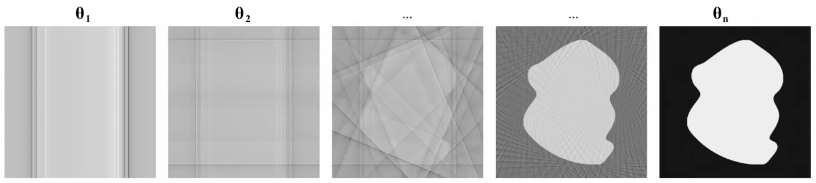

Figure 1.12: Back-projections $q(t, \theta)$ for the different angles [33].

1.1.3 Data analysis: Image visualization and post-processing

The reconstructed tomographic image may be affected by artifacts [36–38]. Artifacts are reconstruction errors that appear in the image but do not belong to the object. They should be recognized, reduced and, whenever possible, eliminated.

The main types of artifacts that can occur in X-ray μ-CT measurements are:

- *Ring artifacts*: derived from detector element failures (Figure 1.13a). These broken elements may appear as white or black pixel values in the image that don't match the object's original values. In the reconstructed image, these appear as circumferences. These can be eliminated by using post-processing operations;

- *Beam Hardening*: when a polychromatic X-ray beam passes through a sample, the photons are attenuated differently depending on the path they encounter. Consequently, the outgoing beam becomes "harder" or more penetrating after it passes through the object. Lower-energy photons are absorbed faster than higher-energy photons (Figure 1.13b). Inhomogeneous beam hardening results in *cupping* (Figure 1.13c) or *streak* (Figure 1.13d) artifacts on the reconstructed image. Also, in this case, the reconstruction image can be improved using post-processing operations;

- *Noise*: scattered radiation or some photons in the direction of higher attenuation can cause noise, which results in degraded image quality and poor contrast resolution (Figure 1.13e). These can be eliminated through the use of filters (smoothing, Gaussian or median filters);
- *Aliasing*: insufficient sampling angles, i.e., data undersampling. It is particularly visible on the edges. In small structures, it manifests as thin bands (Figure 1.13f). Not much correction are possible in the post-processing.

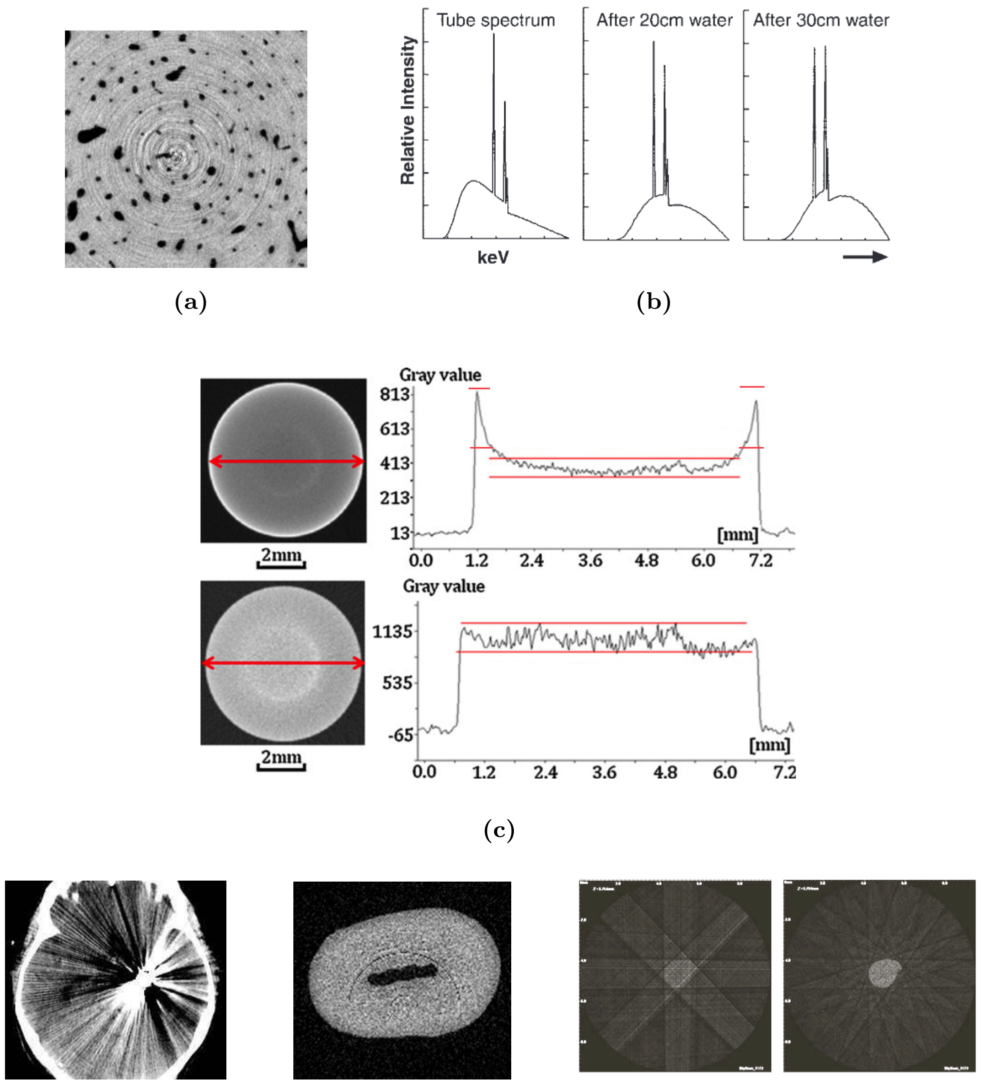

(a) (b)

(c)

(d) (e) (f)

Figure 1.13: Artifacts in reconstructed tomographic image. Example of: (a) ring artifacts, (b) changing energy spectrum of an X-ray beam as it passes through a sample, (c) cupping, (d) streak, (e) noise, (f) aliasing [36–39].

After post-processing of the reconstructed image, data analysis can be performed. Data analysis consists of identifying parameters of scientific interest that depending of sample studied.

1.1.4 Experimental setup: μTomo1 station - STAR IR

The experimental apparatus used in this thesis work for microtomography measurements is part of the STAR research infrastructure and is called the μTomo1 STAR beamline (Figure 1.14). It consists of:

- cone beam microfocus X-ray source (Hamamatsu, 150kV microfocus X-ray source, L12161-07);
- detector (Hamamatsu, flat panel sensor C7942SK-05);
- sample holder;
- motion system;
- PC workstation and software system for data acquisition and analysis.

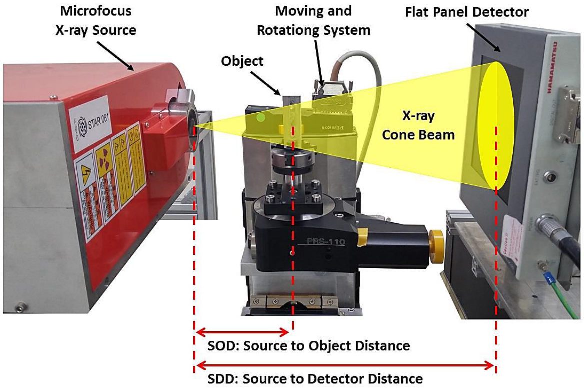

Figure 1.14: μTomo1 STAR beam line [40].

In the following subsections, the characteristics of the various components will be described.

Cone beam microfocus X-ray source

The microfocus and polychromatic X-ray source used in this thesis work is a Hamamatsu model L12161-07 (Figure 1.14). This source works under three different focal spot conditions, specifically:

- 7 or 5 μm - small focus mode;
- 20 μm - middle focus mode;
- 50 μm - large focus mode.

The geometry of the X-ray beam is conical with an opening angle of 43 degrees. The target anode and the cathode are made of tungsten, while the exit window is a 200 nm thick beryllium sheet.

The operating voltage of the tube can vary in a range between 40 and 150 kV, while the operating current of the tube can vary between 10 μA and 500 μA, with a maximum output power that depends on the selected focus mode (small: 10 W or 4 W; middle: 30 W; large: 75 W). If the power is 4 W, it is possible to have a nominal focal spot size of 5 μm in the small focus mode. From the characteristic curve shown in Figure 1.15 it is possible to determine the maximum value of the tube current, once the tube voltage and the focal spot size have been set (in light blue the large focus mode, in green the medium focus mode, and in red the small focus mode).

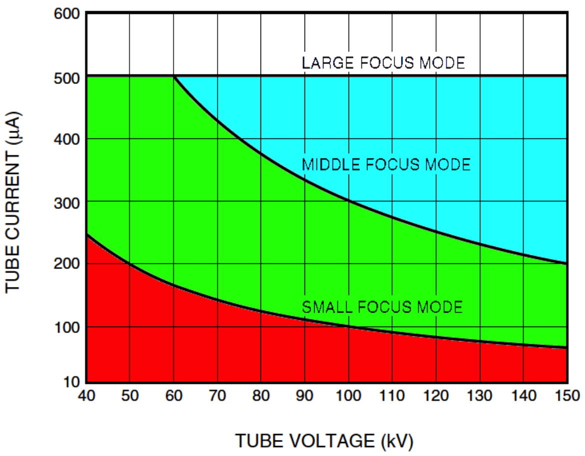

Figure 1.15: Working curves of the microfocus X-ray source Hamamatsu L12161-07 [41].

The size of this focal spot defines the sharpness of the resulting X-ray image. The bigger the focal spot the higher the geometric unsharpness.

Figure 1.16 shows the output spectrum of the X-ray tube used in this thesis work for different voltage values; this consists of a continuous spectrum (bremsstrahlung) with sharp peaks at certain energies (characteristic spectrum).

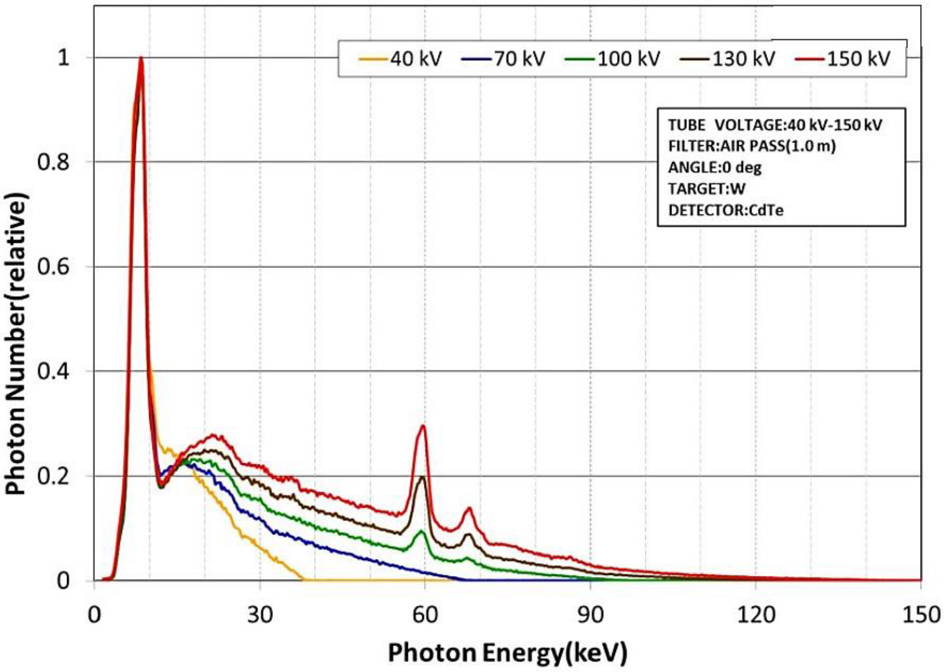

Figure 1.16: Output spectrum of microfocus X-ray sources Hamamatsu L12161-07 at different voltage values. The photon counts were normalized to 1 [41].

Detector

The detector used in this thesis work is a Flat panel sensor Hamamatsu C7942SK-05 (Figure 1.14). This detector is based on two-dimensional arrays of photodiodes CMOS (CCD) directly coupled to a scintillator for X-ray to light conversion. The sensor is composed of a scintillator layer of Gadolinium oxysulfide (Gd2O2S), also called gadolinium sulfoxylate (GOS or Gadox), an inorganic ceramic compound. The detector has 2316 × 2316 active pixels, with a pixel size of 50 μm x 50 μm and the photodiode area is 120 mm × 120 mm. The acquired signal is digitalized and sent to an acquisition card (Frame Grabber). The dynamic range is 12-bit (counts up to 4096). The detector can operate at different pixel binning modalities, namely 1x1, 2x2, and 4x4. The maximum frame rate is 2 in single binning mode and 9 (which is the maximum achievable value) at 4x4 binning. The X-ray energy range is 20 to 150 kV.

Sample holder and motion system

The sample positioning system (by PI miCos Physik Instrumente) provides five degrees of freedom (x, y, ϕ, θ and ω): two linear movements for x,y, one for the rotation stage omega (ω), two stages for tilt angles theta (θ) and phi (ϕ). Figure 1.17 shows a schematic of the uTomo1 beamline sample placement system, where the z-axis represents the direction of propagation of the X-ray beam.

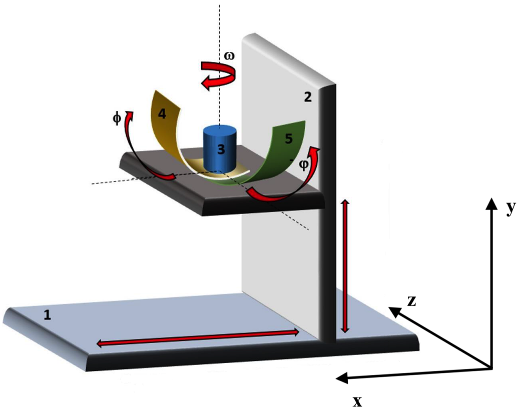

Figure 1.17: Skecth of sample positioning system: (1) x-translator, (2) y-translator, (3) ω-rotator, (4) ϕ-goniometer and (5) ψ-goniometer. The z-axis represents the direction of propagation of the X-ray beam.

The types of motors used for handling are listed below:

1. x-axis: LS-270 Linear Stage for Very High Loads;
2. y-axis: LS-180 Linear Stage for Heavy Loads;
3. ω-rotator: RS-110 Precision Rotation Stage;
4. ϕ-goniometer: WT-90 Goniometer;
5. ψ-goniometer: WT-90 Goniometer.

In addition, the system allows the position of the sample (source-object distance (SOD), Figure 1.14) and the detector (source-detector distance (SDD), Figure 1.14) to be varied with respect to the source. This allows the geometric parameters of the system to be determined, for example, the magnification ratio (M = SOD/SDD) and consequently the scaled pixel size ($\mathrm{P_{size\text{-}scaled} = P_{size\text{-}detector}/M}$).
Defining the magnification and then the scaled pixel size allows images with a resolution ranging from 50 μm (M = 1) to about 5 μm (M $\simeq$ 10).

1.1.5 μ-CT in biological and solid-state materials

As mentioned above, μ-CT is a 3D imaging technique that has applications in numerous fields, including biological and solid-state materials [3–14]. The following discussion concerns the use of μ-CT in the context of biological and solid-state materials, exploring the benefits, challenges, and prospects.

An important advantage of using μ-CT on biological materials is the ability to perform non-destructive analysis, preserving the structure of the sample, which is crucial for further analysis. For example, in tissue biology or biomedical research, μ-CT allows the internal anatomy of organs and tissues to be studied without sectioning the sample, resulting in accurate three-dimensional reconstruction (i.e., virtual histology) [42].

It is particularly useful in the study of soft tissues, such as heart or kidney, but also for bone samples. The micrometer resolution allows the study of morphology and microstructure, which makes μ-CT ideal for studying the structure of tissues and/or small organs and improving understanding of diseases or responses to drug treatments.

Since soft tissues have low absorption contrast, radiopaque agents (e.g., iodine) can be used to increase X-ray attenuation and make it easy to discriminate between different tissue groups. However, care must be taken during staining, as the use of contrast agents may result in image artifacts or difficulties in specimen preparation. To overcome this, phase-contrast μ-CT can be used, which enhances contrast at the edges of soft tissues by exploiting refractive index variations.

Once the images have been acquired, it is important to determine the type of analysis to be performed, based on the proposed goals. For example, in the study of bone regeneration or bone microarchitecture, porosity, bone density, and pore distribution are evaluated; properties that are useful in verifying the effectiveness of materials in regeneration [43, 44]. Or in the case of pathological tissues, such as tumors in ex vivo animal models, once structural changes have been identified, they need to be quantified, evaluating size (e.g., volume), shape, progression, etc [45, 46].

Important applications of μ-CT are also found in the field of solid-state materials. One of the main results is the identification of pores, cracks, and defects within engineering materials, which are essential for improving manufacturing processes, and fundamental to the study of their functional properties, such as permeability, strength [47, 48]. The

μ-CT is often used to perform an analysis of the mechanical properties of solid-state materials, such as fatigue and fracture strength, by studying the distribution of defects and their evolution when subjected to stress, thus allowing prediction of material behavior under stress conditions [47, 48].

Furthermore, μ-CT is particularly useful in the study of composite materials, where the complex interaction between different material phases requires detailed 3D analysis. Composites, being made up of multiple materials with different properties, can present challenges in quality control, especially regarding the distribution and size of the different materials used (such as fibers or reinforcing particles) [49].

μ-CT is, therefore, an extremely versatile tool for both the study of biological and solid-state materials. As its applications are expanding, the continuing evolution of X-ray imaging technology and the development of new data processing techniques promise further improvements in resolution, acquisition speed, and accuracy, opening up new perspectives in many scientific and industrial disciplines.

1.2 Attenuated total reflection Fourier transformed infrared spectroscopy

Infrared (IR) spectroscopy is an absorption spectroscopic technique that is highly sensitive to the chemical composition and structure of molecules; it is very versatile, allowing the application in the study of samples in the liquid, solid, or gaseous state [50]. The high information content present in an infrared spectrum, the high temporal resolution (up to 1μs), the short measurement times, and the small sample amounts required (typically 10-100 μg/μl) make this technique ideal for the analysis of biological systems and especially for the study of structural properties, molecular mechanisms, conformational changes induced by binding between molecules, and folding-unfolding processes of proteins [51].

More recently, Fourier transformed infrared (FTIR) spectroscopy has also been used in medical diagnostic research, and the body of literature on the subject is growing quickly [52]. The method has been used to identify spectral biomarkers in biological systems such as biofluids, including blood and blood components, urine, cells, and tissues. Interestingly, it is possible to distinguish and quantify spectral changes by comparing the experimental profiles of biological samples from healthy and unhealthy people. For instance, these application include neurodegenerative diseases [53, 54], various cancers (brain, breast, and melanoma) [55], COVID-19 [56, 57], and systemic amyloidosis [58]. IR spectroscopy can be applied in different modalities such as attenuated total reflection (ATR) and transmission mode, and may quickly examine samples requiring small quantity and minimal handling.

The analysis of the experimental spectra and the identification of spectral changes are frequently supported by univariate and multivariate statistical analysis.

A typical ATR-FTIR measurements consists of four major steps:

1. sample preparation;
2. data acquisition;
3. pre-processing;
4. data analysis: classification or verification/validation.

Figure 1.18 shows an ATR-FTIR experiment and analysis workflow.

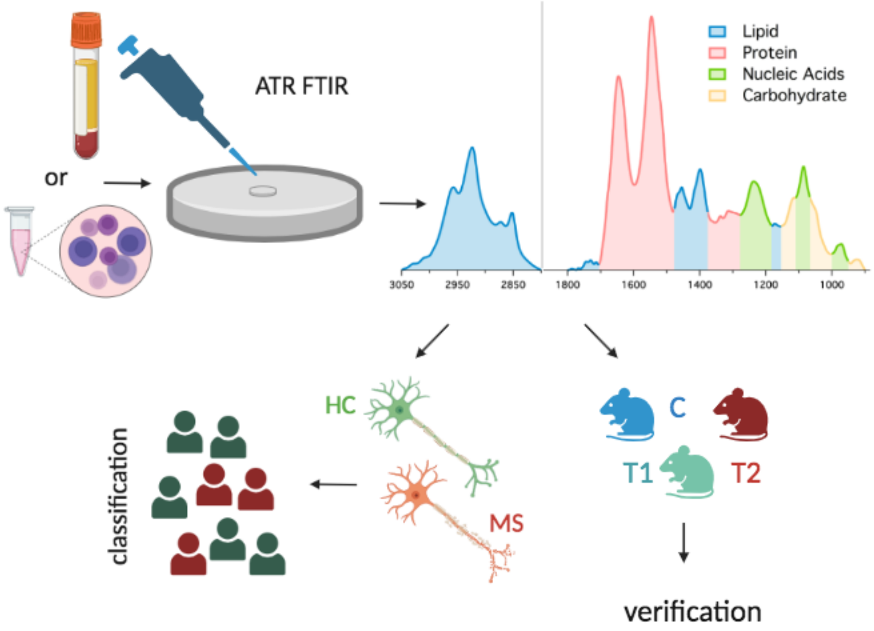

Figure 1.18: Schematic representation of an ATR-FTIR spectroscopy apparatus and processes in biological application.

In particular, a sketch of ATR-FTIR spectroscopy setup and an example of spectrum of a biological system are shown. Then, data analysis is coupled to univariate and multivariate statistical analysis, classification, or verification.
In this thesis, this approach has been applied to investigate rat cardiac cells and plasma samples from healthy individuals and multiple sclerosis patients.

1.2.1 Physical principle of ATR-FTIR spectroscopy and data acquisition

The theory behind FTIR spectroscopy is that two radiation beams will interact and produce an interferogram [50, 59]. The latter is a signal generated in response to the path length difference between the two beams. The Fourier-transform function allows for converting the two domains: frequency and distance.
Before reaching a detector, the radiation from the source passes via an interferometer and a sample. After the signal has been amplified and high-frequency contributions removed by filtering, the data are digitally translated by an analog-to-digital converter and sent to the computer for Fourier processing [50]. A Michelson interferometer, which

has two perpendicularly plane mirrors with one that may move perpendicular to the plane, is the most popular type of interferometer used in FTIR spectrometry (Figure 1.19).

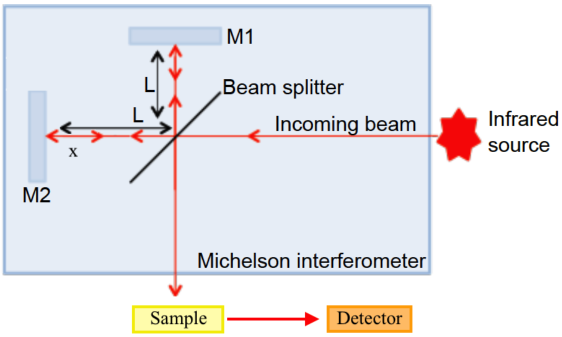

Figure 1.19: Michelson interferometer. Where M1 is the fixed mirror, M2 is the moving mirror, which moves through distance x, and L is the distance from the beam splitter to the mirror [60].

In a Michelson interferometer, an electromagnetic wave is directed to a semi-reflecting mirror (beamsplitter), which transmits part of it and reflects the other part. The reflected part is, in turn, reflected by a fixed mirror (Figure 1.19, M1), while the transmitted part is then reflected by a mirror in motion (M2) at constant velocity. At this point, both beams are sent to the semi-reflecting mirror, where they overlap and reflect onto the samples and, subsequently, sent to the detector. Depending on the optical path difference x, which depends on the position of the moving mirror, the two beams can interfere constructively or destructively. Constructive interference occurs if:

$$2x = 2k\frac{\lambda}{2} \tag{1.27}$$

and destructive interference occurs if:

$$2x = (2k+1)\frac{\lambda}{2} \tag{1.28}$$

where λ is the wavelength of the radiation, and k=(0,1,2,...).

The intensity of the signal arrived at the detector, as a function of the optical path between the two beams, is called the interferogram. This is described by the following equation:

$$I(x) = \int_{0}^{+\infty} I(\nu)cos(2\pi\nu x)d\nu \tag{1.29}$$

where I(ν) represents the intensity of the infrared spectrum as a function of frequency ν. Through the Fourier transform of I(x), it is possible to obtain I(ν):

$$I(\nu) = \int_{-\infty}^{+\infty} I(x)cos(2\pi\nu x)dx \tag{1.30}$$

In practice, to obtain an FTIR spectrum, an interferogram is acquired and, by Fourier Transform, the interferogram is converted into the corresponding FTIR spectra (Figure 1.20a).

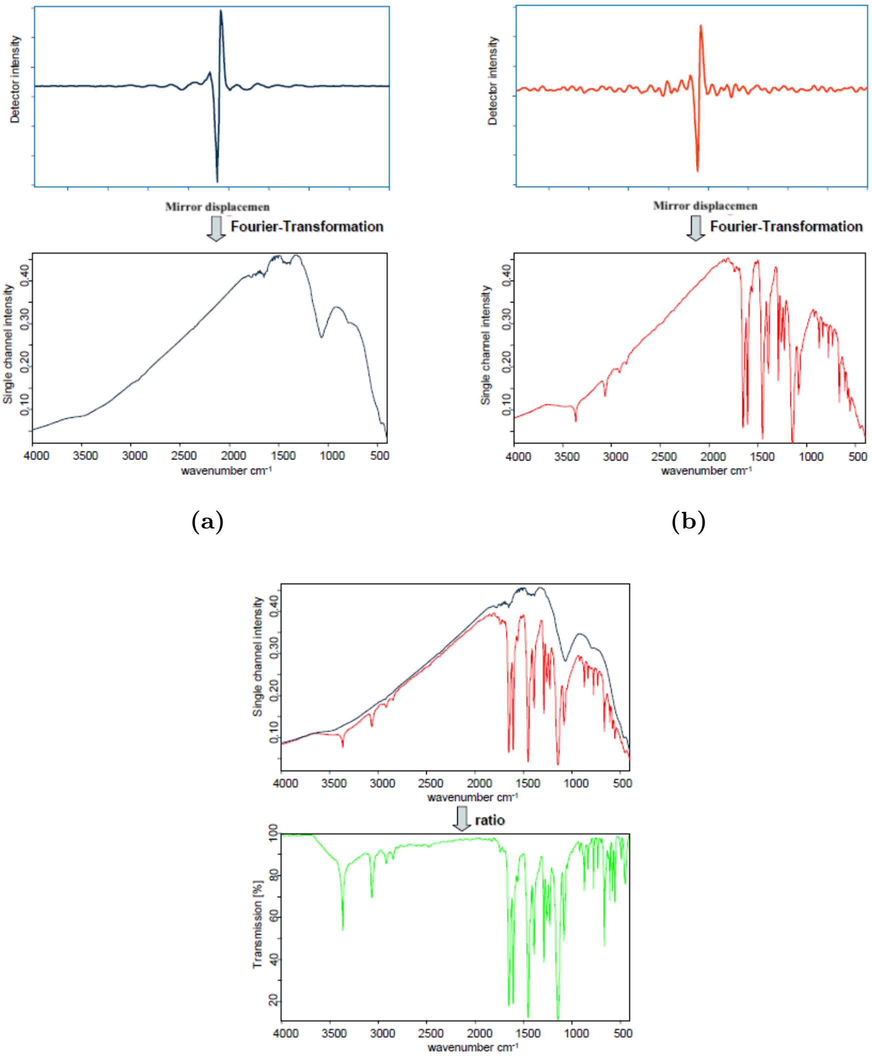

(a) **(b)**

(c)

Figure 1.20: Example of interferogram and corresponding Fourier Transform (FTIR spectrum) for: (a) no sample, (b) sample, and (c) transmittance spectrum [61].

In an FTIR measurement, the interferogram with (S(ν), Figure 1.20a) and without sample (R(ν), Figure 1.20b) are acquired; once the Fourier Transform is applied, by performing the ratio between the two signals, the transmittance spectrum is obtained (T(ν), Figure 1.20c):

$$T(\nu) = \frac{S(\nu)}{R(\nu)} = \frac{I}{I_0} \tag{1.31}$$

where I_0 and I are, respectively, the incident intensity and the intensity of radiation emerging from the sample.

Absorption varies with sample thickness, l, according to Lambert-Beer law [62]:

$$A(\nu) = log\frac{I_0}{I} = c\epsilon(\nu)l \tag{1.32}$$

where A(ν) is the absorbance, c is the sample concentration, $\epsilon(\nu)$ is the molar extinction coefficient. The absorbance and transmittance are, therefore, related by the following equation:

$$A(\nu) = log\frac{1}{T(\nu)} \tag{1.33}$$

Attenuated total reflection

ATR spectroscopy uses the phenomenon of total internal reflection of incident radiation [63–65]. The sample is deposited on a support consisting of a crystal with a high refractive index (ZnSe, Germanium, Diamond, Silicon): the IR beam is reflected several times on the inner surface of the crystal (Figure 1.21), creating an evanescent wave that is projected orthogonally on the sample placed in contact with the crystal.

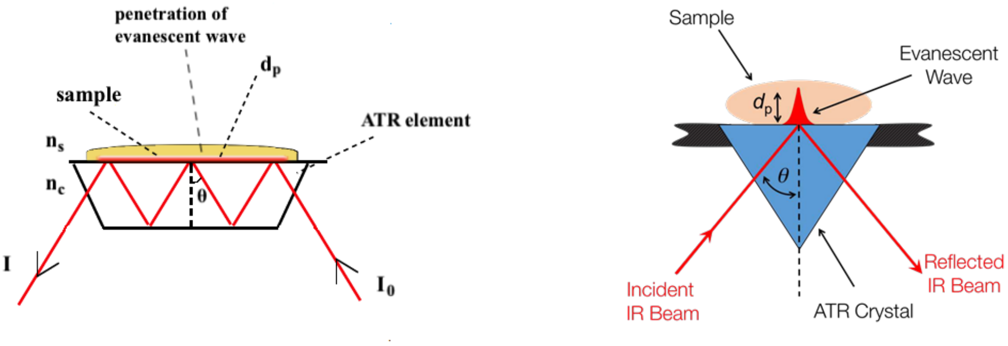

(a) (b)

Figure 1.21: Schematic representation of the ATR setup in infrared spectroscopy [66, 67].

The evanescent wave frequency is equal to that of the incident wave, and it decays exponentially with the distance from the interface:

$$E = E_0 e^{-\frac{z}{d_p}} \tag{1.34}$$

The penetration depth, $\mathrm{d_p}$, of the evanescent wave is given by:

$$d_p = \frac{\lambda}{2\pi n_1 (sin^2\theta - n_{sc}^2)^{\frac{1}{2}}} \tag{1.35}$$

and depends on the wavelength of the infrared light (λ), the angle of incidence (θ), and the refractive indices of the crystal (n_c) and the sample (n_s) (Figure 1.21). In particular, n_sc is the refractive index of the external medium (such as the sample) divided by that of the ATR prism (the crystal material). Depth of penetration is generally between 0.5 and 5 μm.

The critical angle, which is the angle of incidence between the wave and the normal to the surface, realizes the condition of total reflection. Typically, θ_c is equal to 45° and is given by:

$$\theta_\mathrm{c} = sin^{-1}(n_\mathrm{sc}) \tag{1.36}$$

Vibrational modes of molecules

Typically, infrared radiation can be classified into three regions:

- *near-IR*: 14000 - 4000 cm^{-1};
- *mid-IR*: 4000 - 800 cm^{-1};
- *far-IR*: 800 - 100 cm^{-1}.

The energy of infrared radiation can induce transitions between the vibrational levels of a molecule (Figure 1.22). The energy of the molecular vibrational transitions is represented by the frequency ranges of mid-IR and far-IR light. When the energy of an IR photon equals the difference in energy between two vibrational states, the molecule may absorb the photon.

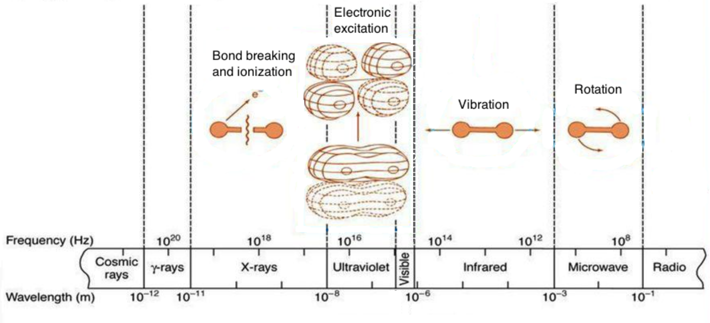

Figure 1.22: Electromagnetic spectrum and modes of molecules [68].

A diatomic molecule is subject to a single mode of vibration: bond stretching. For a polyatomic molecule, the vibrational modes are more numerous (Figure 1.23) [69]:

- *stretching*: change of the interatomic distance; can be *symmetrical* or *asymmetrical*;
- *bending*: deformation of the interatomic bond angle; can be in the plane (*scissoring* and *rocking*) or out of the plane (*twisting* and *wagging*).

Symmetric stretching

(a)

Antisymmetric stretching

(b)

Scissoring

(c)

Twisting

(d)

Rocking

(e)

Wagging

(f)

Figure 1.23: Vibrational modes of molecules [70].

The possible vibrations of a polyatomic molecule consisting of N atoms depend on the number of vibrational degrees of freedom (or modes) of the molecule itself. The molecule possesses $3N$ degrees of freedom (including 3 translational, 3 rotational for nonlinear molecules, and 2 rotational in linear molecules). The molecular vibrational modes are therefore $3N - 5$ if the molecule is linear and $3N - 6$ if it is nonlinear (Table 1.1) [50].

Table 1.1: Degrees of freedom for polyatomic molecules.

Type of degrees of freedom	Linear	Non-linear
Translational	3	3
Rotational	2	3
Vibrational	3N-5	3N-6
Total	3N	3N

ATR-FTIR Spectra

Some of the photons in infrared light are absorbed when their frequency matches the energy of a molecule's vibrational transition, while the remaining light is directed towards the detector. With Lambert-Beer law (eq. 1.32), the amount of absorption can be correlated with the sample concentration. IR spectroscopy can identify many types of molecules. Biological materials can produce extremely dense and complicated spectra with several overlapping bands that are challenging to decipher. Strong absorption bands of liquid water in the mid-IR and far-IR range can be an additional issue with biological samples since they can obscure many other signals. Typically, one must physically eliminate the water component, such as by drying the sample or computationally subtracting a liquid water spectrum from the sample spectra.

Each functional group can have multiple vibrational modes that correspond to different energies (e.g., stretching and bending); the same functional group in different molecules has specific vibrational modes, which result in absorption bands located at characteristic frequencies (called group frequencies), influenced only marginally by the complexity of the molecular structure.

The 1800–900 cm^{-1} region, fingerprint (FP) region, of the mid-IR spectrum is very dense in IR absorbance bands of different molecular components (identifiable through the use of databases), while the region between 3050 and 2800 cm^{-1}, called high wavenumber region or simply high region (HR), is the region interesting for lipids molecules [71, 72]. A typical ATR-FTIR spectrum for a biological complex system is shown in Figure 1.24; the different colors identifying the functional groups of the biological molecular components and their regions:

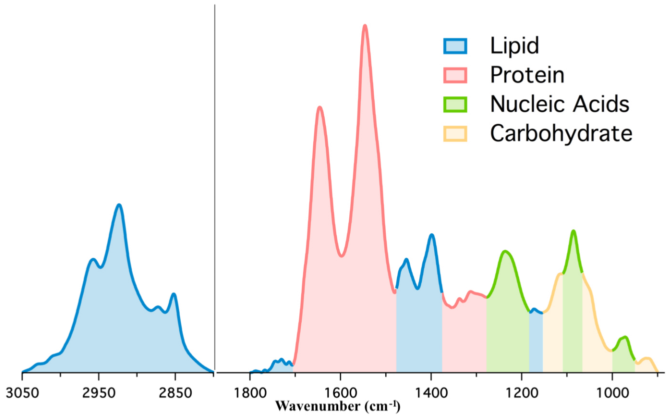

Figure 1.24: ATR-FTIR spectrum, with the different colors identifying the different functional groups and their regions.

1.2.2 Pre-processing and data analysis

Before proceeding with data analysis, several pre-processing steps must be performed [50]. These include:

- *subtraction of the baseline* from the spectrum;
- *smoothing*;
- *normalization* of the spectra;
- *second derivative*, which solves complex spectra whose bands are overlapping and allows discrimination of various components related to different secondary structure elements. The second derivative provides a negative peak for each band in the absorption spectrum.

The parameters to be analyzed may include:

- *wavenumbers shift*;
- *bandwidth*;

- *peak intensity value*;
- *area of specific bands*;
- *ratios of intensities*;
- *ratios of areas*;
- *difference spectra*.

Each of these parameters can provide interesting information. Peak shifts, bandwidth modifications, and differences in peak intensity/area are typical IR band variations that may be related to particular functional group modifications of the relevant molecules in the sample [63]. Specifically, peak shifts and bandwidth offer structural and dynamic information, whereas the Lambert-Beer equation (eq. 1.32) states that band intensity is correlated with the concentration of the respective functional groups of the biomolecules. Statistical methods are used to support the significance of the results obtained (e.g. multivariate statistical analysis, two-tailed parametric t-test or one-way ANOVA).

1.2.3 Experimental setup

The experimental apparatus used for this thesis work is a Tensor II spectrometer from Bruker (Bruker Optics, Germany) equipped with a silicon BioATR II cell optimized for liquid samples (Figure 1.25a).

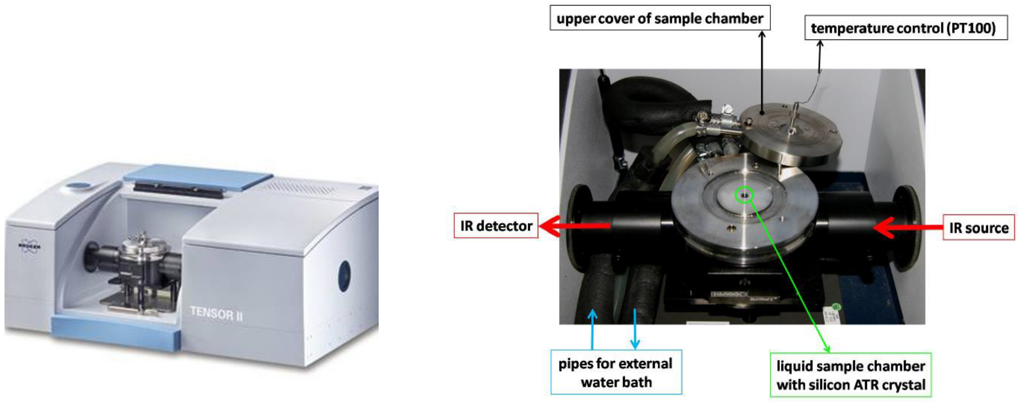

(a) (b)

Figure 1.25: (a) Bruker Tensor II and (b) sample compartment [73].

The cell is thermostatically controlled by connection to a thermal bath, allowing temperature measurements in the 5÷95 °C range. The main components of the spectrometer are:

- IR source;
- Michelson interferometer;
- sample compartment (Figure 1.25b) allows measurement of biological samples and requires a small sample volume (20 μl);
- IR detector: is a Mercury Cadmium Telluride (MCT) detector, inorganic semiconducting material that, when absorbs radiation, becomes conductive, the resistance of the semiconductor is reduced and the current increases. It is only activated at low temperatures (for this, it requires a special liquid nitrogen cooling system), and its sensitivity is inversely proportional to temperature.

The ATR crystal is formed by two layers: the top crystal is silicon (Si), and the one below (which is not in direct contact with the sample) is made of zinc selenide (ZnSe). The diameter of the circular area where the sample is placed is 2 mm.

1.2.4 ATR-FTIR in biological materials

ATR-FTIR spectroscopy is a very powerful and versatile spectroscopic technique for the study of biological materials [50–58]. It is used to determine the chemical properties, molecular interactions, and functional structures of complex samples, such as cells, blood, and biological tissues. The sensitivity and capability of this technique to work with samples in different physical states (liquids, solids, and gases) allows the use of ATR-FTIR spectroscopy in several fields such as biochemistry, biomedicine, and materials science.

This technique is particularly appropriate for biological materials because it does not require complex sample preparations, can be used with hydrated samples (such as biological fluids and tissues), and is a non-destructive technique.

In recent years, the application of ATR-FTIR spectroscopy in biological materials has offered new possibilities in biomedical research, clinical diagnostics, and biomaterials science. Some applications will be discussed in the next few lines.

With ATR-FTIR spectroscopy, it is possible to map biological tissue samples and generate spectral images that represent the distribution of chemical components in biological tissues. This is particularly important in the early diagnosis of diseases, such as cancers, because it makes it possible to identify anomalies in the biochemical structures. An example of application in the field of spectral imaging of biological tissues can be found in a study performed by Kazarian et al. in which tumors were mapped and the distribution of proteins and lipids in human tissue samples analyzed, providing large-scale molecular detail [74].

Moreover, infrared spectroscopy is also used to study the secondary structure of proteins and their interactions with other biomolecules, such as lipids and cell membranes. Such a kind of analysis is important for understanding the biological functioning of proteins and for the development of new drugs targeted to specific protein structures [75].

Important applications also occur in medical diagnostics and biomarker detection. In the study of COVID-19, it was shown the ability to identify virus-specific chemical fingerprints in saliva samples, demonstrating its potential for noninvasive diagnosis [76].

Once the data have been acquired, it is important to determine the type of analysis to be performed, based on the proposed objectives. For example, in medical diagnostic research and biomarker detection, it is important to define the most relevant parameters that can capture modification related to the presence of the disease [77–79].

With continuing technological developments, its potential in the life sciences and medicine is destined to expand further, opening new routes of application.

Chapter 2

Advanced Spectroscopic and Imaging Techniques for Diagnosing Neurodegenerative and Cardiovascular Diseases

Neurodegenerative and cardiovascular diseases affect a high percentage of the world population. Data from World Health Organization (WHO) estimate 2.9 million people worldwide affected by multiple sclerosis (MS), while cardiovascular disease death rate is around 44%. MS is one of the most common neurodegenerative diseases showing various symptoms both physical and cognitive type. It affects mostly young adults, ultimately leading to long-term disability. MS diagnosis is not easy and requires several clinical and instrumental tests (unpleasant and expensive). Still, its misdiagnosis remains a persistent problem with potential consequences for patients and health systems.

Cardiovascular diseases affect the arterial system as a whole and determine the progressive narrowing of the arteries until they are completely blocked. In Western countries, it is still the leading cause of death (death rates around 44%).

Physical techniques are an expanding area in medical/biological sciences. It may be an important support for diagnosing disease and/or monitoring the action of drugs on a multiscale level (biofluids and from cell to organ). In particular, ATR-FTIR spectroscopy and X-ray μ-CT are useful tools (Figure 2.1) for the diagnosis/verification of the aforementioned pathologies. The results presented show how, in both cases, the ATR-FTIR evidences statistically significant spectral differences between "patients" and controls, and how the μ-CT reveals healthy or diseased tissues in three-dimensional virtual histology [42, 77–81].

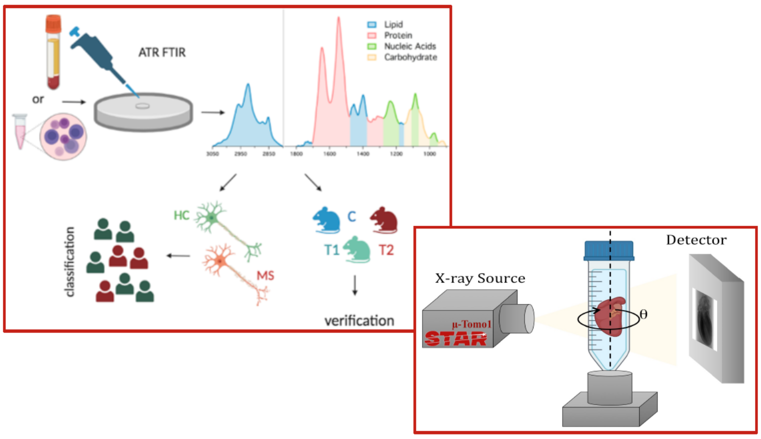

Figure 2.1: Graphical abstract.

2.1 Case study 1: Protective effects of PSELT peptide in cardiovascular disease

Cardiac lipotoxicity has a significant role in the cardiovascular complications associated with obesity. Selenoprotein T (SELENOT) was shown to have a crucial role in the differentiation and protection of cardiomyocytes. This physiological role was explored by using a small peptide fragment (43-52) of Selenoprotein T (PSELT) derived from the SELENOT redox-active motif, to verify the mechanisms through which PSELT could protect cardiomyocytes and the heart from cardiovascular complications.

In this work, the effects of PSELT were investigated by ATR-FTIR and μ-CT on two different levels: on the cellular scale and the whole organs (rat heart).

To do this, palmitic acid (PA) exposure of H9C2 cardiomyocytes (rat cardiac cells) was used to simulate cardiac lipotoxicity, whereas global ischemia was induced in rat hearts (*ex-vivo*). The experimental findings demonstrated that treatment with PSELT reduces cell death induced by PA and global ischemia.

According to spectroscopic characterization, PSELT considerably reduced spectral-related macromolecular alterations (i.e., lipid, protein, nucleic acid, and carbohydrate content) and modulated the PA-induced membrane fluidity. μ-CT X-ray analysis of rat hearts (*ex-vivo*) confirmed that PSELT reduces the effects of global ischemia. Furthermore, μ-CT X-ray was an excellent tool for 3D virtual histology [80, 81].

2.1.1 Introduction

One of the major health problems that significantly increases the risk of cardiovascular disease is obesity [82]. In obese patients, there is an increase in left ventricular mass and adiposity-related myocardial changes, which increases triglyceride deposition in the heart [83]. Myocardial dysfunction is caused by some complicated processes that follow lipid buildup inside the cardiovascular system's cells, ultimately resulting in heart failure. Due to their capacity to modify cellular structures, saturated long-chain fatty acids, such as palmitic acid (PA), play a significant role in this process, known as cardiac lipotoxicity. This process leads to oxidative stress, endoplasmic reticulum stress, impaired insulin signaling, mitochondrial dysfunction, inflammation, and myofibrillar dysfunction, which ultimately results in cell death [84, 85]. Antioxidant defense systems reduce the effects produced by saturated fatty acids; these include selenoproteins, for example, SELENOT [86, 87].

To simulate the ischemic damage on the cardiac system, two approaches were used, taking into account either cells or the global organs:

1. rat heart cells (H9C2) were treated with high serum levels of PA (main circulating saturated fatty acid, which contributes to the development of lipotoxic cardiomyopathy [88]);
2. global ischemia was induced in rat hearts.

2.1.2 Scientific rational

The scientific rationale behind this study is to understand the protective effects of PSELT on cardiomyocytes and the heart under pathological conditions, i.e., PA exposure and global ischemia. This effect was demonstrated at different levels, using advanced characterization techniques: ATR-FTIR spectroscopy was chosen for its ability to detect changes in molecular interactions, while μ-CT was chosen for its ability to provide three-dimensional "virtual histology", making detailed tissue analysis without physical sections. This methodological choice meets specific objectives that combine advanced spectroscopy and imaging techniques to monitor molecular and structural changes, both at the cellular and organ levels, in a highly sensitive and accurate manner. These approaches allow the detection of specific alterations in molecular components to evaluate mechanisms of cellular protection or damage in response to drug treatments or pathological exposures. Data pre-processing, including baseline corrections, normalization for amide II band, and subtraction between treated and control spectra, was performed to quantify differences between the samples. Statistical tests were then performed, to determine and evaluate the significance of the observed differences.

Integration of μ-CT gives a detailed 3D view of structural changes in hearts exposed to global ischemia. It is possible to observe the spatial distribution of tissue damage and to efficiently segment areas of healthy versus damaged tissue, thus allowing quantification of damage (I/R hearts) and comparison with I/R+PSELT and control hearts. This approach provides a visual map of ischemic damage and a quantitative evaluation of affected areas.

The combination of these two techniques provides complementary information on a molecular and structural scale, allowing detailed analysis of the protective effects of PSELT against lipid cardiotoxicity and global ischemia.

2.1.3 Materials and methods

Sample preparation

The samples were prepared and provided by the Cellular and Molecular Cardiovascular Pathophysiology laboratory of the Department of Biology, Ecology and Earth Sciences (DiBEST) of the University of Calabria. In particular, the laboratory designed a small peptide mimetics of SELENOT, called PSELT (peptide 43-52), which includes the redox motif of the entire selenoprotein. The abilities of PSELT to protect H9C2 cardiomyocytes from PA-induced lipotoxicity and reduce the effects of global ischemia in the hearts were tested with ATR-FTIR and μ-CT measures, respectively.

This study used H9C2 cells from rat embryonic heart tissue and *ex vivo* rat hearts. Specifically, control H9C2 cells and H9C2 cells under different treatments (PA, PA+PSELT, and PSELT) and control rat heart *ex vivo*, rat heart with global ischemia and heart with global ischemia but treated with PSELT were studied.

H9C2 cells treatment

The H9C2 cells were exposed for 24 hours to:

1. PA: 100 $\mu mol/L$;
2. PA + PSELT: 5 $nmol/L$;
3. PSELT: 5 $nmol/L$.

Control and treated cells were collected using trypsin and then centrifuged (1500 g, 5 min). Then, 10^6 cells were resuspended in 300 μL of the complete cell culture medium.

Ex vivo rat hearts treatment

Animals and treatments: Male Wistar rats (Envigo-Udine, Italy), were anesthetized with i.p. injections of ethyl carbamate (2 g/kg body weight) and subsequently euthanized. The hearts were rapidly excised, placed in ice-cold perfusion buffer, cannulated through the aorta and perfused according to the Langendorff method at a constant flow of 12 mL/min (37 °C) with Krebs–Henseleit (KH) solution (pH 7.4, gassed with 95% O2 and 5% CO2) (PMID: 35326221; PMID: 30973759).

Ischemia/Reperfusion (I/R) Protocol: Hearts were allowed to stabilize for 40 min with KH solution during which the baseline parameters were recorded. After the stabilization period, the hearts underwent to 30 min of global, no-flow ischemia followed by 120 min of reperfusion to reproduce I/R injury, while the control hearts were only perfused with KH buffer for 190 min.

Experimental Groups: Hearts were randomly assigned to one of the following experimental groups:

- Control group: hearts underwent only 190 min of perfusion;
- Ischemia/reperfusion or global ischemia (I/R) group: hearts were exposed to I/R protocol. In particular, to study the beneficial action of PSELT against myocardial ischemia/reperfusion injury (MIRI) in ex vivo preparations, the Langendorff

perfusion system was employed. After 40 min stabilization, the hearts were exposed to 30 min of global, no-flow ischemia followed by 120 min of reperfusion to reproduce MIRI;

- I/R+PSELT group: after stabilization, PSELT was infused for 20 min before I/R at the concentration of 5 nM. The hearts were treated with PSELT where the peptide was infused at the beginning of the reperfusion to evaluate its pharmacological post-conditioning cardioprotective action.

Staining and heart perfusion: A stock solution of Lugol's iodine was prepared by dissolving 10 g KI plus 5 g I2 in 100 ml deionized water. The stock solution was diluted to 25% with deionized water immediately before use. The solution was used within 48 h of initial preparation and was filtered to minimize precipitate just prior to perfusion. At the end of ex vivo protocols and hemodynamic assessment, the hearts were perfused via the aorta with Lugol's solution. In particular, the hearts were perfused with the Lugol's staining agent over a period of 15-20 min, corresponding to the appropriate time for optimal staining efficacy obtained during our preliminary tests. Once perfusion of contrast solution was complete, the hearts were perfused one final time with 10-15 ml of saline solution. Hearts were then fixed in freshly prepared 4% paraformaldehyde (PFA) for 48 h and washed with 0.83% NaCl (1.5h) twice, 0.83% NaCl + 100% ethanol, 0.83% NaCl + 70% ethanol, and stored at 4°C in 70% ethanol.

ATR-FTIR experiments and data analysis

Infrared spectra were obtained in ATR mode at 37 °C using a Tensor II FTIR spectrometer (Bruker Optics, Ettlingen, Germany), which has a BioATR II thermostated sample holder and an MCT detector (see Paragraph 1.2.3). Before measurement, the sample was degassed, and 20 μL of the cell solution was placed on the ATR silicon crystal and allowed to equilibrate for two minutes. Spectra were acquired for 180 minutes (every 10 minutes) to enhance the absorption signal resulting from cell sedimentation on the crystal utilizing the kinetic option in Opus acquisition software. Each spectrum was composed of an average of 120 scans with a spectral resolution of 4 cm^{-1}. At least three experiments were carried out to improve the statistics, using independent cell culture for each measurement. A cell culture medium was used as a background, and the spectrum was recorded using the same experimental configurations. Once acquired, the correction of the spectra includes the following steps: *i)* baseline correction using the rubber band function; *ii)* averaging of the spectra acquired (using Opus 7 software) that returns an average absorbance spectrum. At this point, replicates of the same cell type were averaged again and then normalized for the area under the amide II band (1597-1481 cm^{-1}), using IgorPro 9 software. To enhance the differences among the samples investigated, difference spectra were calculated from the normalized mean spectra. The difference spectrum was calculated as "treated sample" minus "untreated sample" (control). Finally, the significance of the data obtained between H9C2 control and treated cells was assessed by Student's t-test (Wilcoxon two-tailed, nonparametric, 99% CI) using Prism 9 software. Spectral regions where there is a significant difference in absorption, with p value < 0.0001, were considered significant. The area under the 1700–1600 $\mathrm{cm^{-1}}$ region (protein content) and the 3050–2800 $\mathrm{cm^{-1}}$ region (lipid content) was used to compute the lipid/protein ratio. The bandwidth of the CH_2 symmetric band, centered at 2852 $\mathrm{cm^{-1}}$, was determined at 75% of the height of the peak maximum.

X-ray μ-CT experiments and data analysis

X-ray μ-CT measurements were performed on treated and untreated rat hearts (control). Carefully calibrated X-ray source parameters allow the acquisition of high-quality images of the studied samples. The exposure time has been set to 2500 ms, and the following values have been chosen for the current and tube voltage: 60 kV and 166 μA. This results in a beam power value of 10 W. Sample-detector distance and sample-source distance are 508 mm and 117 mm, respectively. Thus, an equivalent pixel size of 9.36 μm was obtained by equating the optical magnification to 5.34. 3600 X-ray projection images at a 0.1° angular step were acquired. For each projection, 3 images were registered and then averaged to improve the signal-to-noise ratio. The acquired projections are then normalized using flat and dark images and reconstructed using the Feldkamp-Davis-Kress algorithm. The software used for the 3D rendering and image analysis is Fiji (open-source software) and Avizo 3D 2021.2 (commercial program). Before analysis, segmentation was performed to separate healthy from dead tissues. The dead tissues did not absorb iodine, resulting in a different grayscale value from the healthy tissues [89, 90]. The analysis considers the area occupied by the healthy tissues and the area occupied by the dead tissues slice by slice and then calculates the average. At least two replicates were acquired for each sample type, using samples from different animals.

Statistical analysis

The reproducibility and accuracy of the results were assessed by appropriate statistical tests using one-way ANOVA, followed by an unpaired t-test corrected according to Bonferroni for multiple comparisons. A p-value of 0.05 or less was considered significant. The degree of significance for comparing the data with the control group was indicated as $^{*}p < 0.05$; $^{**}p < 0.01$; $^{***}p < 0.001$; $^{****}p < 0.0001$.

2.1.4 Results and discussion

ATR-FTIR analysis on H9C2 rat cells

A typical mean absorbance FTIR spectrum of H9C2 cells in aqueous solution is shown in Figure 2.2. The spectrum includes the signature of important biomolecules in the 3050–2800 and 1800–900 cm^{-1} spectral ranges. The first region, which represents the molecular characteristics of cellular membranes, is assigned to the stretching vibrations of the lipid acyl chain's CH_2 and CH_3 (both symmetric and asymmetric). More intricate spectrum characteristics are seen in the fingerprint region, the spectral zone in the right panel of Figure 2.2, where the contributions of the several biomolecules (lipids, proteins, nucleic acids, and carbohydrates) partially overlap.

The principal peaks are attributed to: nucleic acids (asymmetric and symmetric phosphate stretching at 1125 and 1085 cm^{-1}, respectively), proteins (amide I, 1646 cm^{-1}, amide II, 1546 cm^{-1}, and amide III at 1300 cm^{-1}), lipids ($C = O$ stretching at 1750–1715 cm^{-1}, CH_2 bending at 1470 cm^{-1}), carbohydrates and glycogen (1155 and 1030 cm^{-1}) [91, 92]. See Table 2.1 for a detailed description of the absorption peaks listed in Figure 2.2 [63, 80, 93].

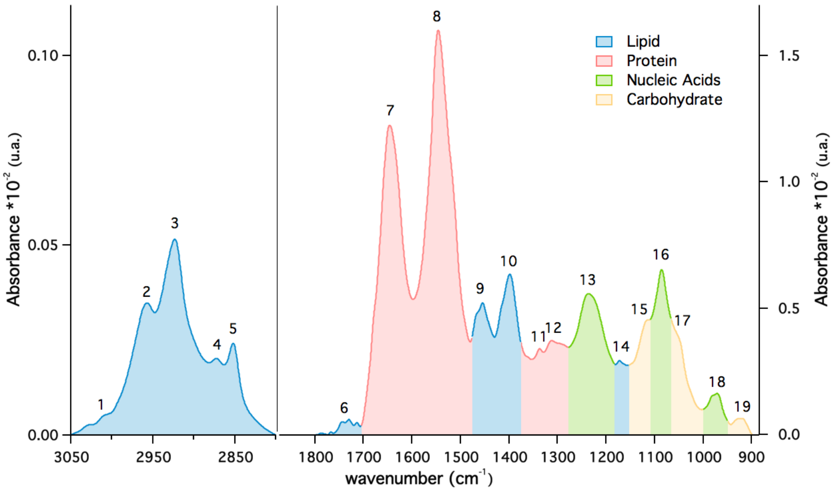

Figure 2.2: Representative ATR-FTIR spectra of H9C2 cells in solution. The high wavenumber region (3050–2800 cm^{-1}) and the fingerprint region (1800–900 cm^{-1}) are displayed. The absorbance of selected functional groups is indicated by peak numbers and listed in Table 2.1.

Table 2.1: Band Assignments of the Main Peak Absorption of Cells. Peak numbers are as indicated in Figure 2.2.

Peak Number	Wavenumber (cm^{-1})	Assignment of Functional Groups
1	3010	Olefinic C=CH stretching vibration (unsaturated lipids)
2	2957	CH_3 asymmetric stretching (lipids)
3	2923	CH_2 asymmetric stretching (lipids)
4	2872	CH_3 symmetric stretching (proteins and lipids)
5	2852	CH_2 symmetric stretching (mainly lipids)
6	1750–1715	C=O stretching (ester functional groups in lipids)
7	1646	Amide I (protein C=O stretching)
8	1546	Amide II (protein NH bending, CN stretching)
9	1456	CH_2 bending (mainly lipids)
10	1399	COO^- symmetric stretching (fatty acids)
11	1337	CH_3 symmetric bending (lipids)
12	1313	CH_2 wagging (lipids)
13	1236	PO_2^- asymmetric stretching, fully hydrogen-bonded (mainly nucleic acids
14	1173	CO–O–C asymmetric stretching (ester bonds in cholesteryl esters)
15	1116	Ribose ring vibrations (RNA)
16	1086	PO_2^- symmetric stretching (nucleic acids and phospholipids)
17	1050	C–O stretching (polysaccharides, glycogen)
18	971	C–N$^{\pm}$–C stretching (nucleic acids)
19	924	Ribose ring vibrations (RNA)

To improve the signal intensity, the spectra were acquired during a period of 180 min. Fig 2.3 a and b shows the time-dependent ATR-FTIR absorption spectra in the two selected spectral regions of H9C2 live cells in solution. As can be seen, during the experiment, the intensity of the ATR-FTIR spectrum increases (Figure 2.3). This is due to the concentration of cells near the ATR crystal (when the crystal is completely covered with cells, the absorption spectrum has reached a saturation value (Figure 2.4)). Spectra for the H9C2 cell sample is shown for demonstration (Figure 2.3). The increas of the intensity was evaluated a specific wavenumber 1540.1 cm^{-1} (amide II) and plotted in Figure 2.4 for the different samples.

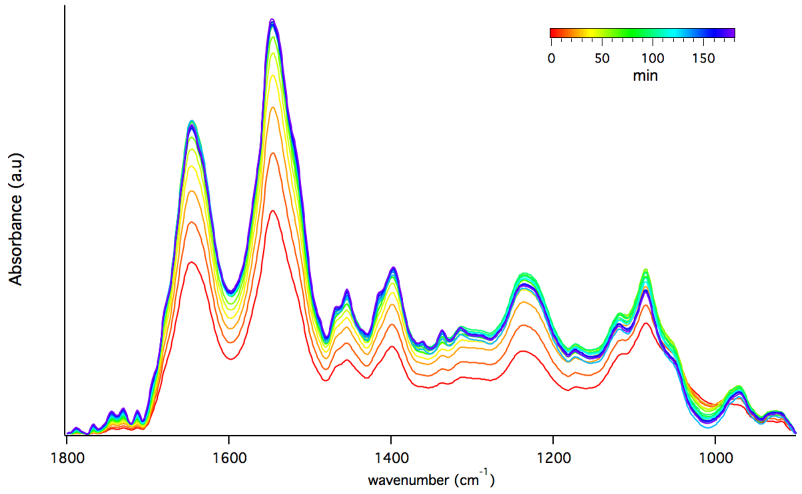

(a)

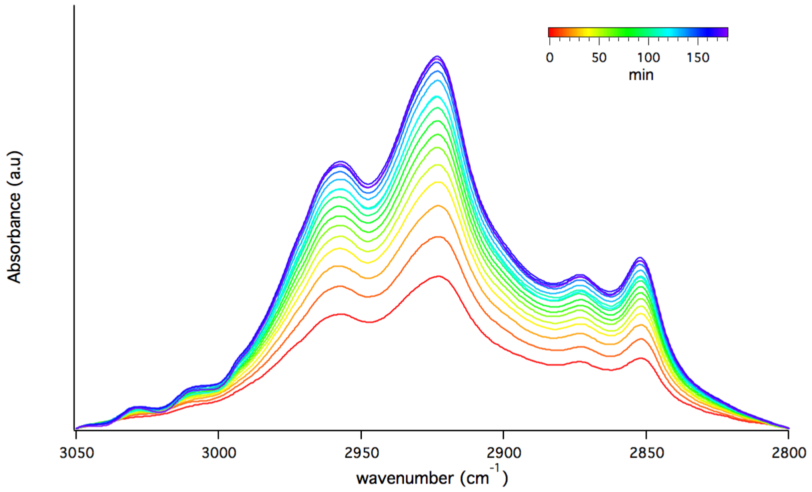

(b)

Figure 2.3: ATR-FTIR spectrum of the (a) fingerprint and (b) high regions of the H9C2 cell sample.

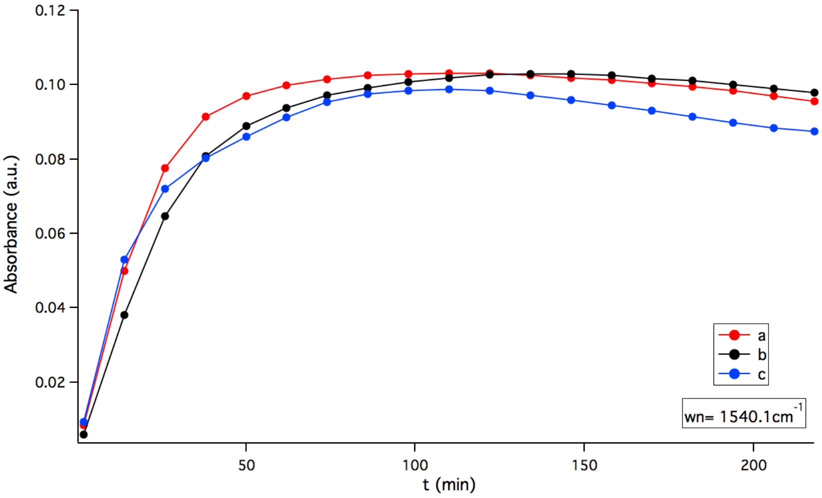

Figure 2.4: Time dependent change of the intensity at 1540 cm^{-1} H9C2 cells. The wavenumber belongs to the amide II absorption assigned to proteins (see Table 2.1). The different replicates acquired were indicated by a, b, c.

In this plot, it can be distinguished an initial sedimentation stage characterized by a rapid increase of the intensity followed by a saturation stage, where the intensity maintains a constant value. This trend is common for all samples investigated. This behavior is typical of live cell samples and was also found for melanoma cells with different metastatic potential [94]. The averages between spectra (Figure 2.5) were calculated by excluding the first three acquisitions and repeating the operation for the different replicates. Then, the three average spectra related to the sample replica are further averaged, resulting in a single average spectrum for the sample considered (Figure 2.6).

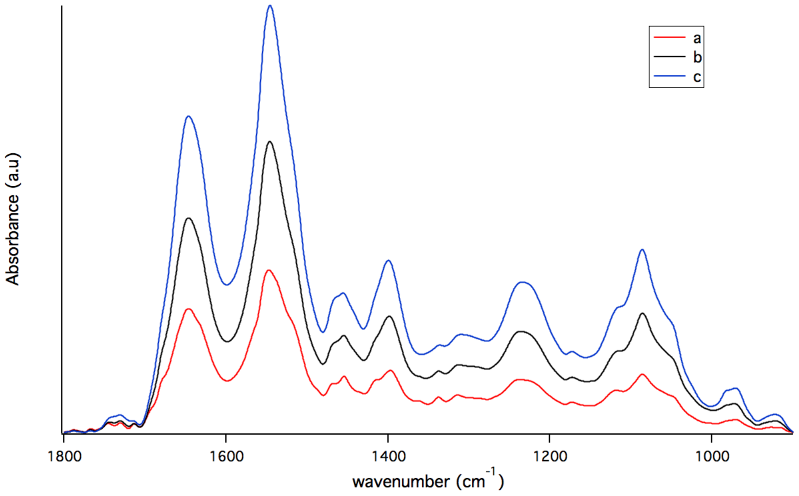

(a)

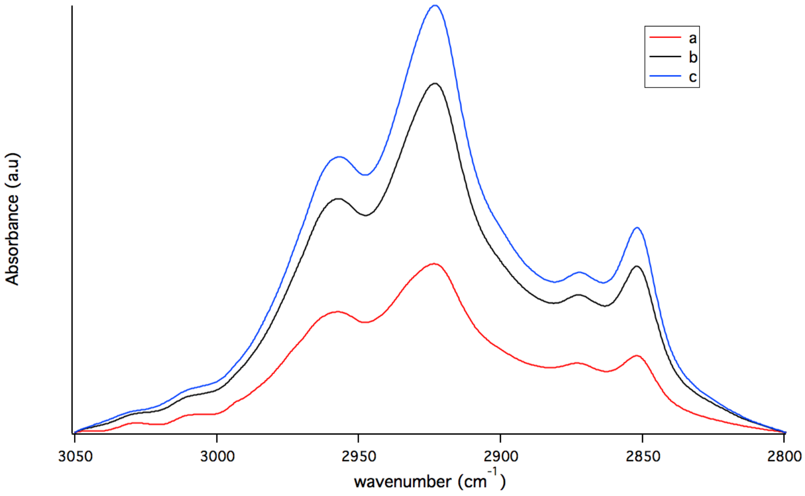

(b)

Figure 2.5: ATR-FTIR average spectrum of the (a) fingerprint and (b) high regions of the different replicates of the H9C2 cell sample.

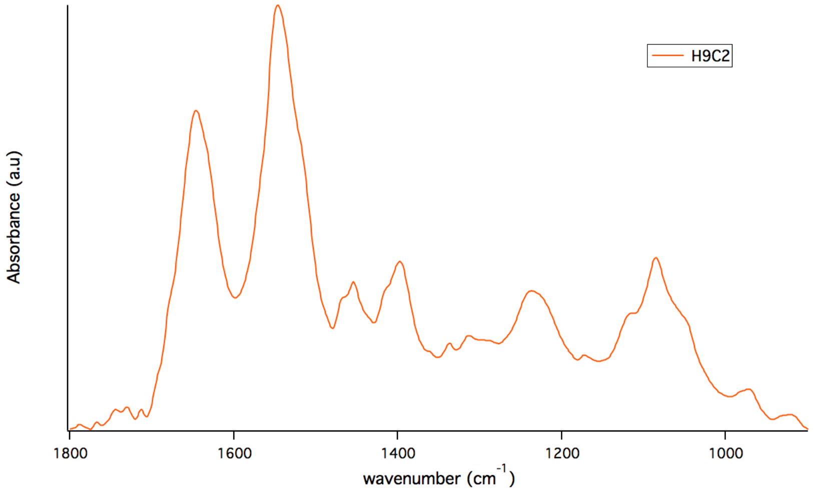

(a)

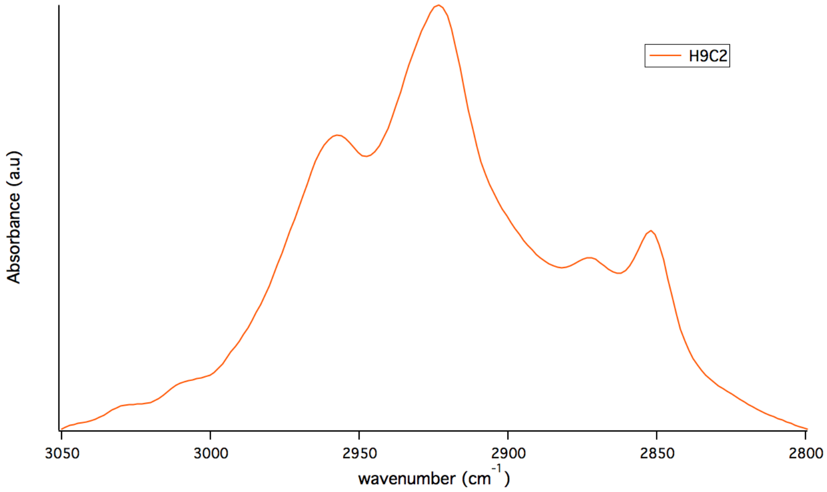

(b)

Figure 2.6: ATR-FTIR averaged spectrum of the mean of the (a) fingerprint and (b) high regions of the H9C2 cell sample.

Finally, the average absorbance spectra of the four different cell samples (H9C2 control, PA, PA+PSELT, and PSELT) analyzed are shown in Figure 2.7. From the comparison of the spectra, no shift in band position was observed, suggesting no appreciable changes in the structure of the cells. However, variations in the spectral intensity are evident.

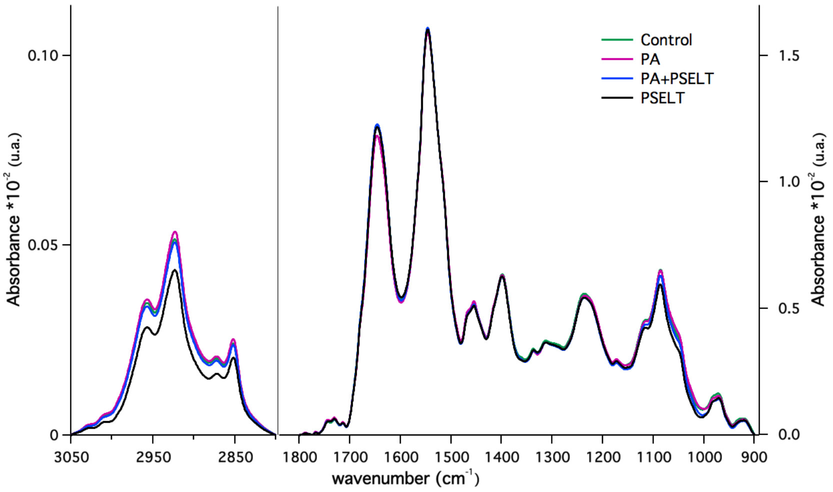

Figure 2.7: Average absorbance spectra of the four different H9C2 control and treated cell samples.

To better visualize the effects of the different treatments, we computed the difference between the mean absorbance spectra of the treated cells minus the mean spectrum of the control cells (Figure 2.8). The absorbance regions with the highest statistical significance ($p < 0.0001$) are indicated by a thicker line. Higher or lower concentrations of the molecular components within the cell are represented by positive or negative peaks in the plot. As seen from Figure 2.8 (red line) when comparing PA-treated H9C2 cells with control cells, significant changes were observed in the amide I region indicating a decrease in protein content. In particular, the peaks at 1655 and 1635 cm^{-1} are assigned to alpha-helix and beta-sheet proteins [93]. Positive peaks were found in the regions assigned to nucleic acid and carbohydrate vibrations, around 1196 and 1046 cm^{-1}, indicating changes in the content of these molecules. Additionally, positive peaks in the lipid component are observed at around 2920 and 1730 cm^{-1}. The lipid/protein ratio and CH_2 symmetric bandwidth were also calculated (see Table 2.2). The lipid/protein ratio increased from 0.200 ± 0.079 (control) to 0.337 ± 0.043 (PA sample), reflecting the differences in the spectra. The CH_2 symmetric band (2852 cm^{-1}) showed a reduction in bandwidth, decreasing from 16.747 ± 0.003 cm^{-1} (control) to 16.030 ± 0.401 cm^{-1} (PA). Such a decrease indicates that the PA treatment reduces the permeability of the cell membrane. When cells were treated with PA and PSELT simultaneously (Figure 2.8, blue line), the differences in the absorption spectrum almost disappeared, but a small reduction in nucleic acid and carbohydrate components remained. The treatment with PSELT alone on the cells (Figure 2.8, green line) included a decrease in the bands corresponding to nucleic acids and carbohydrates as well as the lipid content (note the negative peak at 2922 cm^{-1}).

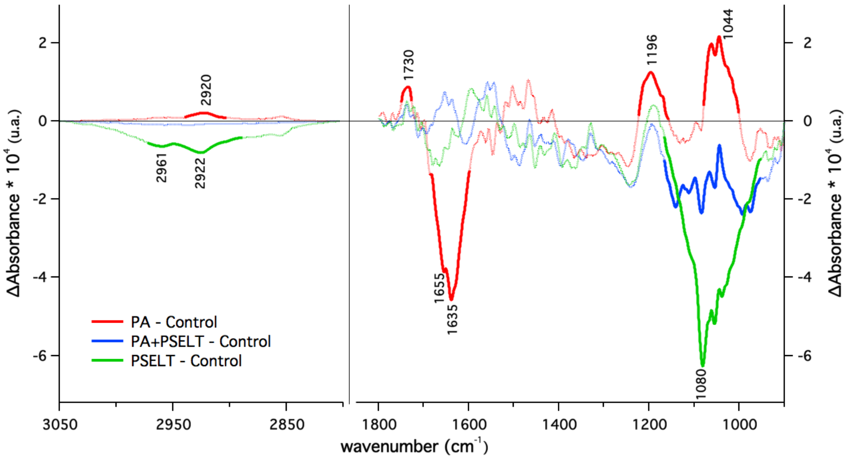

Figure 2.8: Difference spectra between treated cells minus the spectrum of control cells. The regions with the highest statistical significance ($p < 0.0001$) in absorbance were highlighted with a thicker line.

Table 2.2: Bandwidth of symmetric CH_2 and lipid/protein ratio for controlled and treated cells.

Functional group	Control	PA	PA+PSELT	PSELT
Bandwidth of CH_2 symmetric	16.747 ± 0.003	16.030 ± 0.401	16.743 ± 0.205	16.210 ± 0.306
Lipid/protein ratio	0.200 ± 0.079	0.337 ± 0.043	0.391 ± 0.137	0.306 ± 0.001

The positive peaks in the lipid component of PA-treated cells confirm the tendency of saturated fatty acids to cause lipid overload and heart lipotoxicity [95–97]. The α-helix and β-sheet contents of proteins were negatively altered by PA; this result is probably due to the oxidative burst and endoplasmic reticulum stress that PA causes, which may activate unfolded protein response and impair protein synthesis, in agreement with the results of *Zou et al* showing that PA causes a decline in protein synthesis in skeletal muscle by inducting endoplasmic reticulum stress [98]. Next, we found that PA also significantly increased the amount of nucleic acids, which may indicate that cardiomyocytes adopted a first line of defense against cellular damage, trying to rebuild new mitochondria and microsomes. This is consistent with previous research showing that cardiac tissue may increase the content of RNA/DNA for the early regeneration of damaged cell material after certain shocks, including myocardial infarction [99]. The PSELT significantly inhibited the PA-induced lipid accumulation, supporting the peptide's direct role in lowering lipid droplet accumulation. It also lessened the PA-dependent decrease in protein synthesis and increased nucleic acid synthesis. An additional aspect relates to the potential reduction in membrane fluidity observed in H9C2 cells exposed to PA. This may be related to a decrease in the concentration of proteins, cholesterol, unsaturated and saturated lipids, and free radicals, which can stimulate molecular oxidation via various mechanisms [100]. It is interesting to note that PSELT mitigated the reduction in cardiomyocyte membrane fluidity, supporting its ability to improve lipid profile and provide antioxidant protection; indeed, it has been demonstrated that oxygen free radicals can change the fluidity of cell membranes [100]. These findings provide additional insight into the physiologic role of SELENOT in regulating cardiomyocyte homeostasis under oxidative stress brought on by a range of stressors, including lipotoxicity.

X-ray μ-CT analysis

To demonstrate the beneficial effects of PSELT in cardiovascular disease, the effects of this peptide were also studied on ex vivo rat hearts. Rat hearts with global ischemia (I/R) and I/R combined with the action of PSELT were studied. The results were compared with control untreated samples. The first step for microtomographic analysis is the morphological study of the samples. Figure 2.9 shows a 3D rendering (in false colors) of one of the studied samples (Figure 2.9a) and various 2D sections (in grayscale) the yz (Figure 2.9b), xy (Figure 2.9c), and xz (Figure 2.9d) planes. The 2D planes (yz, xy and xz) shown correspond to the colored boxes (blue, red, and green respectively) in the 3D rendering.

The heart (Figure 2.10) is divided into four chambers, two atria (*right atrium (RA)*, and *left atrium (LA)*) and two *ventricles* (*right ventricle (RV)*, and *left ventricle (LV))*. The *ventricles* are separated by the *interventricular septum (IVS)*. We can also see the *left ventricular wall (LVW)* and the *right ventricular wall (RVW)*, the *papillary muscle (PM)*, and the *aorta (Aor)*. The main interest in this study is the left *ventricular wall* and the *interventricular septum.*

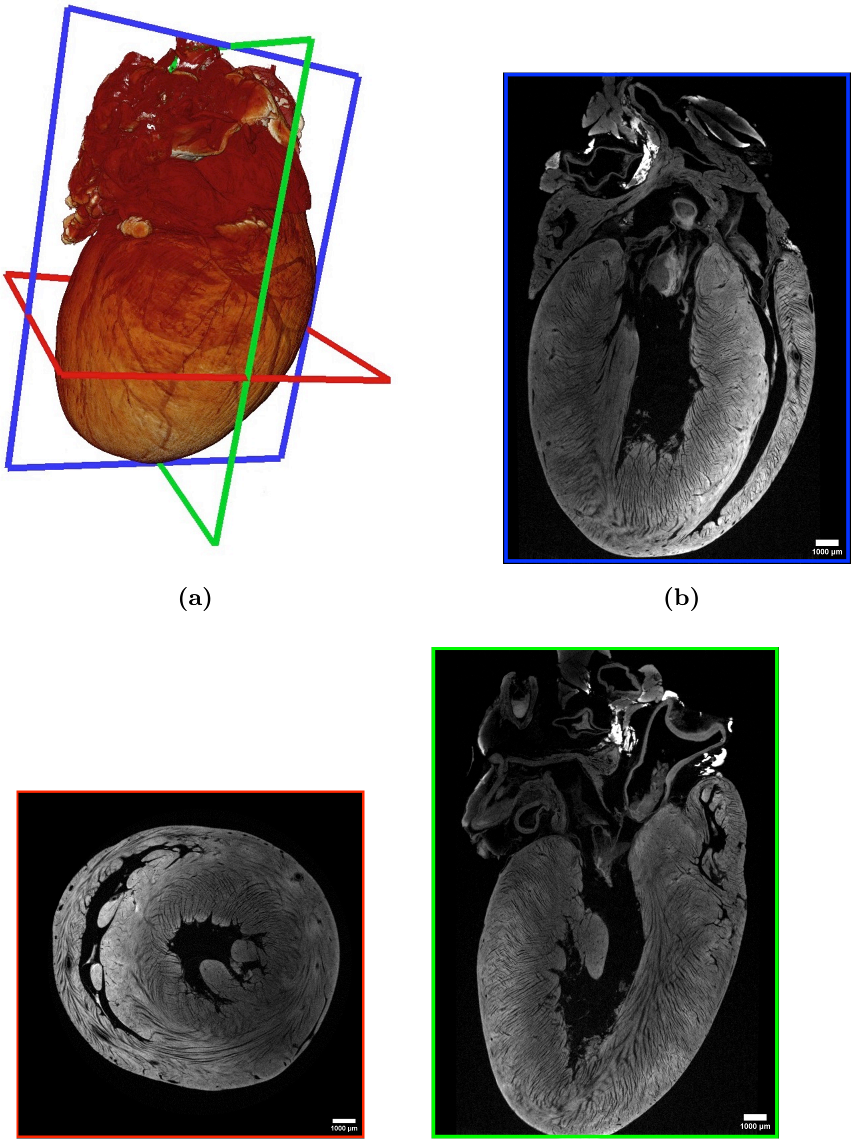

(a) (b)

(c) (d)

Figure 2.9: (a) 3D rendering of the control heart in false colors; and 2D yz (b), xy (c), xz (d) slices in grayscale taken from (a) following the color code of the boxes.

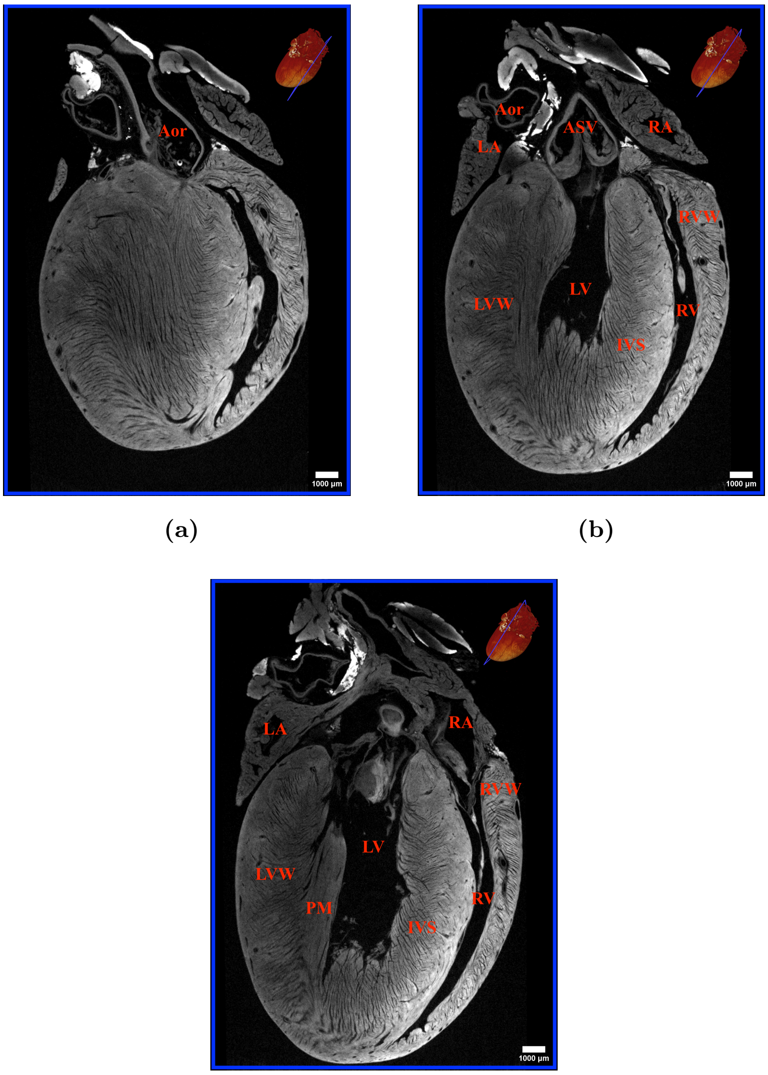

(a) (b)

(c)

Figure 2.10: Morphology of the rat heart: Aor = *Aorta*; RA = *Right Atrium*; RV = *Right Ventricle*; RVW = *Right Ventricular Wall*; IVS = *Interventricular Septum*; LA = *Left Atrium*; LV = *Left Ventricle*; LVW = *Left Ventricular Wall*; PM = *Papillary Muscle*; ASV = *Aortic semilunar valve*; (a), (b), and (c) are three different slices in the yz plane.

From a preliminary visual analysis, it can be seen that the specimen with global ischemia (I/R) has darker striated muscle areas (Figure 2.11). This finding refers to damaged tissues (dead tissue) and failed the iodine staining. By carefully segmenting, "healthy" and "dead" areas of the muscle were separated. A grayscale slice of the different samples (control, I/R, and I/R+PSELT respectively) is shown in Figures 2.11a, 2.11b, 2.11c, while Figures 2.11d, 2.11e, 2.11f show the same slice but virtually colored after segmentation.

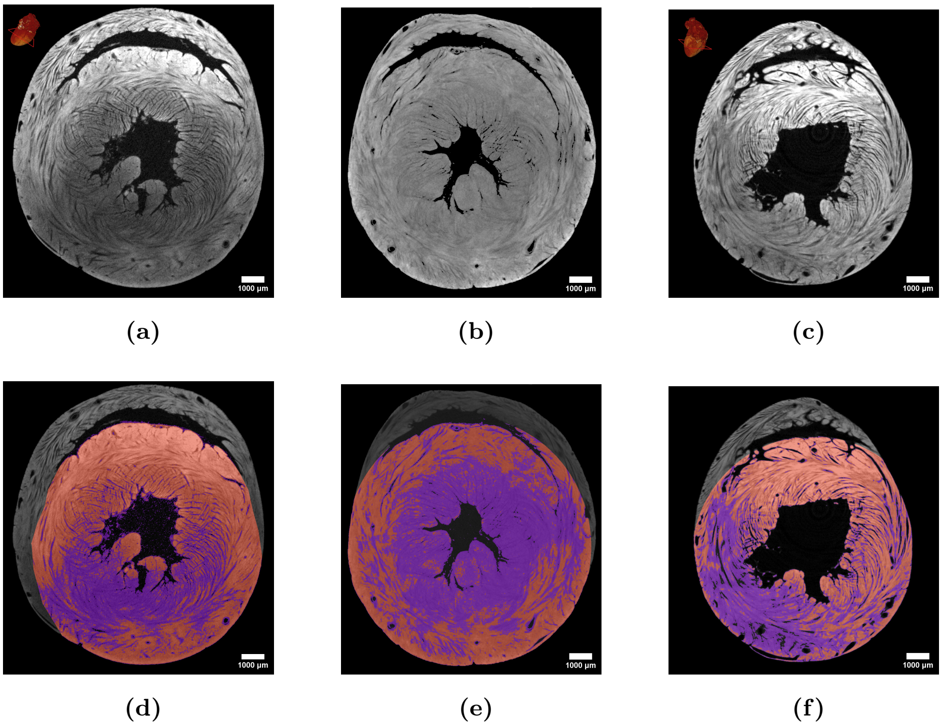

Figure 2.11: 2D slices of rat heart in grayscale and false colors (in orange healthy tissues and purple dead tissues): (a, d) control, (b, e) I/R (b, e), (c, f) I/R+PSELT.

The areas of these regions were calculated for each slice to quantify the healthy and dead tissues compared with the total tissue (LV and IVS). Figure 2.12 shows the virtual cuts where the analyses were performed. Results are shown in Figure 2.13.

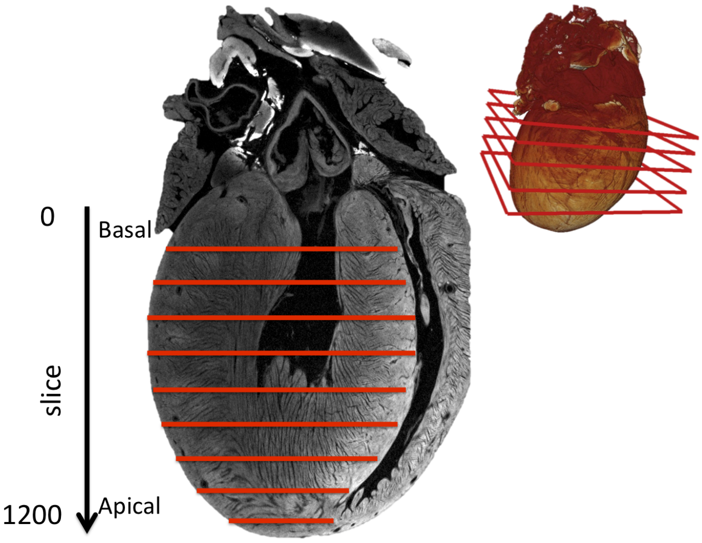

Figure 2.12: Schematic representation of the cutting planes (in red) on where the analyses were performed.

The data clearly show that, in the case of global ischemia, there is a higher percentage of dead tissues out of total tissues compared to the control samples. This percentage is drastically reduced in the samples in which the I/R treatment is combined with PSELT and is comparable with that found for the control hearts, which also show a percentage of dead tissue, probably attributable to the perfusion, which may induce physical stress to the heart. Figure 2.13 shows the trend of the percentage of healthy tissue (Figure 2.13a) and that of dead tissue (Figure 2.13b) relative to total tissue for the different xy virtual cut planes (from slice 0, which corresponds to the basal part of the heart, to slice 1200, which corresponds to the apical part of the heart). The results show that the percentage of dead tissue has a "peak" in the central region of the heart (from about slice 350 to 800). Usually, the basal and apical parts of the heart are the regions that suffer less during global ischemia. The trend in the case of control and I/R+PSELT hearts is similar, confirming the beneficial effects of PSELT on global ischemia-induced damage. These findings are comparable with those obtained by traditional histology, where to calculate the "infarct size" of the heart sectioned, the unstained necrotic tissue is carefully separated from stained with nitro blue tetrazolium viable tissue, and "infarct size" is expressed as a percentage of the total left ventricular mass (Figure 2.14).

However, traditional histology has limitations, which are overcome with μ-CT. In fact, with traditional histology, the number of sections is limited, and three-dimensional information is missed. In particular, with μ-CT a large number of virtual histologies are obtained non-destructively, thus without losing the three-dimensional information.

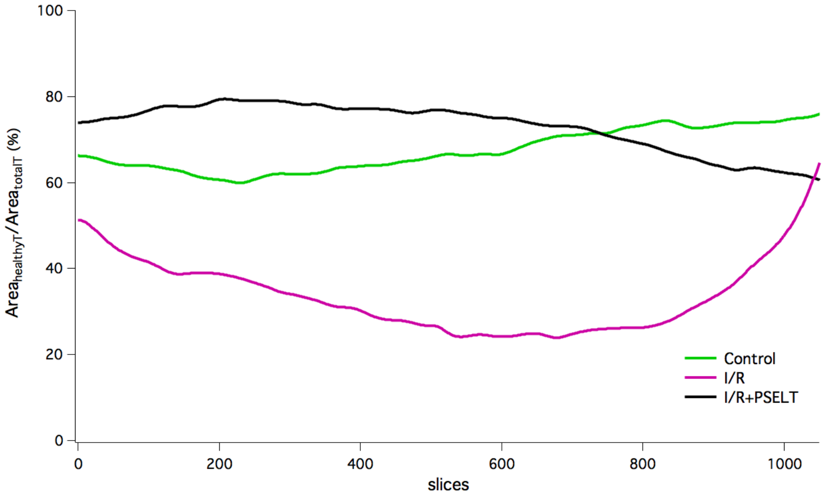

(a)

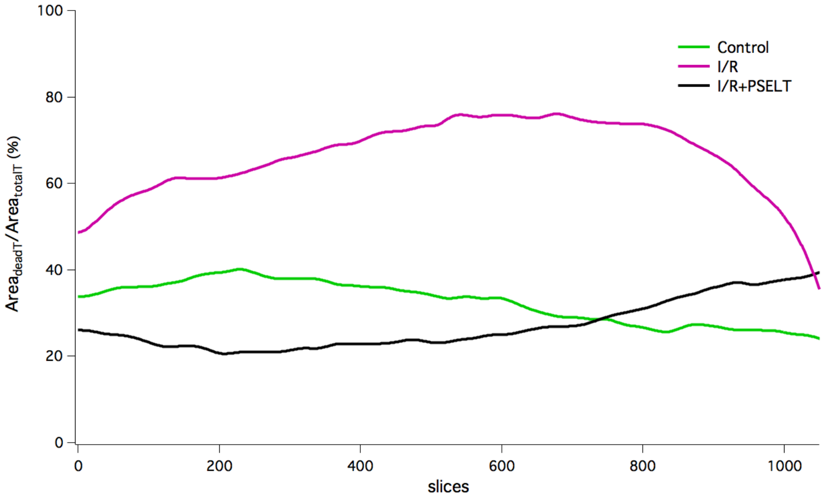

(b)

Figure 2.13: Percentage of (a) healthy tissue and (b) dead tissue with respect to the total tissue in the xy virtual cutting planes for control, I/R, and I/R+PSELT hearts.

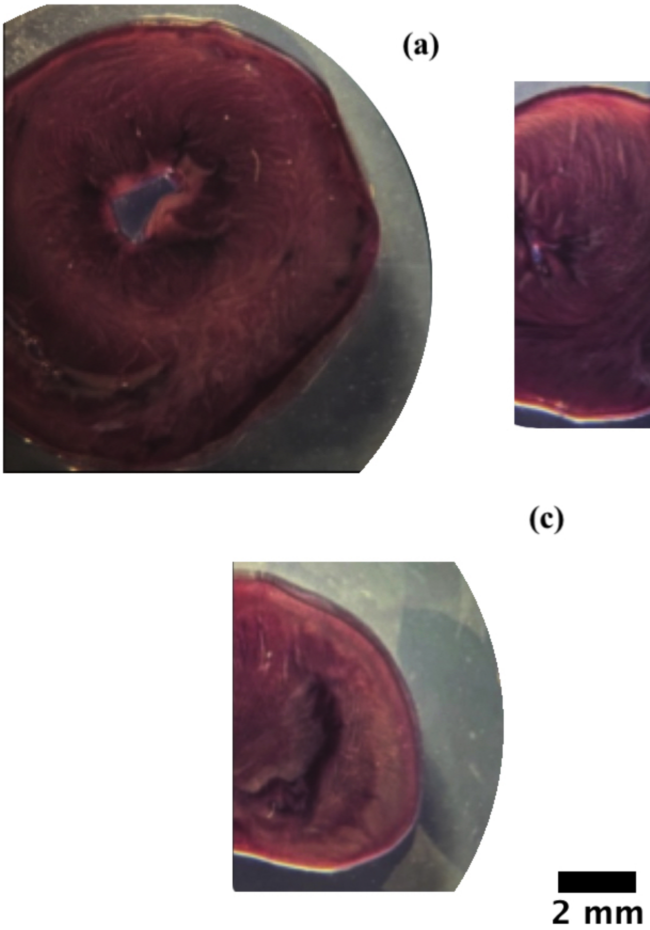

Figure 2.14: Representative images of three different sections ((a) near basal, (b) middle, and (c) apical) of a heart exposed to ischemia/reperfusion (I/R) protocol in Langendorff settings stained with nitro blue tetrazolium to detect infarct areas.

At this point, statistical tests were performed on the experimental data considering the central region of hearts (slice 350 to 800) using one-way ANOVA, followed by unpaired t-test corrected according to Bonferroni for multiple comparisons. Possible statistical differences between the control and "treated" (I/R and I/R+PSELT) hearts were evaluated. The results show (Figure 2.15) that in the case of I/R there is a statistically significant difference ($p<0.0001$) greater than that of I/R+PSELT ($p<0.001$).

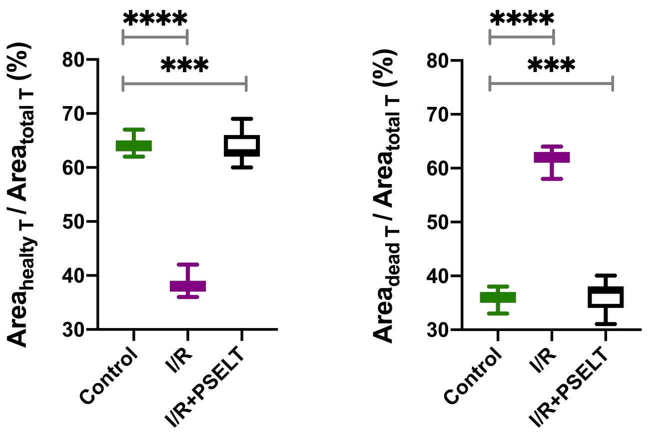

(a) (b)

Figure 2.15: Percentage (a) healthy and (b) dead tissues respect total tissues (LVW + IVS), for a subset of data (central region of hearts, slice 350 to 800). For statistical tests, treated samples were compared with the control sample.

Finally, the mean and standard error of the percentage of healthy and dead tissue to total tissue was calculated. It is worthwhile to mention that to test for biological variability at least two replicates were analyzed for each sample type. The results of the mean and standard error are shown in Table 2.3. Interestingly, the percentage of dead tissue in the case of I/R+PSELT is comparable with the results obtained for the control heart, confirming its action against global ischemia-induced damage.

Table 2.3: Mean and standard error of area of healthy and dead tissues versus area of total tissues.

Sample label	Area$_{\text{healthy T}}$/Area$_{\text{total T}}$ (%)	Area$_{\text{dead T}}$/Area$_{\text{total T}}$ (%)
Control	68.29 ± 0.17	31.71 ± 0.17
I/R	37.31 ± 0.48	62.69 ± 0.48
I/R+PSELT	72.26 ± 0.31	27.74 ± 0.31

Cavities between muscle strips (shown in red in Figure 2.16) were quantified by fractal dimension analysis, a nondimensional parameter that determines the degree of irregularity of a structure [101, 102]. The analysis was conducted for a subset of data, selecting a volume of interest (Figure 2.16). The data shows that the fractal dimension obtained for samples with global ischemia is smaller compared to that determined for the control and I/R+PSELT samples. This result further confirms the action of the peptide in preventing cardiac damage. The volume of the cavities between muscle strips was calculated for the different sample types; the results show that in the case of the

I/R heart, the cavities between muscle strips volume is $(4.96 \pm 0.30)\text{x}10^9$ μm^3, whereas for the control heart and the I/R+PSELT heart it is $(3.53 \pm 0.16)\text{x}10^{10}$ μm^3 and $(5.53 \pm 0.13)\text{x}10^{10}$ μm^3, respectively (error on volume was calculated in accordance with Lin et al. [103]). The results are consistent with the possible contracture of muscle bands during the onset of global ischemia. The data analysis of fractal dimension was also performed on tissues, but as expected, no particular differences were found between the different sample types (Figure 2.16, referred to as HealthyT and DeadT).

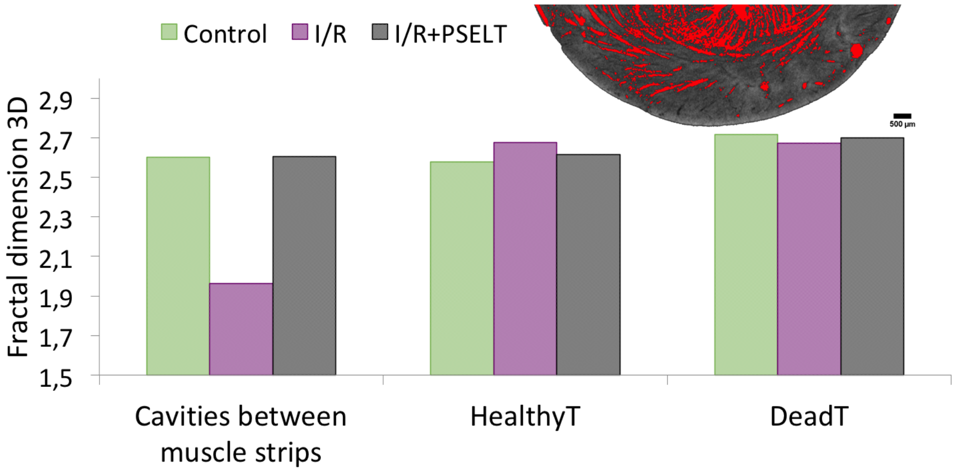

Figure 2.16: Fractal dimension of cavities between muscle strips in a particular volume of interest.

Microtomographic analysis confirms that PSELT mitigates cardiac damage. This work demonstrates that the μ-CT can be a powerful tool for virtual histology. In fact, it is possible to perform a large number of non-destructive histological examinations and to study a sample as a whole, it can identify the various structures of the heart and discriminate healthy tissue from dead tissue.

Although the preliminary stage of the study, due to the limited number of samples, the results obtained are very encouraging.

Results show how the combination of ATR-FTIR and μ-CT is particularly powerful for studying rat cardiac cells and the rat heart with ischemia because the two techniques provide complementary information. ATR-FTIR, with its ability to analyze molecular chemical changes, is ideal for understanding how the responses of functional groups (proteins, lipids, nucleic acids, and carbohydrates) after ischemia or PSELT treatment. On the other hand, μ-CT provides a 3D image of the entire sample, allowing us to visualize the spatial distribution of damage throughout the cardiac tissue.

2.1.5 Conclusions

In conclusion, this study shows that both experimental approaches and data analysis are important tools for biomedical applications. The results indicate that the treatment of both H9C2 cardiac cells and the whole heart organ with the PSELT peptide derived from the SELENOT protein provides a protective effect against the damage caused by PA in H9C2 cardiomyocytes by contrasting cell death, lipid accumulation and against global *ex-vivo* induced myocardial ischemia by reducing the extension of infarct size. In particular, the spectroscopic analysis revealed that PSELT reduced the effects induced by PA treatment in terms of membrane fluidity and protein/lipid contents. The lipid/protein ratio increased from 0.200 ± 0.079 (control) to 0.337 ± 0.043 (PA sample). While the CH_2 symmetric band (2852 cm^{-1}) showed a reduction in bandwidth, decreasing from 16.747 ± 0.003 cm^{-1} (control) to 16.030 ± 0.401 cm^{-1} (PA), indicating that the PA treatment reduces the permeability of the cell membrane. For cells treated with PA and PSELT simultaneously, the absorption spectrum showed no particular differences, but a small reduction in nucleic acid and carbohydrate components remained. In contrast, the treatment with PSELT alone on the cells included a decrease in the bands corresponding to nucleic acids and carbohydrates as well as the lipid content.

On the other hand, by μ-CT X-ray examination of *ex-vivo* rat hearts, it has been demonstrated that PSELT mitigates the consequences of global ischemia. Specifically, the analysis indicates a decrease in the percentage of healthy tissue area compared to total tissue area from (68.29 ± 0.17) % for the control samples to (37.31 ± 0.48) % for hearts with global ischemia (I/R). On the other hand, when global ischemia is combined with treatment (I/R+PSELT) the percentage of healthy tissue area to total tissue area is comparable with that control heart: (72.26 ± 0.31) %. In addition, the fractal dimension for samples with global ischemia (I/R) is smaller than that determined for control and I/R+PSELT samples, increasing from 1.96 for I/R to 2.60 for control and I/R+PSELT. This result further confirms the action of peptide in preventing cardiac damage.

Finally, the potentiality of μ-CT X-ray for 3D virtual histology was clearly assessed.

2.2 Case study 2: Discrimination of Multiple Sclerosis Patients Using ATR-FTIR

Multiple sclerosis, one of the most prevalent neurodegenerative diseases of the central nervous system, causes an enormous variety of physical and cognitive symptoms and can result in permanent physical and cognitive decline. The diagnosis of MS is not easy and require several clinical and instrumental tests. Spectroscopic methods are increasingly being used in the medical field to improve and complement diagnostic clinical processes. In this work, we used ATR-FTIR spectroscopy to analyze plasma samples to discriminate patients with MS from healthy control individuals, and identify potential spectral biomarkers that support diagnosis through rapid noninvasive blood testing. The analysis of the experimental data was supported by a number of statistical methods. The results show an increase in the lipid/protein ratio in MS patients, indicating changes in the level (metabolism) of these molecular components in plasma. In addition, multivariate tools provided a promising success rate in diagnosis through the identification of spectral biomarkers, and that can be further combined to obtain a linear predictor, that provides a simple diagnostic tool in which the contribution of different molecular components is summarized.

2.2.1 Introduction

MS is a chronic inflammatory neurodegenerative disease of the central nervous system (CNS) that induces axonal loss and neuronal demyelination. Most of people affected are young adults and, in some cases, can lead to long-term disability [104]. According to estimates of 2023, 2.9 million worldwide individuals have MS. The disease is more common in industrialized nations and higher socioeconomic levels, with a higher tendency to affected women than men, and a female-to-male ratio of 3:1 [105]. It can occur with different neurological symptoms including visual disturbances, sensory disturbances, motor weakness, incoordination, sleep disturbances, and fatigue [106]. The diagnosis of MS is not easy due to the unspecificity of the symptoms, and the misdiagnosis, particularly at the early stage, is a problem that can have significant effects for patients as well as health systems [107, 108]. The McDonald criteria, revised in 2017, emphasize that there is no single pathognomonic clinical sign or diagnostic test of MS based on the integration of clinical, imaging, and laboratory evidence [109]. For instance, some of these criteria are: a characteristic magnetic resonance imaging (MRI) pattern displaying CNS lesions dispersed in time and space, the cerebrospinal fluid (CSF) study indicating an increase in immunoglobulin (IgG) concentrations, and the presence of oligoclonal bands, and delayed latencies of visual evoked potentials. Blood tests, instead, are frequently performed to rule out other diseases. MS's clinical course is unexpected and highly variable. The early stage of the disease is represented by the clinical isolated syndrome (CIS) and relapsing-remitting (RR) type. Recurring relapses are often associated with CNS area inflammation and demyelination. Neurodegeneration advances and patient disability accumulates when a self-sustaining inflammation takes place and remyelination is inhibited, in this case, the patient is in the secondary progressive (SP) phase of the disease. Some patients may experience a slow and constant development of diseases (primary progressive (PP)). Even in the absence of clinical symptoms, there may be significant disease activity within the central nervous system [107, 109]. The most commonly used measure of clinical outcomes and degree of disability is the Expanded Disability Status Scale (EDSS). The EDSS values range from 0, corresponding to normal neurological status, to 10. Values of 7 or more on the EDSS scale denote a highly compromised clinical condition. Because MS is a complex disease, researchers are constantly looking for novel approaches to combine established diagnostic techniques with innovative complementary methods that can detect and measure new important parameters. This is especially important in the early stages of the disease, when pathological signs may be undefined or mild. The research for new biomarkers or metabolites to be utilized as auxiliary tools in diagnosis and disease progression monitoring is an increasing field of interest in clinical research. CSF is the best source of biomarkers for MS [110–112], but the sampling is quite invasive. In contrast blood samples are simple to obtain and can provide information about the state of the peripheral immune system [110, 113, 114]. In a clinical context, the capacity to characterize biofluids both quantitatively and qualitatively is extremely important. Advanced biophysical/analytical methods, such as IR spectroscopy [115], may be used to detect and quantify biological components (such as proteins, carbohydrates, nucleic acids, and lipids) and search for disease-specific biomarkers. One important advantage of vibrational spectroscopy is its ability to simultaneously investigate several biomolecules present in the samples. It is interesting to note that the comparison of spectral profiles between biological samples from healthy and patients have frequently shown different and measurable changes that validate FTIR spectroscopy as an additional non-invasive tool for the diagnosis and discrimination of several diseases. These findings are frequently supported by multivariate statistical analysis.

2.2.2 Scientific rational

The scientific rationale behind the use of ATR-FTIR spectroscopy to discriminate patients with multiple sclerosis (MS) from healthy individuals is based on a number of clinical and technical considerations that combine the characteristics of the disease and the advantages offered by spectroscopic techniques, supported by rigorous statistical analysis.

ATR-FTIR is a technique that makes it possible to obtain detailed spectral profiles from biological samples, such as blood and plasma. The choice of this technique is related to its ability to: *1.* identify multiple biomolecules simultaneously and detect their possible changes due to neurodegenerative and inflammatory processes; *2.* plasma analysis with ATR-FTIR represents a noninvasive, fast, and easily accessible method, unlike cerebrospinal fluid analysis.

The molecular features and the parameters to be investigated were chosen from comparisons with literature data.

The use of plasma samples as a biological matrix was a central aspect of the methodology, as plasma is easily during routine clinical tests and reflects the pathophysiological state of the organism, providing useful information for disease diagnosis and monitoring.

Finally, the analyses were supported by statistical studies to check their sensitivity and specificity.

2.2.3 Materials and methods

Samples

45 blood samples from MS patients with confirmed diagnosis and 40 blood samples from healthy individuals (healthy control (HC)) were collected at the Annunziata Hospital in Cosenza (Italy) and the Health Center of the University of Calabria. Inclusion criteria, for diseased subjects, were: age in the range 18–70 years and a confirmed MS diagnosis according to the revised McDonald criteria [109]. Exclusion criteria were: concomitant autoimmune disorders (other than MS), and pregnancy.

Clinical and personal information collected included the patients' gender, age, duration of disease, EDSS-estimated disease severity, and current drug therapy. The clinical and demographic information of the subjects participating to the research is summarized in Table 2.4. The MS patient clinical data included:

- *age*: average 42.7, range 22–69 years;
- *gender*: 31 females, 14 males;
- *disease phenotype/form*: 38 RR-MS, 7 SP-MS;
- *disease duration*: from 1 to 47 years. In particular: 37.7% $\leq$ 5 years, 22.2% in the range 6–10 years, 20.0% 11–15 years, 11.1% 16–20 years, 6.6% 24–35 years, and one patient with a diagnosis dating back 47 years.
- *disability degree* in terms of EDSS: range 0.5–7.0. In particular 71% of patients had a mild score (EDSS $\leq$ 3.0), whereas 29% of the patients had a moderate/severe level of disease (EDSS $\geq$ 3.5);
- *drug therapy*: 38/45 patients received immuno-modulatory or suppressive treatment, with the exception of seven.

Individuals in the HC group (including 21 females and 19 males, with ages between 24-60 years, and an outlier of 71 years) had no signs of inflammatory and neurological diseases.

Both group members were of the same ethnic origin (Calabria in southern Italy). Every recruited subject received complete information about the study's objectives, and their signed permission was obtained. The study was approved by the Ethics Committee of the north area of Calabria. Every procedure was carried out in compliance with the applicable rules and regulations.

Table 2.4: Research participant's clinical and demographic information. The age is reported as mean ± standard deviation.

		MS patient	HC
Gender (number of subjects)	F	31	21
	M	14	19
EDSS (number of subjects)	mild (0.5 - 3.0)	32	
	moderate/severe (3.5 - 7.0)	13	
Disease onset (number of subjects)	$\leq$ 10y	27	
	$>$ 10y	18	
Mean age (years)		42.7 ± 11.3	37.3 ± 10.9

Samples (3 mL) of peripheral venous blood were collected in EDTA tubes, and plasma was separated by centrifugation for 15 min at 1500 rpm. Processed plasma was dispensed in 0.15 mL aliquot and stored at - 20 °C until use.

ATR-FTIR measurements

Before the measurements, plasma samples were degassed at 25 °C after being thawed. A Tensor II spectrometer from Bruker (Bruker Optics, Germany) equipped with an MCT detector and a silicon BioATR II cell ideal for liquid samples was used to collect the spectra. A PilotOne thermostat regulated the cell's temperature. After depositing 20 μL of plasma in the sample cell, it was allowed to equilibrate for three minutes at 25 °C. Dulbecco Phosphate Buffer Saline (DPBS) solution, 10 mM at pH 7.4 (from Sigma Aldrich, St. Louis, Missouri, USA), was used as a background spectrum recorded before each measurement and automatically subtracted from the sample spectrum. The spectra were averaged over 120 scans and recorded in the 4000–900 cm^{-1} region with a spectral resolution of 4 cm^{-1}. To evaluate the repeatability, up to five replicate spectra were acquired for each sample.

Using the Bruker Opus software version 7.0, the absorption spectra were pre-processed using the following steps: rubber band baseline correction, vector normalization, and cutting of the fingerprint area (1800–900 cm^{-1}) and high region (3050–2800 cm^{-1}). The absorption spectra recorded for each sample were averaged, to compare individuals rather than spectra. The mean and standard deviation of each class were then calculated by further averaging the acquired 40 HC and 45 MS ATR-FTIR spectra. This procedure is been used because averaged spectra are more representative as they reduce the influence of individual variances. Thirteen smoothing points were used in the Savitsky-Golay procedure to compute the second-order derivatives of the mean spectra. Vector normalization was performed as final step for the second derivative spectra [54, 115].

Statistical analysis

Statistical differences of specific bands in the absorbance of HC and MS groups were assessed using two tailed parametric t-test or one-way ANOVA, followed by unpaired t-test corrected according to Bonferroni for multiple comparisons. A p-value of 0.05 or less was considered significant in all statistical tests. The degree of significance for the comparison of the data with the control group was indicated as $^*p < 0.05$; $^{**}p < 0.01$; $^{***}p < 0.001$; $^{****}p < 0.0001$. Multivariate data analysis, with the support of Professor Francesca Condino of the Department of Economics, Statistics and Finance “Giovanni Anania” of the University of Calabria, was performed using R statistical software on both absorption and second derivative spectra. Three different multivariate data analysis methods have been considered: principal component linear discriminant analysis (PCA-LDA), partial least-squares discriminant analysis (PLS-DA), and random forest (RF). The performance of each classification model was tested using the accuracy (namely the proportion of correct predictions), sensitivity and specificity parameters. The final classification model performance was assessed on the test set, including the sensitivity and specificity parameters, which are respectively described as:

$$Sensitivity = \frac{TP}{TP + FN}$$

$$Specificity = \frac{TN}{TN + FP}$$

where true positives, true negatives, false positives, and false negatives are denoted by the letters TP, TN, FP, and FN.

In contrast to specificity, which shows the likelihood that a test result will be negative in the absence of disease, sensitivity relates to the probability that a test result will be positive when the disease is present.

A plot of sensitivity vs specificity for various cut-off points of test class probabilities, which is known as the Receiver Operating Characteristic (ROC) curve, was determined. How effectively the model can differentiate between MS and HC was determined by taking the area under this curve (AUC). This parameter takes values between 0 (incorrect discrimination) and 1 (correct discrimination).

In addition, a measure of variable importance is derived, depending on the particular method, in order to determine the different IR wavenumber importance in the discrimination process. Based on their biological importance, many spectral markers were chosen from the absorbance spectra and combined in a linear predictor. This index can be used as a simple tool to classify each subject as either healthy or diseased based on whether the final predictor assumes a positive or negative value, or if the corresponding estimated probability is higher or lower than the cutoff of 0.5. Subsequently, the final model from each technique was also used to assess the prediction for patients with different levels of disability, differentiating between moderate/severe and mild disability, as well as between short and long disease duration.

2.2.4 Results and discussion

The two most significant regions in the ATR-FTIR spectra of MS patients and HC are displayed in Figure 2.17: the fingerprint (FP) region in the 1800–900 cm^{-1} range, which is dominated by the amide I and amide II peaks, which are caused by the absorption band of proteins, and the 3050–2800 cm^{-1} range (high region, HR), which contains the symmetric and asymmetric stretching vibrations of CH_2 and CH_3 groups. Table 2.5 details the band assignments of the main plasma absorption peaks in the IR region 3050 - 900 cm^{-1} [104–107].

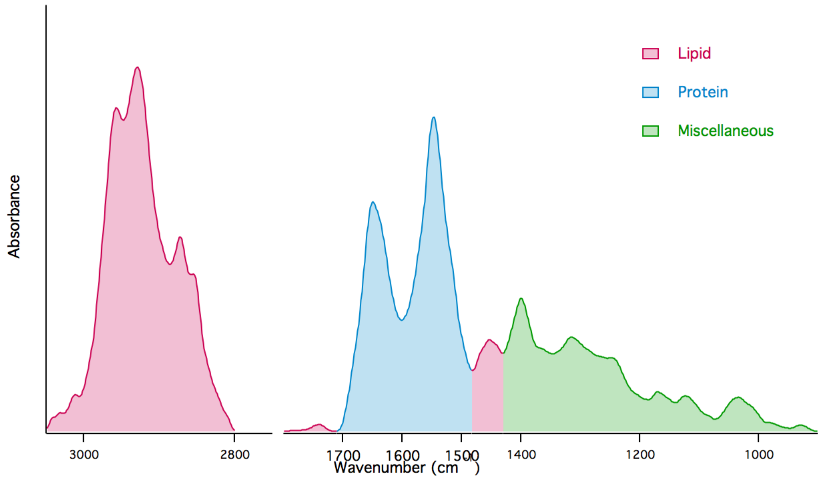

Figure 2.17: Representative ATR-FTIR spectra. The high region (3050–2800 cm^{-1}) and the fingerprint region (1800–900 cm^{-1}) are displayed. The absorbance of particular functional groups is indicated by different colors.

Table 2.5: Band Assignments of the Main Peak Absorption of plasma.

Wavenumber (cm^{-1})	Assignment of Functional Groups
3010	Olefinic C=CH stretching vibration (unsaturated lipids)
2957	CH_3 asymmetric stretching (lipids and proteins)
2923	CH_2 asymmetric stretching (lipids and proteins)
2872	CH_3 symmetric stretching (lipids and proteins)
2852	CH_2 symmetric stretching (lipids and proteins)
1739	C=O stretching (ester functional groups in lipids, fatty acids, cholesterol, triglycerides)
1650	Amide I (protein C=O stretching)
1546	Amide II (protein NH bending, CN stretching)
1480-1430	CH_3, CH_2 bending (mainly lipids)
1399	COO^- symmetric stretching (fatty acids, amino acids)
1337	CH_3 symmetric bending (lipids)
1315	CH_2 wagging (lipids)
1240	PO_2^- asymmetric stretching (nucleic acids, phospholipids)
1173	CO–O–C asymmetric stretching (ester bonds in cholesteryl esters)
1170-1120	C-O and C–O–C stretching ((polysaccharides, glycogen)
971	$C–N^{\pm}–C$ stretching (nucleic acids)
924	Ribose ring vibrations (RNA)

Figures 2.18 and 2.19 show the ATR-FTIR spectra of MS patients and HC in the FP and HR regions. Moreover, Figures 2.20 and 2.21 show the average absorbance

spectra and the second derivative for the two groups. Usually, the second derivative of the absorbance spectra is used to distinguish overlapping neighboring bands.

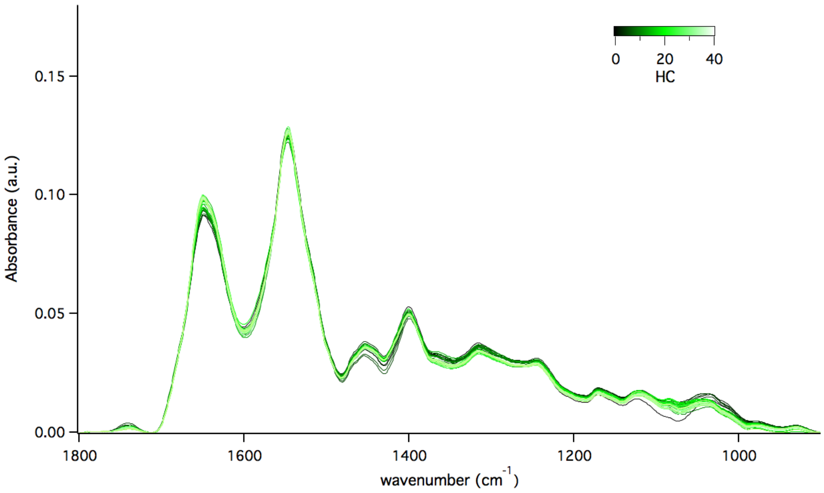

(a)

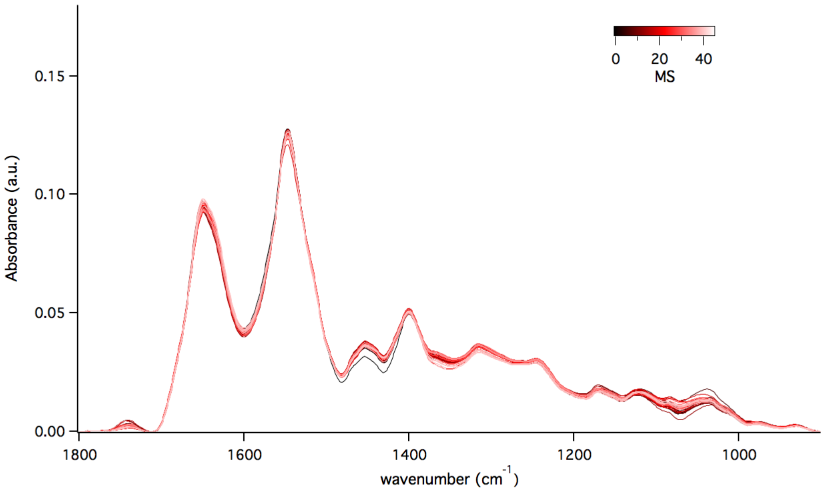

(b)

Figure 2.18: ATR-FTIR spectra of plasma of (a) HC and (b) MS patients in the FP region.

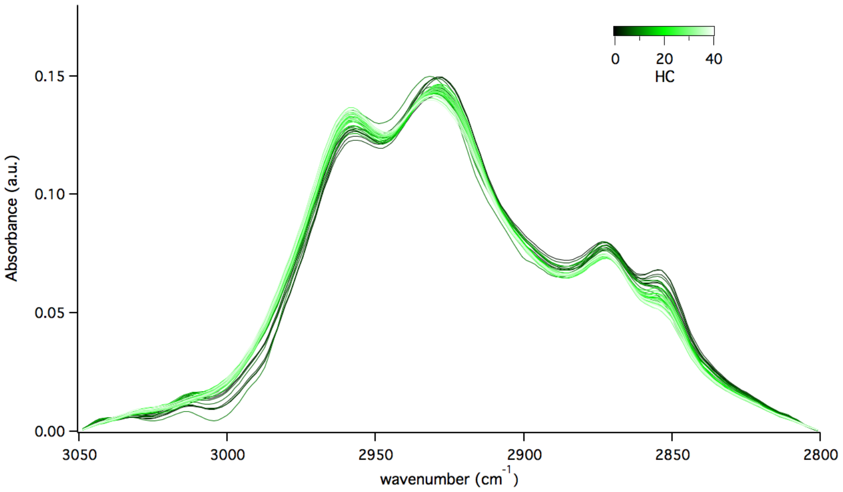

(a)

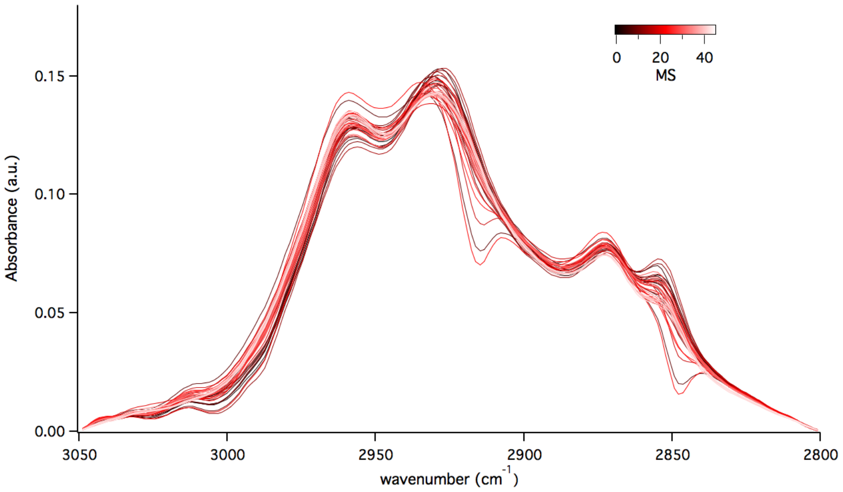

(b)

Figure 2.19: ATR-FTIR spectra of plasma of (a) HC and (b) MS patients in the HR region.

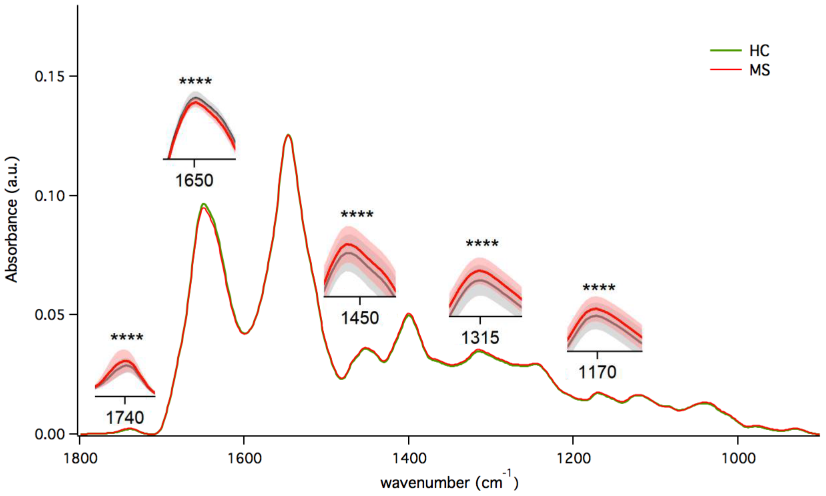

(a)

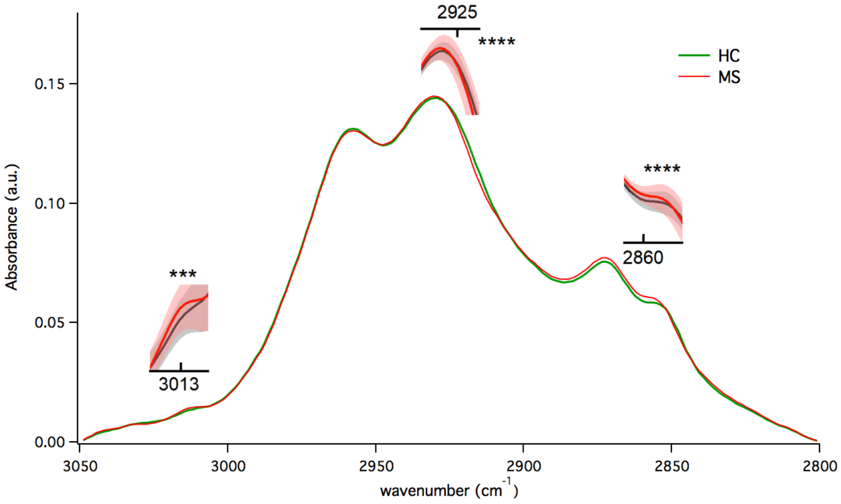

(b)

Figure 2.20: ATR-FTIR average spectra of plasma of HC (green) and MS (red) patients in the (a) FP and (b) HR region. Selected spectral regions are enlarged and the statistical significance is shown according to their p-value (***$p < 0.001$; ****$p<0.0001$).

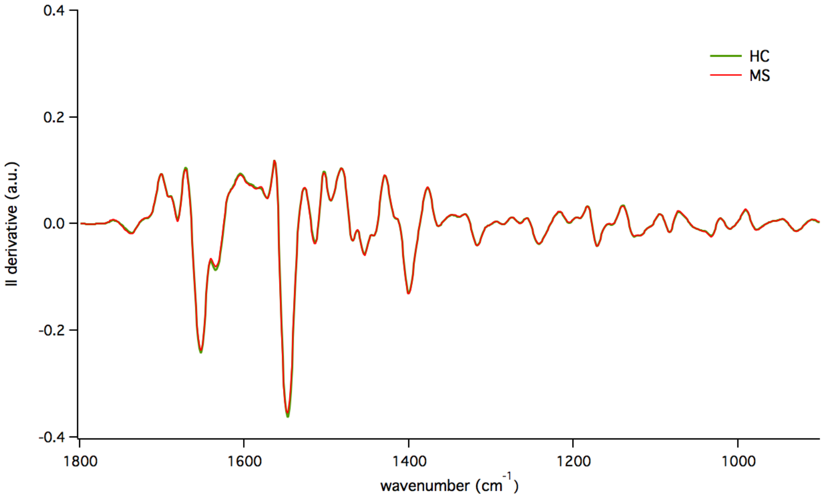

(a)

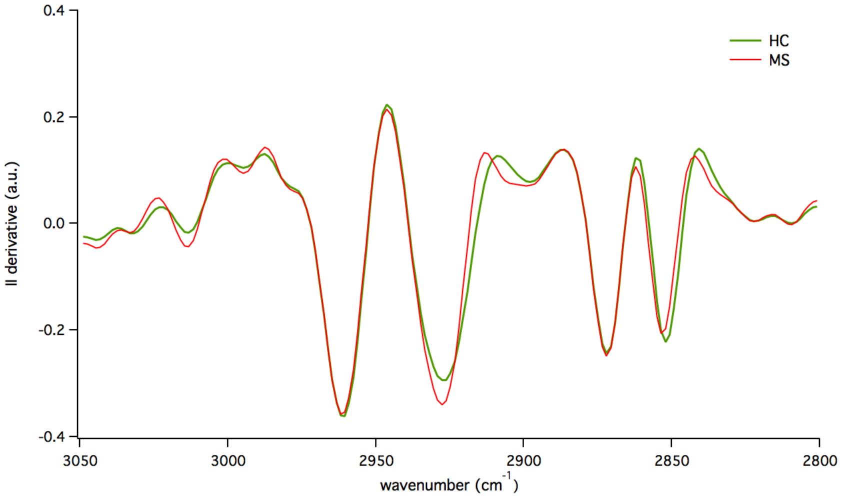

(b)

Figure 2.21: Second derivative vector normalized spectra of plasma of HC (green) and MS (red) patients in the (a) FP and (b) HR region.

The two peaks of greater intensity, in the FP region, are attributed to the amide I and amide II bands and relate mostly to the vibration of the functional groups of proteins (Table 2.5). More than 20000 distinct proteins (a wide concentration range (pg-mg/mL)) contribute to the very complex proteomic profile of blood plasma [116], and it correlates with the spectroscopic response/sensitivity. The proteins with a higher abundance in plasma are:

- *human serum albumin (HSA)*: 60% by weight;
- *immunoglobulin* (IgG): 14%;

- *transferrin*: 6%;
- *fibrinogen*: 4%;

IgG is a β-sheet protein that absorbs at around 1633 cm^{-1}, whereas HSA, which has a common α-helix secondary structure, dominates the peak at 1650 cm^{-1}. Lipids, in the FP region, are the main contributors of the bands centered at 1740 and 1453 cm^{-1}. The stretching vibrations of CH_3 and CH_2 groups in lipids and proteins asymmetric (2960 and 2927 cm^{-1}) and symmetric (2872 and 2852 cm^{-1}) are mostly responsible for the HR region of the ATR-FTIR spectrum. Also contributing in this region are the N–H (NH_3^+) stretching vibrations [50, 63, 91]. Free lipids such as cholesterol, triglycerides, phospholipids, fatty acids, and protein-bound lipids are found in human plasma.

The spectral features of the HC and MS average spectra are very similar, and from visual inspection alone it is difficult to detect specific differences that may be related to the health status. Similar findings were recently found in preliminary FTIR studies performed on blood fractions of MS patients [117, 118]. Since the components of serum and plasma are the same in all individuals, regardless of their healthy condition, this result is expected. Nevertheless, from the average spectrum, emerge there are some variations in the intensity of some peaks, which may be connected through the Lambert-Beer equation to fluctuations in the concentration of the functional groups associated with the relevant chemical component [63] (see Figure 2.20). In particular, the 1750–1725 cm^{-1} region attributed to the ester C=O stretching band of lipids is more intense in the MS group whereas the amide I peak has a lower intensity. This suggests that the concentration and/or metabolism of lipids and proteins are altered. Some studies conducted by Yonar et al and Choo et al on cerebrospinal fluid from MS patients, and on gray matter tissue samples and central nervous system plaques show reduced intensity in the C=O band [119, 120]. This result was interpreted as a consequence of the demyelination process reducing the lipid level. Because of the closeness of the different physiological compartments, the free or degraded lipids can enter the circulatory system. According to a recent study, MS patients' lipoproteins include more lipids than those of healthy controls [121].

Furthermore, oxidized lipids produced by free radicals, which are thought to be involved in the pathophysiology of MS [122], could contribute to the increase in the C=O band's intensity relative to the intensity of the CH_2. In this regard, the ratio between the intensities (I_{1739}/I_{1468}) of the absorption band of the C=O (absorption peak at 1739 cm^{-1}) and of the CH_2 (absorption peak at 1468 cm^{-1}) was determined; the result showed an increase in the intensity of the C=O band compared with the intensity of the CH_2 absorption peak (Figure 2.22). Being characterized by altered lipidomic profiles, MS investigations have used plasma [121], serum [123], and CSF [124] to find potential lipid biomarkers for diagnosis and therapy monitoring. It is interesting to remember that lipids, in addition to be fundamental components of cellular membranes, also play key roles in the signaling and control of the immune system [125].

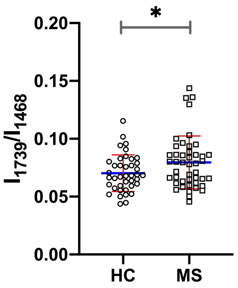

Figure 2.22: Ratio of the intensities of the carbonyl C=O peak and the CH_2 scissoring motion for HC and MS. The blue lines represent the mean values and the red lines are the standard deviation. The degree of significance of the comparison between HC and MS is indicated as *$p<0.05$.

The albumin and IgG quotient in serum and cerebrospinal fluid is an indicator of blood-brain barrier (BBB) integrity. Common in MS is damage of the BBB, which can lead to the extravasation of plasma components through damaged vessels into the central nervous system [126, 127]. This event could explain the observed reduction in amide I band intensity in MS patients. It can also be seen that the olefinic C=CH stretching vibration band at about 3013 cm^{-1} increases in MS patients ($p < 0.001$, Figure 2.20b). In the CSF, the intensity of this band decreases [119]. Furthermore, compared to healthy control subjects, MS patients have an increased intensity of CH_2 asymmetric stretching at about 2927 cm^{-1} ($p < 0.001$, Figure 2.20b).

To better understand the potential variations of significant spectral bands disease-induced, it was calculated the area ratio of molecular components and the intensity ratio of specific functional groups. Two methods were used to determine the lipid/protein ratio (Figure 2.23):

- the ratio of the areas under the 3050–2800 cm^{-1} region (A_{HR}) and the sum of the areas under the amide I and amide II bands ($A_{\text{amide I + amide II}}$),
- the ratio of the intensity of the peaks at 1453 cm^{-1} (I_{1453}) and amide I (1650 cm^{-1}, I_{1650}).

According to both analyses, the lipid/protein ratio of MS patients was higher than that of the control group. This result is consistent with many studies that show elevated levels of lipids in the blood and plasma of MS patients [121, 128–130]. Patients were further separated in terms of disease severity and duration. The results of the lipid/protein ratio maintain statistical significance for MS patients having a mild disability score compared to HC and for the disease duration subgroups. This observation may have an explanation: the metabolic disorder caused by CNS inflammation is significant at an earlier stage of MS and is reflected more in the plasma components. On the other hand, as the disease progresses, the body often compensate the metabolic changes induced by MS, resulting in a subtle level of blood plasma alteration [129–131]. Sex is also an important variable in MS. However, male vs female subgroups separation does not provide statistical differences for the lipid/protein ratios (p-value ranges between 0.527 and 0.923).

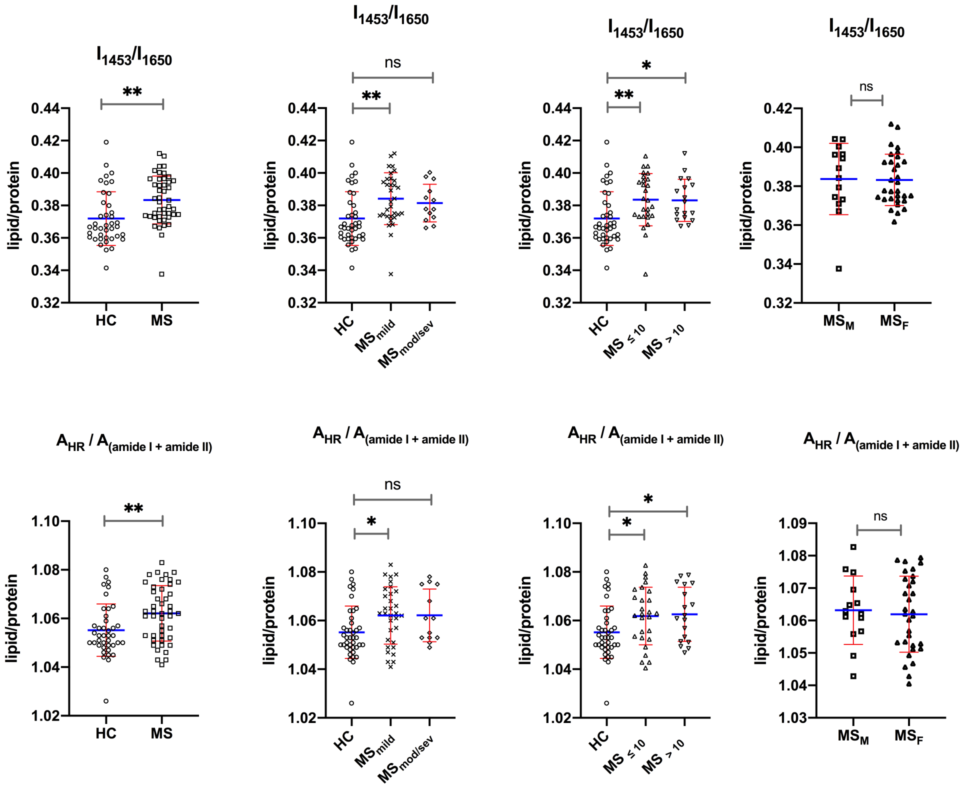

Figure 2.23: Lipid/protein ratio for HC, MS, MS$_{\text{mild}}$, MS$_{\text{mod/sev}}$, MS$_{\leq\ 10\text{y}}$, MS$_{>\ 10\text{y}}$, MS$_{\text{Male}}$ and MS$_{\text{female}}$ groups.

To identify further subtle differences among the spectra registered for the two classes of subjects, multivariate approaches were applied. The analysis was performed on the second derivative spectra of the two classes of samples and in the two regions of the spectrum. For the classification three different models have been tested, PCA-LDA, PLS-DA and RF, and their performance was evaluated by considering either the MS patients as a single group or split in two subgroups corresponding to the severity and duration of the disease. The performance of the final models on the test set for the three multivariate methods in terms of sensitivity and specificity is given in Table 2.6.

Table 2.6: Sensitivity and Specificity for the chemometric models for either the MS group as a whole or separated in subgroups with different EDSS values or disease onset in the FP and HR spectral regions.

		HR		FP	
	Model	Sensitivity (%)	Specificity (%)	Sensitivity (%)	Specificity (%)
MS	PLS-DA	67	83	67	67
	PCA-LDA	78	75	67	67
	RF	78	58	78	83
MS_{mild}	PLS-DA	67	75	67	63
	PCA-LDA	78	75	67	63
	RF	78	63	78	75
$MS_{mod/sev}$	PLS-DA	67	100	67	75
	PCA-LDA	78	75	67	75
	RF	78	50	78	100
$MS_{\leq 10y}$	PLS-DA	67	80	67	60
	PCA-LDA	78	80	67	60
	RF	78	60	78	60
$MS_{>10y}$	PLS-DA	67	86	67	71
	PCA-LDA	78	71	67	71
	RF	78	57	78	100

In summary, the RF model (Table 2.6) produces the best classification in terms of sensitivity (78%) and specificity (83%) for the FP region, whereas the PLS-DA model performs best in the HR region. The smoothed ROC curve, which connects the sensitivity to the specificity of the diagnostic/decisional test, was used to ultimately evaluate the statistical models' correctness and capacity to distinguish between the two groups on the test set. The findings for the two regions are shown in Figure 2.24. In the FP region (Figure 2.24a), the higher AUC value is 0.78 for the RF model; in the HR region (Figure 2.24b), it increases to 0.83 for the PLS-DA model. The outcomes demonstrate that these methods have a significant predictive power.

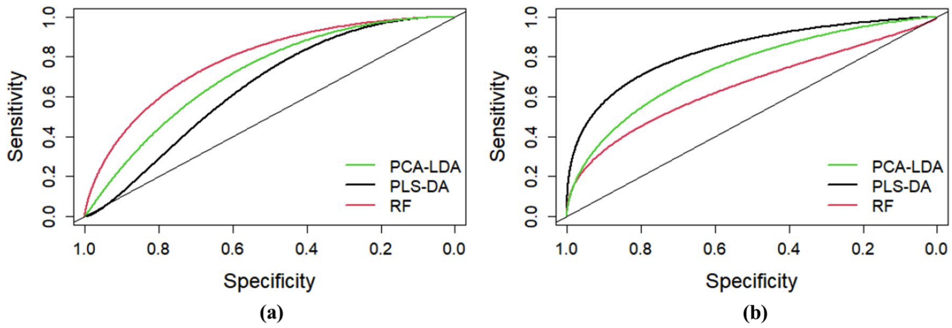

Figure 2.24: Performance measurement of the chemometric methods as described by a smoothed ROC curve considering the (a) FP and (b) HR spectral regions.

Using the PLS-DA and RF methods in the two regions, the most relevant variables (wavenumbers) responsible for classification were obtained: 1320, 1510, 2860, and 3016 cm^{-1}. These wavenumbers can be considered as biomarker peaks, the variations in their intensity correspond to the statistically significant molecular change associated with the disease.

The peak at 1510 cm^{-1} is assigned to amide II, indole ring (tryptophan side chain) [91, 132]. In comparison to the healthy control group, the blood of MS patients included higher levels of glutamic acid and tryptophan [128]. The peak at 1320 cm^{-1} is associated twisting/wagging vibrational modes of CH_2 and CH_3 in collagen and nucleic acids [91]. The peak at 3016 cm^{-1} is assigned to C=CH stretching of unsaturated lipids and CH_2 aromatic stretch of proteins side chain; while the peak at 2860 cm^{-1} to the C–H asymmetric stretching vibration.

These associations suggest that the most important wavenumbers for differentiation may be assigned to distinct groups of molecular species, revealing spectrum changes associated to the corresponding biomolecules in the plasma.

As a further step to possibly improve the discrimination of the two groups of subjects, we have considered a number of spectral biomarkers in a linear combination to obtain a single and simple index, to be used for diagnostic purposes. The following indicators are used in the analysis, and describes:

- the area ratios of molecular components (blu box Figure 2.25):
    - lipid/proteins ($A_{HR}/A_{amide\ I\ +\ amide\ II}$): determined as the area, A_{HR}, corresponding to the region between 3050 and 2800 cm^{-1} and the area corre-

  sponding to the amide I and amide II peak;
  - the area of the olefinic C=CH peak over AHR ($A_{Olefinic}/A_{HR}$);
  - the area of the asymmetric stretching vibration peak of CH_2 (A_{CH_2asym}/A_{HR});
  - area amide I and amide II ($A_{amide\ I}/A_{amide\ II}$);
  - $A_{C=O}/A_{HR}$;
  - $A_{C=O}/A_{1453}$;
  - $A_{HR+C=O}/A_{amide\ I\ +\ amide\ II}$;
  - $A_{CH_2asym}/A_{CH_2sym\ +\ CH_2asym}$;
- the intensity ratio of specific peaks of functional groups (gray box Figure 2.25):
  - I_{1453}/I_{1650};
  - I_{1739}/I_{1468};
- the bandwidth (purple box Figure 2.25) of amide I and of the ester C=O peak at 1739 cm^{-1} ($Bandwidth_{amide\ I}$ and $Bandwidth_{C=O}$). Bandwidth values were determined at 75% of the height of the maximum peak intensity from the baseline;
- the intensity (orange box Figure 2.25) at 1320, 1510, 2860, and 3016 cm^{-1}, selected as important wavenumbers for the discrimination of MS from HC according to the random forest classification algorithm (I_{1320}, I_{1510}, I_{2860}, and I_{3016}).

The average value and the standard deviation of each of these parameters determinate from the 45 MS and 40 HC samples is listed in Table 2.7 and the distribution can be observed in Figure 2.25.

Table 2.7: Spectral indicators. Values are given as average ± standard deviation. The p-value is obtained via unpaired t-test.

Possible diagnostic indicators	HC	MS	p-Value
$A_{HR}/A_{\text{amide I + amide II}}$	1.0552 ± 0.0107	1.0621 ± 0.0114	0.005
$A_{C=O}/A_{HR}$	0.0036 ± 0.0009	0.0042 ± 0.0013	0.028
$A_{C=O}/A_{1453}$	0.0341 ± 0.0080	0.0388 ± 0.0120	0.038
$A_{HR+C=O}/A_{\text{amide I + amide II}}$	1.0591 ± 0.0112	1.0666 ± 0.0122	0.004
$\mathbf{A}_{\mathbf{CH2asym}}/\mathbf{A}_{\mathbf{CH2sym + CH2asym}}$	0.8750 ± 0.0068	0.8744 ± 0.0101	0.776
$A_{\text{CH2asym}}/A_{HR}$	0.4423 ± 0.0059	0.4402 ± 0.0097	0.230
$A_{\text{Olefinic}}/A_{HR}$	0.0110 ± 0.0012	0.0115 ± 0.0015	0.106
$\mathbf{A}_{\mathbf{amide\ I}}/\mathbf{A}_{\mathbf{amide\ II}}$	0.7250 ± 0.0165	0.7115 ± 0.0136	< 0.001
$\mathbf{I}_{\mathbf{1453}}/\mathbf{I}_{\mathbf{1650}}$	0.3719 ± 0.0166	0.3834 ± 0.0148	0.001
I_{1739}/I_{1468}	0.0702 ± 0.0158	0.0796 ± 0.0229	0.034
$\text{Bandwidth}_{C=O}$	16.0404 ± 1.1338	15.9344 ± 1.0337	0.653
$\text{Bandwidth}_{\text{amide I}}$	36.5558 ± 0.7052	36.3905 ± 0.7795	0.310
$\mathbf{I}_{\mathbf{1320}}$	0.0342 ± 0.0012	0.0349 ± 0.0010	0.003
$\mathbf{I}_{\mathbf{1510}}$	0.0559 ± 0.0010	0.0563 ± 0.0008	0.024
$\mathbf{I}_{\mathbf{2860}}$	0.0597 ± 0.0030	0.0616 ± 0.0031	0.004
I_{3016}	0.0120 ± 0.0013	0.0128 ± 0.0016	0.016

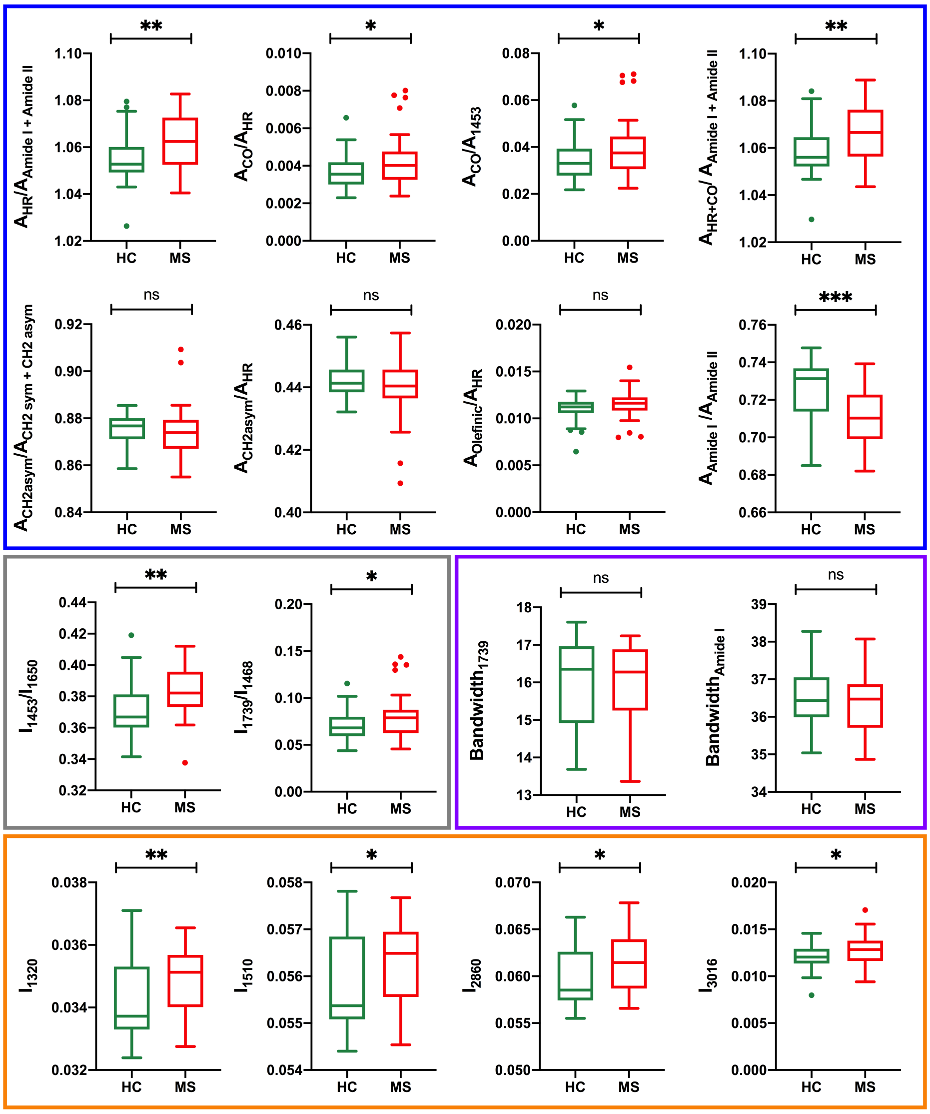

Figure 2.25: Box-plot of the spectral parameters derived from the analysis of the ATR-FTIR absorption spectra, illustrating the distribution of their values in the HC and MS groups.

Almost all of these bioindicators (Table 2.7) show statistical significance, revealing particular biochemical alterations, and then can be good candidates for samples differentiation. Specifically, the MS group has a greater lipid/protein ratio in comparison to the HC group. As previously reported, the increase in the lipid level is observed in the plasma of MS patients and, in parallel, the protein level decreases, as it is evidenced for example by the $A_{\text{amide I}}/A_{\text{amide II}}$ ratio.

These parameters were combined in a linear indicator function to create a concise prediction tool for medical diagnosis. In this regard, the final model was obtained by removing the irrelevant indicators using a backward stepwise selection process that starts with all of the spectral markers listed in Table 2.7. The remaining variables, which mainly contributed to the classification of the two groups of subjects, are the six indicators reported in bold in Table 2.7.

Figure 2.26 shows a comparison of the predicted probability distributions for the HC and MS groups. There are very few samples of misclassified individuals in both groups, and they are situated to the right and left of the threshold value (equal to 0.5), respectively.

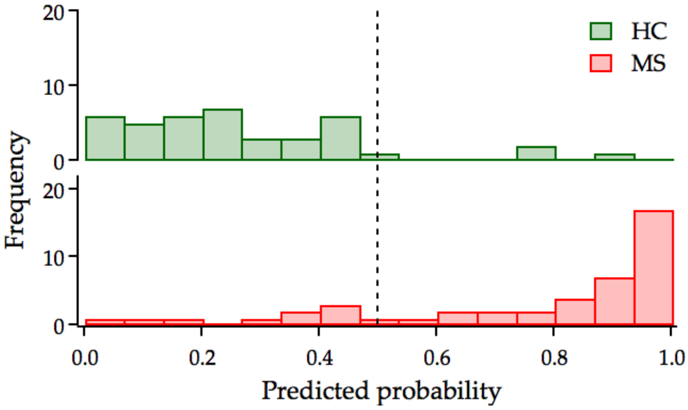

Figure 2.26: Distribution of the predicted probability for (upper panel) HC and (bottom panel) MS individuals. The dashed vertical line indicates the 0.5 score threshold. Score values ≤ 0.5 indicate subjects classified as healthy, score values >0.5 indicate subjects classified as diseased.

Table 2.8 reports the sensitivity, the specificity, and the AUC values for the whole MS group as well as for subgroups based on EDSS scores or the duration of the disease. The indications consistently demonstrate the strong capacity of the model to discriminate between MS and HC. The accuracy of the model is further demonstrated by the global ROC curve, which has an AUC value of 0.9 (Figure 2.27).

Table 2.8: Performance of the fitted linear predictor in distinguishing HC from MS, considered either as a whole group or divided in subgroups according to disability level and disease duration.

	Sensitivity (%)	Specificity (%)	AUC
MS	80.00	92.50	0.90
$\mathrm{MS}_{\mathrm{mild}}$	81.25	92.50	0.90
$\mathrm{MS}_{\mathrm{mod/sev}}$	76.90	92.50	0.89
$\mathrm{MS}_{\leq 10}$	81.50	92.50	0.87
$\mathrm{MS}_{>10}$	77.70	87.90	0.94

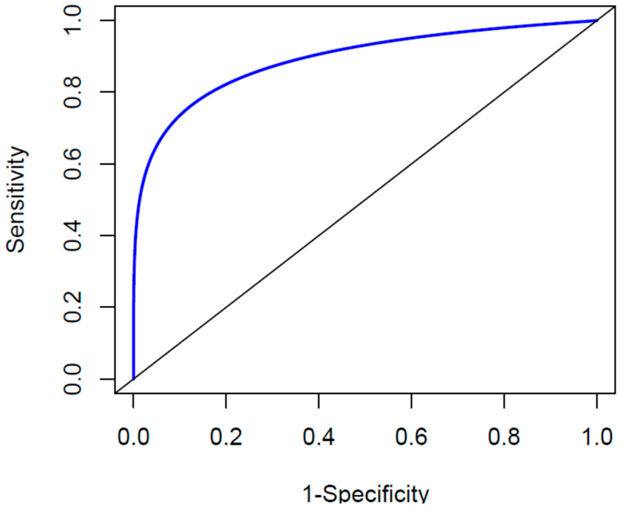

Figure 2.27: Predictive power of the obtained model in distinguishing between HC and MS, as described by a smoothed ROC curve.

With respect to sensitivity and specificity, this simple prediction tool offers a superior categorization for our cohort of data than the study based on random forest, PCA-LDA, and PLS-DA algorithms. In fact, the AUC value is 0.9, and the sensitivity increases from 78 to 80% while the specificity from 83 to 92.5%.

2.2.5 Conclusions

One effective biomolecular profiling technique that may be fully investigated for clinical diagnostic purposes is ATR-FTIR spectroscopy of biofluids easy to collect. The ultimate goal is to monitor and diagnose disorders, primarily of the neurodegenerative type, which are extremely debilitating and challenging to diagnose. The results presented in this study show that there are subtle but statistically significant spectral differences in the plasma of patients affected by multiple sclerosis compared to a control healthy group. Specifically, we observed that the MS group had an increased lipid/protein ratio, which suggests dysregulation of the protein-lipid metabolism. To distinguish between diseased and healthy subjects, three different multivariate techniques were used on the FP region and the HR region of the ATR-FTIR spectra. The findings reveal that the RF model gives best performance in the FP region, with a sensitivity of 78% and specificity of 83%, whereas for the HR region, the best performance is provided by the PLS-DA model. Subsequently, a linear predictor representing a single, easy diagnostic index (with a value range of 0 to 1) was created by combining a set of parameters obtained from univariate and multivariate statistical analysis of the experimental infrared spectra. In comparison to the results obtained by the PCA-LDA, PLS-DA, and RF classification algorithms, the predicted probability derived using this model offers a higher performance. Finally, the study we presented, consisting of human plasma analysis with ATR-FTIR spectroscopy, combined with suitable data analysis, is a very promising diagnostic tool for MS, demonstrating that even for neurological diseases it is possible to obtain very effective discrimination results.

2.3 Case study 3: Characterization of 3D-heart shape in a model of cardiac plasticity

The goldfish (*Carassius auratus*) is emerging as a natural model for evaluating fundamental aspects of the coordinated physiological mechanisms that maintain cardiac steady-state. Its relatively simple design and remarkable morpho-functional plasticity allow adequate responses to various intrinsic and extrinsic stimuli. Understanding the crucial interplay between heart form and function in response to organism requirements has always represented great interest for cardio-scientists to identify new non-invasive methodologies for 3D morphological analysis.

2.3.1 Introduction

The vertebrate heart can physiologically adapt its performance in response to periphery requirements. This is fundamental for the proper functioning and survival of the whole organism. In fish, the heart is characterized by extraordinary morpho-functional flexibility that allows facing a variety of internal and external stimuli, including those that generally are highly challenging and even detrimental for mammals. This trait is mainly expressed in several species by the physiological ability to undergo cardiac structural and functional remodeling in response to environmental challenges (e.g. variations of pH, salinity, temperature, O_2 levels, etc.), exercise and sexual maturation [133], ontogenetic growth [134], exposure to cardioactive substances [135, 136], and pollutants [137]. Remodeling is maximally expressed by the capacity shown by several species to fully regenerate the injured heart (e.g. zebrafish: [138]). The Cyprinid goldfish *C. auratus* is a highly tolerant fish, mainly known for its ability to survive prolonged periods of hypoxia/anoxia [139]. Under O_2 deprivation, the heart undergoes functional remodeling by maintaining its basal hemodynamic performance and response to pressure stimulations. As observed in isolated and perfused *in vitro* preparations, under hypoxia, the goldfish heart improves its performance [140], with stroke volume increasing in a time-dependent manner. This feature is proposed to properly support organ perfusion [140] and the physiological interactions between organs and tissues, thus contributing to animal tolerance [141, 142]. The goldfish heart is also sensitive to temperature changes, with a response that, so far, has been explored only on the electrical properties [143] and in terms of thermal tolerance [144]. Another attractive trait is the capacity to repair and regenerate ventricular tissue damaged by cauterization. This trait, shared with another Cyprinid, the zebrafish [138, 145], is the opposite of the high susceptibility of the mammalian heart, which cannot be repaired after damage [146]. According to the above features, the goldfish is considered an emerging natural model in many fields of cardiovascular research, from environmental-oriented investigations aimed to define the limits of tolerance of biological species challenged by dramatic environmental deterioration, up to cardiac protection, repair, and regeneration, about the urgent problem of the cardiac injury in mammals.

In this study, the goldfish heart, as a high morpho-functional cardiac plasticity model, will be analyzed by X-ray microtomography. By applying this technique to the goldfish heart exposed to challenging environmental stimuli (i.e. hypoxia), it will be possible to obtain information about 3D cardiac modifications (i.e., in shape, curvature, symmetry, angles between the different regions) together with *in situ* changes of chamber structural organization (i.e., atrial and ventricular myocardial arrangement, compact vs trabecular myocardial component, inner atrial and ventricular chamber volumes, bulbar structure), and to correlate these aspects to stress-induced functional changes.

2.3.2 Scientific rational

The scientific rationale of the study, which explores the cardiac plasticity of the goldfish heart, is based on the ability of the heart to respond to physiological stress conditions. This response is studied through a three-dimensional characterization of cardiac morphology using μ-CT.

The goldfish was chosen as a natural model because of its extraordinary ability to regenerate cardiac tissue and adapt to hypoxic conditions, making it particularly interesting for cardiovascular research.

The choice of μ-CT for 3D characterization of the heart is motivated by the need to obtain detailed, non-destructive images that allow visualization of changes in the shape of the heart chambers (atrium, ventricle, arterial bulb). The μ-CT technique is appropriate for this type of analysis because of its high resolution, which allows detection of even small changes in the structure of the heart, providing essential information for understanding the mechanisms of structural adaptation.

2.3.3 Materials and methods

X-ray μ-CT measurements were performed on normoxia and hypoxia goldfish hearts of different size groups. Samples were previously prepared by the Laboratory of Organ and Systems Physiology of the Department of DiBEST - UNICAL as follows:

- *Goldfish mantaining.* Goldfish ranging 6-16 cm in size are maintained in filtered and aerated water. For experimental setup, goldfish were allocated into two tanks (normoxia and hypoxia) and left to acclimate for at least 24 h. Subsequently, aquaria were covered with a Plexiglas lid and the water was continuously bubbled with nitrogen gas (hypoxia) or regular air (normoxia). Oxygen values were maintained at 2.0 ± 0.5 mg/L in the hypoxic experimental tank and at 8.4 ± 0.3 mg/L in the normoxic one. Oxygen saturation in the aquaria was continuously monitored using an oxygen analyzer. Animals were sacrificed after anesthesia, weighed, and then ventrally opened behind the pectoral fins. Hearts were perfused *in situ* and blocked in diastole or systole and processed for microtomography analysis.

- *Staining procedure.* After anesthetization by immersion in MS222, animals are ventrally opened and perfused *in situ* under a stereomicroscope. Perfusion can be performed by directly inserting an input cannula in the sinus venosus. The perfused heart receives Ringer's solution (in mmol L-1: NaCl 124.9, KCl 2.49, $MgSO_4$ 0.94, NaH_2 PO_4 1.0, Glucose 5.0, $NaHCO_3$ 15.0, and CaC_{l2} 1.2, pH 7.7) equilibrated with a mixture of 99.5% O2 and 0.5% CO_2 (normoxia) or 10% O_2, 0.5% CO_2 and 89.5% N_2 (hypoxia). For the staining procedure, hearts are blocked in diastole or systole with an excess of KCl or CaCl, respectively and then perfused with a 3,75% Lugol solution. Hearts are fixed for 24 hours in 4% PFA and subsequently stained in 7.5% Lugol's solution for 48 hours. After staining, hearts are dehydrated in graded ethanol.

The parameters used for microtomographic investigation were:

- exposure time: 5000 ms;

- current of X-ray tube: 60 kV;

- voltage of X-ray tube: 166 μA;
- power of X-ray tube: 10 W;
- sample-detector distance: 808 mm;
- sample-source distance: 117 mm;
- equivalent pixel size: 6.32 μm;
- magnification: 7.90.

3600 X-ray projection images at a 0.1° angular step were acquired. For each projection, 3 images were acquired and then averaged to improve the signal-to-noise ratio. The acquired projections are then normalized using flat and dark images and reconstructed using the Feldkamp-Davis-Kress algorithm. The software used for the 3D rendering and image analysis is Fiji (open-source software) and Avizo 3D 2021.2 (commercial program). Before analysis, segmentation is performed to distinguish the different structures of goldfish hearts. Next, the analysis is carried out to obtain information about 3D cardiac modifications and changes in chamber structural organization. Information about the samples analyzed is shown in Table 2.9.

Table 2.9: List and information on goldfish heart samples used in this work.

ID sample	Weight of goldfish (g)	Rearing	Blocked condition
A	4.0	Normoxia	Diastole
B	4.4	Normoxia	Diastole
F	4.4	Chronic hypoxia	Diastole
0	22.0	Normoxia	Diastole
2	23.0	Normoxia	Systole
3	23.0	Normoxia	Systole
Z	40.3	Normoxia	Diastole
GD	80.4	Normoxia	Diastole
GS	81.2	Normoxia	Systole

2.3.4 Results and discussion

The results presented in this section are still under study and represent a pilot study. So far, the first step is the identification of optimal parameters for making measurements: starting from staining procedures (in collaboration with the Laboratory of Organ and

Systems Physiology of the Department of DiBEST - UNICAL), to tomographic parameters and segmentation procedures.

In order to find the optimal tomography parameters, phantoms, i.e., an animal biological tissue of equal density (Z), were used. Different tests were carried out to optimize the instrumental condition such as by varying the object-detector distance, applied voltage and tube current, exposure time, and the number of acquisitions to be performed. The final parameters are given in the "Materials and Methods" section. Samples named (ID sample in 2.9) as A, B, F, 0, 2, 3, and Z were used for staining tests; this corresponds to the staining described in the "Materials and methods" section.

Figure 2.28 shows the 3D rendering of the goldfish heart together with the 2D sections in different planes in grayscale; in particular, the xy, yz, and xz cut planes are shown. The colors of the boxes (green, red, and blue corresponding to the Figures 2.28c, 2.28b, 2.28d) correspond to the planes evidenced in the 3D rendering (Figure 2.28a).

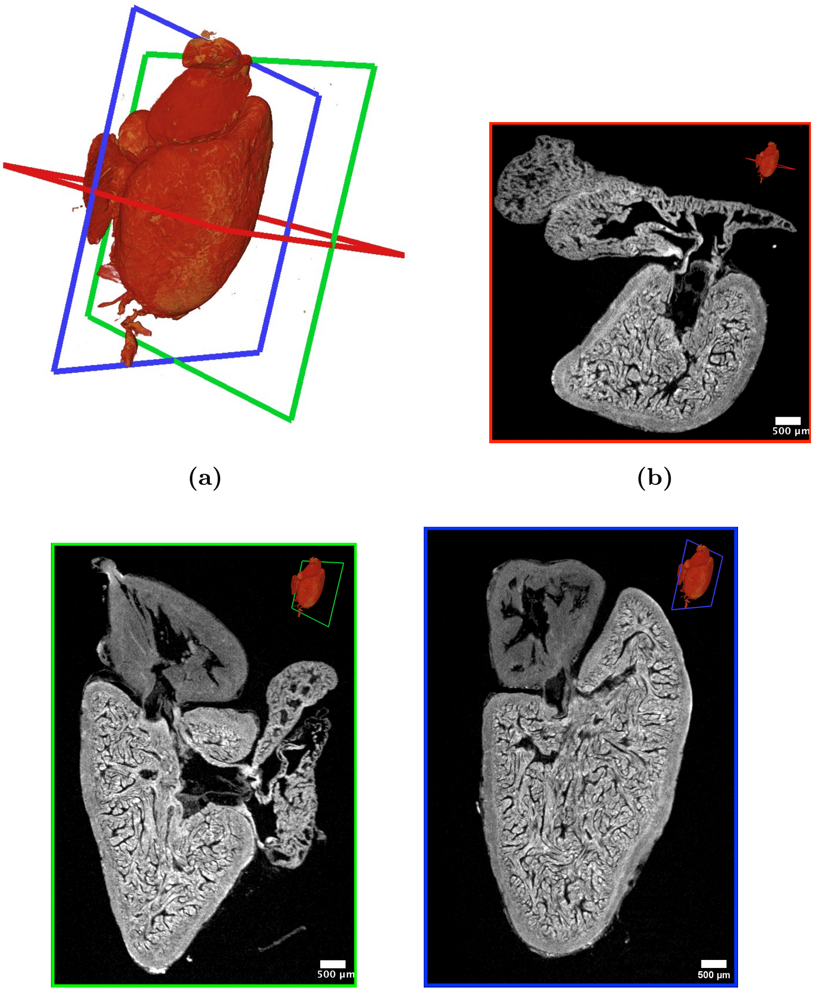

(a) (b)

(c) (d)

Figure 2.28: 3D rendering in false colors; and 2D xy (b), yz (c), xz (d) slices in grayscale taken from (a) following the color code of the frames.

At this point, a morphological study can be made. As shown in Figure 2.29, the goldfish heart appears to consist of four chambers: *sinus venosus (SV)*, *atrium (A)*, *ventricle (V)* and *bulbus arteriosus (BA)*. The heart of *C. auratus* also includes two distinct structures corresponding to the *atrium-ventricular (AV)* region and the *conus arteriosus (CA)* [137, 147].

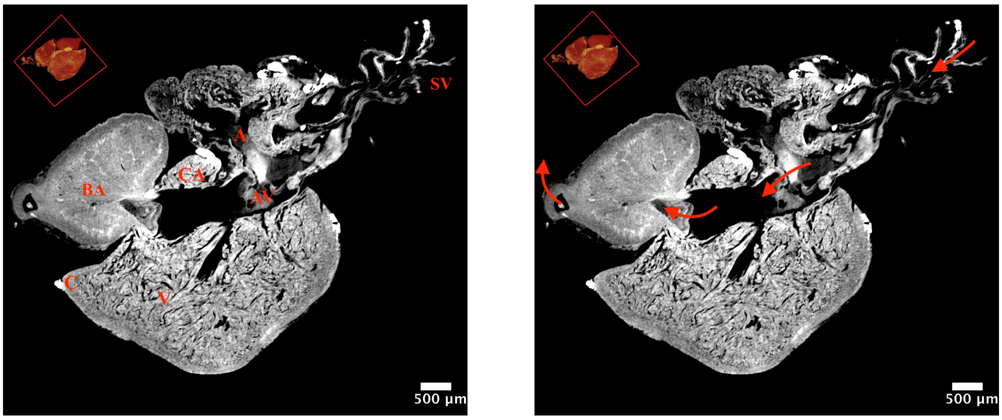

(a) (b)

Figure 2.29: Goldfish heart morphology: 2D slice of heart Z, xy plane. The internal structures of the heart are shown in (a), and the blood passage is shown by the red arrows in (b). SV = *sinus venosus*, A = *atrium*, V = *ventricle*, BA = *bulbus arteriosus*, AV = *atrium-ventricular*, and CA = *conus arteriosus*.

The *sinus venosus* (SV) pushes blood into the *atrial* cavity (A). The *atrium* (A) appears to be quite large, comparable in size to that of the *ventricle* (V). In fact, the volume ratio of atrium to ventricle is 0.99, and atrium to total heart (excluding empty cavities) is 0.44 (the results refer to the sample named GD). The *atrium-ventricular* (AV) region provides support to the *atrium-ventricular* valve. The ventricle of the goldfish heart exhibits a sack-shaped structure and is composed of an external compact (*compacta*) layer and an inner spongy layer (*spongiosa*). The *compacta* appears thicker at the base of the ventricle and thinner proceeding toward the apices. The spongy layer contains numerous trabecules, which divide the ventricle into small *lacunae*, with progressively smaller inter-trabecular voids (Figure 2.30). Figure 2.30a shows, with different colors, how the lacunae are progressively smaller. Specifically, the color scale indicates small lacunae in blue and larger lacunae in pink. The *conus arteriosus* is interposed between the *ventricle* and the *bulbus arteriosus* (AB) and provides support for the valve complex [148].

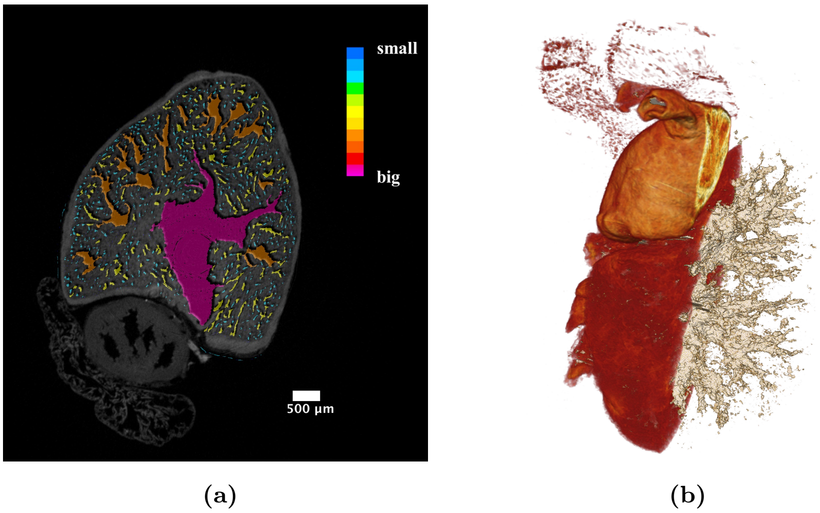

Figure 2.30: Ventricle lacunae: (a) 2D slice, where the color scale indicates the size of the lacunae (blue = small lacunae, Pink = large lacunae); (b) 3D visualization of the *lacunae* (dendritic shape).

The results are comparable with conventional histology. For further verification, a microtomographic measurement (Figure 2.31a) and histological examination (Figure 2.31b) were carried out at sample ID 0. As shown in Figure 2.31, the results are satisfactory. In particular, the *bulbus arteriosus*, the *ventricle*, with *compacta* and *spongiosa* zone, and the *atrium* can be visible.

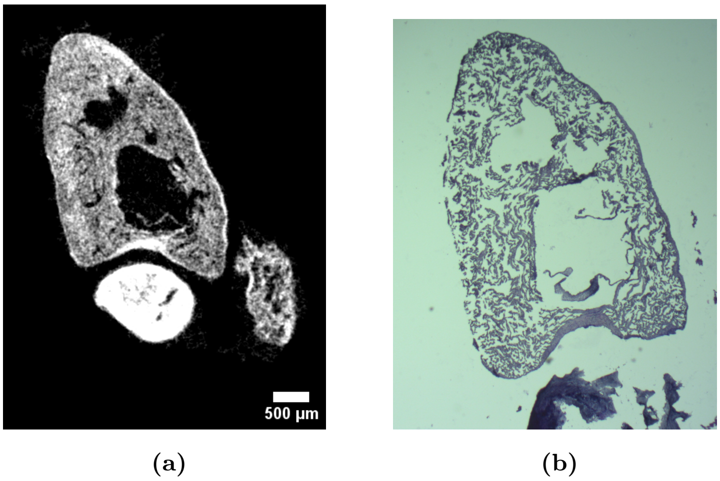

Figure 2.31: (a) μ-CT slice and (b) histological examination of the sample 0.

Interesting is the morphological differences between hearts blocked in diastole and those blocked in systole (Figures 2.32, 2.33). In particular, it can be seen that the heart blocked in systole (Figures 2.32b, 2.33b) is contracted compared to the heart blocked in diastole (Figures 2.32a, 2.33a). As a result, the lacunae are larger in the sample blocked in diastole. In fact, the percentage of *ventricle lacunae* to *ventricular* volume results to be 80.31% for the heart blocked in diastole and 13.90% for the heart blocked in systole.

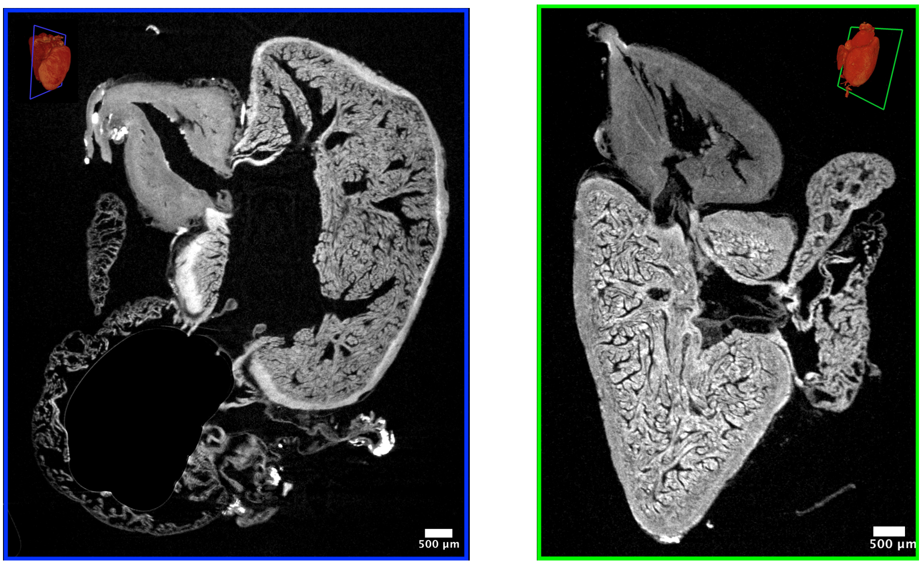

(a) **(b)**

Figure 2.32: Comparison of hearts blocked in (a) diastole and (b) systole.

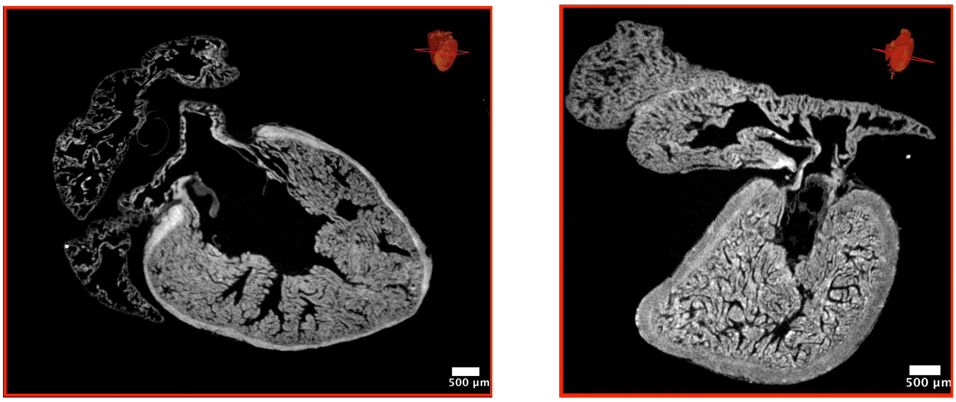

(a) **(b)**

Figure 2.33: Comparison of hearts blocked in (a) diastole and (b) systole.

Differences in the thickness of the *compacta* and percentage of *ventricular lacunae* volume to *ventricular* volume are observed in hearts of different sizes (different goldfish weights), but blocked in the same condition (diastole). The comparison was made between the ID Z heart and the GD sample (Figure 2.34).

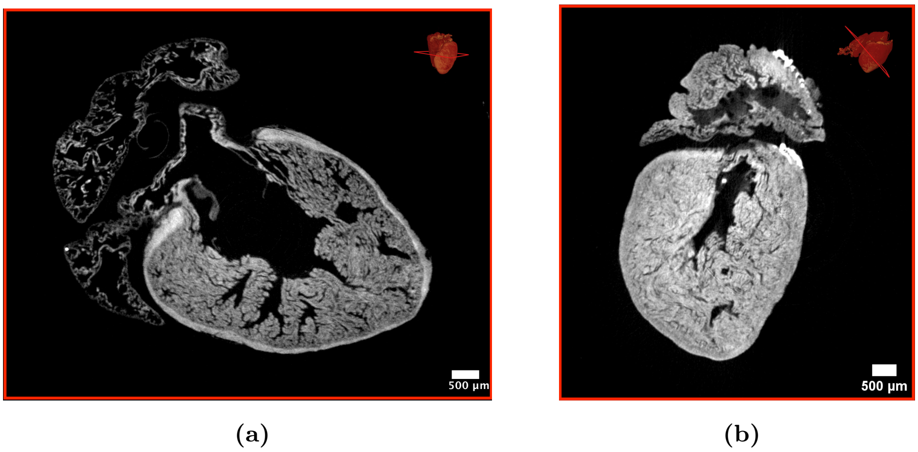

Figure 2.34: Comparison of hearts blocked in diastole of different sizes/weight: (a) GD and (b) Z hearts.

Specifically, we find that the thickness of the *compacta* varies from 59.71 ± 4.27 μm to 104.60 ± 7.05 μm, indicating that the *compacta* increases in size with the goldfish size. The same increase is found in the percentage of *ventricular lacunae* volume relative to *ventricle* volume changing from 43.55% (Z heart) to 80.31% (GD heart).

Table 2.10 summarizes the overall results. Data are reported as mean ± error; error on volume was calculated in accordance with Lin et al, while error on average *compacta* thickness was calculated as standard error [103].

Table 2.10: Blocking condition, Weight (g), $V_{\text{ventricular lacunae}}/V_{\text{ventricle}}$ (%), and Compacta thickness (μm) for different samples.

Blocking	Weight (g)	$\frac{V_{\text{ventricular lacunae}}}{V_{\text{ventricle}}}$ (%)	Compacta thickness (μm)
Diastole	4.2	12.89 ± 1.82	18.28 ± 0.82
Diastole	22.5	16.19 ± 1.36	37.54 ± 1.56
Diastole	40.3	17.27 ± 0.69	59.71 ± 4.27
Diastole	80.4	20.17 ± 0.47	104.60 ± 7.05
Systole	23.0	4.09 ± 1.40	38.95 ± 2.20
Systole	81.2	9.33 ± 0.69	114.07 ± 5.71

Figure 2.35 shows how as the size, and thus weight, of the goldfish heart changes,

there is an increase in the volume (in percentage) occupied by the *ventricular lacunae*, relative to the *ventricle*. The data show a linear dipendence; for hearts blocked in diastole, the equation of the line is given by y_{V_D}=0.09x+13.33 with an R^2 of 0.95; whereas, for hearts blocked in systole we have y_{V_S}=0.09x+2.02 with an R^2 of 1.00. Although the data of blocked hearts in systole are only two, we can get an idea of the trend of the percentage of the volume occupied by *ventricular lacunae* compared with the volume of the *ventricle*. As can be seen, the two fits have the same slope, but the percentage of *ventricular lacunae* volume to *ventricular* volume for samples blocked in systole is smaller than those blocked in diastole; this reduction is expected since hearts blocked in systole are in a contraction phase.

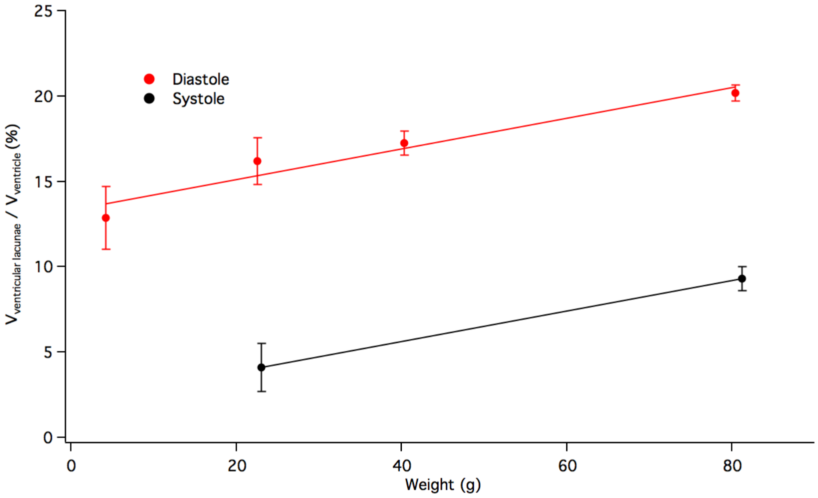

Figure 2.35: Percentage of the volume occupied by *ventricular lacunae* relative to *ventricle* volume as a function of the weight of goldfish. In red hearts blocked in diastole, and in black hearts blocked in systole.

Figure 2.36 shows the average thickness of the *compacta* as a function of the weight of the goldfish for different blocking conditions. Again, a linear trend of the experimental data is observed. A small change in the slope of the curve can be seen. In particular, the thickness of the *compacta* for samples blocked in diastole is slightly slower (y_{C_D}=1.14x+13.02, $R_D{}^2$=0.99 and y_{C_S}=1.29x+9.26, $R_S{}^2$=1.00). The results obtained with hearts blocked in systole, because there are few samples, can only help in the analysis but cannot provide additional information.

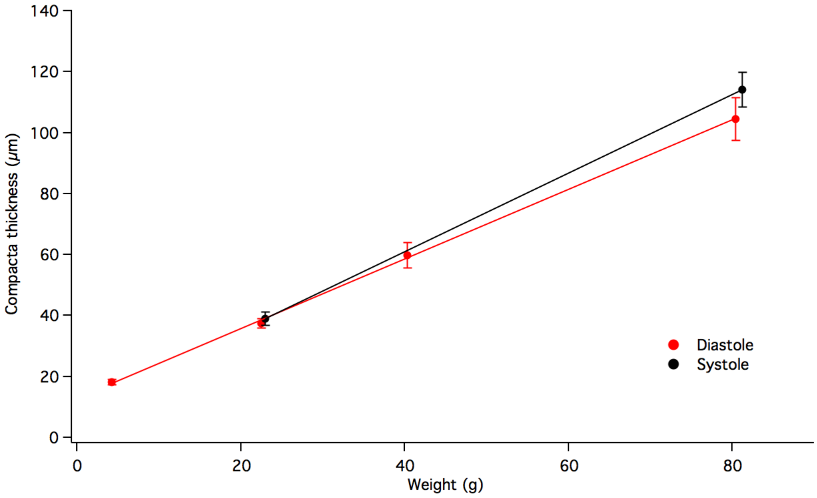

Figure 2.36: Average thickness of *compacta* as a function of weight of goldfish. In red hearts blocked in diastole, and in black hearts blocked in systole.

Table 2.11 and Figure 2.37 show a comparison of two samples of the same weight blocked in the same conditions (diastole) and differently exposed to normoxia and hypoxia. The results show that in the case of hypoxia there is an increase in the average thickness of the *compacta*, as reported by Filice et al [149]. Statistical tests (two tailed parametric t-test, 99% confidence interval) carried out on the thickness of the *compacta* show that among the different exposure conditions, there are statistically significant differences ($p<0.0001$, $****$).

Table 2.11: Blocking and exposure condition, Weight (g), $V_{\text{ventricular lacunae}}/V_{\text{ventricle}}$ (%), and *Compacta* thickness (μm) for different samples.

Blocking	Exposure	Weight (g)	$\frac{V_{\text{ventricular lacunae}}}{V_{\text{ventricle}}}$ (%)	*Compacta* thickness (μm)
Diastole	Normoxia	4.2	12.89 ± 1.82	18.28 ± 0.82
Diastole	Hypoxia	4.4	14.57 ± 1.70	33.71 ± 1.50

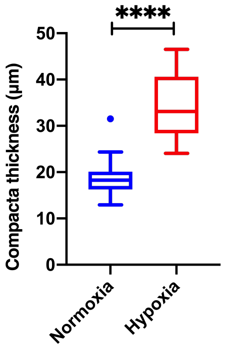

Figure 2.37: *Compacta* thickness (μm) for different exposure condition.

The results show that the goldfish heart changes its morphology linearly (*ventricular lacunae* volume and *compacta* thickness) as the weight of the sample changes. The findings of this preliminary study are encouraging. Although much focus has been placed on finding the tomographic parameters, early results show that μ-CT is a powerful technique for the study of morphological changes in the goldfish heart following hypoxia and for species of different sizes.

2.3.5 Conclusions

The use of noninvasive techniques, such as X-ray microtomography, for 3D morphological analysis is of significant support. Indeed, in this preliminary study, differences in the shape of the heart (such as the thickness of the *compacta* and volume occupied by *ventricular lacunae*) are shown, which may help the understanding of the interplay between the structure and the function of the heart in response to the organism's requirements. In addition, μ-CT is an excellent tool for three-dimensional virtual histology.

Chapter 3

Characterization of Manufacturing Defects in 3D-Printed Materials Using X-ray Micro-Computed Tomography (μ-CT)

The following studies focus on the characterization and impact of manufacturing defects in 3D-printed materials, particularly in relation to their mechanical properties and structural integrity (Figure 3.1).

Both studies employed X-ray micro-computed tomography (μ-CT) to detect and analyze defects within 3D-printed samples. In the first study, 3D-printed PA12 samples were examined for porosity and crack propagation after undergoing plastic deformation through repeated loading-unloading cycles. The findings revealed significant porosity in the samples, which was likely introduced during the manufacturing process. The porosity increased with plastic deformation and influenced the crack growth behavior, highlighting its potential impact on material performance.

The second study focused on a Ti-6Al-4V alloy produced using selective laser melting (SLM), a technique known for creating components with superior mechanical properties. However, like in the first study, defects such as inclusions and porosity were identified using X-ray μ-CT, and these defects were found to compromise the material's fatigue performance and mechanical strength, particularly under combined axial and torsional loads.

In summary, both studies underscore the importance of understanding and mitigating defects in 3D-printed materials, as these defects can significantly affect the structural integrity and mechanical properties of the final components. The use of X-ray μ-CT as a diagnostic tool proved essential in identifying and analyzing these defects, offering insights that could lead to improved manufacturing techniques and more reliable 3D-printed components.

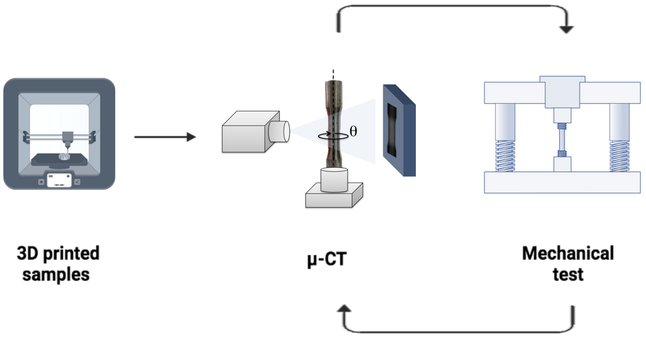

Figure 3.1: Graphical abstract.

3.1 Case study 4: Effects of porosity on specimens printed by selective laser sintering

3D printing is a widely used technology in different fields, including ergonomics, construction, medicine, and transportation. Its widespread use is attributed to its capacity to create intricate pieces of materials without requiring post-processing or component assembly. Nevertheless, the fabrication process might result in various defects such as inclusions or porosity. It is important to comprehend the role of defects and promote techniques that may support and limit their occurrence.

In this study, experimental tests on 3D-printed PA12 dogbone samples that have undergone plastic deformation have been used to characterize their porosity. Specifically, several loading-unloading procedures have been conducted. After each procedure, X-ray μ-CT has been utilized to detect defects in manufacturing and examine the process of crack propagation after a quasi-static loading test. Analysis of the sample shows a significant porosity that could have been caused during manufacture. The porosity percentage as well as the pore diameters increases as a consequence of the plastic deformation of the sample. Furthermore, porosity influences the process of crack growth.

3.1.1 Introduction

Over the past several years, many engineering areas, including automotive [150], aerospace [151, 152], or energy [153], as well as biomedical [154], construction [155], or ergonomic [156], have shown an increasing interest in additive manufacturing (AM) technique. This is because components characterized by complex shapes can be obtained quite easily, thus reducing time-to-market requirements [157, 158]. The AM method allows obtaining final parts layer by layer [159] from different raw materials, e.g., metals [160], polymers [161], or ceramics [162], as well as it could be employed for composite fabrication [163–165], through different fabrication strategies. One of the most widespread methods for creating 3D objects through the overlay of 2D profile layers is selective laser sintering (SLS). In SLS, a high-power laser is used to melt the powdered material selectively as it is spread out on a printing plate layer by layer. Parts produced with the SLS technique are subject to process variability [166–169] as well as powder quality [170, 171]. Specifically, 3D printed parts can be incurred in geometric errors [172], surface roughness [173, 174], and internal defects [175–177], including porosity or inclusion. The use of 3D-printed structural components is also dependent on the ability to understand the mechanism that causes the development of defects during the fabrication process and their role during mechanical stress [172, 178–180]. The μ-CT technique is one of the most interesting methods for porosity evaluations since it permits the reconstruction of defect forms and their distribution [181, 182]. Additionally, μ-CT makes it possible to detect whether 3D-printed objects include unmelted powder [176]. This study presents the morphological characterization of the dogbone samples realized by the SLS technique. Specifically, structural proprieties of 3D printed materials have been identified using μ-CT. Furthermore, quasi-static loading conditions have been applied to 3D-printed components to generate plastic strain and to study the effect of porosity during fracture development. The mechanical test has been performed at various plastic strain levels to do an ex-situ μ-CT study.

3.1.2 Scientific rational

In this work, we aim to understand the relationship between the structural defects of 3D printed samples generated during the SLS printing process and the mechanical properties of the material. For this purpose, mechanical tests were performed under progressive loading and analyzed with μ-CT. The aim of this measurement was to study the internal porosity of the samples and verify its impact on the strength and durability of the material under real stresses. The use of μ-CT at each unloading stage is crucial to monitor the development of internal defects during the application of load, due to its ability to provide detailed 3D images.

3.1.3 Materials and methods

Samples

3D printed samples (dogbone, Figure 3.2) have been fabricated using the EOS Forminga P110 3D printer (Eos, Germany), available at the Laboratory of Physical Prototyping (LPF @STAR lab) at the University of Calabria, with a commercial nylon powder (EOSITIN P/PA2200). The laser type used for sintering is CO2, 30 W. PA2200 is a fine powder of polyamide 12 (PA12) with a nominal average grain size equal to 56 μm. Samples have been fabricated with a mixing ratio of virgin and recycled powder. Sample dimensions have been chosen according to the standard protocol ASTM-D 638-14 [183]. In particular, the type IV [183] sample geometry has been selected for our purpose. Sample dimensions are reported in Figure 3.2.

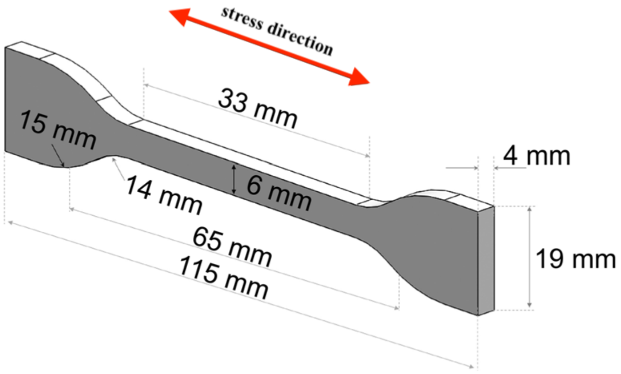

Figure 3.2: Model of dogbone samples employed for mechanical characterization. The arrow represents the stress direction.

Mechanical tests

Mechanical tests have been carried out using an electromechanical testing machine, i.e., MTS model 42 (MTS Systems Corporation, USA) equipped with a 5 kN loading cell. From mechanical tests on dogbone samples, stress-strain curves were obtained.

Tensile tests have been carried out at a 0.5 mm/min displacement rate. A schematic of mechanical tests carried out to follow the crack propagation mechanism is reported in Figure 3.3a. In particular, the sample has been subjected to $\Delta = 10$ mm elongation, and after that, the load has been removed, and a μ-CT analysis has been carried out (Figure 3.3b).

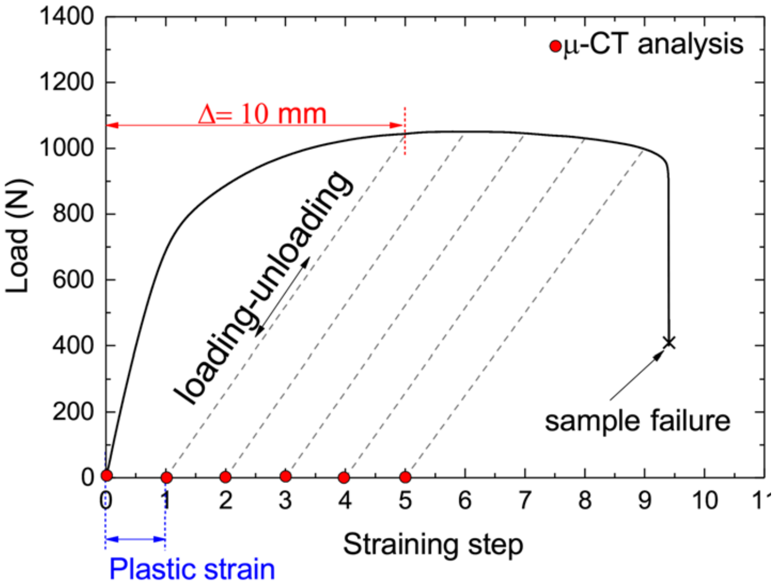

(a)

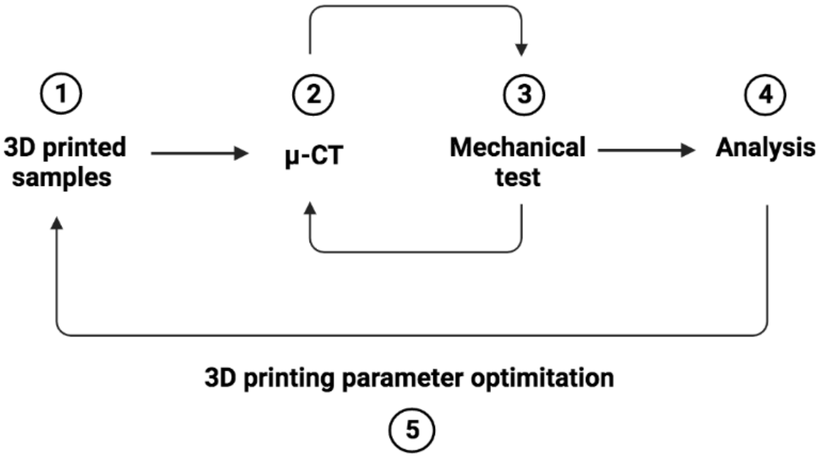

(b)

Figure 3.3: (a) Loading-unloading step plot. The solid line represents the theoretical curve corresponding to a unique stress induced continuously on the sample. (b) Working diagram.

After each unloading phase, residual plastic deformation was detected in the sample. The loading procedure has been repeated until sample failure. Tests have been carried out on two different samples. For simplicity, the reported results are referred to one sample since similar results have been obtained for both dogbones. Mechanical tests were carried out in collaboration with the Department of Mechanical, Energy and Management Engineering of the University of Calabria.

μ-CT analysis

The parameters used for μ-CT investigation were:

- exposure time: 500 ms;
- current of X-ray tube: 120 kV;
- voltage of X-ray tube: 84 μA;
- power of X-ray tube: 10 W;
- sample-detector distance: 200 mm;
- sample-source distance: 200 mm;
- equivalent pixel size: 25 μm;
- magnification: 2.

The μ-CT of the dogebone is based on the acquisition 1800 X-ray projection images performed at a 0.2° angular step were acquired (Figures 3.4a, 3.4b). The acquired projections are then normalized using flat and dark images and reconstructed using the Feldkamp-Davis-Kress algorithm (Figure 3.4c). The software used for the 3D rendering (Figure 3.4d) and image analysis is Fiji (open-source software) and Avizo 3D 2021.2 (commercial program).

Segmentation was performed to separate defects (pores) from the sample. The sample's tomographic reconstructions were aligned to identify the same area of interest for the different loading step conditions (undeformed, steps 1–5). The pore characteristics of the dogbone-shaped samples have been determined by gray-level segmentation. We have eliminated from the μ-CT analysis results the smallest pores, i.e., pores with a volume lower than 2^3 voxels.

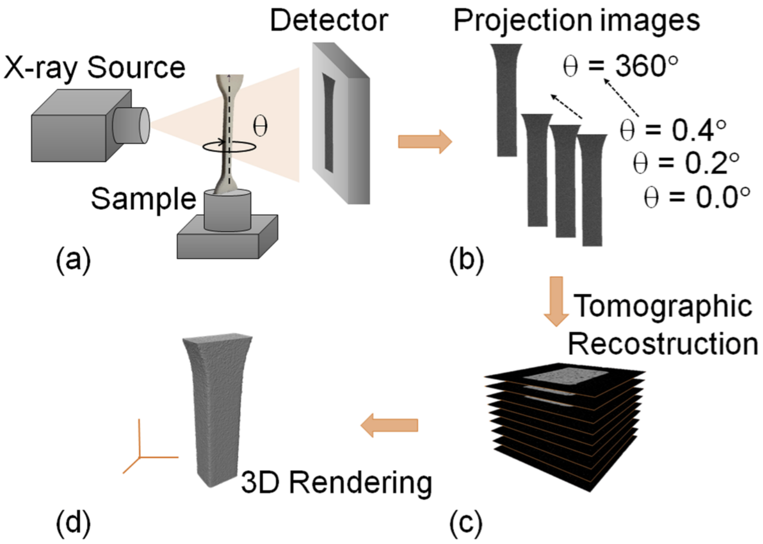

Figure 3.4: Rapresentation of the different steps followed during μ-CT analysis: (a) Illustration of the μ-CT set-up. (b) Set of X-ray projections at different rotation angles. (c) μ-CT virtual reconstructed slices of the sample. (d) 3D rendering of the sample.

3.1.4 Results and discussion

Mechanical test

Tensile tests have been carried out to produce plastic deformation on samples and to identify the mechanical properties of additive manufactured parts. The direction of the stress is indicated by the red arrow in Figure 3.2. Dogbone samples have been subjected to different loading-unloading steps until sample failure occurs. Stress-strain curves for all steps are reported in Figure 3.5 (typical stress-strain curve shown in the dashed-line curve).

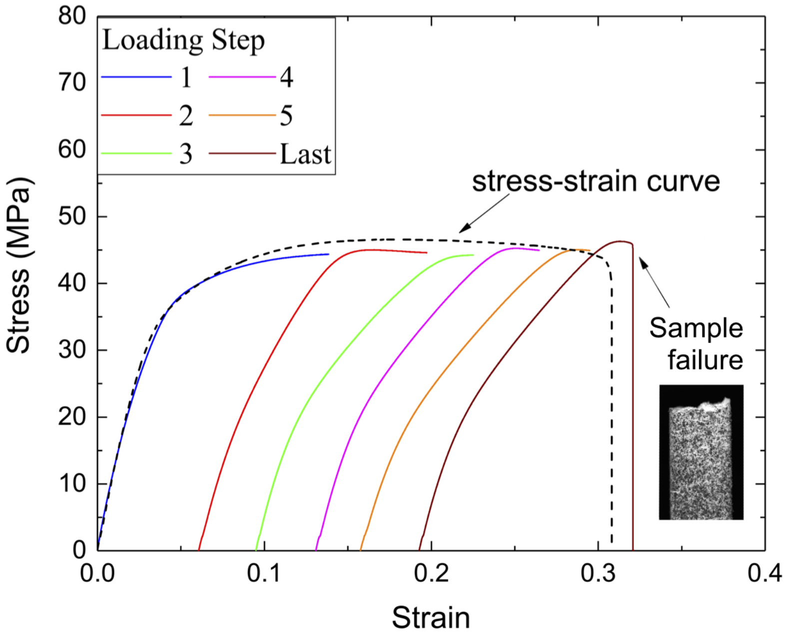

Figure 3.5: Stress-stain curves for different steps. The dashed line represents the theoretical curve corresponding to a unique stress induced continuously on the sample.

A progressive decrease in the plastic strain plateau may be seen after each step. From the second step, a slope shift can be seen in the elastic region. Furthermore, the slope change point occurs for lower stress values by increasing the step. This process has been explained in terms of the formation of high-dimension defects and material softening as a consequence of damage accumulation. Similarly, Nizina et al. observed a notable variance in the sample's stress-strain curve for the same material that was indicative of structural defects [184].

Porosity analysis

The sample was loaded and unloaded several times to evaluate the evolution of the internal defects as a function of plastic strain. Following each loading-unloading procedure, μ-CT was used to examine the sample. Porosity was characterized qualitatively and quantitatively by considering the following features of the pores: volume, diameter, and sphericity.

The porosity volume percentage measured at each loading-unloading step is reported in Figure 3.6. In particular, the total porosity volume percentage was calculated as global pores volume divided by sample volume. Furthermore, porosity percentages in the sample were determined separately for the skin and the core as distinct printing conditions were used for the two regions. Specifically, the core porosity was obtained as the volume of pores measured into the inner volume divided by the core volume. Similarly, skin porosity is calculated by dividing the volume of pores on the skin volume by the volume of the skin. For thee starting condition, or in strain step 0, we measured a total porosity percentage of about 2.8% (Figure 3.6a).

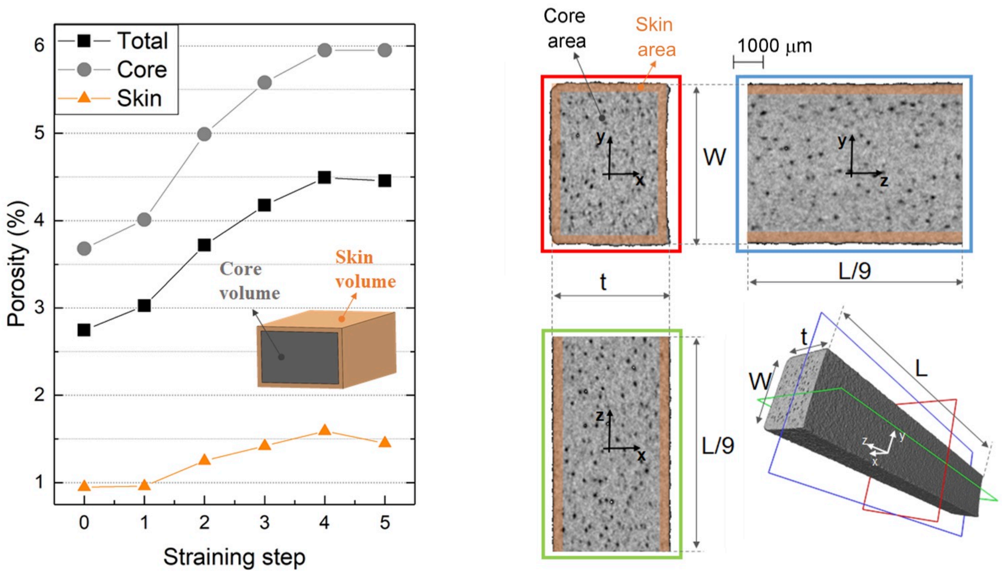

(a) **(b)**

Figure 3.6: (a) Porosity percentage as a function of loading step for the total sample, the core, and the skin (zero point is referred to undeformed starting condition); (b) porosity distribution along sample (the green, red, and blue rectangles represent the section location).

However, the skin was found to have a very low porosity value of about 1.0% (Figure 3.6a), indicating a reduction in the occurrence of holes on the sample external surface that may be ascribed to the varied printing settings. This value increased to 3.7% when the core volume was considered. In Figure 3.6b, we show xy, xz, and yz sections of the undeformed sample to emphasize the pore distribution in the core volume (in gray) and in the skin volume (in orange). The overall porosity volume percentage for the core found in the undeformed sample, as seen in Figure 3.7, is consistent with the findings of other authors on the same material for samples manufactured under similar experimental condition [185].

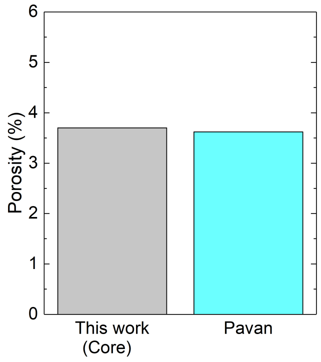

Figure 3.7: Porosity percentage values compared to the results obtained by Pavan et al. [185].

The porosity percentage (see Figure 3.6a) increases with the loading step (i.e., sample plastic deformation). At the last loading step, the total porosity percentage rises to 4.5%, corresponding to a 60% increase compared to the porosity level of the undeformed sample. Similarly, increments of porosity were observed for the core and the skin, i.e., 62% and 53% respectively. This result could be releted to two different mechanisms: *i)* an increase of the pores volume due to the external load and *ii)* micro-crack development that leads to pore coalescence. Moreover, by increasing the plastic deformation, the porosity percentage increases, and the pore size becomes detectable: in the undeformed sample, the size of some pores is lower than the μ-CT resolution. However, it is also possible to notice a small decrease in the porosity percentage value before sample failure (Figure 3.6a). This result has been explained by considering the occurrence of a large crack in the last loading step at the outer surface. It is well known that, during crack propagation, the stored energy is released. For this reason, some small pores could be reclosed during crack propagation; thus, they are no longer detachable by μ-CT analysis.

For a better investigation of this process, the porosity variation was evaluated in three separate sections of the sample (Figure 3.8): the crack section (A1), the portion far from the fracture (A3), and, lastly, the section between the previous ones (A2). For each of the loading steps that were examined, the porosity of section A1 increased. This increase could be related to both mechanisms mentioned before and the crack propagation. On the contrary, for both A2 and A3 sections, a decrease in porosity was noted at step 5, or just before sample failure. This result confirms that such decrease is related to the energy release that occurs during crack propagation.

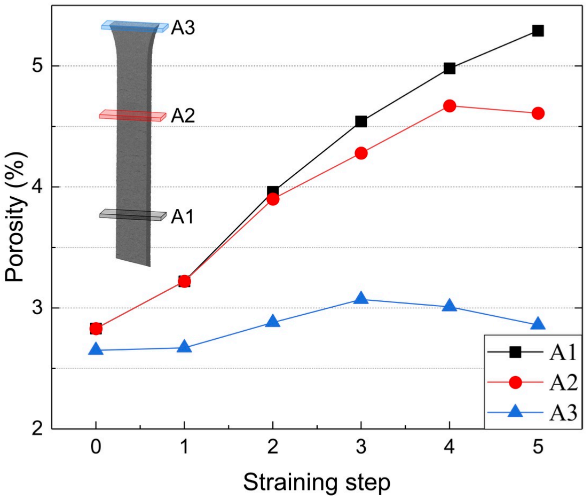

Figure 3.8: Porosity evolution in function of loading step for different sample sections: the crack section (A1), the portion far from the fracture (A3), and the section between the previous ones (A2). Zero point is referred to undeformed condition.

The growth of pores and coalescence, discussed above, is also confirmed by the results reported in Figure 3.9, where are compared two sections referring to a generic 3D cutting plane of the same sample in the undeformed condition and at the last step, before sample failure.

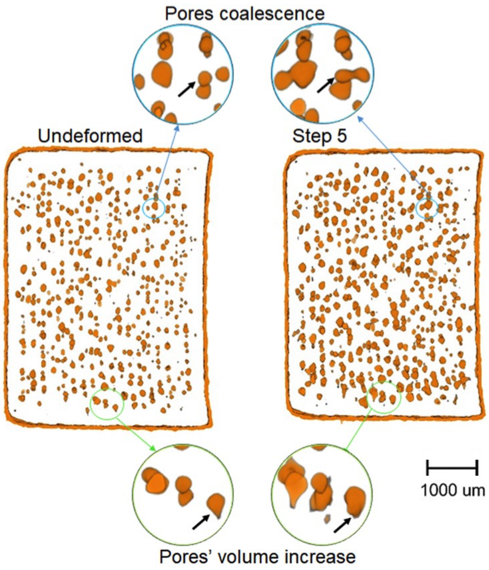

Figure 3.9: Mechanisms involved during sample plastic deformation: pore volume increases and pore coalescence.

As can be seen, there is an increase in the pore volume following the plastic deformation of the sample. In particular, the volume variations measured for the pore indicated by the black arrow provide an increase in volume of 92%. In addition, the coalescence mechanisms following the sample loading-unloading steps are also shown in the corresponding inset of Figure 3.9. This process contributes to the formation of internal cracks, characterized by an irregular shape, which could act as stress concentration points [186]. Again, the volume increased by 53% with respect to the undeformed state.

Pore geometrical characteristics

The influence of external loading on porosity was assessed by means of geometrical factors characterizing the porosity, such as volume, diameters, and sphericity. Specifically, the following equations were used to estimate the sphericity (S) and diameter (d) of the pores:

$$S = \frac{\pi^{1/3}(6V)^{2/3}}{A} \tag{3.1}$$

$$d = \sqrt[3]{\frac{6V}{\pi}} \tag{3.2}$$

where V and A are the pores volume and pores surface respectively. The analysis allows the identification of the mechanism related to sample failure connected with defect formation in manufacturing. Results obtained on volume were reported in Figures 3.10, 3.11a, 3.12; while in Table 3.1, it was reported the weighted average values of each parameter for all steps (the parameters have been weighted to the number of pores observed in each step).

The data results refer to the entire sample; that is, the skin and core were analyzed jointly. In fact, no appreciable geometrical distinctions were found between pores that are found at the skin surface and those found at the core, even if the two regions have different pore concentrations.

Parameters have been reported as a function of the percentage of pores, calculated as the number of pores of each step divided by the total number of pores.

Table 3.1: Weighted average values of pores volume, diameter, and sphericity obtained after different loading steps.

Step	Volume (x10^6 μm^3)	Diameter (μm)	Sphericity
Undeformed	1.34	126.05	0.62
Step 1	1.45	129.73	0.61
Step 2	1.72	138.23	0.60
Step 3	1.89	142.36	0.59
Step 4	2.16	146.71	0.57
Step 5	2.16	147.10	0.59

The data in Figure 3.10 show that going from the undeformed to step 5, the number of pores with small volumes reduces and, consequently, the number of pores with large volumes increases. It is noteworthy to emphasize that during steps 4 and 5, some pores with a very high volume were observed (higher than 8×10^6 μm^3 (V_4)). The presence of these big pores is connected with the crack propagation and coalescence processes in addition to the volume increase induced by plastic deformation. Moreover, as reported in Table 3.1, the weighted average of the volume increases by 61%, from $1.34{\times}10^6$ μm^3 in the undeformed condition to $2.16{\times}10^6$ μm^3 in the last step.

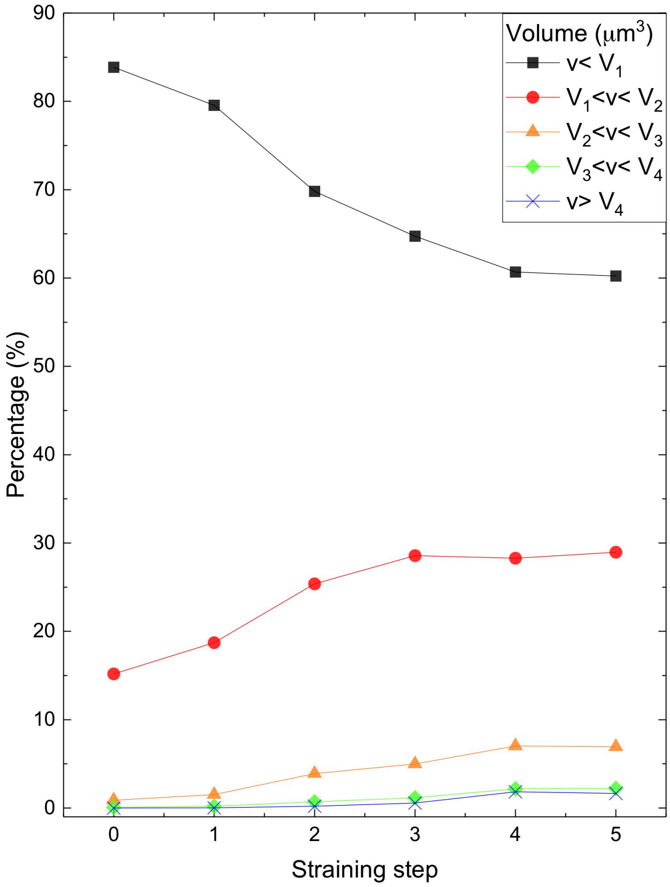

Figure 3.10: Dependence of the pores volume on the loading steps. Volume range correspond to the following values: $V_1 = 2 \times 10^6$ μm^3, $V_2 = 4 \times 10^6$ μm^3, $V_3 = 6 \times 10^6$ μm^3, $V_4 = 8 \times 10^6$ μm^3.

Information on the diameter distribution are given in Figure 3.11a. The weighted average of the pore sizes in the undeformed step was 126 μm. Overall, it was found that increasing the plastic deformation of the sample increased the number of pores with larger sizes. Moreover, the average pore diameter value at the last step was found to be equal to 147 μm, with an increase of 17% when compared to the initial value. The global behavior was found to be close to that obtained by other authors on the same material using similar values of energy density employed during 3D printing. Our data on porosity are compared with Pavan et al. results in Figure 3.11b. The global distribution of the diameter curve we found is similar and, as obtained by Pavan et al., the percentage of pores that are characterized by the modal value is around 0.8% [185].

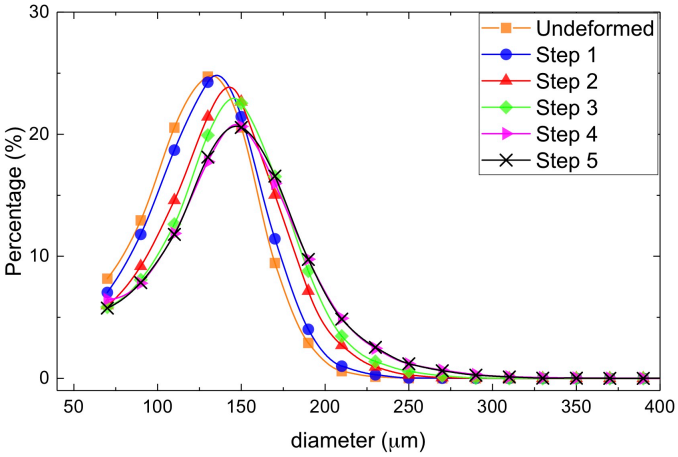

(a)

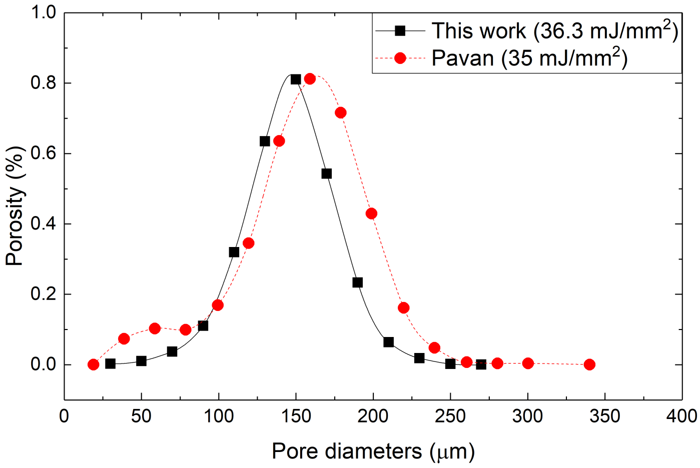

(b)

Figure 3.11: (a) Percentage of pores with different diameters as a function of loading step and (b) equivalent diameter behavior in comparison with results obtained by Pavan et al. [185].

Finally, Figure 3.12 shows the sphericity of the pores for the different loading steps. Compared to the undeformed material up to loading step 3 the aspect ratio of the pores aspect ratio is modified, resulting in lower sphericity values. Then moving from step 4 to step 5, it is possible to notice an inversion of the trend, i.e., the sphericity weighted average value increases, as reported in Table 3.1. This behavior could be attributed to energy release due to crack propagation. In fact, pore deformation has an elastic component that is released during crack propagation thus permitting pores to regain a more spherical shape. Overall, by moving from the undeformed conditions to the last loading step, pore geometry is modified, resulting in higher diameters and more irregular shapes, i.e., the sphericity weighted average value decreases by 5%, from 0.62 to 0.59.

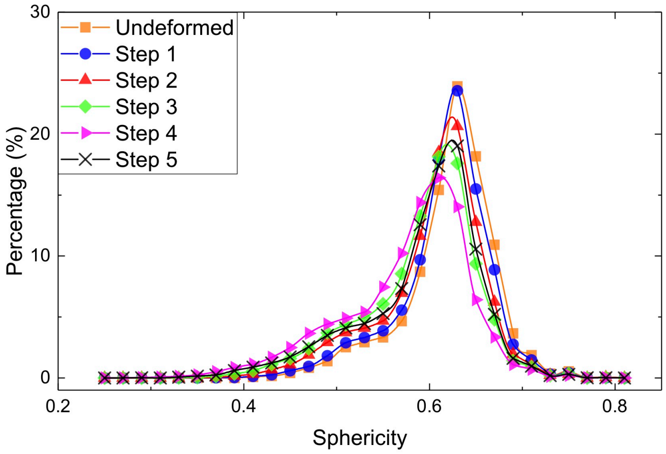

Figure 3.12: Percentage of pores with different sphericity as a function of loading step. The value 1 corresponds to a perfect sphere.

Figures 3.13 and 3.14 show the sphericity and surface of the pores as a function of their volume for undeformed conditions (Figures 3.13a, 3.14a) and for the last step (Figures 3.13b, 3.14b). It is possible to note a significant increase in pores surface after sample plastic deformation as well as a decrease in the sphericity parameter. This behavior is combined with an increase in the pores volume.

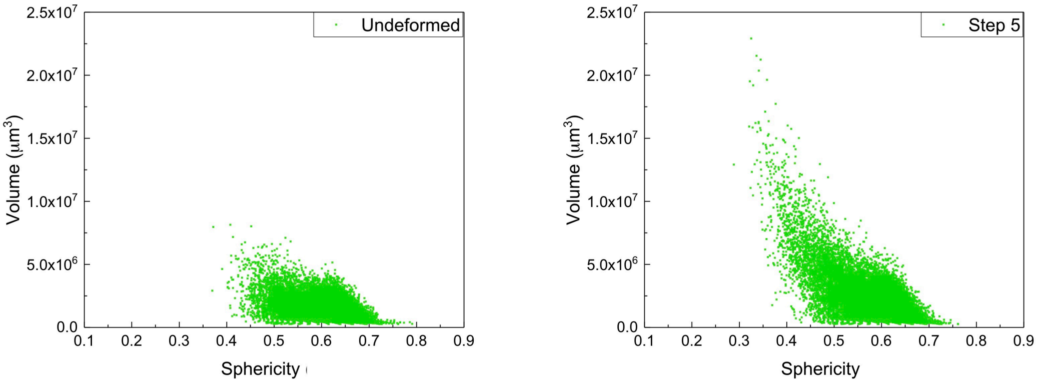

(a) **(b)**

Figure 3.13: Pore volume as a function of sphericity measured for (a) undeformed sample and (b) at step 5.

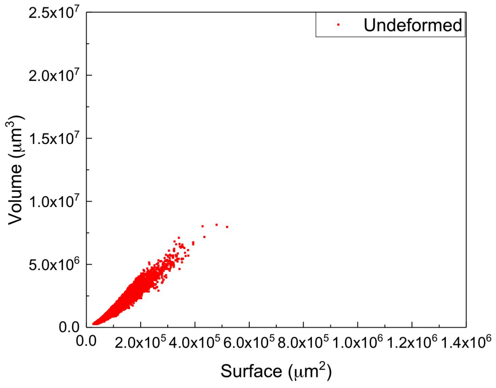

(a) **(b)**

Figure 3.14: Pore volume as a function of pore surface measured for (a) undeformed sample and (b) at step 5.

Crack propagation mechanism

Figure 3.15 shows the evolution of the pores, in different areas of the sample. Using μ-CT analysis, the mechanism of crack propagation can be mapped on the whole sample.

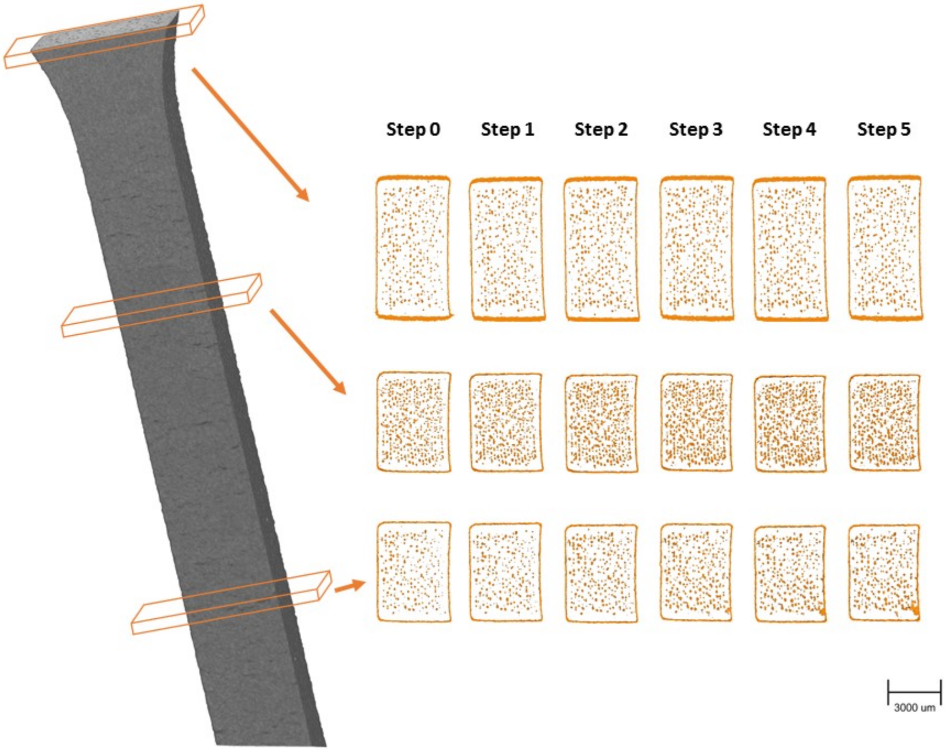

Figure 3.15: Crack propagation mechanism.

The crack evolution on 3D views for different loading steps is given in Figure 3.16. The 3D cutting plane reported refers to sections of the same sample at different loading steps where the main crack occurs, i.e., the crack that leads to sample failure. Cracks develop typically starting from the sample surface. The occurrence of porosity near to outer surface contributes to crack propagation through the coalescence mechanism. Different macroscopic cracks have been observed and, almost all of them originated from surface roughness. Moreover, the presence of inner defects, originating from large pores, modifies the sample failure mechanism. A fragile failure mechanism was observed, i.e., sudden sample collapse without any necking. Moreover, fracture surfaces are characterized by dimple morphology, with a large presence of pores.

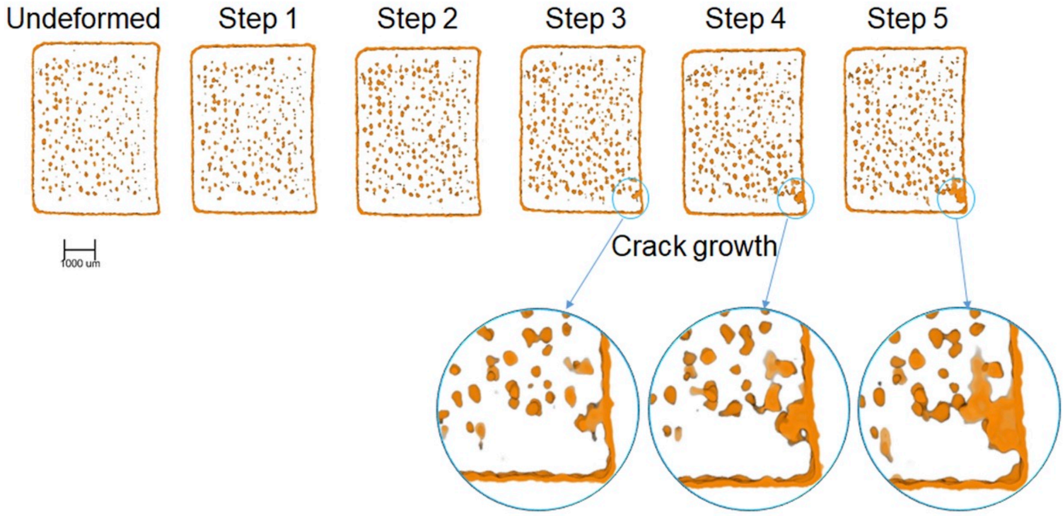

Figure 3.16: Crack propagation mechanism. The reported images are referred to sections where the main crack occurs.

Sample profiles were extracted and average values at each step have been compared. It is observed a reduction in sample width and thickness by increasing the loading step (Figure 3.17).

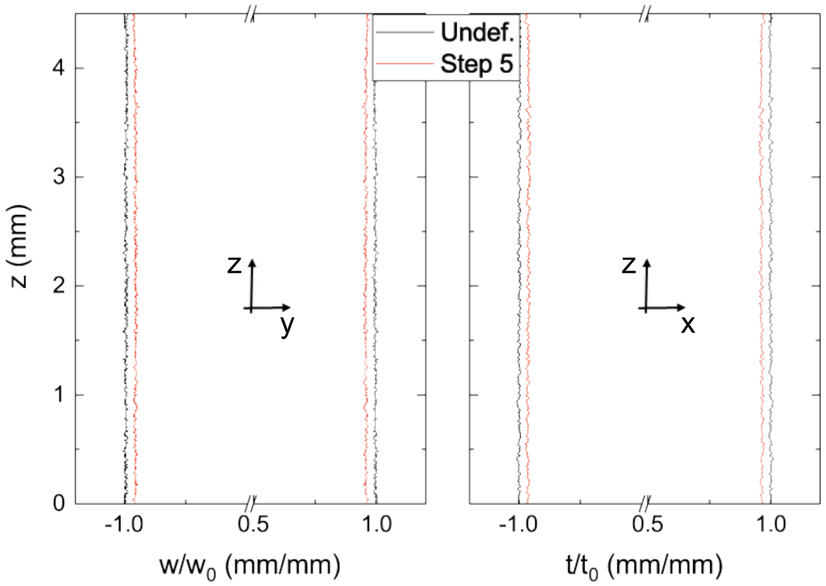

Figure 3.17: Normalized sample profiles in undeformed condition and at step 5 (dimensions are not in scale).

3.1.5 Conclusions

The morphology of an additive manufactured sample has been characterized through μ-CT analysis to evaluate the presence of production defects, i.e., porosity, as well as their influence on the failure mechanism. Data analysis reveals the presence of a high percentage of porosity in 3D printed components, due to the fabrication process. Plastic deformation leads to an increase in the porosity percentage measured whereas, right before sample failure, a slight decrease was observed due to the energy release mechanism. Plastic strain modifies pore volume and their aspect ratio resulting in more elongated defects and, in some cases, leads to the coalescence of two or more close pores into a single bigger one. This mechanism could be dangerous for structural parts since it leads to the development of macro-defects that reduce significantly sample resistance. Moreover, high roughness acts as a crack initiation point. Overall, sample failure is dominated by a fragile behavior, due to the high porosity percentage.

3.2 Case study 5: Evaluation of crack growth in additive manufactured Ti-6Al-4V alloy samples under stress condition

One of the most promising additive manufacturing techniques for producing components with excellent mechanical features is selective laser melting (SLM). However, fatigue performance and mechanical qualities may be compromised by defects formed during production. Using X-ray μ-CT, it is possible to examine the fracture behavior in an SLM Ti-6Al-4V alloy sample under in-phase axial and torsional loads. The defects of the material were detected and analyzed.

3.2.1 Introduction

The titanium alloy is a material chosen for many engineering applications for its high strength-to-weight ratio, good corrosion resistance, and elevated service temperature [187]. Additive manufacturing procedures are frequently utilized to create components with complicated shapes using this material as a powder. Many factors, including surface roughness, porosity, flaws, residual stress, and microstructure features, which can differ greatly across samples, influence the fatigue strength of SLM components [188, 189]. Typically, components made with the SLM technique show inclusions, pores, and a lack of fusion (LOF). LOF defects are the primary cause of fatigue crack initiation, depending on the shape and location of these defects [190, 191]. In most cases, the defects where the fracture originates are located near or at the surface of the material and are characterized by a larger effective area [192]. The μ-CT is a suitable approach to precisely evaluate microstructural characteristics such as grain size distribution, LOF, inclusion, porosity, volume percentage of phases, and fatigue fracture location [193]. In this work specifically, X-ray microtomography is used to examine the crack behavior within an SLM Ti-6Al-4V alloy sample that was strained with in-phase axial and torsional loads. Defects were found in the material volume of the SLM sample. In particular, a sub-volume containing more significant defects was examined, and the critical defect was identified and investigated.

3.2.2 Scientific rational

The scientific motivation for this study is based on the need to understand how defects affect the fatigue resistance of components produced with SLM. Although the SLM is an excellent technique in additive manufacturing, capable of creating components with complex geometries and excellent mechanical properties, defects can form during the process that can affect the strength and durability of the component.
To evaluate this problem, μ-CT is used to detect and analyze defects within the material in detail. The high-resolution images obtained for the internal structure of the samples, provides detailed information on the size, location, and shape of the defects. This information can be used to accurately assess how these defects contribute to crack propagation under mechanical loading.

3.2.3 Materials and methods

X-ray microcomputed tomography was carried out on a thin-walled tubular sample with a wall thickness of 0.85 mm, designed according to the ASTM standard E2207 (see Figure 3.18) [194].

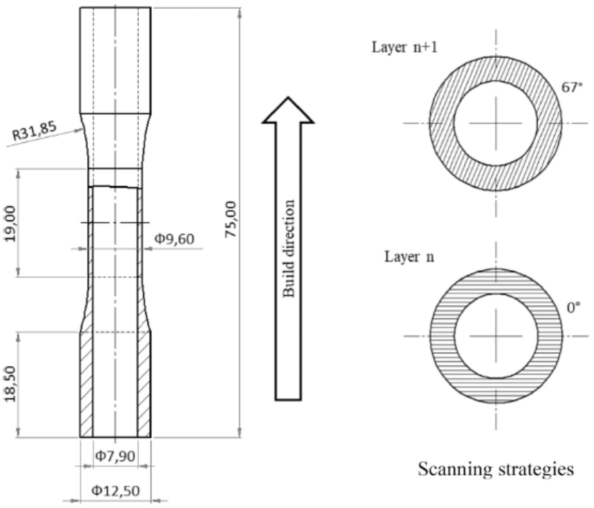

Figure 3.18: Thin-walled tubular specimen geometry with nominal dimensions in millimeters and laser scanning strategies.

A multiaxial fatigue test was carried out by a biaxial testing machine Instron ElectroPulse E10000 equipped with a tensile and torsional load cell of 10kN and 100 Nm, respectively. The test was carried out in load control, using proportional axial and torsional loading. The test consists of N = 77954 cycles periodically stopped at pre-established cycles to carry out the scan by X-ray μ-CT. It cannot be ruled out that the stops to run μ-CT analysis have influenced the total life reached.

Mechanical tests were performed by the Department of Mechanical, Energy, and Management Engineering at the University of Calabria.

X-ray microtomography measurements were made under two different magnification conditions (M=2 and M=9). Magnification 2 acquisitions were made to identify the regions where the cracks were formed. After that, the major cracks were identified, and tomographic images were acquired in the regions of interest with magnification 9 to increase the resolution and study the propagation of failure as a function of the number of stress cycles (Figure 3.19). Table 3.2 summarizes the parameters used for the different measurements.

Table 3.2: Parameters used for μ-CT measurements.

Parameters	Value used	
Current of X-ray tube (kV)	120	
Voltage of X-ray tube (μA)	83	
Power of X-ray tube (W)	10	
Magnification	2	9
Exposure time (s)	0.5	2.5
Sample-detector distance (mm)	200	800
Sample-source distance (mm)	200	100
Equivalent pixel size (μm)	25	5.55

The total number of acquired projections is 1800. We collected the projection with angular steps of 0.2° and, to improve the statistics for each angular position, three images were acquired. Each projection has been normalized by using flat and dark images. The sample virtual reconstruction is obtained using the Feldkamp-Davis-Kress algorithm [31]. The 3D visualization and analysis were carried out using Fiji ImageJ and Avizo 3D 2021.2 commercial software.

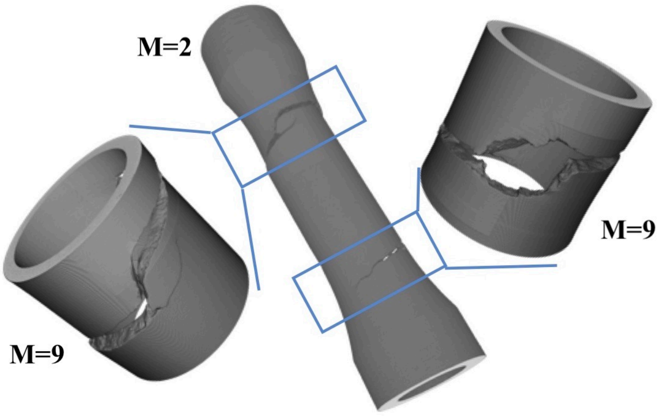

Figure 3.19: 3D renderings of the sample at magnification 2 and of the volumes of interest at magnification 9. The blue boxes indicate the enlarged regions where the measurements with higher resolution were made.

3.2.4 Results and discussion

Detection of defects

An initial analysis was performed on the sample not subjected to any mechanical stress (Figure 3.20a), in order to assess the morphology, size, and location of the initial defects. Subsequently, the analysis was repeated after each mechanical stress. The detected preexisting defects described in terms of pores and LOF (Figures 3.20b, 3.20c, 3.20d) are typical of the SLM manufacturing process, and they are randomly and unevenly distributed (Figure 3.20b). As shown in Figures 3.20c, 3.20d, the defects are mainly arranged on one side of the sample and near the outer surface of the tubular sample.

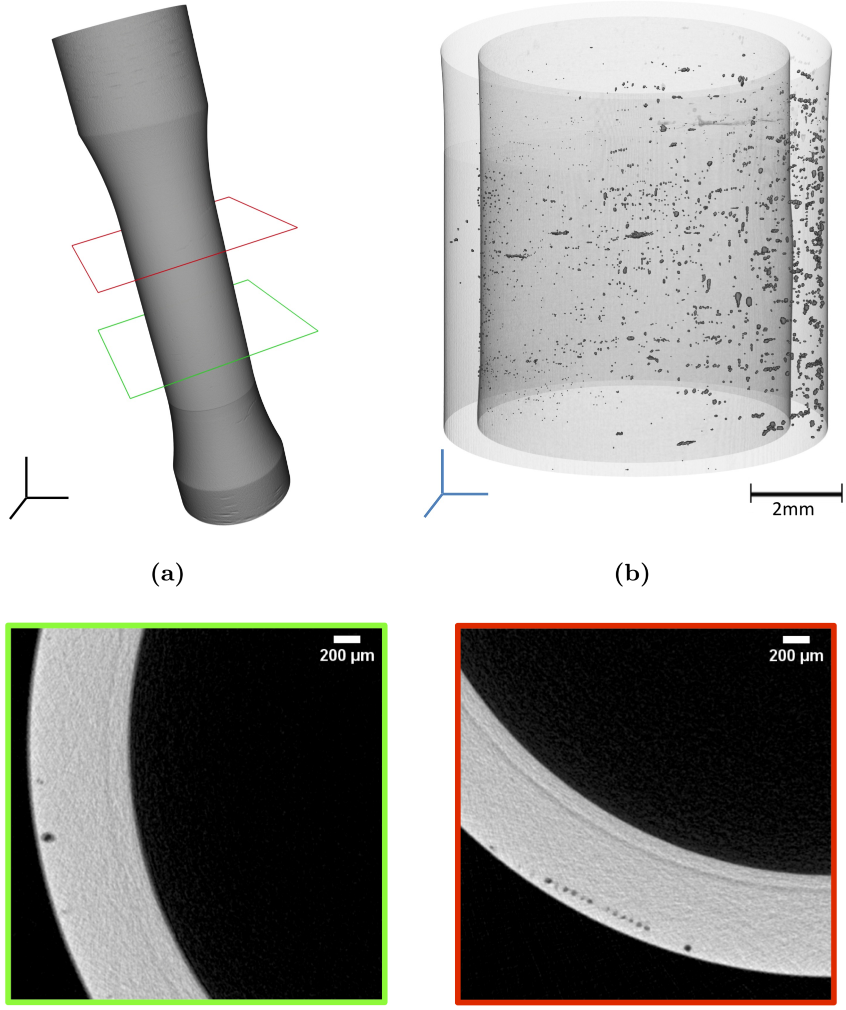

(a) (b) (c) (d)

Figure 3.20: μ-CT images: (a) 3D virtual reconstructed sample not subjected to mechanical stress; (b) a segmented view of the reconstructed volume that shows the porosity and LOF defects distribution. In the red and green boxes are shown two different planes displaying (c) LOF defects and pores and (d) aligned internal defects.

The analysis of defects shows that they have different shapes (Figure 3.21a). In particular, volume (Figure 3.21b) and sphericity (Figure 3.21c) were analyzed both separately and simultaneously (Figure 3.21d). As can be seen, most of the defects have a very small volume (around 0.2x10^6 μm^3), whereas there are few large volume defects (from 0.8x10^6 μm^3 to 1.6x10^6 μm^3). In addition, most of the volumes have a nearly spherical shape (sphericity, defined in section 3.1.4, eq. 3.1, takes values from 0 to 1, where 1 represents a perfect sphere). By correlating volume and sphericity (Figure

3.21d), it can be seen that larger volume defects have a less spherical shape that can be attributed to LOF defects; these can become potential crack initiators. Instead, smaller volume defects have a near-spherical shape, this is probably because they are gas pores.

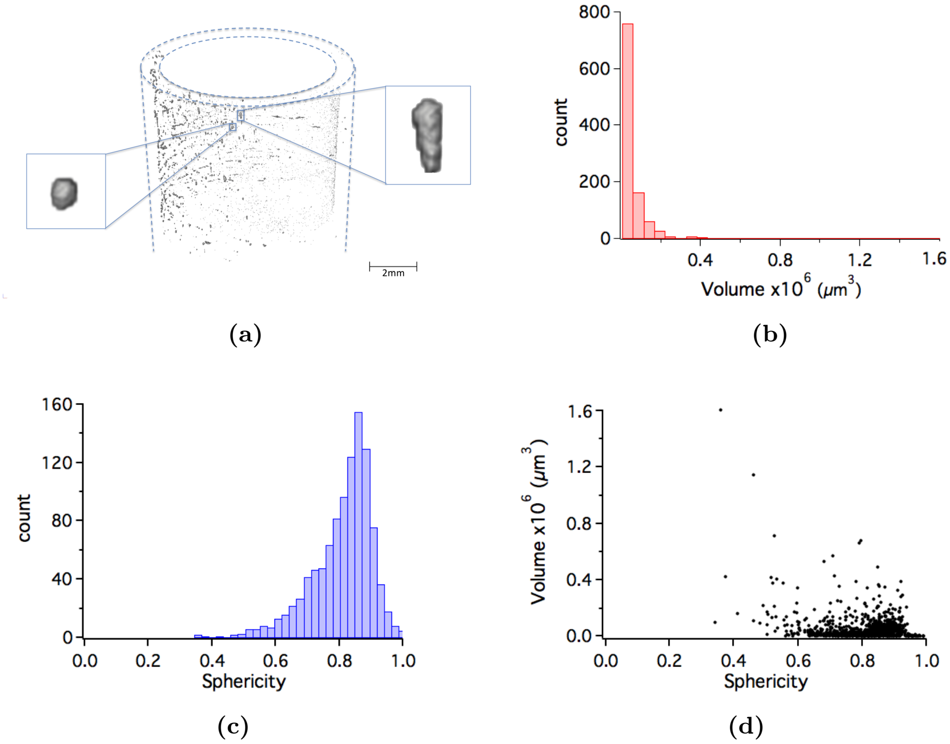

(a) **(b)**

(c) **(d)**

Figure 3.21: Defect shape analysis: (a) zoom in on two types of defects (spherical or elongated); (b) histograms of volume and (c) sphericity of the defects; (d) defects volume as a function of sphericity.

Figure 3.22 shows, for a selected subvolume of interest, the variation in the shape and volume of some defects in the sample. The defects were isolated from the rest of the sample (inner and outer surfaces of the sample are shown in the figure). As it can be seen, going from N=10000 cycles to N=50000 cycles, the size of the defects increases (except for the defect indicated by ID 1, see Table 3.3). Moreover, the formation of two additional defects (ID 6 and 7) is observed; probably in the acquisition of the first cycles the size of these defects was smaller than the resolution of the μ-CT.

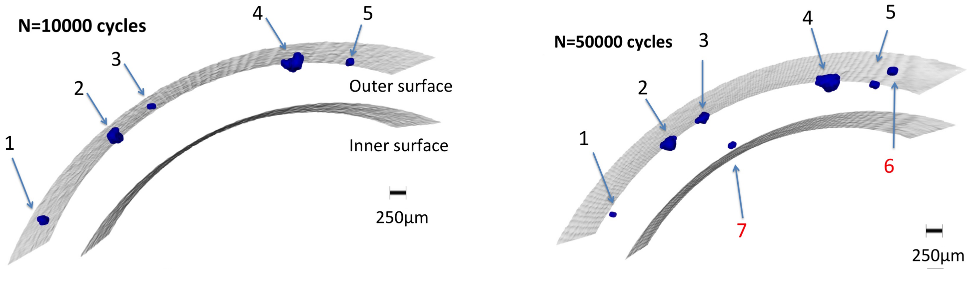

(a) (b)

Figure 3.22: Defect dependence on the stress cycles. μ-CT images of a subvolume of material with surface defects observed after a different number of cycles: (a) N=10000 cycles and (b) N=50000 cycles.

Table 3.3: Volume of detected defects in the material's sub-volume at two different numbers of cycles.

Defect ID	N = 10000 cycles Volume (x10^6 μm^3)	N = 50000 cycles Volume (x10^6 μm^3)
1	0.03	0.03
2	2.20	5.50
3	0.05	0.55
4	4.70	5.40
5	0.14	0.22
6	-	0.22
7	-	0.03

Behavior of the critical defect

As a further step, we studied the trend of defect propagation for different cycles of mechanical stress to evaluate the crack evolution. Usually, crack initiation occurs near or on the surface (outer and/or inner); it can start from the surface notch, near-surface pores, or LOF defects, and their volume increases during cyclic loading. Figure 3.23 shows the crack propagation for different loading steps, for measurements made at magnification 2. Specifically, Figure 3.23a shows a three-dimensional reconstruction of the sample, while Figure 3.23b shows a virtual cut of the 3D reconstruction, to emphasize the internal crack propagation. The red and blue boxes show the regions where the cracks formed that then resulted in the fracture of the sample. As can be seen from Figure 3.23, the crack forms from cycle 68475.

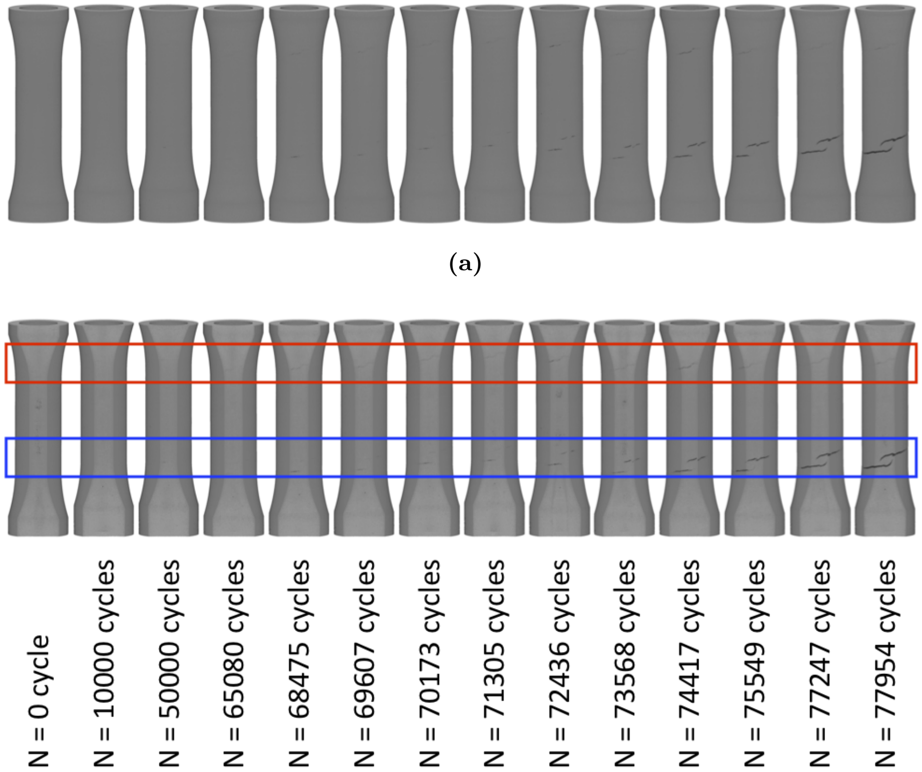

(a)

(b)

Figure 3.23: Crack propagation for different loading steps, for measurements made at magnification 2: (a) three-dimensional reconstruction of the sample, and (b) a virtual cut of the 3D reconstruction. The red and blue boxes show the regions where the cracks formed that then resulted in the fracture of the sample.

Once the initial phase of the crack was identified, magnification 9 measurements were made. Figure 3.24 shows the damage propagation up to the step before the sample fracture. Specifically, Figure 3.24a shows the 3D reconstruction of the volume of interest, while Figure 3.24b shows the crack propagation in transparency.

Figure 3.24 refers to the crack shown with a blue box in Figure 3.23b. A similar trend was observed for the crack in the red box.

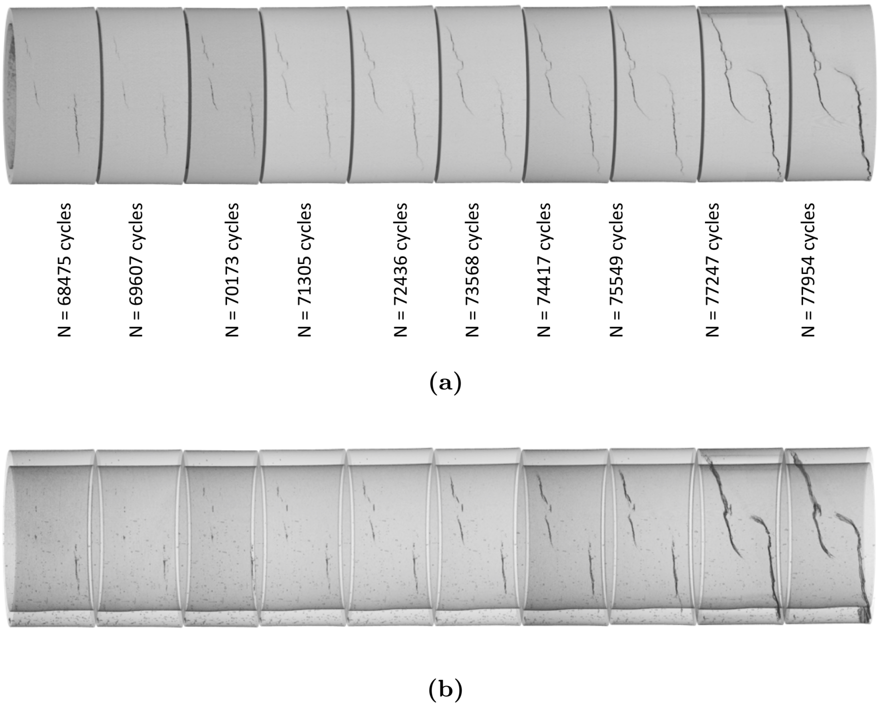

Figure 3.24: Fatigue crack growth behavior for different loading steps, for measurements made at magnification 9: (a) three-dimensional reconstruction of the sample, and (b) visualization in transparency of the 3D reconstruction.

The μ-CT images indicate that the final fracture of the sample under in-phase axial and torsional loading is due to the interaction of two macro crack-front propagation (Figures 3.23, 3.24). The damage during the cyclic loading is due to the interaction between adjacent small defects. At this point, the area of the projected crack in the print plane of the specimen was determined. The area was determined using Murakami's method [192, 195, 196]. The crack growth curve was evaluated by measuring the effective area of the critical crack detected for a different number of cycles. Figure 3.25 shows the evolution of the effective crack area as a function of the number of cycles. The growth rate initially increases slowly and after N = 75549 cycles it increases rapidly.

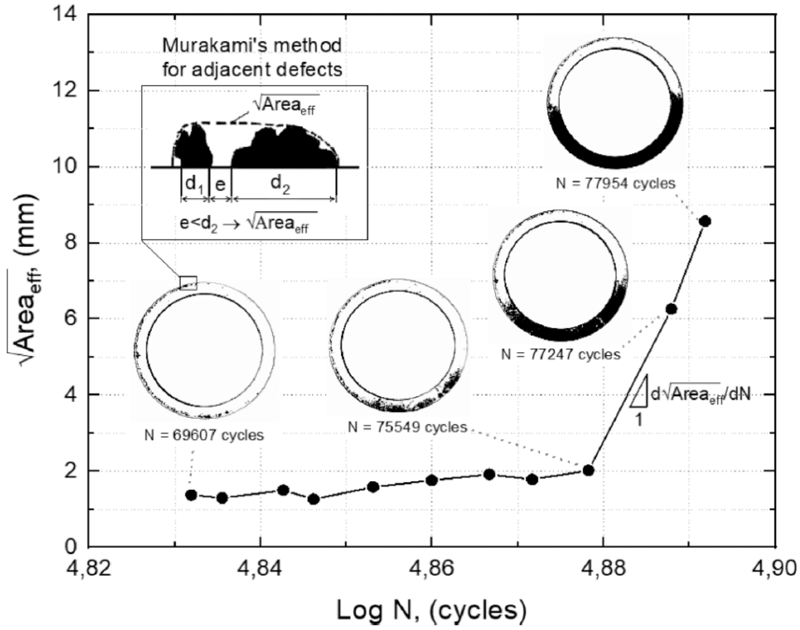

Figure 3.25: Fatigue crack growth behavior and Murakami's method (black color is the crack and white is the undamaged solid material).

3.2.5 Conclusions

In this study, in-phase axial and torsional loading was used to stress an SLM Ti6Al4V alloy sample that incorporates manufacturing defects. μ-CT scan performed after each stress step allows to investigate the behavior of crack development throughout the sample's lifetime. The findings demonstrate that the combination of adjacent small defects, to form a bigger single defect, causes the damage under cyclic loading. Moreover, the crack growth rate curve trend was obtained by measuring the effective area for different cycles. The results show that X-ray microtomography is an excellent physical method for studying defect propagation in materials.

Chapter 4

Application of X-ray μ-CT for Advanced Characterization of Photonics-Related Optical Fibers

4.1 Case study 6: Characterization of the index profile of optical fibers

In this study, we propose X-ray μ-CT as a new technique for characterizing optical fibers (Figure 4.1). Compared with more conventional characterization methods, such as optical techniques or energy-dispersive X-ray spectroscopy, μ-CT offers several advantages. For example, being based on X-ray absorption, μ-CT does not require a vacuum environment to operate and is virtually unaffected by fiber coating or bending [197–200].

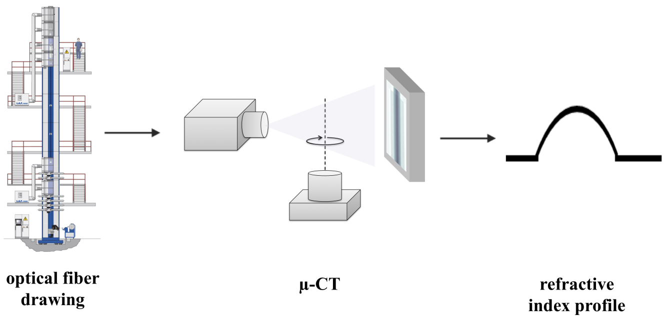

Figure 4.1: Graphical abstract.

4.1.1 Introduction

Fiber optics is used in a variety of technologies, from telecommunications to lasers or endoscopy. In the medical field, optical fibers are widely used for diagnostic and therapeutic purposes. For example, optical fibers can be used in endoscopes to perform detailed examinations of internal organs without the need for heavily invasive procedures.

Standard optical fibers consist of a core and a cladding. These have a different refractive index: usually light is confined in the core because the latter has a higher refractive index than the cladding. This structure allows the signal to propagate along the fiber through continuous internal reflections. In the realm of standard optical fibers, particularly compelling are the so-called graded-index fibers, which have a gradually changing refractive index within their core. On the other hand, the widespread use of optical fiber technologies has led to the development of new types of fibers, generally referred to as specialty optical fibers, made of non-silica materials such as soft glass. Generally speaking, during the fiber drawing process, the material is likely contaminated so that the fiber may lose its optical quality. In this sense, it is crucial to develop techniques capable of characterizing the optical fiber at the micrometric scale.

The characterization of optical fibers mainly consists of the measurement of their refractive index profile. For such a purpose, several techniques have been developed, either non-optical, like chemical etching combined with atomic force microscopy [201], or all-optical, e.g., based on the refraction [202], the reflection [203, 204] and the interference of laser beams [205]. Most of the fiber characterization techniques involve so-called longitudinal methods, i.e., a probe interacts with the fiber facet. Despite their efficiency, these techniques present several drawbacks, e.g., the need for a high-quality cleaved facet. Polishing the latter makes these methods inherently destructive, hence of difficult application to fiber-based devices. Moreover, longitudinal techniques provide information about the refractive index only in the vicinity of the fiber tip. Hence, longitudinal techniques do not allow for a mapping of the refractive index distribution throughout the entire fiber volume. On the other hand, in transverse techniques, the probe goes through the fiber, perpendicularly to its axis. The most notable example is optical tomography. The latter, however, suffers from some limitations, e.g., the presence of plastic coating or jacket hinders light propagation. In this framework, absorption contrast μ-CT provides remarkable advantages, e.g., μ-CT can be carried out independently of the fiber bending and even in the presence of a coating. Therefore, it is possible to perform μ-CT without removing the fiber plastic jacket.

In this PhD work, we systematically applied μ-CT for the analysis of several types of optical fibers, which were made by different manufacturers. Specifically, we proposed a method that exploits μ-CT in order to determine the local values of different optical parameters, such as the core/cladding relative index difference. The validity of our method was confirmed by means of comparisons with other complementary techniques, such as energy-dispersed X-ray (EDX) spectroscopy.

4.1.2 Scientific rational

The scientific motivation behind this study is based on the innovation that μ-CT provides in the characterization of optical fibers. Traditionally, these fibers are analyzed using optical methods or EDX, but these have significant limitations. In fact, these methods require working under vacuum conditions or are negatively affected by the presence of protective coatings on the fiber. In contrast, μ-CT offers numerous advantages, including the ability to perform measurements without removing the plastic coating on the fibers and extract 3D information.

4.1.3 Materials and methods

Different optical fibers were characterized, from commercial to specialty fibers. Details of the samples analyzed are given in Table 4.1.

Table 4.1: List of optical fiber samples used in this work. The diameters refer to the core and cladding, respectively. All of the values are taken from the datasheet provided by the manufacturer. In the case of sample L, the three values correspond to the inner and outer diameters of the smallest core, and the inner diameter of the widest cladding, respectively.

ID Sample	Type	Manufacturer	Diameters (μm)	Description
A	SIF	Thorlabs	50/125	Pure silica core
B	GIF	Alcatel	50/125	Ge-doped silica core
C	GIF	Thorlabs	50/125	Ge-doped silica core
F	SIF	Thorlabs	100/190	ZBLAN ZrF_4
G	SIF	Verre Fluoré	90/150	ZBLAN ZFG
H	GIF	University of Warsaw	/	Boron-silicate
I	GIF	University of Warsaw	/	Lead-bismuth-gallate PBG
L	PCF	GLOphotonics	44/143/187	/
M	/	PMMA	/	/

The parameters used for μ-CT measurements are shown in Table 4.2.

Table 4.2: Parameters used for μ-CT measurements.

Parameters	Value used
Current of X-ray tube (kV)	60
Voltage of X-ray tube (μA)	166
Power of X-ray tube (W)	10
Magnification	11
Exposure time (s)	7.0
Sample-detector distance (mm)	100
Sample-source distance (mm)	1000
Equivalent pixel size (μm)	4.54

3600 X-ray projections at a 0.1° angular step were acquired. In each step, the radiographic image was averaged over 3 acquisitions to improve the signal-to-noise ratio. The acquired projections were then normalized and reconstructed. The software used for the 3D rendering and image analysis were Fiji and Avizo 3D 2021.2.

Relationship between absorption coefficient and refractive index

To define the refractive index of optical fibers, considering both absorption and refractive properties, we introduce the refractive index complex variable:

$$\tilde{n} = n + i\kappa \tag{4.1}$$

When studying the refractive index of fibers by optical methods, the imaginary part κ is often neglected, since the absorption of silica glass, which is related to κ, is rather low at optical frequencies [206]. Therefore, the refractive index is identified only with its real part n. When using X-ray μ-CT, on the other hand, the role of κ is crucial since it relies on the absorption properties at X-ray frequencies. The μ-CT allows a 3D mapping of the absorption coefficient (μ), which is related to κ by:

$$\kappa \propto \mu \tag{4.2}$$

Eq. 4.2 holds only for monochromatic waves. However, at the X-ray frequencies used in this work, the chromatic dispersion of $\tilde{n}$ is negligible. Therefore, we can assume direct proportionality between κ and μ, despite the polychromaticity of our source. According to this assumption, μ-CT measurements of μ can be identified with κ measurements, within a multiplicative constant.

It is worth to underline that in this work we are relating the values of κ and n which belong to distant spectral ranges: X-rays and visible, respectively.

4.1.4 Results and discussion

μ-CT of different silica fibers

In this section, we report the analysis of the index profile of glass optical fibers. In particular, spans of multimode optical fiber (MMF) (step-index fiber (SIF) and graded-index fiber (GIF)) and photonic crystal fiber (PCF) were studied (ID sample A, B and L respectively).

A 3D rendering of the SIF, GIF, and PCF is shown in Figure 4.2. From a visual comparison of the three samples shown in Figure 4.2, one can immediately appreciate that μ-CT is able to capture their structural features. Indeed, for standard MMFs (SIF and GIF, Figures 4.2a and 4.2c respectively) one can distinguish core and cladding, that is, the inner and outer parts of the optical fiber. While the double cladding structure of the PCF honeycomb is clearly appreciable (Figure 4.2e). In fact, both outer and inner cladding can be recognized, as well as the radial structure supporting the latter. As it can be seen from Figure 4.2e, the inner Kagome structure of sample L is not clearly distinguishable. This is because the latter is rather thin: its typical size is of about a few microns, which is below the resolution achieved by our μ-CT set-up.

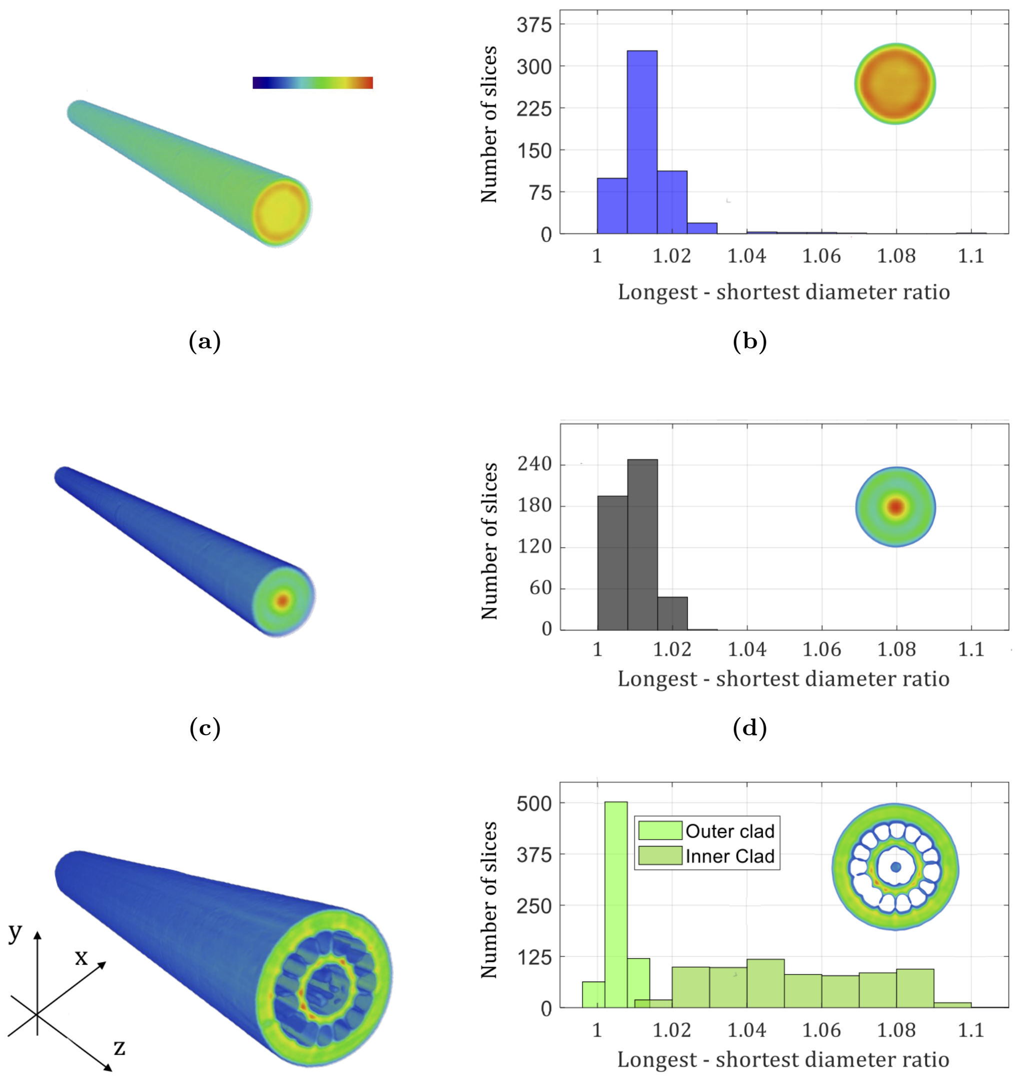

(a) (b)

(c) (d)

(e) (f)

Figure 4.2: (a,c,e) Tomographic 3D reconstruction of samples A, B, and L. (b,d,f) Statistical occurrence of the ratio between the longest and the shortest diameter. The inset shows a single 2D slice of the 3D reconstruction in (a,c,e).

In order to verify the uniformity of the optical fibers considered, their circularity, defined as the ratio of long to short diameter, was calculated. The SIF and GIF samples turned out to be rather circular, while the PCF shows a slight asymmetry in its diameter. Figures 4.2b, 4.2d and 4.2f show the statistical distribution of circularity (in the xy plane, along the z axis of the sample). Because the PCF had a double-cladding structure, statistics were carried out for both the inner and outer cladding. The diameter ratio distribution associated with a SIF or GIF peaks at 1.01. This is consistent with the nominal value of fiber non-circularity of 1%, as provided by the fiber manufacturer. Similar values are obtained for the outer PCF cladding. While there is a rather different distribution of the diameter ratio for the inner PCF cladding (see Figure 4.2f).

A section in the xy plane of standard MMF fibers and the respective attenuation profile is shown in Figure 4.3. In addition to the geometry of the sample (Figures 4.3a, 4.3c), μ-CT can also acquire information about the refractive index difference between core and cladding. The profiles of μ, normalized to their peak values μ_{max}, are reported in Figures 4.3b and 4.3d for samples A, and B, respectively. By comparing Figures 4.3b and 4.3d, one can visually appreciate the difference between SIF and GIF. The inner part (core) of the SIFs is rather homogeneous, while, moving from the fiber axis toward the edges, the same curve increases slightly, before dropping to zero at the cladding/air interface. This slight increase can be attributed to the presence of F (fluorine) doping within the cladding. In fact, fluorine increases absorption at X-ray frequencies (i.e., κ) and, at the same time, reduces the value of n, thus ensuring optical beam waveguide [207]. This is the hallmark of the stepwise change in refractive index when moving from core to cladding.

The GIF sample (Figure 4.3d) is characterized by a progressive color change when moving from the fiber axis to its edges: this is attributable to the parabolic gradation of its refractive index. The μ-CT profile is higher in the core than in the cladding. This is due to the presence of doping with Ge (germanium), which provides the gradation index of the core, and thus increases both n and κ. Specifically, inside the fiber core, the μ-CT trace exhibits a bell-shaped profile, which is highlighted by a parabolic fit (red solid line in Figure 4.3d).

In the characterization of optical fibers by μ-CT, doping plays a key role, as it is responsible for the absorption contrast that enables the distinction between different materials. Figure 4.3f shows the PCF profile (ID sample L) along the red dashed line in Figure 4.3e. In this case, because of the resolution around 5 μm, the internal structure cannot be seen, and therefore detailed information about the fiber profile cannot be given.

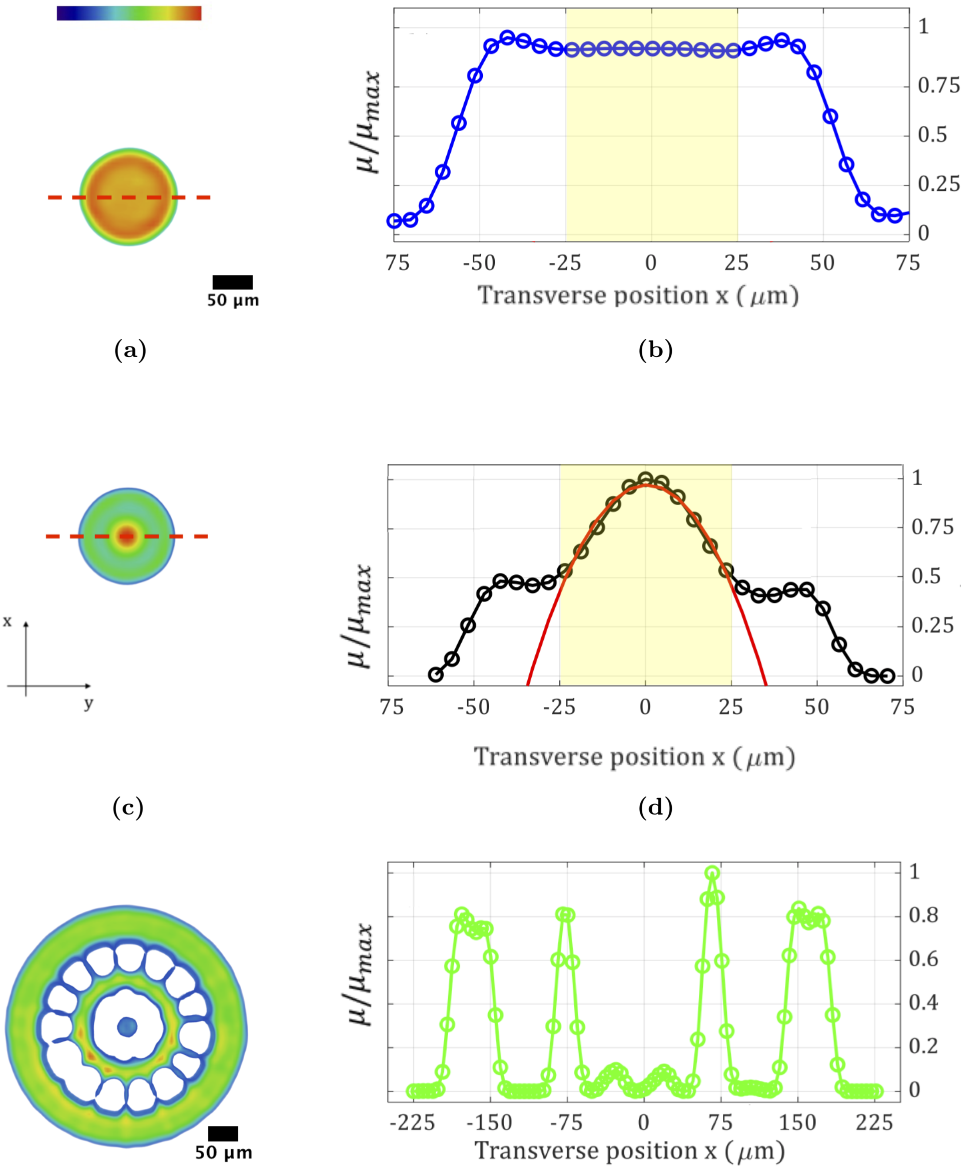

(a) (b)

(c) (d)

(e) (f)

Figure 4.3: (a,c,e) 2D slice of sample A, B and L. (b,d,f) Corresponding profile along the dashed red lines in (a,c,e). The yellow area highlights the core size, while the red solid curve in (d) is a parabolic fit to the experimental data. The scale bar of the PFC is different than the scale bar of the SIF and GIF.

Figure 4.4 shows a comparison between the nominal profiles of the refractive index of the fiber and those obtained μ-CT measurements. As can be seen from the figure, the refractive index profile in the core of the GIF has the same trend of the absorption coefficient retrieved by μ-CT (Figures 4.4c, 4.4d). For the SIF (Figures 4.4a, 4.4b), instead, the profile of μ and n are opposite. This is due to the fact that, in the case of the SIF, the cladding is doped with F, which is lighter than the material of the core (pure SiO_2). The other way around, in the GIF, the silica core is doped with Ge, which has a higher atomic number than both Si and O, thus leading to an increase of the absorption coefficient at X-ray frequencies. In any case, our method permits to retrieve the *shape* of the refractive index profile, which is the same as that of the doping.

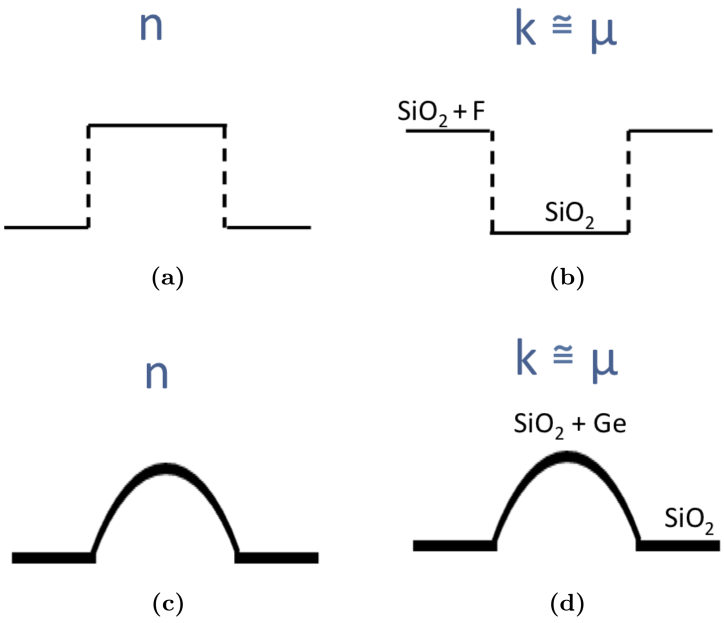

Figure 4.4: Comparison between profiles obtained by (a,c) optical techniques and (b,d) μ-CT measurements. (a,b) SIF fibers, (c,d) GIF fibers.

Comparison of tomography with EDX measurements

To validate the method, a comparison was made with EDX spectroscopy measurements. EDX spectroscopy allows for tracing the characteristic X-ray emission of the doping [208]. EDX spectroscopy enables the detection of characteristic X-ray emission from the material elements, allowing for the spatial mapping of their concentration. EDX spectroscopy permits to verify that the spatial profile of κ_{core} follows that of the doping concentration at the fiber facet.

For this purpose, two fiber samples doped with Ge from different manufacturers were analyzed. Specifically, we analyze two samples of multimode GIF: one produced by Alcatel (sample ID B, Table 4.1) and one produced by Thorlabs (sample ID C).

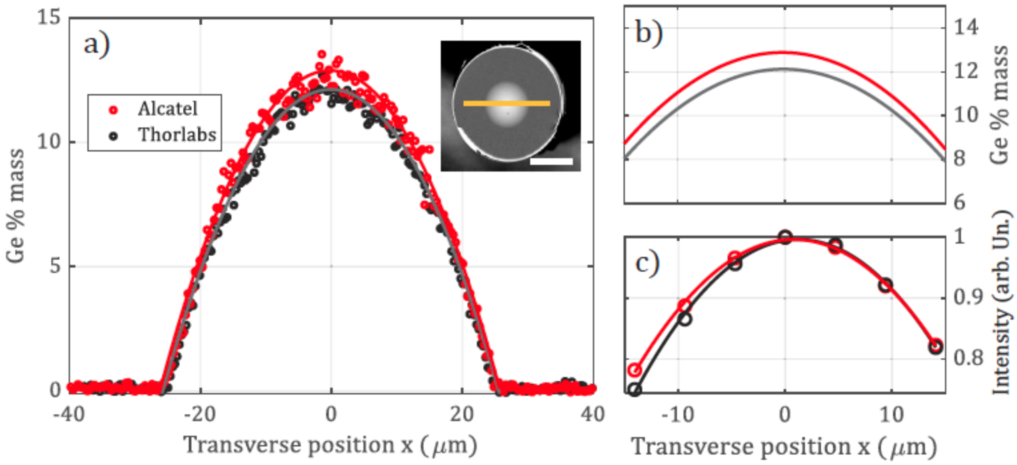

Figure 4.5: Comparison between μ-CT and EDX measurements of samples B and C, marked as "Alcatel" and "Thorlabs", respectively. (a) Ge concentration (% in mass) along the yellow line traced on the SEM image in the inset. The white bar is 50 μm long. (b) Zoom-in of the parabolic fit curves in (a). (c) μ-CT experimental data (void circles) and corresponding parabolic fit of the samples in (a).

By plotting the Ge intensity along the yellow line in the inset of Figure 4.5a, the doping concentration (% in mass) is obtained. It can be seen that the concentration of Ge decreases from the center of the core towards the core/cladding interface. The experimental data for both samples are well represented by a parabola (see the solid lines in Figure 4.5a). The two EDX traces have different peak values (as shown in Figure 4.5b). This difference in Ge concentration must lead to a different core/cladding index contrast at optical frequencies, although the samples have the same nominal value. The comparison of Ge intensity profiles obtained from EDX analysis (Figures 4.5a and 4.5b) and μ-CT measurements (Figure 4.5c) confirmed the reliability of both methods in determining the grading factor of the fibers. Specifically, the ratio between the convexity parameter of the parabolic fit, which is proportional to the ratio between the grading factor g of the two fibers, turns out to be fully consistent when both methods are used. Indeed, we estimate a discrepancy of less than 5% between the ratio between the values of g calculated from either EDX or μ-CT. This agreement highlights the advantages of μ-CT over purely optical techniques in distinguishing subtle differences in optical fiber properties.

μ-CT of different soft glass fibers

In this section, special optical fibers based on new materials and manufacturing techniques are analyzed. In particular, fibers with IDs F, G, H, and I were analyzed.

The 3D renderings of μ-CT images of samples F-I are shown in Figures 4.6a-d. Two color scales were used: red for SIF and blue for GIF. A section of each fiber in the xy plane is shown in Figure 4.6e-h, respectively, while its corresponding profile is shown in Figure 4.6i-l, respectively. The results show, as expected, that the μ-CT profile in the core of SIF is flat, while that in the core of GIF has a parabolic shape.

In particular, we see that for SIF $I_\mu(x)$ remains nearly flat near the center of the fiber core, i.e., $|x| \simeq 0$. In contrast, a pronounced change in $I_\mu(x)$ is observed in the cladding, which we label as Δ. This variation is associated with the difference in density between the core and the cladding materials, thus, their difference in refractive index. In the insets of Figures 4.6i,j we emphasize these variations. For GIF, on the other hand, a parabolic profile is observed in the core, as indicated in the inset of Figures 4.6k-l.

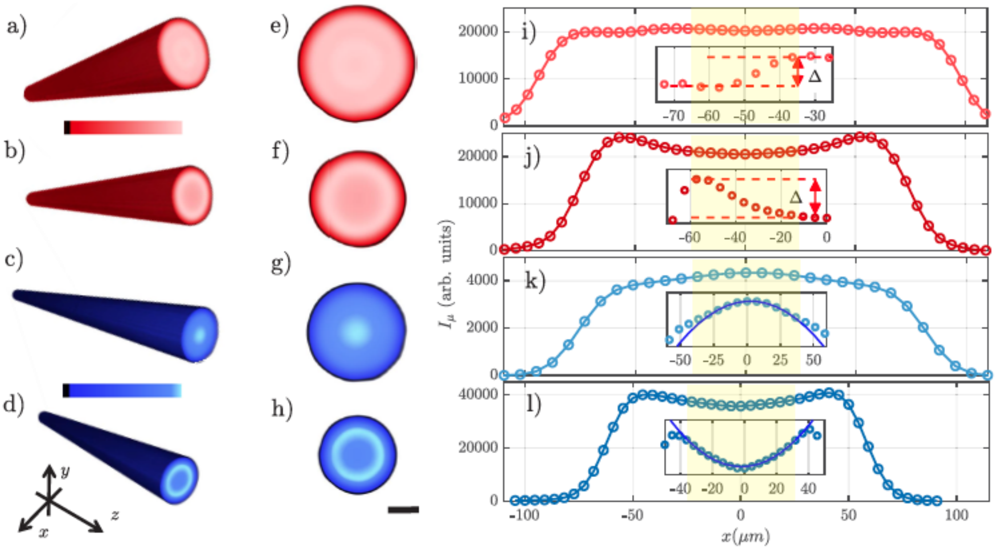

Figure 4.6: Results of μ-CT measurements on soft glass fibers. (a-d) 3D rendering of the μ-CT intensity I_μ for samples F-I, respectively. (e-f) Single slices of (a-d). (i-l) I_μ profile extracted along the diameter of (e-h). The insets show the details of the core/cladding interface (i,j) and the core center (k,l). At the bottom of (d) the reference system is illustrated, whose origin is on the fiber axis, which is parallel to the z direction for all fibers. The black bar at the bottom of (h) is 50 μm long and is the reference for (e-h).

The differences between fibers can be seen. In particular, different behavior of I_μ is observed, i.e., parabola with negative or positive convexity for GIF and/or increasing or decreasing I_μ when passing from core to cladding in SIF. This depends on the fiber manufacturing process, i.e., the core and cladding materials.

Figure 4.7 shows the scanning electron microscope (SEM) images of samples F-I and their respective EDX measurements.

The differences observed in the EDX measurements of the two SIF (samples F and G) indicate the use of different materials in their composition. In sample F, the core and cladding have nearly identical concentrations of fluorine, lanthanum, and zirconium (Figure 4.7a1), with the higher refractive index of the core achieved through a different concentration of barium and lead (see Figure 4.7a2). On the other hand, sample G shows variations in concentrations of barium, zirconium, and hafnium between the core and cladding (Figures 4.7b1 and 4.7b2). The presence of a distinct SIF profile is evident in both cases.

Sample H displays a parabolic concentration profile of elements such as oxygen, barium, lead, and potassium, characteristic of a GIF (Figures 4.7c1-c3). In contrast, the refractive index profile of sample I is less clear from the EDX traces (Figures 4.7d1-d3). The disparities in the EDX results explain the different behaviors of I_μ for the various fibers. In sample F, the substitution of barium for lead in the core results in a higher core refractive index, leading to a greater I_μ in the core compared to the cladding. On the other hand, sample G achieves the core/cladding refractive index difference by substituting hafnium for zirconium.

The relationship between I_μ and the chemical composition is not as straightforward in sample H due to minimal variations between the core and cladding. However, μ-CT analysis was effective in capturing the parabolic shape of I_μ (and hence of n) in the core.

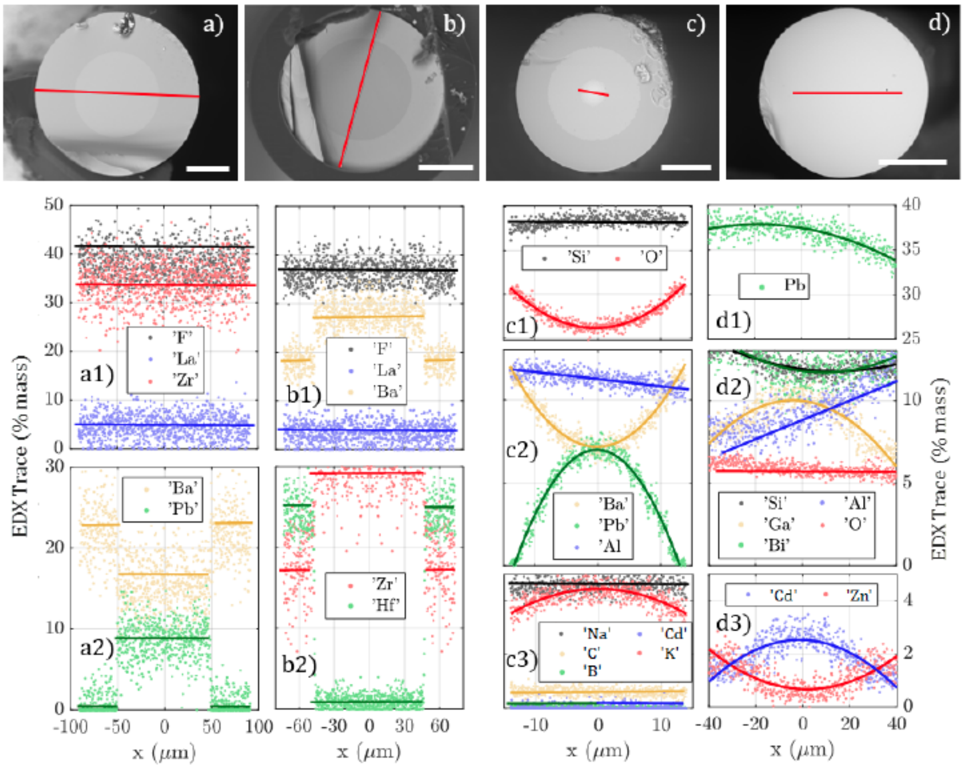

Figure 4.7: (a-d) Scanning electron microscope images of samples F-I, respectively. (a1-d3) EDX traces taken along the red lines in (a-d). The white bars in (a-d) are 50 μm long.

Figure 4.8 summarizes the results obtained, to compare the effectiveness of μ-CT when applied to soft glass fibers (samples F-I) or standard silica fibers (samples A-C). The easiest way to compare our samples in terms of their response to μ-CT, is to consider the values of I_μ on the fiber axis, i.e., at $x = y = 0$. It is also convenient to define an effective value of the atomic number (Z_{eff}) as follows

$$Z_{\text{eff}}(x) = \sum_i Z_i \cdot [X_i](x), \tag{4.3}$$

where the index i runs over the elements which compose the fiber core material. Each element has an x-dependent concentration $[X_i](x)$, which can be retrieved from the EDX traces in Figure 4.7. The definition of Z_{eff} will be useful to compare silica and soft glass fibers in terms of their X-ray absorption properties.

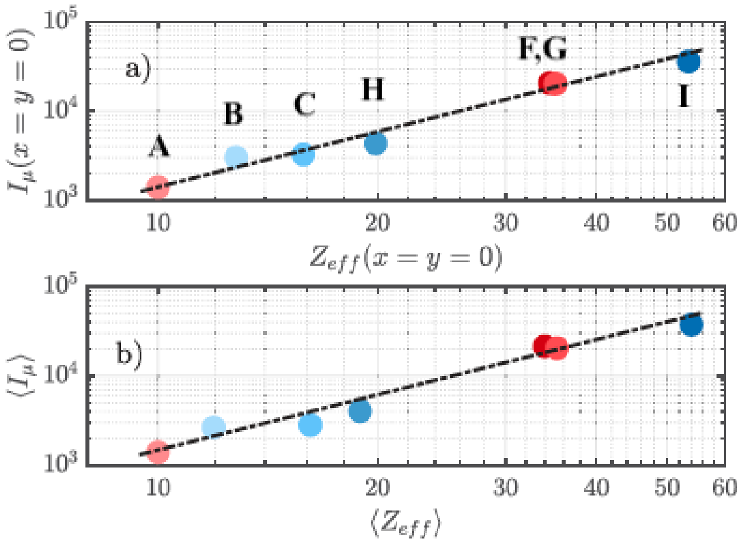

Figure 4.8: Comparison between soft glass and silica fibers in terms of their μ-CT response. (a,b) μ-CT intensity on the fiber axis (a) and averaged over the fiber core (b) vs the effective atomic number Z_{eff}.

The values for I_μ measured along the axis of all fibers are displayed in a log-log plot as a function of Z_{eff} in Figure 4.8a. Due to the presence of high atomic number (Z) elements, the μ-CT intensity for soft glasses is higher compared to silica. The log-log plot reveals an empirical correlation between I_μ and Z_{eff}. The experimental points appear to be aligned, with the fitting curve represented by the dot-dashed black line following the equation

$$I_\mu = \alpha Z_{\text{eff}}^N, \tag{4.4}$$

where α is a constant and N accounts for the nonlinearity of the relationship between I_μ and Z_{eff}. The slope of this line in Figure 4.8a is approximately $N \simeq 2$. To validate this empirical relationship, we used the equation to fit the averaged values of I_μ and Z_{eff} over the fiber core, denoted as $\langle I_\mu \rangle$ and $\langle Z_{\text{eff}} \rangle$. Remarkably, we also found $N \simeq 2$ in this case. The parallel fitting lines in both Figures 4.8a and b suggest a quadratic-like dependence between I_μ and Z_{eff}. This implies that for samples with a Z_{eff} ratio of 2, the fiber containing heavier elements would require approximately $1/4$ of the time to achieve the same μ-CT intensity as the other. This aspect, which might seem trivial at first sight, turns out to be rather important. In our experimental setup, each silica sample demanded up to 10 hours of acquisition time. Reducing acquisition time not only mitigates X-ray detector degradation but also lowers the cost of individual tomographies, key factors for potential industrial applications of μ-CT in optical fiber characterization.

μ-CT of PMMA fibers and identification of laser-induced damage

In this section, we examine the characteristics of plastic optical fiber (PMMA fiber, identified as sample ID M) and focus on defects induced by laser treatment.

Figure 4.9a shows the 3D reconstruction of the PMMA fiber. The image on the top of the panel displays the 3D reconstruction of the fiber. In the middle image, we have adjusted the color transparency to emphasize the presence of damage (red area within the fiber volume). This damage becomes even more pronounced in the lower image of Figure 4.9a, where we have applied a thresholding filter to the intensity scale.

The damaged volume exhibits a non-spherical shape (with a sphericity of 0.65) and measures 39 μm in width and 73 μm in length. Figures 4.9b and c show two transverse slices of the tomographic image at different longitudinal positions (corresponding to the colors in the middle image of Figure 4.9a). Specifically, the slice in Figure 4.9c intersects the damage, while Figure 4.9b is associated with a position distant from the damage. The intensity profiles along the dot-dashed lines in Figures 4.9b and c are presented in Figure 4.9d. The red and green curves align perfectly except within the damaged region. Notably, the red curve reaches a minimum close to zero within this region, indicating a reduction in local material density. Conversely, at the edges of the damage, the density increases, as indicated by the local maximum of the red curve.

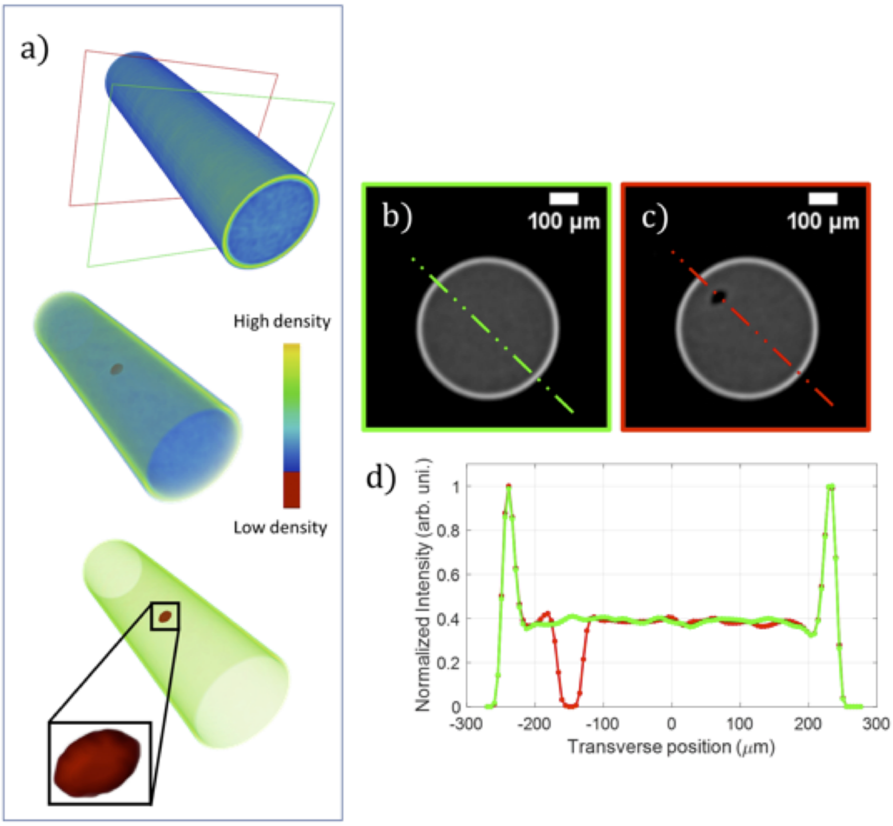

Figure 4.9: (a) 3D rendering of the optical fiber within different visualizations: tomographic reconstruction (top); transparency-enhanced visualization (middle); after applying a thresholding filter in order to emphasize the damage (bottom), which is shown in the inset. (b,c) Slices of tomographic reconstruction along the cutting planes in (a): the red and the green boxes show the inner part of the PMMA fiber with and without damage, respectively; (d) intensity profile traces corresponding to the dot-dashed lines in (b,c).

4.1.5 Conclusions

In this study, we have introduced the μ-CT technique as a tool to characterize optical fibers. Through experimentation, we have shown the capability of μ-CT in resolving the refractive index profiles of optical fibers. Specifically, we have successfully applied this technique to both silica and soft glass optical fibers. μ-CT measurements were verified through EXD measurements. Furthermore, we have employed this technique to determine the profiles of plastic fibers and investigate the presence of laser-induced damage.

Our findings are particularly significant for the potential application of μ-CT for characterizing different types of optical fibers, whose refractive index profiles are challenging to determine when using standard techniques.

Conclusions

In this thesis work, advanced physical techniques were used to study different materials on different scales. μ-CT and ATR-FTIR spectroscopy, separately, have supported the understanding of biological systems and engineering systems. In particular, the effects of pharmacological treatments on cells and organs were studied and also a non-invasive methodology as a support to the diagnosis of multiple sclerosis disease was explored. At the same time, engineering components were studied for the identification of defects and to evaluate mechanical properties of materials. Furthermore, a new method for the characterization of optical fibers was proposed.

A crucial aspect of this thesis is the complementarity between μ-CT and ATR-FTIR techniques. While μ-CT offers 3D visualization of the internal structures of samples, allowing detailed analysis of morphology and physical structure, ATR-FTIR spectroscopy focuses on the molecular and biochemical aspect, providing information on the chemical components present in the sample.

This combination of approaches makes it possible to cover a full spectrum of analysis: from 3D structure to the identification of molecular changes induced by the interaction with drugs or due to a pathological state, providing an expanded and detailed view of the studied sample.

This synergy becomes particularly evident in the biomedical context. Indeed, μ-CT allows examination of the internal structure of small organs without destroying it, while ATR-FTIR allows identification of any biochemical changes that may be associated with disease and/or drug interaction. Together, these techniques can provide a more complete and accurate diagnosis by combining structural and biochemical analysis.

Both techniques show different advantages. In particular, the noninvasive feature of μ-CT makes it possible to obtain three-dimensional images with micrometer resolution in a non-destructive manner, a useful advantage for both biological and engineering applications, ensuring sample integrity and reproducible measurements. In addition, it can be considered as a tool for virtual histology, providing detailed information on the morphology of biological samples, without the need to physically section them. In a biomedical context, such applications turn out to have great advantages, think of the possibility of investigating tumor tissue without the need for thin sections. These advantages are also important in engineering research, where the identification of internal defects in materials may improve component quality and prevent structural failure. Also, telecommunications and optical sensors may benefit from such studies, because, by using 3D visualization, the performance of optical fibers can be monitored and improved without external alteration.

On the other hand, ATR-FTIR investigation of blood and cells turns out to have different advantages: one among all is the possibility of analyzing biological samples without special preparations or chemical staining. This is particularly useful for blood and cells, as it reduces the risk of altering the biochemical characteristics of the samples. In addition, because the technique allows obtaining complete biochemical profiles of samples, thus detecting the presence of proteins, lipids, carbohydrates, and nucleic acids, it makes it possible to identify molecular changes related to specific diseases or physiological conditions.

For each case study, it was identified what the possible goals were to be achieved and then identified the best measurement technique to use. Once the technique was identified and measurements were made, the next step was to determine the best analysis to perform for the specific measurement. When possible, results were compared with literature data and/or other techniques.

The results obtained highlight the protective effects of PSELT, a small peptide derived from the SELENOT protein, on cardiac cells and on the entire heart, revealing its potential as a therapeutic agent for global myocardial ischemia; as well as μ-CT results demonstrate its validity as a tool for three-dimensional virtual histology.

Furthermore, the application of ATR-FTIR spectroscopy for biomolecular profiling in the diagnosis of multiple sclerosis proves to be a promising tool in classifying healthy and diseased individuals with high sensitivity and specificity.

In addition, the use of non-invasive techniques such as μ-CT for 3D morphological analysis provides information on the structural characteristics of biological samples, such as goldfish hearts, improving the understanding of their function.

On the other hand, studying samples produced with additive manufacturing through μ-CT analysis offers detailed information on the presence of manufacturing defects and their influence on failure mechanisms.

Finally, μ-CT has been employed to characterize the refractive index profile of optical fibers, offering an innovative tool for the non-destructive characterization of different types of fibers.

Overall, the studies presented in this thesis show the different applications of experimental physical techniques and data analysis in biomedical research, materials science, and optical fiber characterization, demonstrating the importance of interdisciplinary approaches in the advancement of scientific knowledge and of technological innovation.

Bibliography

[1] Avinash C Kak and Malcolm Slaney. *Principles of computerized tomographic imaging*. SIAM, 2001.

[2] Godfrey N Hounsfield. Computerized transverse axial scanning (tomography): Part 1. description of system. *The British journal of radiology*, 46(552):1016–1022, 1973.

[3] EJ Morton, S Webb, JE Bateman, LJ Clarke, and CG Shelton. Three-dimensional x-ray microtomography for medical and biological applications. *Physics in Medicine & Biology*, 35(7):805, 1990.

[4] Orestis L Katsamenis, Michael Olding, Jane A Warner, David S Chatelet, Mark G Jones, Giacomo Sgalla, Bennie Smit, Oliver J Larkin, Ian Haig, Luca Richeldi, et al. X-ray micro-computed tomography for nondestructive three-dimensional (3d) x-ray histology. *The American journal of pathology*, 189(8):1608–1620, 2019.

[5] Laura Maugeri, Mauro DiNuzzo, Marta Moraschi, Charles Nicaise, Inna Bukreeva, Fabio Mangini, Federico Giove, Alessia Cedola, and Michela Fratini. Fractal dimension analysis of high-resolution x-ray phase contrast micro-tomography images at different threshold levels in a mouse spinal cord. *Condensed Matter*, 3(4):48, 2018.

[6] Luca Brombal, Sandro Donato, Diego Dreossi, Fulvia Arfelli, Deborah Bonazza, Adriano Contillo, Pasquale Delogu, Vittorio Di Trapani, Bruno Golosio, Giovanni Mettivier, et al. Phase-contrast breast ct: the effect of propagation distance. *Physics in Medicine & Biology*, 63(24):24NT03, 2018.

[7] Romina Conte, Raffaele Filosa, Vincenzo Formoso, Francesco Gagliardi, Raf-

faele G Agostino, and Giuseppina Ambrogio. Analysis of extruded pins manufactured by friction stir forming for multi-material joining purposes. In *AIP conference proceedings*. AIP Publishing, 2019.

[8] Sara Stelitano, Alberto Rullo, Luigi Piredda, Elisabetta Mecozzi, Luigi Di Vito, Raffaele Giuseppe Agostino, Raffaele Filosa, Vincenzo Formoso, Giuseppe Conte, and Alfonso Policicchio. The deltah lab, a new multidisciplinary european facility to support the h2 distribution & storage economy. *Applied Sciences*, 11(7):3272, 2021.

[9] Veerle Cnudde and Matthieu Nicolaas Boone. High-resolution x-ray computed tomography in geosciences: A review of the current technology and applications. *Earth-Science Reviews*, 123:1–17, 2013.

[10] François Renard, Dominique Bernard, Jacques Desrues, and Audrey Ougier-Simonin. 3d imaging of fracture propagation using synchrotron x-ray microtomography. *Earth and Planetary Science Letters*, 286(1-2):285–291, 2009.

[11] E Rosenberg, R Ferreira de Paiva, P Guéroult, and J Lynch. Microtomography applications in rock analysis and related fields. *Proceedings of the Deutsche Gesellschaft für Zerstörungsfreie Prüfung-DGZfP*, pages 9–18, 1999.

[12] Sara Stabile, Francesca Palermo, Inna Bukreeva, Daniela Mele, Vincenzo Formoso, Roberto Bartolino, and Alessia Cedola. A computational platform for the virtual unfolding of herculaneum papyri. *Scientific Reports*, 11(1):1695, 2021.

[13] MP Morigi, Franco Casali, Matteo Bettuzzi, Rosa Brancaccio, and V d'Errico. Application of x-ray computed tomography to cultural heritage diagnostics. *Applied Physics A*, 100:653–661, 2010.

[14] Raffaele Giuseppe Agostino, S Donato, Tommaso Caruso, E Colavita, F Zanini, A D'alessio, D Pisarra, and A Taliano Grasso. Microtomographic studies as a tool in the identification of a new ceramic class: the metal-imitating pottery as grave goods among brettians and lucanians. *Microchemical Journal*, 126:138–148, 2016.

[15] Burton L Henke, Eric M Gullikson, and John C Davis. X-ray interactions: pho-

toabsorption, scattering, transmission, and reflection at e= 50-30,000 ev, z= 1-92. *Atomic data and nuclear data tables*, 54(2):181–342, 1993.

[16] X-Ray Data Booklet. X-ray data booklet. *Laboratory, Univ. California*, 2001.

[17] Jens Als-Nielsen and Des McMorrow. *Elements of modern X-ray physics.* John Wiley & Sons, 2011.

[18] Willi A Kalender. *Computed tomography: fundamentals, system technology, image quality, applications.* John Wiley & Sons, 2011.

[19] Reginald William James. The optical principles of the diffraction of x-rays. *(No Title)*, 1962.

[20] Shu-Ang Zhou and Anders Brahme. Development of phase-contrast x-ray imaging techniques and potential medical applications. *Physica Medica*, 24(3):129–148, 2008.

[21] José Baruchel, Jean-Yves Buffiere, and Eric Maire. *X-ray tomography in material science.* Hermes Science Publications, 2000.

[22] Fulvia Arfelli, M Assante, V Bonvicini, A Bravin, Giovanni Cantatore, Edoardo Castelli, L Dalla Palma, M Di Michiel, Renata Longo, A Olivo, et al. Low-dose phase contrast x-ray medical imaging. *Physics in Medicine & Biology*, 43(10): 2845, 1998.

[23] Randolf Hanke, Theobald Fuchs, Michael Salamon, and Simon Zabler. X-ray microtomography for materials characterization. In *Materials characterization using Nondestructive Evaluation (NDE) methods*, pages 45–79. Elsevier, 2016.

[24] CXRO Center for X-Ray Optics. X-ray interactions with matter. URL `https://henke.lbl.gov/optical_constants/`.

[25] Robert A Lewis. Medical phase contrast x-ray imaging: current status and future prospects. *Physics in medicine & biology*, 49(16):3573, 2004.

[26] Wataru Yashiro, Wolfgang Voegeli, and Hiroyuki Kudo. Exploring frontiers of 4d x-ray tomography. *Applied Sciences*, 11(19):8868, 2021.

[27] A. Taylor. Ts imaging, 2018. URL `http://ts-imaging.science.unimelb.edu.au/Services/Simple/`.

[28] T Jensen. Refraction and scattering based x-ray imaging. *University of Copenhagen: Copenhagen, Denmark*, 2010.

[29] Jiang Hsieh. *Computed tomography: principles, design, artifacts, and recent advances*. SPIE press, 2003.

[30] Faycal Kharfi. Mathematics and physics of computed tomography (ct): demonstrations and practical examples. *Imaging and radioanalytical techniques in interdisciplinary research-fundamentals and cutting edge applications*, 117:113–116, 2013.

[31] Lee A Feldkamp, Lloyd C Davis, and James W Kress. Practical cone-beam algorithm. *Josa a*, 1(6):612–619, 1984.

[32] S Valton, F Peyrin, and D Sappey-Marinier. A fdk-based reconstruction method for off-centered circular trajectory cone beam tomography. *IEEE transactions on nuclear science*, 53(5):2736–2745, 2006.

[33] https://visielab.uantwerpen.be/astra-training.

[34] Chris C Shaw. *Cone beam computed tomography*. Taylor & Francis, 2014.

[35] Stuart R Stock. *Microcomputed tomography: methodology and applications*. CRC press, 2019.

[36] Kaan Orhan et al. Micro-computed tomography (micro-ct) in medicine and engineering. Technical report, Springer, 2020.

[37] Julia F Barrett and Nicholas Keat. Artifacts in ct: recognition and avoidance. *Radiographics*, 24(6):1679–1691, 2004.

[38] Wim Dewulf, Ye Tan, and Kim Kiekens. Sense and non-sense of beam hardening correction in ct metrology. *CIRP annals*, 61(1):495–498, 2012.

[39] Jun Wang, Shijie Wang, Yang Chen, Jiasong Wu, Jean-Louis Coatrieux, and Limin Luo. Metal artifact reduction in ct using fusion based prior image. *Medical physics*, 40(8):081903, 2013.

[40] STAR RI. μtomo1. URL `https://star.unical.it/mutomo1/`.

[41] Hamamatsu. Hamamatsu l12161-07. URL `https://www.hamamatsu.com/content/dam/hamamatsu-photonics/sites/documents/99_SALES_LIBRARY/etd/L12161-07_TXPR1023E.pdf`.

[42] Mariacristina Filice, Maria Caterina Crocco, Raffaele Giuseppe Agostino, Riccardo Cristoforo Barberi, Daniela Amelio, Sandra Imbrogno, Vincenzo Formoso, and Maria Carmela Cerra. An x-ray computed μ-tomography analysis for the characterization of 3d-heart shape in a model of cardiac plasticity. *Vascular pharmacology*, 155:107310, 2024.

[43] Asami Udagawa, Shuichi Sato, Akira Hasuike, Mamoru Kishida, Yoshinori Arai, and Koichi Ito. Micro-ct observation of angiogenesis in bone regeneration. *Clinical oral implants research*, 24(7):787–792, 2013.

[44] Andrew J Burghardt, Thomas M Link, and Sharmila Majumdar. High-resolution computed tomography for clinical imaging of bone microarchitecture. *Clinical Orthopaedics and Related Research®*, 469(8):2179–2193, 2011.

[45] Charlene M Downey, Arvind K Singla, Michelle L Villemaire, Helen R Buie, Steven K Boyd, and Frank R Jirik. Quantitative ex-vivo micro-computed tomographic imaging of blood vessels and necrotic regions within tumors. *PloS one*, 7 (7):e41685, 2012.

[46] Michael J Paulus, Shaun S Gleason, Stephen J Kennel, Patricia R Hunsicker, and Dabney K Johnson. High resolution x-ray computed tomography: an emerging tool for small animal cancer research. *Neoplasia*, 2(1-2):62–70, 2000.

[47] Chiara Morano, Maria Caterina Crocco, Vincenzo Formoso, and Leonardo Pagnotta. Effect of induced plastic strain on the porosity of pa12 printed through selective laser sintering studied by x-ray computed micro-tomography. *The International Journal of Advanced Manufacturing Technology*, 125(7-8):3229–3240, 2023.

[48] Danilo A Renzo, Maria C Crocco, Carmine Maletta, Leonardo Pagnotta, Emanuele Sgambitterra, Filippo Berto, Franco Furgiuele, Raffaele Filosa, Joseph J

Beltrano, Riccardo C Barberi, Raffaele G Agostino, and Vincenzo Formoso. X-ray computed μ-tomography analysis to evaluate the crack growth in an additive manufactured ti-6al-4v alloy sample stressed with in-phase axial and torsional loading. *International Journal of Fatigue*, 175:107727, 2023.

[49] Maria C Crocco, Carmelo Scuro, Raffaele Filosa, Rosamaria Codispoti, Mario Ferraro, Andrea Solano, Raffaele G Agostino, Riccardo C Barberi, Renato S Olivito, and Vincenzo Formoso. Experimental study on the mechanical properties of basalt frcm made of various matrices: Validation by x-ray microtomography. *Journal of Materials in Civil Engineering*, 35(10):04023334, 2023.

[50] Barbara H Stuart. *Infrared spectroscopy: fundamentals and applications.* John Wiley & Sons, 2004.

[51] Andreas Barth. Infrared spectroscopy of proteins. *Biochimica et Biophysica Acta (BBA)-Bioenergetics*, 1767(9):1073–1101, 2007.

[52] Wolfgang Petrich. Mid-infrared and raman spectroscopy for medical diagnostics. *Applied Spectroscopy Reviews*, 36(2-3):181–237, 2001.

[53] Lisa M Miller, Megan W Bourassa, and Randy J Smith. Ftir spectroscopic imaging of protein aggregation in living cells. *Biochimica et biophysica acta (BBA)-biomembranes*, 1828(10):2339–2346, 2013.

[54] Maria Paraskevaidi, Camilo LM Morais, Kássio MG Lima, Julie S Snowden, Jennifer A Saxon, Anna MT Richardson, Matthew Jones, David MA Mann, David Allsop, Pierre L Martin-Hirsch, et al. Differential diagnosis of alzheimer's disease using spectrochemical analysis of blood. *Proceedings of the National Academy of Sciences*, 114(38):E7929–E7938, 2017.

[55] Alexandra Sala, David J Anderson, Paul M Brennan, Holly J Butler, James M Cameron, Michael D Jenkinson, Christopher Rinaldi, Ashton G Theakstone, and Matthew J Baker. Biofluid diagnostics by ftir spectroscopy: A platform technology for cancer detection. *Cancer letters*, 477:122–130, 2020.

[56] Arghya Banerjee, Abhiram Gokhale, Renuka Bankar, Viswanthram Palanivel, Akanksha Salkar, Harley Robinson, Jayanthi S Shastri, Sachee Agrawal, Gunter

Hartel, Michelle M Hill, et al. Rapid classification of covid-19 severity by atr-ftir spectroscopy of plasma samples. *Analytical Chemistry*, 93(30):10391–10396, 2021.

[57] Liyang Zhang, Meng Xiao, Yao Wang, Siqi Peng, Yu Chen, Dong Zhang, Dongheyu Zhang, Yuntao Guo, Xinxin Wang, Haiyun Luo, et al. Fast screening and primary diagnosis of covid-19 by atr–ft-ir. *Analytical Chemistry*, 93(4): 2191–2199, 2021.

[58] Diletta Ami, Paolo Mereghetti, Andrea Foli, Masayoshi Tasaki, Paolo Milani, Mario Nuvolone, Giovanni Palladini, Giampaolo Merlini, Francesca Lavatelli, and Antonino Natalello. Atr-ftir spectroscopy supported by multivariate analysis for the characterization of adipose tissue aspirates from patients affected by systemic amyloidosis. *Analytical chemistry*, 91(4):2894–2900, 2019.

[59] Robert M Silverstein and G Clayton Bassler. Spectrometric identification of organic compounds. *Journal of Chemical Education*, 39(11):546, 1962.

[60] F Siebert. *Vibrational Spectroscopy in Life Science.* Wiley-VCH Verlag GmbH & Co. KGaA, 2008.

[61] Bruker. What is ft-ir spectroscopy. URL `https://www.bruker.com/it/products-and-solutions/infrared-and-raman/ft-ir-routine-spectrometer/what-is-ft-ir-spectroscopy/difference-ir-vs-ftir.html`.

[62] Charles R Cantor and Paul Reinhard Schimmel. *Techniques for the study of biological structure and function.* WH Freeman San Francisco, 1980.

[63] Lukas K Tamm and Suren A Tatulian. Infrared spectroscopy of proteins and peptides in lipid bilayers. *Quarterly reviews of biophysics*, 30(4):365–429, 1997.

[64] Milan Milosevic. Internal reflection and atr spectroscopy. *Applied Spectroscopy Reviews*, 39(3):365–384, 2004.

[65] Erik Goormaghtigh, Vincent Raussens, and Jean-Marie Ruysschaert. Attenuated total reflection infrared spectroscopy of proteins and lipids in biological membranes. *Biochimica et Biophysica Acta (BBA)-Reviews on Biomembranes*, 1422 (2):105–185, 1999.

[66] Katherine Victoria Oliver. *Infrared spectroscopy as a clinical diagnostic method for detection of disease states: developments and applications in kidney diseases and cancer diagnoses*. PhD thesis, UCL (University College London), 2015.

[67] Qd-europe. Attenuated total reflexion atr fundamentals band distortion and band shift. URL `https://qd-europe.com/de/en/`.

[68] Marwa El-Azazy. Infrared spectroscopy: Principles, advances, and applications. *Books on Demand*, 2019.

[69] EB Wilson and JC Decius. Pc cross molecular vibrations, 1955.

[70] Xin Liu. *Organic Chemistry I*. KPU.

[71] Mohammed Z Albahar. *Selective toluene disproportionation over ZSM-5 zeolite*. The University of Manchester (United Kingdom), 2018.

[72] Zanyar Movasaghi, Shazza Rehman, and Dr Ihtesham ur Rehman. Fourier transform infrared (ftir) spectroscopy of biological tissues. *Applied Spectroscopy Reviews*, 43(2):134–179, 2008.

[73] Bruker. Bruker, . URL `https://www.bruker.com/en.html`.

[74] SG Kazarian and KLA Chan. Applications of atr-ftir spectroscopic imaging to biomedical samples. *Biochimica et Biophysica Acta (BBA)-Biomembranes*, 1758 (7):858–867, 2006.

[75] Stefanie Elizabeth Glassford. *Applications of ATR-FTIR spectroscopic imaging to proteins*. PhD thesis, Imperial College London, 2013.

[76] Adriana Martinez-Cuazitl, Gustavo J Vazquez-Zapien, Miguel Sanchez-Brito, Jorge H Limon-Pacheco, Melissa Guerrero-Ruiz, Francisco Garibay-Gonzalez, Raul J Delgado-Macuil, Maria G Garcia de Jesus, Miguel A Corona-Perezgrovas, Armando Pereyra-Talamantes, et al. Atr-ftir spectrum analysis of saliva samples from covid-19 positive patients. *Scientific Reports*, 11(1):19980, 2021.

[77] Maria Caterina Crocco, María Fernanda Heredia Moyano, Ferdinanda Annesi, Rosalinda Bruno, Domenico Pirritano, Francesco Del Giudice, Alfredo Petrone,

Francesca Condino, and Rita Guzzi. Atr-ftir spectroscopy of plasma supported by multivariate analysis discriminates multiple sclerosis disease. *Scientific Reports*, 13(1):2565, 2023.

[78] MC Crocco, MF Heredia Moyano, F Annesi, R Bruno, D Pirritano, F Del Giudice, A Petrone, F Condino, and R Guzzi. Blood based infrared spectroscopy supported by chemometric methods discriminates multiple sclerosis disease. *Physica Medica: European Journal of Medical Physics*, 115, 2023.

[79] Francesca Condino, Maria Caterina Crocco, Domenico Pirritano, Alfredo Petrone, Francesco Del Giudice, and Rita Guzzi. A linear predictor based on ftir spectral biomarkers improves disease diagnosis classification: An application to multiple sclerosis. *Journal of Personalized Medicine*, 13(11):1596, 2023.

[80] Carmine Rocca, Anna De Bartolo, Rita Guzzi, Maria Caterina Crocco, Vittoria Rago, Naomi Romeo, Ida Perrotta, Ernestina Marianna De Francesco, Maria Grazia Muoio, Maria Concetta Granieri, et al. Palmitate-induced cardiac lipotoxicity is relieved by the redox-active motif of selenot through improving mitochondrial function and regulating metabolic state. *Cells*, 12(7):1042, 2023.

[81] Maria Caterina Crocco, Carmine Rocca, Anna De Bartolo, Riccardo C. Barberi, Raffaele G. Agostino, Raffaele Filosa, Tommaso Angelone, Rita Guzzi, and Vincenzo Formoso. Protective effects of pselt peptide in cardiovascular disease. *SILS confernce*, 2024.

[82] Tiffany M Powell-Wiley, Paul Poirier, Lora E Burke, Jean-Pierre Després, Penny Gordon-Larsen, Carl J Lavie, Scott A Lear, Chiadi E Ndumele, Ian J Neeland, Prashanthan Sanders, et al. Obesity and cardiovascular disease: a scientific statement from the american heart association. *Circulation*, 143(21):e984–e1010, 2021.

[83] Lidia S Szczepaniak, Robert L Dobbins, Gregory J Metzger, Greta Sartoni-D'Ambrosia, Debbie Arbique, Wanpen Vongpatanasin, Roger Unger, and Ronald G Victor. Myocardial triglycerides and systolic function in humans: in vivo evaluation by localized proton spectroscopy and cardiac imaging. *Magnetic Resonance in Medicine: An Official Journal of the International Society for Magnetic Resonance in Medicine*, 49(3):417–423, 2003.

[84] Konstantinos Drosatos and P Christian Schulze. Cardiac lipotoxicity: molecular pathways and therapeutic implications. *Current heart failure reports*, 10:109–121, 2013.

[85] Imo A Ebong, David C Goff Jr, Carlos J Rodriguez, Haiying Chen, and Alain G Bertoni. Mechanisms of heart failure in obesity. *Obesity research & clinical practice*, 8(6):e540–e548, 2014.

[86] Carmine Rocca, Teresa Pasqua, Loubna Boukhzar, Youssef Anouar, and Tommaso Angelone. Progress in the emerging role of selenoproteins in cardiovascular disease: Focus on endoplasmic reticulum-resident selenoproteins. *Cellular and Molecular Life Sciences*, 76:3969–3985, 2019.

[87] Jun Lu and Arne Holmgren. Selenoproteins. *Journal of Biological Chemistry*, 284 (2):723–727, 2009.

[88] Laura L Listenberger, Xianlin Han, Sarah E Lewis, Sylvaine Cases, Robert V Farese Jr, Daniel S Ory, and Jean E Schaffer. Triglyceride accumulation protects against fatty acid-induced lipotoxicity. *Proceedings of the National Academy of Sciences*, 100(6):3077–3082, 2003.

[89] Juliana Martins de S e Silva, Irene Zanette, Peter B Noël, Mateus B Cardoso, Melanie A Kimm, and Franz Pfeiffer. Three-dimensional non-destructive soft-tissue visualization with x-ray staining micro-tomography. *Scientific reports*, 5 (1):14088, 2015.

[90] Pidassa Bidola, Juliana Martins de Souza e Silva, Klaus Achterhold, Enkhtsetseg Munkhbaatar, Philipp J Jost, Anna-Lena Meinhardt, Kirsten Taphorn, Marie-Christine Zdora, Franz Pfeiffer, and Julia Herzen. A step towards valid detection and quantification of lung cancer volume in experimental mice with contrast agent-based x-ray microtomography. *Scientific Reports*, 9(1):1325, 2019.

[91] Ihtesham ur Rehman, Zanyar Movasaghi, and Shazza Rehman. *Vibrational spectroscopy for tissue analysis.* CRC press, 2012.

[92] Günnur Güler, Ummu Guven, and Gulperi Oktem. Characterization of

cd133+/cd44+ human prostate cancer stem cells with atr-ftir spectroscopy. *Analyst*, 144(6):2138–2149, 2019.

[93] Nihal Simsek Ozek, Serkan Tuna, A Elif Erson-Bensan, and Feride Severcan. Characterization of microrna-125b expression in mcf7 breast cancer cells by atr-ftir spectroscopy. *Analyst*, 135(12):3094–3102, 2010.

[94] Refael Minnes, Mati Nissinmann, Yael Maizels, Gabi Gerlitz, Abraham Katzir, and Yosef Raichlin. Using attenuated total reflection–fourier transform infrared (atr-ftir) spectroscopy to distinguish between melanoma cells with a different metastatic potential. *Scientific reports*, 7(1):4381, 2017.

[95] Ting Gui, Yunlun Li, Shijun Zhang, Nan Zhang, Ying Sun, Fengzhen Liu, Qingfa Chen, and Zhibo Gai. Docosahexaenoic acid protects against palmitate-induced mitochondrial dysfunction in diabetic cardiomyopathy. *Biomedicine & Pharmacotherapy*, 128:110306, 2020.

[96] Kuen-Ming Wu, Yuan-Man Hsu, Mei-Chin Ying, Fuu-Jen Tsai, Chang-Hai Tsai, Jing-Gung Chung, Jai-Sing Yang, Chih-Hsin Tang, Li-Yi Cheng, Po-Hua Su, et al. High-density lipoprotein ameliorates palmitic acid-induced lipotoxicity and oxidative dysfunction in h9c2 cardiomyoblast cells via ros suppression. *Nutrition & metabolism*, 16(1):1–13, 2019.

[97] Qingxun Hu, Huiliang Zhang, Nicolás Gutiérrez Cortés, Dan Wu, Pei Wang, Jing Zhang, Julie A Mattison, Eric Smith, Lisa F Bettcher, Mingyi Wang, et al. Increased drp1 acetylation by lipid overload induces cardiomyocyte death and heart dysfunction. *Circulation research*, 126(4):456–470, 2020.

[98] Lu Zou, Xiaoyan Li, Nan Wu, Pengyu Jia, Chunting Liu, and Dalin Jia. Palmitate induces myocardial lipotoxic injury via the endoplasmic reticulum stress-mediated apoptosis pathway. *Molecular medicine reports*, 16(5):6934–6939, 2017.

[99] Ben D Perry, Jill A Rahnert, Yang Xie, Bin Zheng, Myra E Woodworth-Hobbs, and S Russ Price. Palmitate-induced er stress and inhibition of protein synthesis in cultured myotubes does not require toll-like receptor 4. *PLoS One*, 13(1): e0191313, 2018.

[100] Sigmundur Gudbjarnason, CHRISTIAN DE SCHRYVER, CHIYO CHIBA, JIRO YAMANAKA, and RICHARD J BING. Protein and nucleic acid synthesis during the reparative processes following myocardial infarction. *Circulation Research*, 15 (4):320–326, 1964.

[101] Gabriella Captur, Luis R Lopes, Vimal Patel, Chunming Li, Paul Bassett, Petros Syrris, Daniel M Sado, Viviana Maestrini, Timothy J Mohun, William J McKenna, et al. Abnormal cardiac formation in hypertrophic cardiomyopathy: fractal analysis of trabeculae and preclinical gene expression. *Circulation: Cardiovascular Genetics*, 7(3):241–248, 2014.

[102] Francisco J Esteban, Jorge Sepulcre, Nieves Vélez de Mendizábal, Joaquín Goñi, Juan Navas, Juan Ruiz de Miras, Bartolome Bejarano, Jose C Masdeu, and Pablo Villoslada. Fractal dimension and white matter changes in multiple sclerosis. *Neuroimage*, 36(3):543–549, 2007.

[103] Qingyang Lin, SJ Neethling, Katherine J Dobson, L Courtois, and Peter D Lee. Quantifying and minimising systematic and random errors in x-ray microtomography based volume measurements. *Computers & Geosciences*, 77:1–7, 2015.

[104] DS Reich, CF Lucchinetti, and PA Calabresi. Multiple sclerosis. *New Engl J Med*, 378:169–180, 2018.

[105] Mitchell T Wallin, William J Culpepper, Emma Nichols, Zulfiqar A Bhutta, Tsegaye Tewelde Gebrehiwot, Simon I Hay, Ibrahim A Khalil, Kristopher J Krohn, Xiaofeng Liang, Mohsen Naghavi, et al. Global, regional, and national burden of multiple sclerosis 1990–2016: a systematic analysis for the global burden of disease study 2016. *The Lancet Neurology*, 18(3):269–285, 2019.

[106] Ron Milo. Effectiveness of multiple sclerosis treatment with current immunomodulatory drugs. *Expert opinion on pharmacotherapy*, 16(5):659–673, 2015.

[107] Wallace J Brownlee, Todd A Hardy, Franz Fazekas, and David H Miller. Diagnosis of multiple sclerosis: progress and challenges. *The Lancet*, 389(10076):1336–1346, 2017.

[108] Andrew J Solomon and John R Corboy. The tension between early diagnosis and misdiagnosis of multiple sclerosis. *Nature Reviews Neurology*, 13(9):567–572, 2017.

[109] Alan J Thompson, Brenda L Banwell, Frederik Barkhof, William M Carroll, Timothy Coetzee, Giancarlo Comi, Jorge Correale, Franz Fazekas, Massimo Filippi, Mark S Freedman, et al. Diagnosis of multiple sclerosis: 2017 revisions of the mcdonald criteria. *The Lancet Neurology*, 17(2):162–173, 2018.

[110] Violaine K Harris, John F Tuddenham, and Saud A Sadiq. Biomarkers of multiple sclerosis: current findings. *Degenerative neurological and neuromuscular disease*, pages 19–29, 2017.

[111] Jesse Huang, Mohsen Khademi, Lars Fugger, Örjan Lindhe, Lenka Novakova, Markus Axelsson, Clas Malmeström, Clara Constantinescu, Jan Lycke, Fredrik Piehl, et al. Inflammation-related plasma and csf biomarkers for multiple sclerosis. *Proceedings of the National Academy of Sciences*, 117(23):12952–12960, 2020.

[112] Viviana Nociti, Marina Romozzi, and Massimiliano Mirabella. Update on multiple sclerosis molecular biomarkers to monitor treatment effects. *Journal of Personalized Medicine*, 12(4):549, 2022.

[113] Joachim Burman, H Zetterberg, Moa Fransson, A SI Loskog, Raili Raininko, and Jan Fagius. Assessing tissue damage in multiple sclerosis: a biomarker approach. *Acta Neurologica Scandinavica*, 130(2):81–89, 2014.

[114] Pia Kivisäkk, Brian C Healy, Katiana Francois, Roopali Gandhi, Taha Gholipour, Svetlana Egorova, Velina Sevdalinova, Francisco Quintana, Tanuja Chitnis, Howard L Weiner, et al. Evaluation of circulating osteopontin levels in an unselected cohort of patients with multiple sclerosis: relevance for biomarker development. *Multiple Sclerosis Journal*, 20(4):438–444, 2014.

[115] Matthew J Baker, Júlio Trevisan, Paul Bassan, Rohit Bhargava, Holly J Butler, Konrad M Dorling, Peter R Fielden, Simon W Fogarty, Nigel J Fullwood, Kelly A Heys, et al. Using fourier transform ir spectroscopy to analyze biological materials. *Nature protocols*, 9(8):1771–1791, 2014.

[116] Matthew J Baker, Shawn R Hussain, Lila Lovergne, Valérie Untereiner, Caryn Hughes, Roman A Lukaszewski, Gérard Thiéfin, and Ganesh D Sockalingum. Developing and understanding biofluid vibrational spectroscopy: a critical review. *Chemical Society Reviews*, 45(7):1803–1818, 2016.

[117] Youssef El Khoury, Nicolas Collongues, Jérôme De Sèze, Vildan Gulsari, Christine Patte-Mensah, Gilles Marcou, Alexandre Varnek, Ayikoé Guy Mensah-Nyagan, and Petra Hellwig. Serum-based differentiation between multiple sclerosis and amyotrophic lateral sclerosis by random forest classification of ftir spectra. *Analyst*, 144(15):4647–4652, 2019.

[118] Magdalena Kołodziej, Karolina Chrabąszcz, Ewa Pięta, Natalia Piergies, Julia Rudnicka-Czerwiec, Halina Bartosik-Psujek, Czesława Paluszkiewicz, Marian Cholewa, and Wojciech M Kwiatek. Spectral signature of multiple sclerosis. preliminary studies of blood fraction by atr ftir technique. *Biochemical and Biophysical Research Communications*, 593:40–45, 2022.

[119] Dilek Yonar, Levent Ocek, Bedile Irem Tiftikcioglu, Yasar Zorlu, and Feride Severcan. Relapsing-remitting multiple sclerosis diagnosis from cerebrospinal fluids via fourier transform infrared spectroscopy coupled with multivariate analysis. *Scientific reports*, 8(1):1025, 2018.

[120] Michael Jackson, William C Halliday, Henry H Mantsch, et al. Infrared spectroscopic characterisation of multiple sclerosis plaques in the human central nervous system. *Biochimica et Biophysica Acta (BBA)-Molecular Basis of Disease*, 1182 (3):333–337, 1993.

[121] AR Gafson, Tom Thorne, CIJ McKechnie, B Jimenez, R Nicholas, and PM Matthews. Lipoprotein markers associated with disability from multiple sclerosis. *Scientific Reports*, 8(1):17026, 2018.

[122] Steven M LeVine and David L Wetzel. Chemical analysis of multiple sclerosis lesions by ft-ir microspectroscopy. *Free Radical Biology and Medicine*, 25(1):33–41, 1998.

[123] Jörn Lötsch, Susanne Schiffmann, Katja Schmitz, Robert Brunkhorst, Florian

Lerch, Nerea Ferreiros, Sabine Wicker, Irmgard Tegeder, Gerd Geisslinger, and Alfred Ultsch. Machine-learning based lipid mediator serum concentration patterns allow identification of multiple sclerosis patients with high accuracy. *Scientific reports*, 8(1):14884, 2018.

[124] L Nogueras, H Gonzalo, M Jové, J Sol, A Gil-Sanchez, JV Hervás, P Valcheva, C Gonzalez-Mingot, MJ Solana, S Peralta, et al. Lipid profile of cerebrospinal fluid in multiple sclerosis patients: a potential tool for diagnosis. *Scientific reports*, 9(1):11313, 2019.

[125] Luke AJ O'Neill, Rigel J Kishton, and Jeff Rathmell. A guide to immunometabolism for immunologists. *Nature reviews immunology*, 16(9):553–565, 2016.

[126] Steven M LeVine. Albumin and multiple sclerosis. *BMC neurology*, 16(1):1–12, 2016.

[127] Marco Puthenparampil, Paula Tomas-Ojer, Thorsten Hornemann, Andreas Lutterotti, Ilijas Jelcic, Mario Ziegler, Andreas J Hülsmeier, Carolina Cruciani, Wolfgang Faigle, Roland Martin, et al. Altered csf albumin quotient links peripheral inflammation and brain damage in ms. *Neurology-Neuroimmunology Neuroinflammation*, 8(2), 2021.

[128] Pablo Villoslada, Cristina Alonso, Ion Agirrezabal, Ekaterina Kotelnikova, Irati Zubizarreta, Irene Pulido-Valdeolivas, Albert Saiz, Manuel Comabella, Xavier Montalban, Luisa Villar, et al. Metabolomic signatures associated with disease severity in multiple sclerosis. *Neurology-Neuroimmunology Neuroinflammation*, 4 (2), 2017.

[129] Pavan Bhargava and Daniel C Anthony. Metabolomics in multiple sclerosis disease course and progression. *Multiple Sclerosis Journal*, 26(5):591–598, 2020.

[130] Lachlan Porter, Alireza Shoushtarizadeh, George A Jelinek, Chelsea R Brown, Chai K Lim, Alysha M de Livera, Kelly R Jacobs, and Tracey J Weiland. Metabolomic biomarkers of multiple sclerosis: a systematic review. *Frontiers in molecular biosciences*, 7:574133, 2020.

[131] SL Andersen, FBS Briggs, JH Winnike, Y Natanzon, S Maichle, KJ Knagge, LK Newby, and SG Gregory. Metabolome-based signature of disease pathology in ms. *Multiple sclerosis and related disorders*, 31:12–21, 2019.

[132] Andreas Barth. The infrared absorption of amino acid side chains. *Progress in biophysics and molecular biology*, 74(3-5):141–173, 2000.

[133] A Kurt Gamperl and AP Farrell. Cardiac plasticity in fishes: environmental influences and intraspecific differences. *Journal of Experimental Biology*, 207(15): 2539–2550, 2004.

[134] Maria Carmela Cerra, Sandra Imbrogno, Daniela Amelio, Filippo Garofalo, E Colvee, B Tota, and JM Icardo. Cardiac morphodynamic remodelling in the growing eel (anguilla anguilla l.). *Journal of experimental biology*, 207(16):2867–2875, 2004.

[135] Mariacristina Filice, Daniela Amelio, Filippo Garofalo, Sabrina David, Alberto Fucarino, Frank Bo Jensen, Sandra Imbrogno, and Maria Carmela Cerra. Angiotensin ii dependent cardiac remodeling in the eel anguilla anguilla involves the nos/no system. *Nitric Oxide*, 65:50–59, 2017.

[136] Sandra Imbrogno, Filippo Garofalo, Daniela Amelio, Carla Capria, and Maria Carmela Cerra. Humoral control of cardiac remodeling in fish: Role of angiotensin ii. *General and Comparative Endocrinology*, 194:189–197, 2013.

[137] Mariacristina Filice, Serena Leo, Rosa Mazza, Daniela Amelio, Filippo Garofalo, Sandra Imbrogno, Maria Carmela Cerra, and Alfonsina Gattuso. The heart of the adult goldfish carassius auratus as a target of bisphenol a: A multifaceted analysis. *Environmental Pollution*, 269:116177, 2021.

[138] Kenneth D Poss, Lindsay G Wilson, and Mark T Keating. Heart regeneration in zebrafish. *Science*, 298(5601):2188–2190, 2002.

[139] Philip E Bickler and Leslie T Buck. Hypoxia tolerance in reptiles, amphibians, and fishes: life with variable oxygen availability. *Annu. Rev. Physiol.*, 69:145–170, 2007.

[140] Sandra Imbrogno, C Capria, Bruno Tota, and Frank Bo Jensen. Nitric oxide improves the hemodynamic performance of the hypoxic goldfish (carassius auratus) heart. *Nitric Oxide*, 42:24–31, 2014.

[141] S Imbrogno, M Filice, MC Cerra, and A Gattuso. No, co and h2s: What about gasotransmitters in fish and amphibian heart? *Acta Physiologica*, 223(1):e13035, 2018.

[142] Alfonsina Gattuso, Filippo Garofalo, Maria C Cerra, and Sandra Imbrogno. Hypoxia tolerance in teleosts: implications of cardiac nitrosative signals. *Frontiers in Physiology*, 9:366, 2018.

[143] Maedeh Bazmi and Ariel L Escobar. Excitation–contraction coupling in the goldfish (carassius auratus) intact heart. *Frontiers in Physiology*, 11:1103, 2020.

[144] Elizabeth O Ferreira, Katja Anttila, and Anthony P Farrell. Thermal optima and tolerance in the eurythermic goldfish (carassius auratus): relationships between whole-animal aerobic capacity and maximum heart rate. *Physiological and Biochemical Zoology*, 87(5):599–611, 2014.

[145] Pascal J Lafontant, Alan R Burns, Jamie A Grivas, Mary A Lesch, Tanmoy D Lala, Sean P Reuter, Loren J Field, and Tyler D Frounfelter. The giant danio (d. aequipinnatus) as a model of cardiac remodeling and regeneration. *The Anatomical Record: Advances in Integrative Anatomy and Evolutionary Biology*, 295(2): 234–248, 2012.

[146] Jamie Grivas, Maria Haag, Adedoyin Johnson, Trina Manalo, Julia Roell, Tanmoy L Das, Evelyn Brown, Alan R Burns, and Pascal J Lafontant. Cardiac repair and regenerative potential in the goldfish (carassius auratus) heart. *Comparative Biochemistry and Physiology Part C: Toxicology & Pharmacology*, 163:14–23, 2014.

[147] F Garofalo, S Imbrogno, B Tota, and D Amelio. Morpho-functional characterization of the goldfish (carassius auratus l.) heart. *Comparative Biochemistry and Physiology Part A: Molecular & Integrative Physiology*, 163(2):215–222, 2012.

[148] Mariacristina Filice, Maria Carmela Cerra, and Sandra Imbrogno. The goldfish carassius auratus: an emerging animal model for comparative cardiac research. *Journal of Comparative Physiology B*, 192(1):27–48, 2022.

[149] Mariacristina Filice, Alfonsina Gattuso, Sandra Imbrogno, Rosa Mazza, Daniela Amelio, Alessia Caferro, Claudio Agnisola, José Manuel Icardo, and Maria Carmela Cerra. Functional, structural, and molecular remodelling of the goldfish (carassius auratus) heart under moderate hypoxia. *Fish Physiology and Biochemistry*, pages 1–19, 2024.

[150] R. Leal, F. M. Barreiros, L. Alves, F. Romeiro, J. C. Vasco, M. Santos, and C. Marto. Additive manufacturing tooling for the automotive industry. *International Journal of Advanced Manufacturing Technology*, 92:1671–1676, 9 2017. ISSN 14333015. doi: 10.1007/s00170-017-0239-8.

[151] Francis Froes and Rodney Boyer. *Additive manufacturing for the aerospace industry*. Elsevier, first edition edition, 2 2019.

[152] Yu-Cheng Wang, Toly Chen, and Yung-Lan Yeh. Advanced 3d printing technologies for the aircraft industry: a fuzzy systematic approach for assessing the critical factors. *The International Journal of Advanced Manufacturing Technology*, 105: 4059–4069, 2019.

[153] Albert Tarancón and Vincenzo Esposito. *3D Printing for Energy Applications*. Wiley Online Library, 2021.

[154] Mohammed Maniruzzaman. *3D and 4D printing in biomedical applications: process engineering and additive manufacturing*. John Wiley & Sons, 2019.

[155] Yifan Pan, Yulu Zhang, Dakang Zhang, and Yuying Song. 3d printing in construction: state of the art and applications. *The International Journal of Advanced Manufacturing Technology*, 115(5-6):1329–1348, 2021.

[156] Tjaša Kermavnar, Alice Shannon, and Leonard W. O'Sullivan. The application of additive manufacturing / 3d printing in ergonomic aspects of product design: A systematic review. *Applied Ergonomics*, 97, 11 2021. ISSN 18729126. doi: 10.1016/j.apergo.2021.103528.

[157] Chiara Morano, Luigi Bruno, Leonardo Pagnotta, and Marco Alfano. Analysis of crack trapping in 3d printed bio-inspired structural interfaces. *Procedia Structural Integrity*, 12:561–566, 2018.

[158] M Frascio, C Mandolfino, F Moroni, M Jilich, A Lagazzo, M Pizzorni, L Bergonzi, C Morano, M Alfano, and M Avalle. Appraisal of surface preparation in adhesive bonding of additive manufactured substrates. *International Journal of Adhesion and Adhesives*, 106:102802, 2021.

[159] ASTM. Additive manufacturing-general principles-terminology iso/astm 52900:2015, 2015. URL `www.iso.orgwww.astm.org`.

[160] Antonella Sola and Alireza Nouri. Microstructural porosity in additive manufacturing: The formation and detection of pores in metal parts fabricated by powder bed fusion. *Journal of Advanced Manufacturing and Processing*, 1, 7 2019. ISSN 2637-403X. doi: 10.1002/amp2.10021.

[161] John Ryan C. Dizon, Alejandro H. Espera, Qiyi Chen, and Rigoberto C. Advincula. Mechanical characterization of 3d-printed polymers. *Additive Manufacturing*, 20:44–67, 3 2018. ISSN 22148604. doi: 10.1016/j.addma.2017.12.002.

[162] M. Saâdaoui, F. Khaldoun, J. Adrien, H. Reveron, and J. Chevalier. X-ray tomography of additive-manufactured zirconia: Processing defects – strength relations. *Journal of the European Ceramic Society*, 40:3200–3207, 7 2020. ISSN 1873619X. doi: 10.1016/j.jeurceramsoc.2019.04.010.

[163] Vamsi Krishna Balla, Kunal H. Kate, Jagannadh Satyavolu, Paramjot Singh, and Jogi Ganesh Dattatreya Tadimeti. Additive manufacturing of natural fiber reinforced polymer composites: Processing and prospects. *Composites Part B: Engineering*, 174, 10 2019. ISSN 13598368. doi: 10.1016/j.compositesb.2019.106956.

[164] Easir Arafat Papon, Anwarul Haque, and Sameer B. Mulani. Process optimization and stochastic modeling of void contents and mechanical properties in additively manufactured composites. *Composites Part B: Engineering*, 177:107325, 11 2019. ISSN 1359-8368. doi: 10.1016/J.COMPOSITESB.2019.107325.

[165] Praveenkumara Jagadeesh, Madhu Puttegowda, Sanjay Mavinkere Rangappa, Karfidov Alexey, Sergey Gorbatyuk, Anish Khan, Mrityunjay Doddamani, and Suchart Siengchin. A comprehensive review on 3d printing advancements in polymer composites: technologies, materials, and applications. *The International Journal of Advanced Manufacturing Technology*, 121(1-2):127–169, 2022.

[166] B. Caulfield, P. E. McHugh, and S. Lohfeld. Dependence of mechanical properties of polyamide components on build parameters in the sls process. *Journal of Materials Processing Technology*, 182:477–488, 2 2007. ISSN 09240136. doi: 10.1016/j.jmatprotec.2006.09.007.

[167] Anton du Plessis. Effects of process parameters on porosity in laser powder bed fusion revealed by x-ray tomography. *Additive Manufacturing*, 30, 12 2019. ISSN 22148604. doi: 10.1016/j.addma.2019.100871.

[168] K. Moussaoui, W. Rubio, M. Mousseigne, T. Sultan, and F. Rezai. Effects of selective laser melting additive manufacturing parameters of inconel 718 on porosity, microstructure and mechanical properties. *Materials Science and Engineering A*, 735:182–190, 9 2018. ISSN 09215093. doi: 10.1016/j.msea.2018.08.037.

[169] Michele Pavan, M. Faes, D. Strobbe, Brecht Van Hooreweder, Tom Craeghs, David Moens, and W Dewulf. On the influence of inter-layer time and energy density on selected critical-to-quality properties of pa12 parts produced via laser sintering. *Polymer Testing*, 61:386–395, 03 2017.

[170] Silvia Vock, Burghardt Klöden, Alexander Kirchner, Thomas Weißgärber, and Bernd Kieback. Powders for powder bed fusion: a review. *Progress in Additive Manufacturing*, 4(4):383–397, 2019.

[171] Zhao Zhang, XX Yao, and P Ge. Phase-field-model-based analysis of the effects of powder particle on porosities and densities in selective laser sintering additive manufacturing. *International Journal of Mechanical Sciences*, 166:105230, 2020.

[172] Ehsan Malekipour and Hazim El-Mounayri. Common defects and contributing parameters in powder bed fusion am process and their classification for online

monitoring and control: a review. *The International Journal of Advanced Manufacturing Technology*, 95, 03 2018. doi: 10.1007/s00170-017-1172-6.

[173] Ebubekir Koç, Sultan Zeybek, Burçin Özbay Kısasöz, Cemal İrfan Çalışkan, and Mustafa Enes Bulduk. Estimation of surface roughness in selective laser sintering using computational models. *The International Journal of Advanced Manufacturing Technology*, 123(9-10):3033–3045, 2022.

[174] Anish Sachdeva, Sharanjit Singh, and Vishal S Sharma. Investigating surface roughness of parts produced by sls process. *The International Journal of Advanced Manufacturing Technology*, 64:1505–1516, 2013.

[175] Ahmad Y. Al-Maharma, Sandeep P. Patil, and Bernd Markert. Effects of porosity on the mechanical properties of additively manufactured components: a critical review. *Materials Research Express*, 7, 12 2020. ISSN 20531591. doi: 10.1088/2053-1591/abcc5d.

[176] F. H. Kim, S. P. Moylan, E. J. Garboczi, and J. A. Slotwinski. Investigation of pore structure in cobalt chrome additively manufactured parts using x-ray computed tomography and three-dimensional image analysis. *Additive Manufacturing*, 17:23–38, 10 2017. ISSN 22148604. doi: 10.1016/j.addma.2017.06.011.

[177] I. Maskery, N.T. Aboulkhair, M.R. Corfield, C. Tuck, A.T. Clare, R.K. Leach, R.D. Wildman, I.A. Ashcroft, and R.J.M. Hague. Quantification and characterisation of porosity in selectively laser melted al–si10–mg using x-ray computed tomography. *Materials Characterization*, 111:193–204, 2016. ISSN 1044-5803. doi: https://doi.org/10.1016/j.matchar.2015.12.001. URL `https://www.sciencedirect.com/science/article/pii/S1044580315300711`.

[178] Amol S Ghanekar, Richard H Crawford, and Douglas Watson. Optimization of sls process parameters using d-optimality. In *2003 International Solid Freeform Fabrication Symposium*, 2003.

[179] Hadi Zarringhalam, Neil Hopkinson, NF Kamperman, and JJ De Vlieger. Effects of processing on microstructure and properties of sls nylon 12. *Materials Science and Engineering: A*, 435:172–180, 2006.

[180] Andreas Wegner and Gerd Witt. Correlation of process parameters and part properties in laser sintering using response surface modeling. *Physics Procedia*, 39:480–490, 2012.

[181] Anton du Plessis, Philip Sperling, Andre Beerlink, Lerato Tshabalala, Shaik Hoosain, Ntombi Mathe, and Stephan G. le Roux. Standard method for microct-based additive manufacturing quality control 1: Porosity analysis. *MethodsX*, 5:1102–1110, 1 2018. ISSN 22150161. doi: 10.1016/j.mex.2018.09.005.

[182] Göran Flodberg, Henrik Pettersson, and Li Yang. Pore analysis and mechanical performance of selective laser sintered objects. *Additive Manufacturing*, 24:307–315, 2018. ISSN 2214-8604. doi: https://doi.org/10.1016/j.addma.2018.10.001.

[183] ASTM. D 638-00 standard test method for tensile properties of plastics 1, 2014. URL `www.astm.org`.

[184] Tatyana Nizina, Dmitriy Nizin, Nadezhda Kanaeva, and Denis Artamonov. Method for analyzing the kinetics of damage accumulation in the structure of polymer materials under tensile stresses. *AIP Conference Proceedings*, 2371(1): 020010, 2021. doi: 10.1063/5.0059899.

[185] Michele Pavan, Tom Craeghs, Peter Van Puyvelde, Jean-Pierre Kruth, and Wim Dewulf. Understanding the link between process parameters, microstructure and mechanical properties of laser sintered pa12 parts through x-ray computed tomography. *Procedia of the 2nd International Conference on Progress in Additive Manufacturing*, page 0, 05 2016.

[186] Wei Liu, Chaoyue Chen, Sansan Shuai, Ruixin Zhao, Longtao Liu, Xiaodong Wang, Tao Hu, Weidong Xuan, Chuanjun Li, Jianbo Yu, et al. Study of pore defect and mechanical properties in selective laser melted ti6al4v alloy based on x-ray computed tomography. *Materials Science and Engineering: A*, 797:139981, 2020.

[187] Matthew J Donachie. *Titanium: a technical guide*. ASM international, 2000.

[188] Shunyu Liu and Yung C Shin. Additive manufacturing of ti6al4v alloy: A review. *Materials & Design*, 164:107552, 2019.

[189] Anton Du Plessis, Ina Yadroitsava, and Igor Yadroitsev. Effects of defects on mechanical properties in metal additive manufacturing: A review focusing on x-ray tomography insights. *Materials & Design*, 187:108385, 2020.

[190] Qian Chu Liu, Joe Elambasseril, Shou Jin Sun, Martin Leary, Milan Brandt, and Peter Khan Sharp. The effect of manufacturing defects on the fatigue behaviour of ti-6al-4v specimens fabricated using selective laser melting. *Advanced Materials Research*, 891:1519–1524, 2014.

[191] Yukitaka Murakami. *Metal fatigue: effects of small defects and nonmetallic inclusions*. Academic Press, 2019.

[192] Yoichi Yamashita, Takao Murakami, Rei Mihara, Masami Okada, and Yukitaka Murakami. Defect analysis and fatigue design basis for ni-based superalloy 718 manufactured by selective laser melting. *International Journal of Fatigue*, 117: 485–495, 2018.

[193] S Romano, A Brückner-Foit, A Brandão, J Gumpinger, T Ghidini, and S Beretta. Fatigue properties of alsi10mg obtained by additive manufacturing: Defect-based modelling and prediction of fatigue strength. *Engineering Fracture Mechanics*, 187:165–189, 2018.

[194] ASTM. Astm e2207–15. standard practice for strain-controlled axial-torsional testing with thin walled tube specimens. in: Annual book of astm standards, 03. american society of testing and materials, 2006.

[195] Y Murakami, S Kodama, and S Konuma. Quantitative evaluation of effects of non-metallic inclusions on fatigue strength of high strength steels. i: Basic fatigue mechanism and evaluation of correlation between the fatigue fracture stress and the size and location of non-metallic inclusions. *International Journal of Fatigue*, 11(5):291–298, 1989.

[196] Ali Fatemi, Reza Molaei, Shahriar Sharifimehr, Nam Phan, and Nima Shamsaei. Multiaxial fatigue behavior of wrought and additive manufactured ti-6al-4v including surface finish effect. *International Journal of Fatigue*, 100:347–366, 2017.

[197] SR Sandoghchi, GT Jasion, NV Wheeler, S Jain, Z Lian, JP Wooler, RP Boardman, N Baddela, Y Chen, J Hayes, et al. X-ray tomography for structural analysis of microstructured and multimaterial optical fibers and preforms. *Optics Express*, 22(21):26181–26192, 2014.

[198] Mario Ferraro, Maria C Crocco, Fabio Mangini, Maxime Jonard, Francesco Sangiovanni, Mario Zitelli, Raffaele Filosa, Joseph J Beltrano, Antonio De Luca, Riccardo C Barberi, et al. X-ray computed μ-tomography for the characterization of optical fibers. *Optical Materials Express*, 12(11):4210–4222, 2022.

[199] Maria C Crocco, Fabio Mangini, Raffaele Filosa, Andrea Solano, Raffaele G Agostino, Riccardo C Barberi, Vincent Couderc, Mariusz Klimczak, Adam Filipkowski, Ryszard Buczynski, et al. Soft glass optical fiber characterization with x-ray computed microtomography. *Optical Materials Express*, 14(1):70–81, 2023.

[200] Kevin Kiedrowski, Mario Ferraro, Raphael Jauberteau, Stefan Wabnitz, Maria Caterina Crocco, Vincenzo Formoso, Marco Jupé, and Detlev Ristau. Comparing the laser-induced damage distribution in pofs with raytracing simulations. *Optical Materials Express*, 14(5):1430–1445, 2024.

[201] Qian Zhong and Daryl Inniss. Characterization of the lightguiding structure of optical fibers by atomic force microscopy. *Journal of lightwave technology*, 12(9): 1517–1523, 1994.

[202] Matt Young. Optical fiber index profiles by the refracted-ray method (refracted near-field scanning). *Applied optics*, 20(19):3415–3422, 1981.

[203] Masahiro Ikeda, Mitsuhiro Tateda, and Haruo Yoshikiyo. Refractive index profile of a graded index fiber: measurement by a reflection method. *Applied Optics*, 14 (4):814–815, 1975.

[204] Chun-Jen Weng, Ken-Yuh Hsu, and Yung-Fu Chen. Exploiting the image of the surface reflectivity to measure refractive index profiling for various optical fibers. *Optics Express*, 23(9):11755–11762, 2015.

[205] HM Presby, W Mammel, and RM Derosier. Refractive index profiling of graded index optical fibers. *Review of Scientific Instruments*, 47(3):348–352, 1976.

[206] Govind P Agrawal. Nonlinear fiber optics. In *Nonlinear Science at the Dawn of the 21st Century*, pages 195–211. Springer, 2000.

[207] Chunming Chen and Yogesh Jaluria. Effects of doping on the optical fiber drawing process. *International journal of heat and mass transfer*, 52(21-22):4812–4822, 2009.

[208] Daisuke Shindo and Tetsuo Oikawa. *Analytical electron microscopy for materials science*. Springer Science & Business Media, 2013.

[209] Mònica López-Prat, Raffaele Giuseppe Agostino, Sudipa Ray Bandyopadhyay, Begoña Carrascosa, Maria Caterina Crocco, Raffaella De Luca, Raffaele Filosa, Vincenzo Formoso, Carla Lancelotti, Noor Agha Noori, et al. Architectural terracruda sculptures of the silk roads: new conservation insights through a diagnostic approach based on non-destructive x-ray micro-computed tomography. *Studies in Conservation*, 67(4):209–221, 2022.

[210] Paola Donato, Sandro Donato, Luis Barba, Gino Mirocle Crisci, Maria Caterina Crocco, Mariano Davoli, Raffaele Filosa, Vincenzo Formoso, Giancarlo Niceforo, Alejandro Pastrana, et al. Influence of chemical composition and microvesiculation on the chromatic features of the obsidian of sierra de las navajas (hidalgo, mexico). *Minerals*, 12(2):177, 2022.

[211] P Donato, L Barba, MC Crocco, M Davoli, R De Rosa, S Donato, R Filosa, G Lanzafame, G Niceforo, A Pastrana, et al. Study of the micro-vesiculation of the obsidian source of sierra de las navajas (state of hidalgo, mexico). In *Beyond the Glass Mountains-papers presented for the 2019 International Obsidian Conference 27-29 May 2019, Sárospatak*, pages 9–18. Prime Rate Kft, 2021.

[212] RG Agostino et al. Multiphoton ionization of standard optical fibers. *Photonics Research*, 10(6):1394–1400, 2022.

[213] Mario Ferraro, Fabio Mangini, Yifan Sun, Mario Zitelli, Maria Caterina Crocco, Vincenzo Formoso, Raffaele Giuseppe Agostino, Riccardo Cristoforo Barberi, Antonio De Luca, Alessandro Tonello, et al. Fiber optics in the multiphoton ioniza-

tion regime. In *2022 Italian Conference on Optics and Photonics (ICOP)*, pages 1–4. IEEE, 2022.

[214] Mario Ferraro, Fabio Mangini, Yifan Sun, Mario Zitelli, Rocco Crescenzi, Alioune Niang, Maria Caterina Crocco, Vincenzo Formoso, Raffaele G Agostino, Riccardo Barberi, et al. Laser-induced damages in silica multimode optical fibers. In *Fiber Lasers and Glass Photonics: Materials through Applications III*, volume 12142, pages 166–172. SPIE, 2022.

[215] Andrea Smeriglio, Giuseppe Elettivo, Simone Caputo, Maria Caterina Crocco, Joseph John Beltrano, Antonello Nucera, Marco Castriota, Vincenzo Formoso, Riccardo Cristoforo Barberi, Armando Taliano Grasso, et al. A non-destructive archaeometric study of a hellenistic gold jewel. In *International Conference Florence Heri-Tech: the Future of Heritage Science and Technologies*, pages 61–74. Springer, 2022.

[216] Raffaele Filosa, Giuseppe S Elettivo, Mario Ferraro, Salvatore Procopio, Antonella Nicolino, Maria C Crocco, Joseph J Beltrano, Riccardo C Barberi, Vincenzo Formoso, Rita Guzzi, et al. Nonlinear optical effects in natural topaz. *Journal of Luminescence*, 263:120076, 2023.

[217] Andrea Smeriglio, Raffaele Filosa, Maria Caterina Crocco, Vincenzo Formoso, Riccardo Cristoforo Barberi, Andrea Solano, Maria Cerzoso, Annalisa Polosa, Valerio Cerrone, and Raffaele Giuseppe Agostino. A numismatic study of roman coins through x-ray fluorescence and x-ray computed μ-tomography analysis. *Acta IMEKO*, 12(4):1–7, 2023.

[218] MC Crocco, R Filosa, A Smeriglio, V Formoso, RC Barberi, A Solano, M Cerzoso, A Polosa, V Cerrone, and RG Agostino. A non-destructive archaeometric study of roman coins. *Journal of Instrumentation*, 19(05):C05025, 2024.

[219] Andrea Smeriglio, MARIA CATERINA Crocco, Raffaele Filosa, Vincenzo Formoso, Andrea Solano, Riccardo Cristoforo Barberi, Maria Cerzoso, Raffaele Giuseppe Agostino, et al. Roman coins from the “brettii and enotri” museum: a non-destructive archaeometric study by x-ray fluorescence spectroscopy and x-ray microtomography. In *2022 IMEKO TC-4 International Conference on*

Metrology for Archaeology and Cultural Heritage University of Calabria, Italy, October 19-21, 2022, 2022.

Appendix A

Appendix

This appendix summarily reported scientific articles produced during the doctoral period but not shown in the thesis. In these papers, my contribution was to make μ-CT and Electron paramagnetic resonance (EPR) spectroscopy measurements, process, analyze the data, structure, and write the paper when it pertains to X-ray microtomography and EPR.

A.1 Architectural Terracruda Sculptures of the Silk Roads: New Conservation Insights Through a Diagnostic Approach Based on Non-Destructive X-ray μ-CT

STUDIES IN CONSERVATION
https://doi.org/10.1080/00393630.2020.1862605

ORIGINAL RESEARCH OR TREATMENT PAPER

Architectural *Terracruda* Sculptures of the Silk Roads: New Conservation Insights Through a Diagnostic Approach Based on Non-Destructive X-ray Micro-Computed Tomography

Mònica López-Prat[1], Raffaele Giuseppe Agostino[2], Sudipa Ray Bandyopadhyay[3], Begoña Carrascosa[1], Maria Caterina Crocco[2], Raffaella De Luca[4], Raffaele Filosa[2], Vincenzo Formoso[2], Carla Lancelotti[5], Noor Agha Noori[6], Alessandra Pecci[7], José Simón-Cortés[1] and Domenico Miriello[4]

[1]Departament de Conservació i Restauració de Béns Culturals, Universitat Politècnica de València, Valencia, Spain; [2]Dipartimento di Fisica and STAR-Lab, Università della Calabria, Arcavacata di Rende, Italy; [3]Department of Ancient Indian History and Culture, University of Calcutta, Calcutta, India; [4]Dipartimento di Biologia, Ecologia e Scienze della Terra, Università della Calabria, Arcavacata di Rende, Italy; [5]CaSEs Research Group, Universitat Pompeu Fabra, Barcelona, Spain; [6]Archaeology Institute of Afghanistan, Kabul, Afghanistan; [7]ERAAUB Research Group, Universitat de Barcelona, Barcelona, Spain

Figure A.1: Paper: Architectural Terracruda Sculptures of the Silk Roads: New Conservation Insights Through a Diagnostic Approach Based on Non-Destructive X-ray Micro-Computed Tomography.

The research (Figure A.1) presents the results of the study of a fragment of architectural terracruda sculpture from the Buddhist archaeological site of Tepe Narenj (Kabul, Afghanistan, fifth-ninth centuries CE) through X-ray μ-CT analysis. The use of X-ray micro-computed tomography has enabled the analysis of this artwork without the need to destroy the sample, offering valuable insights into the materials used and the sculpting techniques employed.

Through the non-invasive X-ray μ-CT examination of the sample, we observed the stratigraphy (Figure A.2) and the presence of organic components, now degraded, (Figure A.3) in these sculpting. In this regard, the μ-CT has provided valuable information on this artistic process. The results show a high proportion of organic material within the clay mixture, previously unnoticed, is significant for conservation. Understanding the role of organic materials is essential to prevent damage to the sculptures during consolidation and restoration work [209].

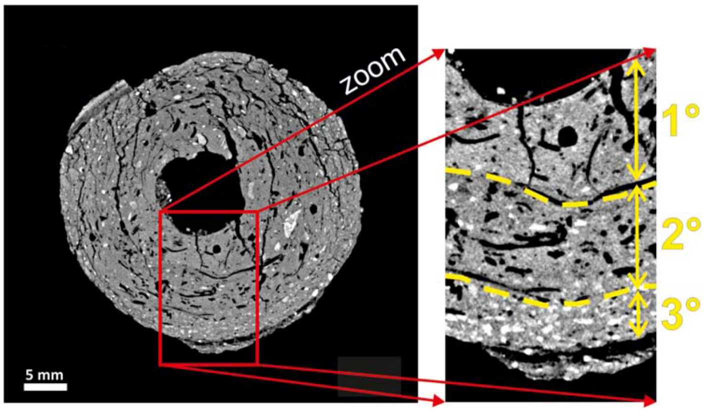

Figure A.2: Equatorial section of the sample, with a close-up of the three main layers.

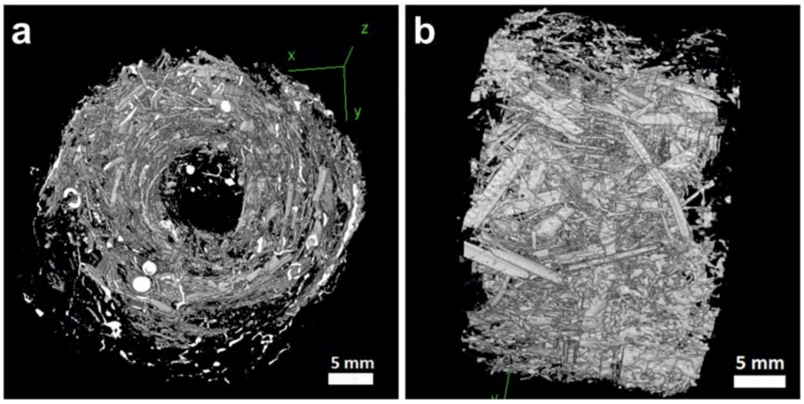

Figure A.3: (a) 3D rendering of the voids shown in the equatorial section; (b) 3D rendering of the voids rotated 90 degrees from the equatorial position.

A.2 Influence of Chemical Composition and Microvesiculation on the Chromatic Features of the Obsidian of Sierra de las Navajas (Hidalgo, Mexico)

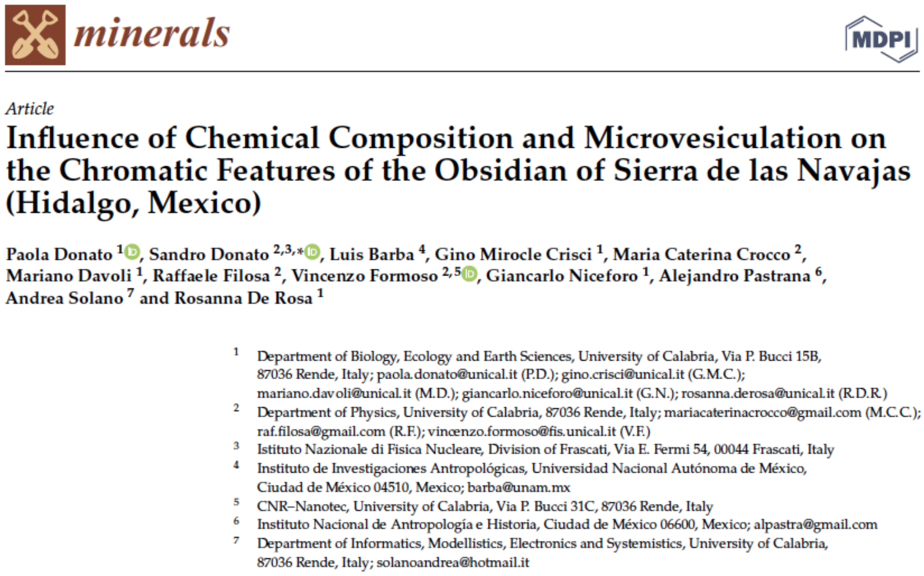

minerals MDPI

Article

Influence of Chemical Composition and Microvesiculation on the Chromatic Features of the Obsidian of Sierra de las Navajas (Hidalgo, Mexico)

Paola Donato [1], Sandro Donato [2,3,*], Luis Barba [4], Gino Mirocle Crisci [1], Maria Caterina Crocco [2], Mariano Davoli [1], Raffaele Filosa [2], Vincenzo Formoso [2,5], Giancarlo Niceforo [1], Alejandro Pastrana [6], Andrea Solano [7] and Rosanna De Rosa [1]

[1] Department of Biology, Ecology and Earth Sciences, University of Calabria, Via P. Bucci 15B, 87036 Rende, Italy; paola.donato@unical.it (P.D.); gino.crisci@unical.it (G.M.C.); mariano.davoli@unical.it (M.D.); giancarlo.niceforo@unical.it (G.N.); rosanna.derosa@unical.it (R.D.R.)
[2] Department of Physics, University of Calabria, 87036 Rende, Italy; mariacaterinacrocco@gmail.com (M.C.C.); raf.filosa@gmail.com (R.F.); vincenzo.formoso@fis.unical.it (V.F.)
[3] Istituto Nazionale di Fisica Nucleare, Division of Frascati, Via E. Fermi 54, 00044 Frascati, Italy
[4] Instituto de Investigaciones Antropológicas, Universidad Nacional Autónoma de México, Ciudad de México 04510, Mexico; barba@unam.mx
[5] CNR–Nanotec, University of Calabria, Via P. Bucci 31C, 87036 Rende, Italy
[6] Instituto Nacional de Antropología e Historia, Ciudad de México 06600, Mexico; alpastra@gmail.com
[7] Department of Informatics, Modellistics, Electronics and Systemistics, University of Calabria, 87036 Rende, Italy; solanoandrea@hotmail.it

Figure A.4: Paper: Influence of Chemical Composition and Microvesiculation on the Chromatic Features of the Obsidian of Sierra de las Navajas (Hidalgo, Mexico).

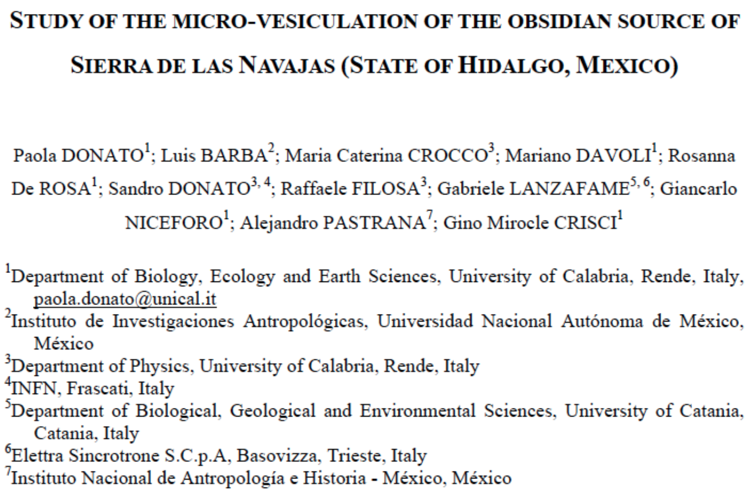

STUDY OF THE MICRO-VESICULATION OF THE OBSIDIAN SOURCE OF SIERRA DE LAS NAVAJAS (STATE OF HIDALGO, MEXICO)

Paola DONATO[1]; Luis BARBA[2]; Maria Caterina CROCCO[3]; Mariano DAVOLI[1]; Rosanna De ROSA[1]; Sandro DONATO[3, 4]; Raffaele FILOSA[3]; Gabriele LANZAFAME[5, 6]; Giancarlo NICEFORO[1]; Alejandro PASTRANA[7]; Gino Mirocle CRISCI[1]

[1]Department of Biology, Ecology and Earth Sciences, University of Calabria, Rende, Italy, paola.donato@unical.it
[2]Instituto de Investigaciones Antropológicas, Universidad Nacional Autónoma de México, México
[3]Department of Physics, University of Calabria, Rende, Italy
[4]INFN, Frascati, Italy
[5]Department of Biological, Geological and Environmental Sciences, University of Catania, Catania, Italy
[6]Elettra Sincrotrone S.C.p.A, Basovizza, Trieste, Italy
[7]Instituto Nacional de Antropología e Historia - México, México

Figure A.5: Conference proceedings: Study of the micro-vesiculation of the obsidian source of Sierra De Las Navajas (State of Hidalgo, Mexico).

Obsidians from Sierra de las Navajas in Mexico are known for their color ranging from dark green to light green to golden (as opposed to Lipari obsidians, which are black). To correlate visual characteristics (color) with compositional and microstructural features, we performed a study (Figures A.4, A.5) by Wave Dispersion System associated with Electron Probe Micro-Analyzer, Scanning Electron Microscope observation, and μ-CT analysis.

Our results show that the green color of obsidian is due to a high iron content. SEM observation and μ-CT study showed no presence of microcrystals, while vesicles of different sizes, shapes, and orientations were present. The light green samples incorporate several vesicles within them, while the darker samples are not vesiculated. When a high concentration of vesicles is present, the sample shows a golden coloration. The μ-CT analysis (Figure A.6) showed how the orientation of vesicles along preferential directions and their distribution in bands determine the variation in color intensity and shade on differently oriented surfaces.

The results confirm that X-ray μ-CT provides a detailed view of the 3D shape and internal distribution of vesicles it can thus be a valuable tool for studies of the pre- and post-eruptive history of obsidian [210, 211].

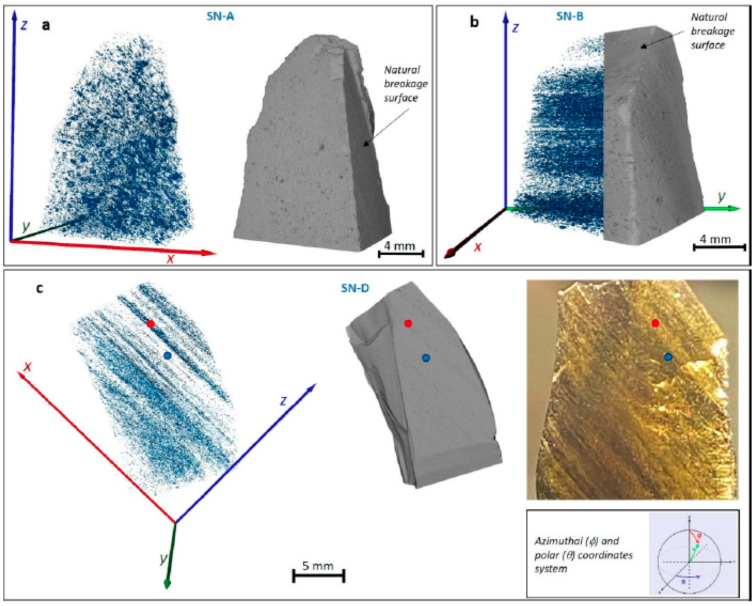

Figure A.6: 3D rendering of the obsidians and vesicles obtained from X-ray microtomography analysis for different samples: (a) SN-A, (b) SN-B, (c) SN-D.

A.3 Multiphoton ionization of standard optical fibers

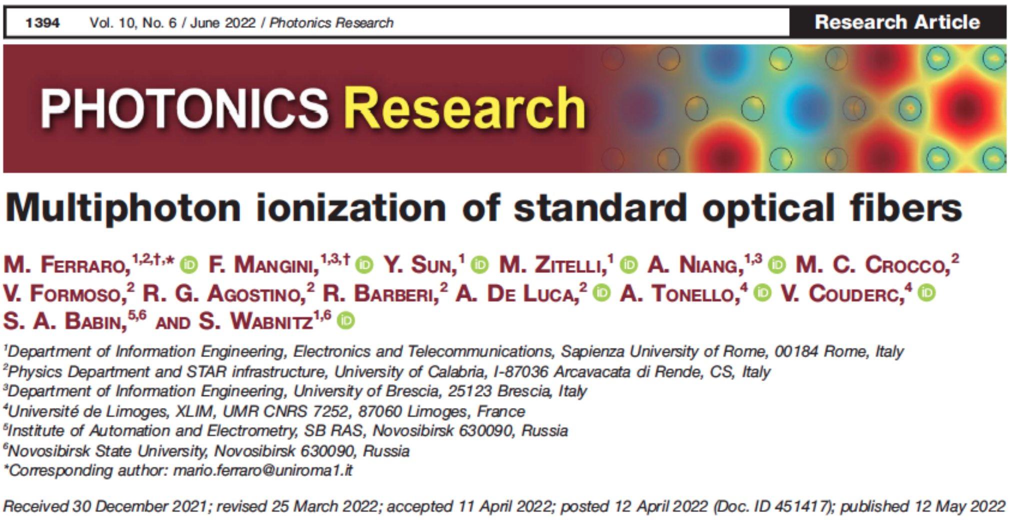

1394 Vol. 10, No. 6 / June 2022 / *Photonics Research* **Research Article**

PHOTONICS Research

Multiphoton ionization of standard optical fibers

M. Ferraro,[1,2,†,*] **F. Mangini,**[1,3,†] **Y. Sun,**[1] **M. Zitelli,**[1] **A. Niang,**[1,3] **M. C. Crocco,**[2] **V. Formoso,**[2] **R. G. Agostino,**[2] **R. Barberi,**[2] **A. De Luca,**[2] **A. Tonello,**[4] **V. Couderc,**[4] **S. A. Babin,**[5,6] **and S. Wabnitz**[1,6]

[1]*Department of Information Engineering, Electronics and Telecommunications, Sapienza University of Rome, 00184 Rome, Italy*
[2]*Physics Department and STAR infrastructure, University of Calabria, I-87036 Arcavacata di Rende, CS, Italy*
[3]*Department of Information Engineering, University of Brescia, 25123 Brescia, Italy*
[4]*Université de Limoges, XLIM, UMR CNRS 7252, 87060 Limoges, France*
[5]*Institute of Automation and Electrometry, SB RAS, Novosibirsk 630090, Russia*
[6]*Novosibirsk State University, Novosibirsk 630090, Russia*
**Corresponding author: mario.ferraro@uniroma1.it*

Received 30 December 2021; revised 25 March 2022; accepted 11 April 2022; posted 12 April 2022 (Doc. ID 451417); published 12 May 2022

Figure A.7: Paper: Multiphoton ionization of standard optical fibers.

SPIE. Event: SPIE Photonics Europe, 2022, Strasbourg, France

Laser-induced damages in silica multimode optical fibers

Mario Ferraro[a,b], Fabio Mangini[a,c], Yifan Sun[a], Mario Zitelli[a], Rocco Crescenzi[a], Alioune Niang[a], Maria C. Crocco[b], Vincenzo Formoso[b], Raffaele G. Agostino[b], Riccardo Barberi[b], Antonio De Luca[b], Alessandro Tonello[d], Sergey A. Babin[e,f], Vincent Couderc[d], and Stefan Wabnitz[a,g]

[a]Department of Information Engineering, Electronics and Telecommunications, Sapienza University of Rome, Via Eudossiana 18, 00184 Rome, Italy
[b]STAR Research Infrastructure and Physics Department, University of Calabria, I-87036 Arcavacata di Rende, CS, Italy
[c]Department of Information Engineering, University of Brescia, Via Branze 38, 25123 Brescia, Italy
[d]Université de Limoges, XLIM, UMR CNRS 7252, 123 Avenue A. Thomas, 87060 Limoges, France
[e]Novosibirsk State University, Pirogova 1, Novosibirsk 630090, Russia
[f]Institute of Automation and Electrometry, Novosibirsk 630090, Russia
[g]CNR-INO, Istituto Nazionale di Ottica, Via Campi Flegrei 34, 80078 Pozzuoli (NA), Italy

Figure A.8: Conference proceedings: Laser-induced damages in silica multimode optical fibers.

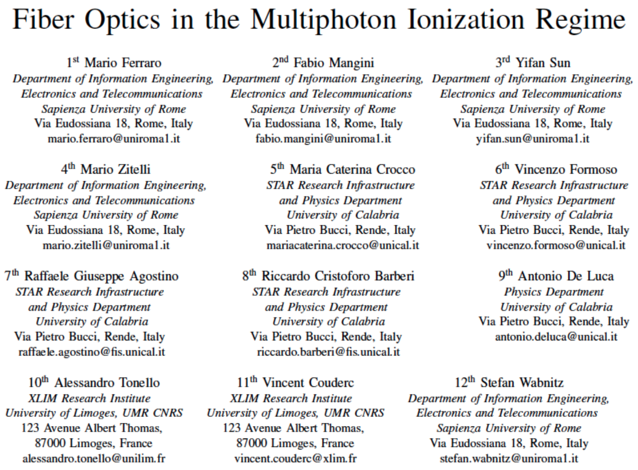

Fiber Optics in the Multiphoton Ionization Regime

1st Mario Ferraro
Department of Information Engineering,
Electronics and Telecommunications
Sapienza University of Rome
Via Eudossiana 18, Rome, Italy
mario.ferraro@uniroma1.it

2nd Fabio Mangini
Department of Information Engineering,
Electronics and Telecommunications
Sapienza University of Rome
Via Eudossiana 18, Rome, Italy
fabio.mangini@uniroma1.it

3rd Yifan Sun
Department of Information Engineering,
Electronics and Telecommunications
Sapienza University of Rome
Via Eudossiana 18, Rome, Italy
yifan.sun@uniroma1.it

4th Mario Zitelli
Department of Information Engineering,
Electronics and Telecommunications
Sapienza University of Rome
Via Eudossiana 18, Rome, Italy
mario.zitelli@uniroma1.it

5th Maria Caterina Crocco
STAR Research Infrastructure
and Physics Department
University of Calabria
Via Pietro Bucci, Rende, Italy
mariacaterina.crocco@unical.it

6th Vincenzo Formoso
STAR Research Infrastructure
and Physics Department
University of Calabria
Via Pietro Bucci, Rende, Italy
vincenzo.formoso@unical.it

7th Raffaele Giuseppe Agostino
STAR Research Infrastructure
and Physics Department
University of Calabria
Via Pietro Bucci, Rende, Italy
raffaele.agostino@fis.unical.it

8th Riccardo Cristoforo Barberi
STAR Research Infrastructure
and Physics Department
University of Calabria
Via Pietro Bucci, Rende, Italy
riccardo.barberi@fis.unical.it

9th Antonio De Luca
Physics Department
University of Calabria
Via Pietro Bucci, Rende, Italy
antonio.deluca@unical.it

10th Alessandro Tonello
XLIM Research Institute
University of Limoges, UMR CNRS
123 Avenue Albert Thomas,
87000 Limoges, France
alessandro.tonello@unilim.fr

11th Vincent Couderc
XLIM Research Institute
University of Limoges, UMR CNRS
123 Avenue Albert Thomas,
87000 Limoges, France
vincent.couderc@xlim.fr

12th Stefan Wabnitz
Department of Information Engineering,
Electronics and Telecommunications
Sapienza University of Rome
Via Eudossiana 18, Rome, Italy
stefan.wabnitz@uniroma1.it

Figure A.9: Conference proceedings: Fiber Optics in the Multiphoton Ionization Regime.

In these researches (Figures A.7, A.8, A.9), we studied the multiphoton ionization of standard optical fibers, specifically using intense laser pulses to ionize the atoms that make up the structure of the fiber itself. We have characterized the material changes produced. In particular, the damage characteristics are studied by optical microscopy and X-ray microtomography. Our results (Figure A.10) show that X-ray imaging can be a powerful and previously unused tool for detecting micrometer-sized features of glassy structures, such as standard optical fibers [212–214].

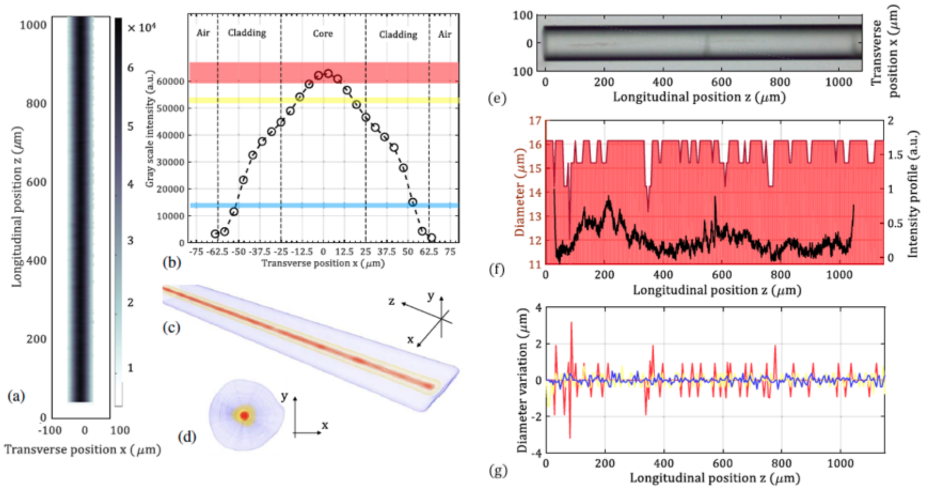

Figure A.10: (a) Radiography of a GRIN 50/125 fiber. (b) Corresponding intensity profile along the transverse direction x. (c) 3D rendering and (d) slice in the xy plane of the μ-CT image of the fiber. Analysis of fiber damages: (e) Optical microscope image. (f) Comparison between the intensity profile along the fiber axis in (e) (black curve) with the diameter of the red zone (red area). (g) Variation along z of the diameter of each zone.

A.4 A Non-destructive Archaeometric Study of a Hellenistic Gold Jewel

Springer

Chapter 5
A Non-destructive Archaeometric Study
of a Hellenistic Gold Jewel

Andrea Smeriglio, Giuseppe Elettivo, Simone Caputo,
Maria Caterina Crocco, Joseph John Beltrano, Antonello Nucera,
Marco Castriota, Vincenzo Formoso, Riccardo Cristoforo Barberi,
Armando Taliano Grasso, Giada Chiodo, and Raffaele Giuseppe Agostino

Figure A.11: Paper: A Non-destructive Archaeometric Study of a Hellenistic Gold Jewel.

In this research (Figure A.11) we studied an archaeological find consisting of a piece of Hellenistic gold jewelry set with a gemstone. It was found in the Serre Boscose locality in the municipality of Cariati (CS), Italy, and was probably produced by the Greek colony of Taranto, Italy. We carried out a non-destructive study of the gold jewel by X-ray μ-CT to recover its internal structure and describe the details of the metalwork. Sources on the technological processes used in the art of ancient goldsmithing are largely fragmentary, and an ongoing effort must be developed to describe these processes. The use of non-destructive techniques makes possible to study the morphology of the artifact, allowing the technological processes used in its production to be recovered. The μ-CT allowed us to acquire the volumetric model of the find (Figure A.12a) and to characterize its internal structure with a resolution of 10 μm (Figure A.12b). The results aided the identification and description of the manufacturing methods used by Hellenistic goldsmiths [215].

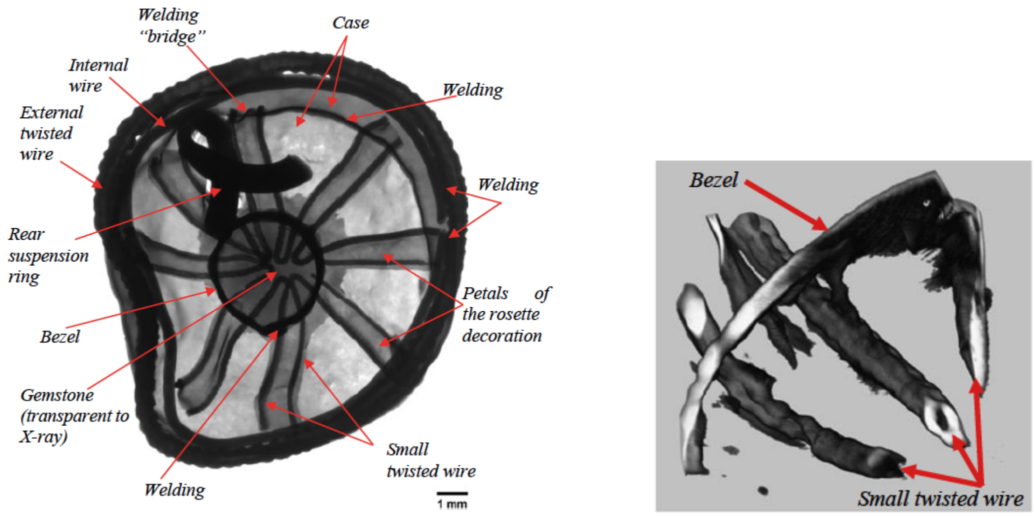

(a)

(b)

Figure A.12: (a) X-ray radiography of the jewel in frontal projection. The arrows point to parts composing the earring. (b) Virtual X-ray cross-section in which is visible the tubular structure of the small twisted wire.

A.5 Experimental Study on the Mechanical Properties of Basalt FRCM Made of Various Matrices: Validation by X-Ray Microtomography

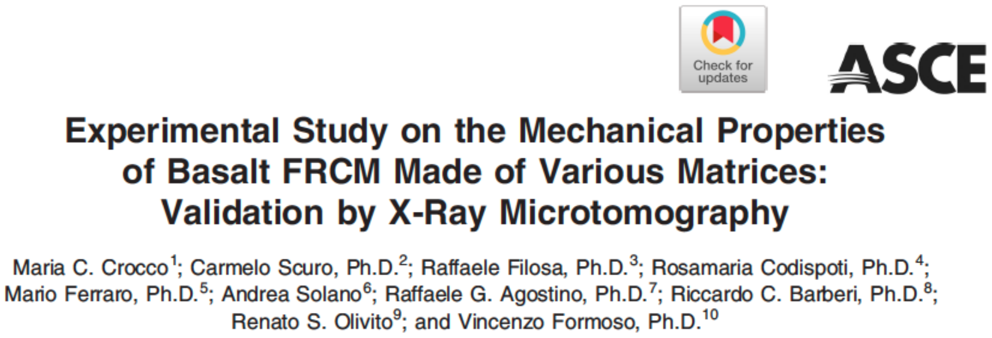

Experimental Study on the Mechanical Properties of Basalt FRCM Made of Various Matrices: Validation by X-Ray Microtomography

Maria C. Crocco[1]; Carmelo Scuro, Ph.D.[2]; Raffaele Filosa, Ph.D.[3]; Rosamaria Codispoti, Ph.D.[4];
Mario Ferraro, Ph.D.[5]; Andrea Solano[6]; Raffaele G. Agostino, Ph.D.[7]; Riccardo C. Barberi, Ph.D.[8];
Renato S. Olivito[9]; and Vincenzo Formoso, Ph.D.[10]

Figure A.13: Paper: Experimental Study on the Mechanical Properties of Basalt FRCM Made of Various Matrices: Validation by X-Ray Microtomography.

In this paper (Figure A.13), fibro-reinforced mortar (basalt) matrices with different compositions and mechanical properties were studied. One matrix made with an inorganic resin and two organic ones (same resin, but different resin mortar weight ratios, and using water in one case) were studied. These were analyzed in terms of compressive strength, flexural strength, and tensile strength. Subsequently, by X-ray μ-CT, the correlation between the voids in the mortar and the adhesion between matrix and fiber were evaluated. X-ray μ-CT imaging was used to obtain a non-destructive two-dimensional and three-dimensional characterization of the specimens and to detect cracks and voids (Figure A.14). The 3D map returned the precise location of voids and damage in the different samples analyzed. The μ-CT results are in agreement with those of the mechanical tests, showing that organic resins provide better adhesion with basalt fibers (Figure A.15). In particular, it is deduced that the matrices made with organic resin are characterized by a greater number of voids within their fiber reinforcement. In contrast, specimens made with inorganic resin were more uniform in terms of fiber density [49].

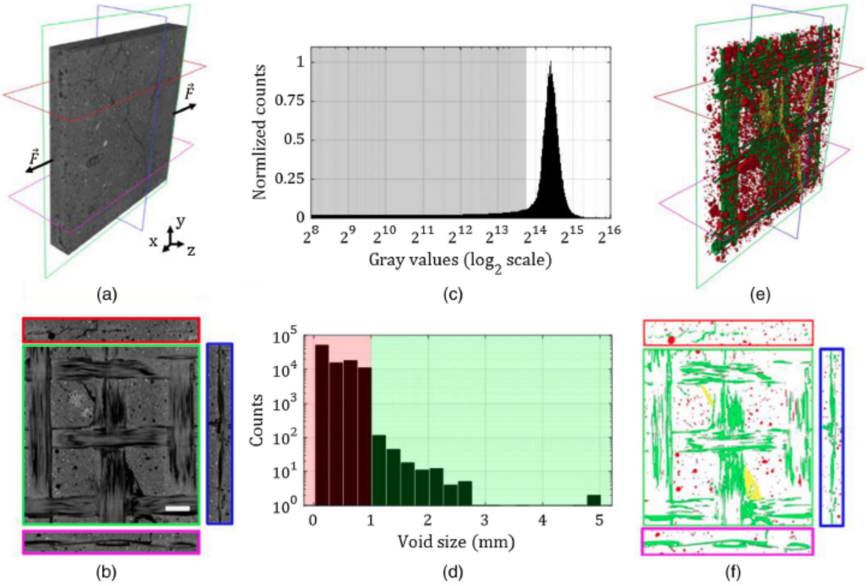

Figure A.14: Analysis of the μ-CT images of the sample: (a) 3D rendering; and (b) 2D slices taken from (a) following the color code of the frames. The scale bar in (b) is 3 mm long; (c and d) segmentation process that applies a threshold filter on the gray scale values (c) and a color code to the voxel size (d); and (e and f) same as (a and b) after the segmentation process in (c and d).

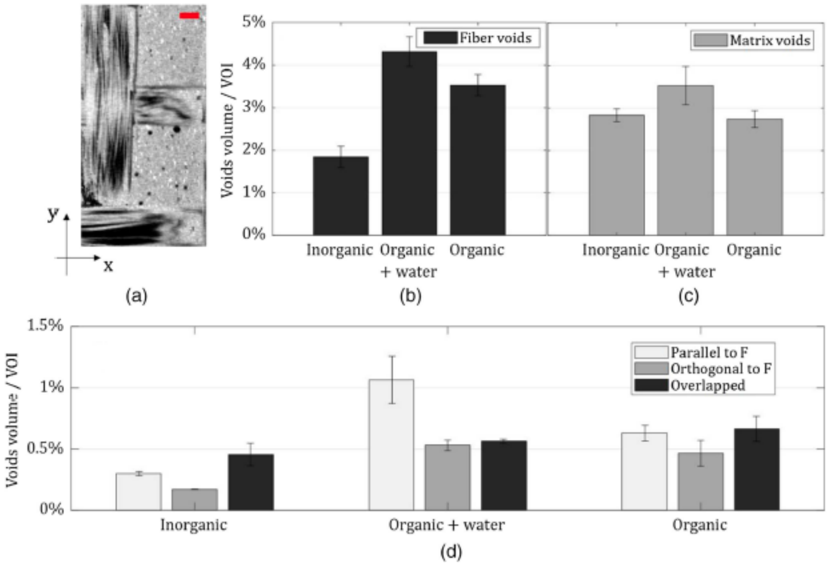

Figure A.15: (a) xy slice, the scale-bar is equal to 1 mm. (b) Voids volume of fiber. (c) Voids volume of matrix. (d) Comparison among the fibers displaced either parallel or orthogonal to the tensile stress direction (x).

A.6 Nonlinear optical effects in natural topaz

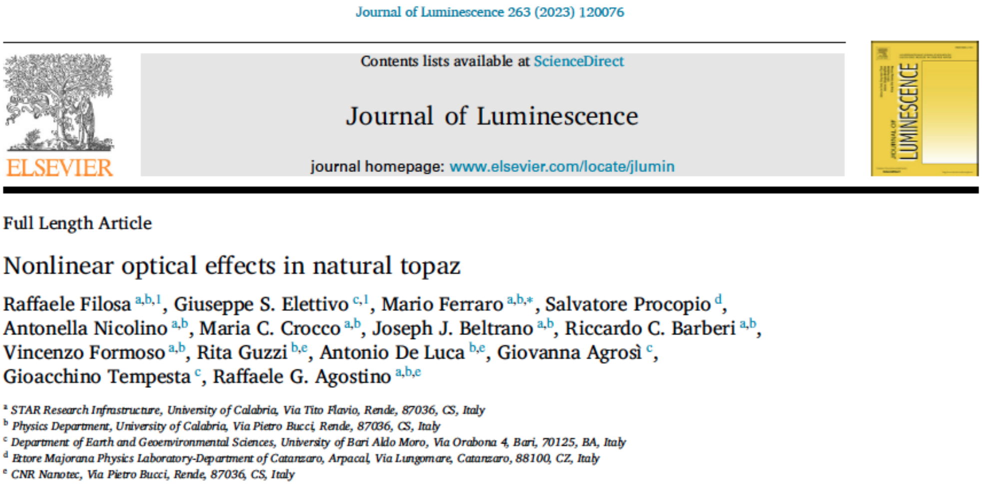

Journal of Luminescence 263 (2023) 120076

Contents lists available at ScienceDirect

Journal of Luminescence

journal homepage: www.elsevier.com/locate/jlumin

Full Length Article

Nonlinear optical effects in natural topaz

Raffaele Filosa [a,b,1], Giuseppe S. Elettivo [c,1], Mario Ferraro [a,b,*], Salvatore Procopio [d],
Antonella Nicolino [a,b], Maria C. Crocco [a,b], Joseph J. Beltrano [a,b], Riccardo C. Barberi [a,b],
Vincenzo Formoso [a,b], Rita Guzzi [b,e], Antonio De Luca [b,e], Giovanna Agrosì [c],
Gioacchino Tempesta [c], Raffaele G. Agostino [a,b,e]

[a] *STAR Research Infrastructure, University of Calabria, Via Tito Flavio, Rende, 87036, CS, Italy*
[b] *Physics Department, University of Calabria, Via Pietro Bucci, Rende, 87036, CS, Italy*
[c] *Department of Earth and Geoenvironmental Sciences, University of Bari Aldo Moro, Via Orabona 4, Bari, 70125, BA, Italy*
[d] *Ettore Majorana Physics Laboratory-Department of Catanzaro, Arpacal, Via Lungomare, Catanzaro, 88100, CZ, Italy*
[e] *CNR Nanotec, Via Pietro Bucci, Rende, 87036, CS, Italy*

Figure A.16: Paper: Nonlinear optical effects in natural topaz.

In this paper (Figure A.16) we investigate the nonlinear optical properties of natural topaz (Figure A.18). The observation of nonlinear phenomena related to multiphoton absorption effects is reported in natural gemstones. In particular, we revealed that the presence of AlO_4-related defects is responsible for the color change of topaz upon irradiation with ionizing radiation. In this work, we tracked the evolution of the absorbance spectrum as a consequence of hard X-ray irradiation, which led our colorless topaz sample to acquire a yellow/brown color (Figure A.18). The use of intense laser beams made possible to detect the presence of rare-earth elements, such as ytterbium and neodymium, that are not detected by standard characterization techniques of natural gems, e.g., those based on X-ray fluorescence, X-ray μ-CT (Figure A.17), EPR (Figure A.19), linear optical fluorescence and absorbance measurements. Our results demonstrate that luminescence measurements induced by nonlinear optical effects are a complementary technique for characterizing the optical and physicochemical properties of natural gems [216].

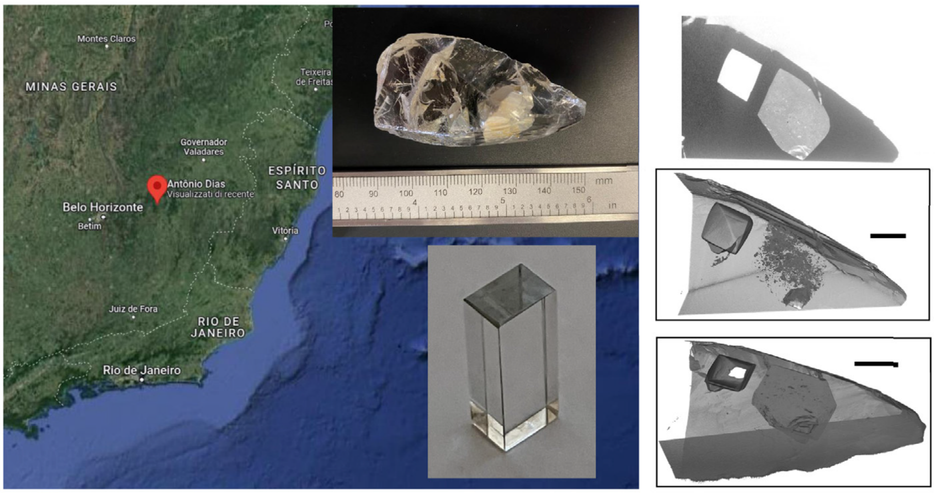

Figure A.17: Natural topaz sample. (a) Geographical position of the mine. (b) Image of the whole sample. (c) Single tomographic slice. (d, e) Tomographic 3D rendering of the sample with different orientations. (f) Image of the parallelepiped-shaped piece of the sample which is used for the characterization.

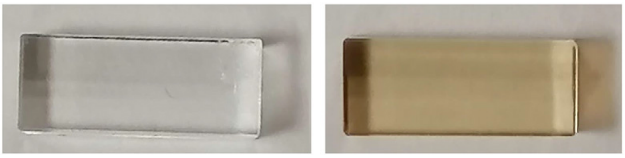

Figure A.18: Picture of the sample (left) before and (right) after 95 h of X-ray irradiation.

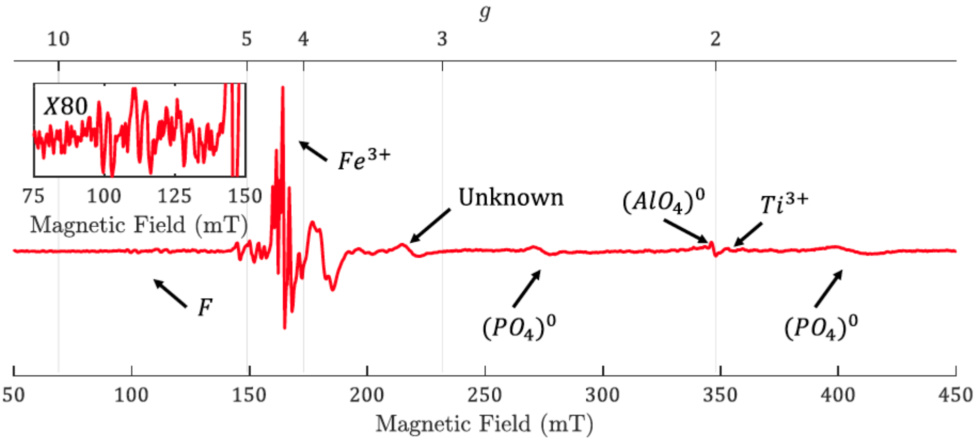

Figure A.19: EPR spectrum of natural topaz recorded at room temperature. The top axis represents the g parameter, whose value is calculated as $g = h\nu/\beta H$, where h is the Planck constant, ν is the microwave frequency, β is the Bohr magneton, and H is the magnetic field.

A.7 A non-destructive archaeometric study of Roman coins

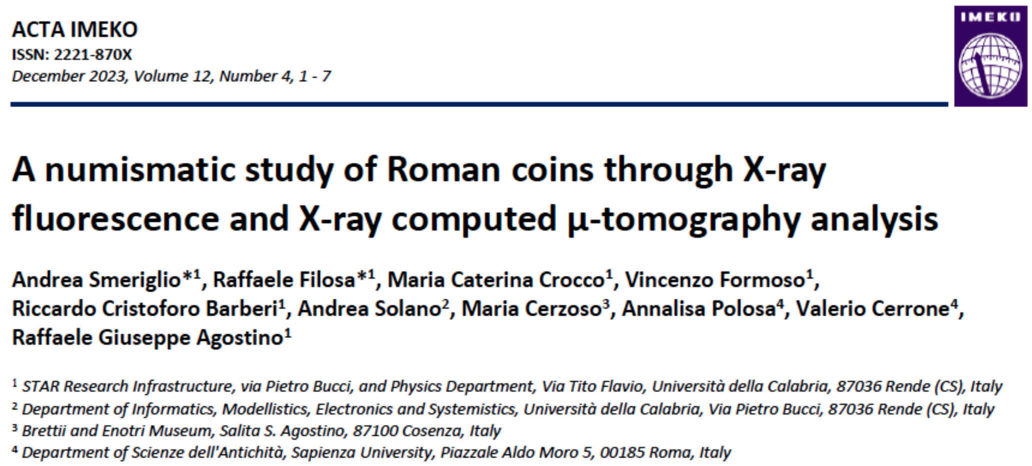

ACTA IMEKO
ISSN: 2221-870X
December 2023, Volume 12, Number 4, 1 - 7

A numismatic study of Roman coins through X-ray fluorescence and X-ray computed µ-tomography analysis

Andrea Smeriglio*[1], Raffaele Filosa*[1], Maria Caterina Crocco[1], Vincenzo Formoso[1], Riccardo Cristoforo Barberi[1], Andrea Solano[2], Maria Cerzoso[3], Annalisa Polosa[4], Valerio Cerrone[4], Raffaele Giuseppe Agostino[1]

[1] STAR Research Infrastructure, via Pietro Bucci, and Physics Department, Via Tito Flavio, Università della Calabria, 87036 Rende (CS), Italy
[2] Department of Informatics, Modellistics, Electronics and Systemistics, Università della Calabria, Via Pietro Bucci, 87036 Rende (CS), Italy
[3] Brettii and Enotri Museum, Salita S. Agostino, 87100 Cosenza, Italy
[4] Department of Scienze dell'Antichità, Sapienza University, Piazzale Aldo Moro 5, 00185 Roma, Italy

Figure A.20: Paper: A numismatic study of Roman coins through X-ray fluorescence and X-ray computed μ-tomography analysis.

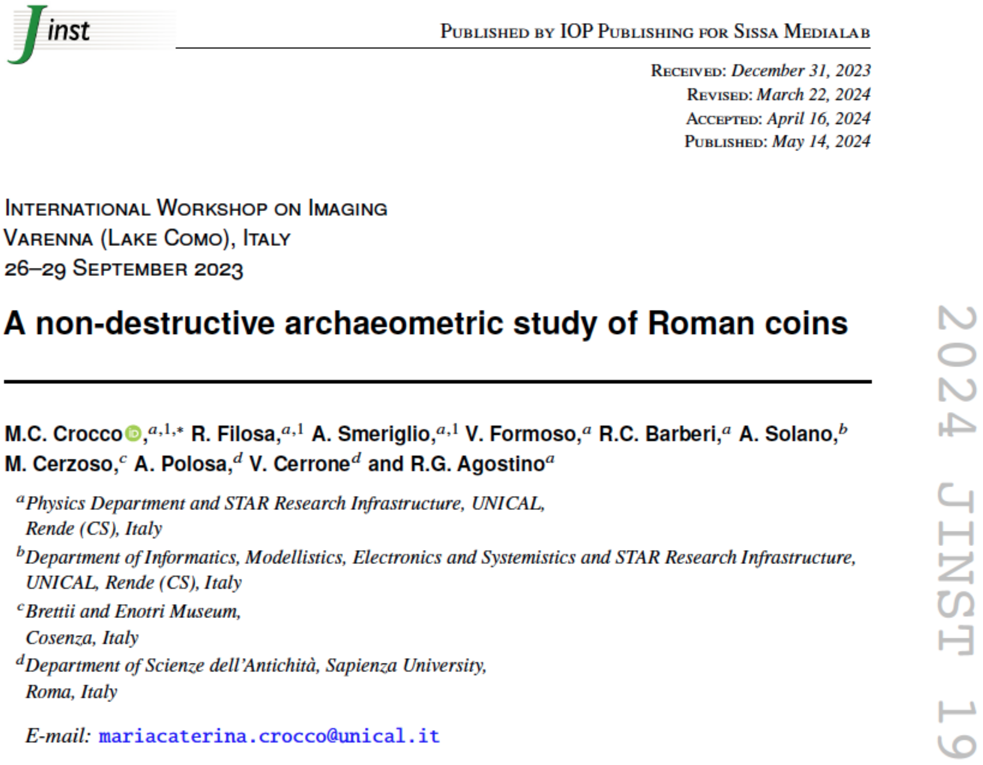

Jinst
PUBLISHED BY IOP PUBLISHING FOR SISSA MEDIALAB

RECEIVED: December 31, 2023
REVISED: March 22, 2024
ACCEPTED: April 16, 2024
PUBLISHED: May 14, 2024

INTERNATIONAL WORKSHOP ON IMAGING
VARENNA (LAKE COMO), ITALY
26–29 SEPTEMBER 2023

A non-destructive archaeometric study of Roman coins

M.C. Crocco,[a,1,*] R. Filosa,[a,1] A. Smeriglio,[a,1] V. Formoso,[a] R.C. Barberi,[a] A. Solano,[b] M. Cerzoso,[c] A. Polosa,[d] V. Cerrone[d] and R.G. Agostino[a]

[a] Physics Department and STAR Research Infrastructure, UNICAL, Rende (CS), Italy
[b] Department of Informatics, Modellistics, Electronics and Systemistics and STAR Research Infrastructure, UNICAL, Rende (CS), Italy
[c] Brettii and Enotri Museum, Cosenza, Italy
[d] Department of Scienze dell'Antichità, Sapienza University, Roma, Italy

E-mail: mariacaterina.crocco@unical.it

2024 JINST 19

Figure A.21: Paper: A non-destructive archaeometric study of Roman coins.

2022 IMEKO TC-4 International Conference on
Metrology for Archaeology and Cultural Heritage
University of Calabria, Italy, October 19-21, 2022

Roman coins from the "Brettii and Enotri" museum: a non-destructive archaeometric study by X-ray fluorescence spectroscopy and X-ray microtomography

Smeriglio Andrea[a,b], Crocco Maria Caterina[a,b], Filosa Raffaele[a,b], Formoso Vincenzo[a,b], Solano Andrea[a,c], Barberi Riccardo Cristoforo[a,b], Cerzoso Maria[d], Agostino Raffaele Giuseppe[a,b]

[a] STAR Research Infrastructure, Università della Calabria, Via Tito Flavio, 87036 Rende (CS), Italy
[b] Physics Department, Università della Calabria, Via Pietro Bucci, 87036 Rende (CS), Italy
[c] Department of Informatics, Modellistics, Electronics and Systemistics, Università della Calabria, Via Pietro Bucci, 87036 Rende (CS), Italy
[d]Brettii and Enotri Museum, Salita S. Agostino, 87100 Cosenza, Italy

Figure A.22: Conference proceedings: Roman coins from the "Brettii and Enotri" museum: a non-destructive archaeometric study by X-ray fluorescence spectroscopy and X-ray microtomography.

In these papers (Figures A.20, A.21, A.22), thirteen Roman coins have been the subject of a non-destructive numismatic and archaeometric analysis. In particular, we studied thirty Roman coins that were discovered in the so-called "Grotta delle Ninfe" near Cerchiara di Calabria in Calabria, Italy, and are currently preserved at the Brettii and Enotri Museum in Cosenza, Calabria, Italy. These coins, due to the nearby sulphurous water source, have followed a degradation process. The inscriptions cannot be read at all because of a heavy layer of corrosion products. In this work, we characterized by X-ray fluorescence and X-ray μ-CT to identify the constituent material, coinage stamp, and inscriptions present on the coins. We were able to decipher some inscriptions using the μ-CT, and we discovered the provenance and manufacturing era of the coins by numismatic research (Figures A.23, A.24). With our study, we have found that some coins are in orichalcum, while others are in copper. Furthermore, we have identified the historical period to which they belong and we can conclude that the coins were minted during the reign of Augustus, Vespasian, Domitian, and Trajan, the imperial era coinage [217–219].

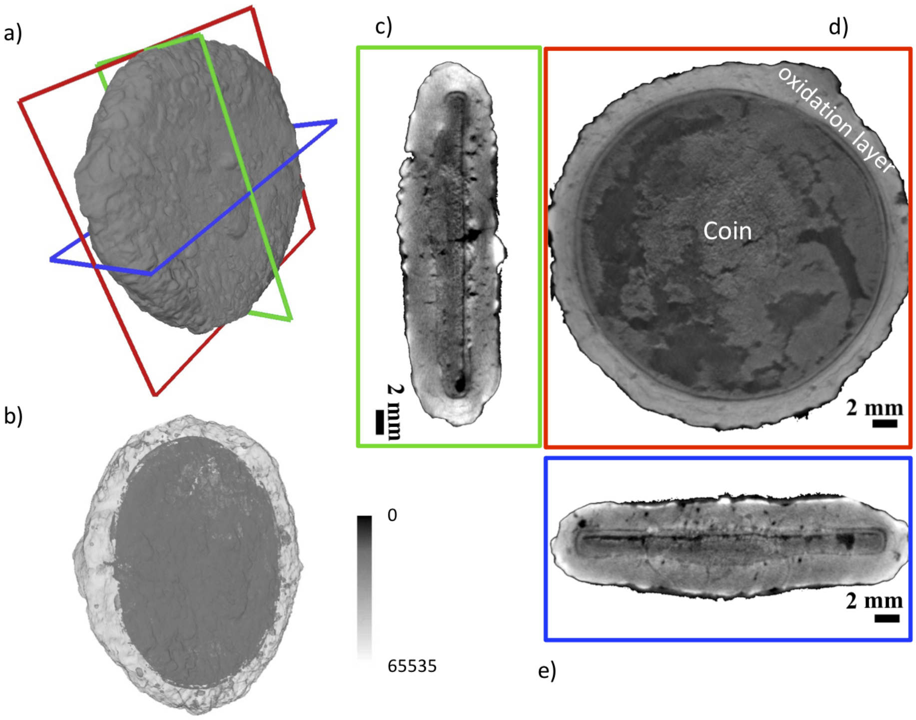

Figure A.23: (a,b) 3D rendering of one of the highly degraded coins and (c,d,e) xz, xy, yz tomographic planes.

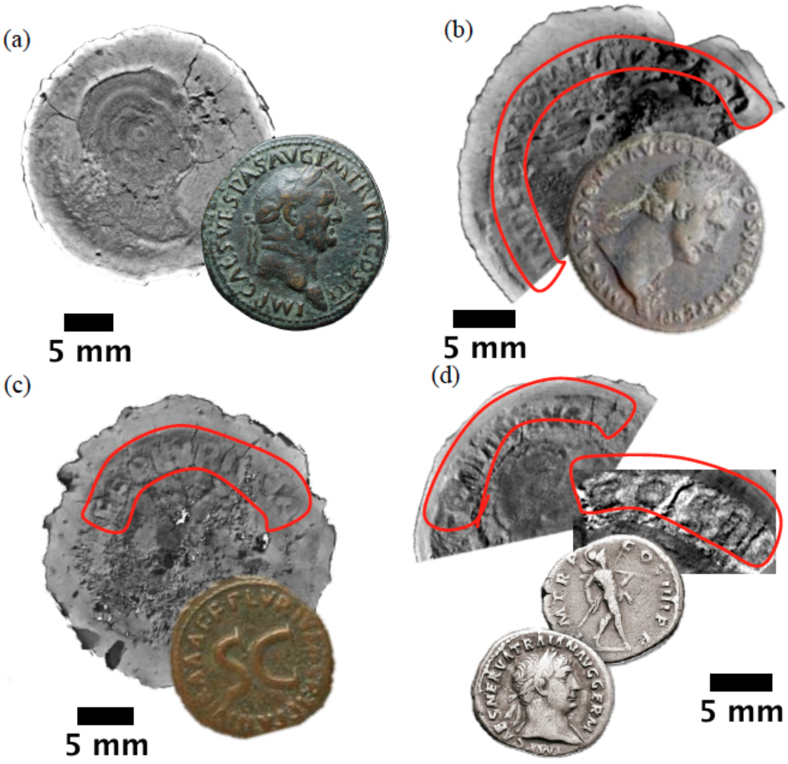

Figure A.24: Some μ-CT results.